

JYU DISSERTATIONS 345

Mira Ahinko

Computational Cytochrome P450 Mediated Metabolism and Virtual Screening



UNIVERSITY OF JYVÄSKYLÄ
FACULTY OF MATHEMATICS
AND SCIENCE

JYU DISSERTATIONS 345

Mira Ahinko

Computational Cytochrome P450 Mediated Metabolism and Virtual Screening

Esitetään Jyväskylän yliopiston matemaattis-luonnontieteellisen tiedekunnan suostumuksella
julkisesti tarkastettavaksi tammikuun 15. päivänä 2021 kello 12.

Academic dissertation to be publicly discussed, by permission of
the Faculty of Mathematics and Science of the University of Jyväskylä,
on January 15 2021 at 12 o'clock noon.



JYVÄSKYLÄN YLIOPISTO
UNIVERSITY OF JYVÄSKYLÄ

JYVÄSKYLÄ 2021

Editors

Varpu Marjomäki

Department of Biological and Environmental Science, University of Jyväskylä

Ville Korkiakangas

Open Science Centre, University of Jyväskylä

Copyright © 2021, by University of Jyväskylä

Permanent link to this publication: <http://urn.fi/URN:ISBN:978-951-39-8496-0>

ISBN 978-951-39-8496-0 (PDF)

URN:ISBN:978-951-39-8496-0

ISSN 2489-9003

ABSTRACT

Ahinko, Mira

Computational cytochrome P450 mediated metabolism and virtual screening

Jyväskylä: University of Jyväskylä, 2021, 69 p.

(JYU Dissertations

ISSN 2489-9003; 345)

ISBN 978-951-39-8496-0 (PDF)

Yhteenvedo: Laskennallinen sytokromi P450 -välitteinen metabolia ja virtuaaliseulonta

Computational drug design aids to lower the costs and amount of experimental testing required to identify potent bioactive lead molecules for biological target macromolecules, usually proteins. Computational prediction and analysis of cytochrome P450 (CYP) enzyme mediated metabolism can be used to assess bioavailability, potential drug-drug interactions and metabolic reaction products, and thus to abandon or re-design potentially harmful lead compounds, improve drug candidate bioavailability, and to design prodrugs that are activated at a metabolic event. Virtual screening (VS), in turn, is used to find novel bioactive compounds from a large virtual molecular database, filtering the number of compounds subjected to experimental testing. In this doctoral thesis, protein structure-based methods were utilized for computational prediction and analysis of CYP metabolism and VS. Metrics of binding free energy, ligand stability and accessibility for metabolic reaction in the CYP ligand binding site are suggested for future prediction and analysis protocols of CYP metabolism using molecular dynamics (MD) simulations. Using these metrics and expert analysis, MD simulations offered rationalization of catalytic and inhibitory activities of novel CYP ligands. Novel profluorescent tool molecules are presented for experimental CYP assays. Molecular modelling and docking aided to identify the most potent target CYP enzymes for these compounds. Moreover, further MD simulations suggested an essential role of water interactions and access channel composition for the fluorescent catalysis of the tool molecules in the CYP1 enzyme family. Finally, a workflow and practical discussion for a priorly developed protein binding site negative image-based (NIB) VS methodology, Panther, is presented. The presented results, computational methods, and tool molecules offer potent tools for drug development and ideas for the further development of the methods.

Keywords: Cytochrome P450; Computer-aided drug design; Site of metabolism prediction; Virtual screening.

Mira Ahinko, University of Jyväskylä, Department of Biological and Environmental Science and Nanoscience Center, P.O. Box 35, FI-40014 University of Jyväskylä, Finland

TIIVISTELMÄ

Ahinko, Mira

Laskennallinen sytokromi P450 –välitteinen metabolia ja virtuaaliseulonta

Jyväskylä: Jyväskylän yliopisto, 2021, 69 p.

(JYU Dissertations

ISSN 2489-9003; 345)

ISBN 978-951-39-8496-0 (PDF)

Yhteenvedo: Laskennallinen sytokromi P450 –välitteinen metabolia ja virtuaaliseulonta

Laskennallista lääkeainesuunnittelua käytetään lääkeainekehityksessä johtolankamolekyylien etsinnässä ja optimoinnissa. Menetelmien avulla voidaan vähentää kokeellisten menetelmien käyttöä sekä niistä koituvia kustannuksia. Sytokromi P450 (CYP) –entsyymien välittämän metabolian laskennallisella ennustuksella voidaan arvioida biosaatavuutta, lääkeaineiden potentiaalisia yhteisvaikutuksia sekä metabolian reaktiotuotteita. Tiedon avulla kehityksessä voidaan hylätä tai optimoida haitallisia molekyylejä, parantaa johtolankamolekyylien biosaatavuutta, ja suunnitella aihiolääkeaineita, jotka aktivoituvat aktiivisiksi lääkeaineiksi metabolisessa reaktiossa. Virtuaaliseulontaa käytetään uusien bioaktiivisten molekyylien etsintään laajoista virtuaalisista molekyylylitietokannoista. Väitöskirjatyössä käytettiin laskennallisia proteiinin rakenteeseen perustuvia menetelmiä CYP-metabolian ennustukseen ja arviointiin sekä virtuaaliseulontaan. Molekyylidynamiikka (MD) sekä MD-simulaatioista saatavat sitoutumisenergiaa, ligandin stabiilisuutta sekä ligandin läheisyyttä CYP-entsyymien reaktiokeskukseen kuvaavat metriikat auttoivat selittämään uusien CYP-ligandien metaboliaa. Metriikoita ehdotetaan käytettäväksi tulevissa MD-pohjaisissa CYP-tutkimuksissa. Työssä esitellään uusia profluoresoivia työkalumolekyylejä CYP-entsyymien kokeellisiin tutkimuksiin. Potentiaalisimmat kohde-entsyymit tunnistettiin molekyyylimallinnuksen ja -telakoinnin avulla. Lisäksi MD-simulaatioissa havaittiin, että vesimolekyylit ja entsyymien sitoutumistaskuihin johtavat kanavat ovat tärkeässä roolissa työkalumolekyylien sitoutumisessa ja selektiivisyydessä CYP1-perheen entsyymeihin. Työssä esitetään myös käytännönläheinen virtuaaliseulontan prosessi aiemmin kehitetylle Panther-menetelmälle. Työssä esitellyt tulokset, laskennalliset menetelmät ja työkalumolekyylit tarjoavat sekä valmiita työkaluja lääkeainekehitykseen että ideoita menetelmien jatkokehitykseen.

Avainsanat: Metaboliakohdan ennustus; Sytokromi P450; Tietokoneavusteinen lääkeainesuunnittelu; Virtuaaliseulonta.

Mira Ahinko, Jyväskylän yliopisto, Bio- ja ympäristötieteiden laitos ja Nanotiedekeskus, PL 35, 40014 Jyväskylän yliopisto

Author's address Mira Ahinko
Department of Biological and Environmental Science and
Nanoscience Center
P.O. Box 35
FI-40014 University of Jyväskylä
Finland
mira.m.k.ahinko@jyu.fi

Supervisors Professor Olli Pentikäinen, PhD
Institute of Biomedicine
University of Turku
Kiinamyllynkatu 10
FI-20520 Turku
Finland

Professor Perttu Permi, PhD
Department of Biological and Environmental Science,
Department of Chemistry and Nanoscience Center
P.O. Box 35
FI-40014 University of Jyväskylä
Finland

Reviewers Docent Maija Lahtela-Kakkonen, PhD
School of Pharmacy
University of Eastern Finland
P.O. Box 1627
FI-70211 Kuopio
Finland

Professor Jukka Hakkola, MD, PhD
Research Unit of Biomedicine
P.O. Box 5000
FIN-90014 University of Oulu
Finland

Opponent Docent Tuomo Laitinen, PhD
School of Pharmacy
University of Eastern Finland
P.O. Box 1627
FI-70211 Kuopio
Finland

CONTENTS

LIST OF ORIGINAL PUBLICATIONS

ABBREVIATIONS

1	INTRODUCTION	11
2	REVIEW OF THE LITERATURE.....	13
2.1	Metabolism in toxicology and drug development.....	13
2.2	Computational prediction and analysis of CYP metabolism.....	18
2.2.1	Enzyme structure-based methods	20
2.2.2	Ligand-based methods	23
2.2.3	Integrative tools, isoform selectivity and metabolite prediction .	25
2.2.4	Method of choice.....	26
2.3	Virtual screening.....	27
2.3.1	Negative image-based screening with Panther	29
3	AIMS OF THE STUDY	30
4	MATERIAL AND METHODS.....	31
4.1	Databases (I-V)	31
4.2	Ligand preparation (I-V)	31
4.3	Protein comparison and preparation (I-V).....	32
4.4	Molecular docking and virtual screening (I-V)	32
4.5	Molecular dynamics simulations (I, II, IV)	32
4.5.1	Preparation	32
4.5.2	Simulation.....	33
4.5.3	Analysis.....	34
4.6	Visualization and figure preparation (I-V)	34
5	REVIEW OF THE RESULTS	35
5.1	Finding substrate binding mode and site of metabolism (I, II)	35
5.1.1	Binding mode prediction based on MMGBSA (I, II).....	36
5.1.2	Enhanced stability and distance analysis (II)	38
5.1.3	MMGBSA in other applications (II).....	40
5.1.4	The effect of post-minimization (II).....	40
5.2	Profluorescent tool molecules – one binding mode of interest (III, IV) .	41
5.2.1	Identification of target isoforms.....	42
5.2.2	The CYP1A subfamily and CYP2A6	42
5.2.3	CYP1B1	44
5.2.4	CYP2D6 and 2C19	45
5.2.5	Novel tool molecules	45
5.2.6	Indicators and contributors of catalytic efficiency	46
5.2.7	Effects of channels and solvent interactions in the CYP1 family .	47
5.3	Finding active molecules with negative image-based screening (V) ...	49
5.3.1	The screening workflow	49
6	DISCUSSION	52

7 CONCLUSIONS	56
<i>Acknowledgements</i>	57
YHTEENVETO (RÉSUMÉ IN FINNISH).....	58
REFERENCES.....	61

LIST OF ORIGINAL PUBLICATIONS

The thesis is based on the following original papers, which will be referred to in the text by their Roman numerals I–V. M.A. was responsible for all computational results (I, III–IV) or all computational results regarding cytochrome P450 (II). In the case of virtual screening, M.A. performed the negative image-based virtual screening and rescoring, calculated the benchmarking metrics, and produced the updated release of the Panther software (V). M.A. prepared most of the provided workflow and figures with the contribution of other authors (V). S.N. and O.T.P (II) or S.T.K. (V) were responsible for other computational results. R.O.J., C.F., M.H.P., T.J.N., S.A., H.R. and M.P. (I) or R.O.J., J.H. and H.R. (III–IV) were responsible for experimental results. The studies were designed by R.O.J. and O.T.P. with the contribution of all authors (I, III, IV), by all authors (II), or by M.A., S.T.K. and P.A.P. with the contribution of all authors (V). M.A. was supervised by O.T.P. (I–IV) or O.T.P. and P.A.P. (V). The articles were written with the contribution of all authors.

- I Juvonen R.O., Kuusisto M., Fohrgrup C., Pitkänen M.H., Nevalainen T.J., Auriola S., Raunio H., Pasanen M. & Pentikäinen O.T. 2016. Inhibitory effects and oxidation of 6-methylcoumarin, 7-methylcoumarin and 7-formylcoumarin via human CYP2A6 and its mouse and pig orthologous enzymes. *Xenobiotica* 46: 14–24.
- II Ahinko M.*, Niinivehmas S.*, Jokinen E. & Pentikäinen O.T. 2019. Suitability of MMGBSA for the selection of correct ligand binding modes from docking results. *Chemical Biology & Drug Design* 93: 522–538.
- III Juvonen R.O., Ahinko M., Huuskonen J., Raunio H. & Pentikäinen O.T. 2019. Development of new Coumarin-based profluorescent substrates for human cytochrome P450 enzymes. *Xenobiotica* 49: 1015–1024.
- IV Juvonen R.O., Ahinko M., Huuskonen J., Raunio H. & Pentikäinen O.T. Substrate selectivity of coumarin derivatives by human CYP1 enzymes: *in vitro* enzyme kinetics and *in silico* modelling. Manuscript.
- V Ahinko M.*, Kurkinen S.T.*, Niinivehmas S.P., Pentikäinen O.T. & Postila P.A. 2019. A Practical Perspective: The Effect of Ligand Conformers on the Negative Image-Based Screening. *International Journal of Molecular Sciences* 20: 2779.

* Equal contribution

ABBREVIATIONS

2D	two-dimensional
3D	three-dimensional
3D-QSAR	three-dimensional quantitative structure-activity relationship
6MC	6-methylcoumarin
7FC	7-formylcoumarin
7MC	7-methylcoumarin
ADMET	absorption, distribution, metabolism, excretion and toxicity
AR	androgen receptor
AUC	area under curve
BSP-SLIM	Binding Site Prediction with Shape-based LIgand Matching with binding pocket
EF	enrichment factor
EF X%	enrichment factor for the X% of top results
EFd X%	enrichment factor among top results when X% of top decoys are considered
COX-2	cyclooxygenase-2
CYP	cytochrome P450
DUD	Directory of Useful Decoys
DUD-E	Directory of Useful Decoys - Enhanced
NIB	negative image-based
MD	molecular dynamics
ML	machine learning
MMGBSA	molecular mechanics generalized Born surface area
MMPBSA	molecular mechanism Poisson-Boltzmann surface area
PDB	Protein Data Bank
PDE4B	phosphodiesterase 4B
QM	quantum mechanics or quantum mechanical
RMSD	root mean square deviation
RMSD _{LH}	combined root mean square deviation of ligand and heme
SOM	site of metabolism
STD	standard deviation
ROC	receiver operator characteristics
VS	virtual screening

1 INTRODUCTION

Computational tools that model and predict biochemical events are an integral part of drug development. They are used in wide scope from the finding of novel lead compounds for drug development to safety assessment of the lead compounds. Virtual screening (VS) is used to filter a extensive virtual small-molecule databases to find compounds that could bind and thus modulate the function of a specific protein target that has been identified to participate in a malicious biological pathway. In turn, patient safety assessment is central for drug development to prevent drugs with adverse effects to reach the market. One part of safety assessment is the analysis and prediction of a molecule's absorption, distribution, metabolism, excretion and toxicity (ADMET) properties in human. Metabolism modifies the structure of the molecule that enters the body, called a xenobiotic. A change in the xenobiotic's structure can also change its function and effects. Many of the resulting product metabolites are harmless inactivated molecules. From this perspective, the metabolic clearance of a drug molecule can decrease the drug concentration below therapeutic levels faster than desired. On the other hand, adverse drug-drug interactions often arise from metabolism, and metabolic reactions have a big role in the activation of toxic carcinogenic molecules. It is essential to identify such compounds in preclinical drug development before they reach clinical tests and the market.

The motives to utilize and develop computational tools for drug development concern academic and industrial communities and governments. The main motives are to decrease the use of animal experiments, that is an ethical issue in drug and chemical development and testing, and to decrease the costs by filtering the number of molecules to be tested experimentally. Some examples of regulatory drivers include the European Union regulations for registration, evaluation, authorization and restriction of chemicals (REACH) and the Cosmetics Directive that contain aims to reduce and ban the use of animal testing.

Many computational tools have been developed for biochemical modelling throughout the last decades and the momentum is expected to continue. In this study, computational methods utilized in the prediction of metabolism mediated by the cytochrome P450 (CYP) enzyme family and virtual screening are

reviewed. Existing methods are used to model interactions of small molecules and proteins, evaluated, and further developed. The methods concerning computational CYP metabolism are mainly based on molecular dynamics simulations, where the atomic interactions, energetics and dynamics are modelled for complexes with a small molecule bound at the binding cavity of a metabolic enzyme. The virtual screening approach is based on the comparison of small molecules with the negative image of a target protein binding cavity. The study discusses some of the advantages and limitations of these computational methods and offers ideas for their utilization.

2 REVIEW OF THE LITERATURE

2.1 Metabolism in toxicology and drug development

Analysis of metabolism is an essential part of the efficacy and patient safety assessment of lead compounds in drug discovery development (Issa *et al.* 2017, Zhang and Tang 2018). The biological purpose of xenobiotic metabolism in the body is to increase the water solubility of exogenous molecules and thus make them ready for excretion via urine. The reactions catalyzed by metabolic enzymes change the structure of the molecule and thus the function of the molecule may also be affected. Most metabolic reactions lead to inactivation of a therapeutic or toxic parent compound, but close to 10% of these lead to active, toxic or reactive metabolites (Testa *et al.* 2012). On the one hand, the inactivation pathways are an issue in drug development as they can render drug concentrations below therapeutic levels. On the other hand, toxicity issues are related to approximately one-third of failures in the pharmaceutical industry and, in an example from one company, 28% of these have been associated with metabolism (Guengerich 2011). Xenobiotic biotransformations are traditionally divided into phase I and phase II metabolism, which categorize the pathways to either redox and hydrolysis or conjugation reactions (Testa *et al.* 2012). CYP enzymes are a major part in the phase I metabolism. They catalyze 40% of all metabolic reactions (Testa *et al.* 2012) and catalyze 95% of metabolic reactions of all chemicals and 96% of reactions on drugs under development or in the market (Rendic and Guengerich 2015). In the bioactivation of toxic and reactive chemicals, CYPs contribute to 66% of the reactions (Rendic and Guengerich 2012). In contrast to adverse effects that can arise from metabolism, CYP enzymes are also established and potential anti-cancer drug development targets due to their role in certain cancers and their potential to activate a therapeutic drug molecule at specific tissues (Bruno and Njar 2007). Due to their vast role in the metabolism and toxicity, most of the tools to assess metabolism are developed specifically for CYP enzymes. However, the contribution of other enzymes such as UDP-glucuronosyltransferases, dehydrogenases and hydrolases should not be dismissed (Testa *et al.* 2012).

In the human genome, the superfamily of CYPs consists of 57 genes, and the enzymes participate in a vast array of both endogenous functions and xenobiotic metabolism (Nebert *et al.* 2013). Based on amino acid sequence identity, CYP enzymes are arranged into families and subfamilies that are designated an Arabic numeral and a letter, respectively. Families constitute of enzymes that share about 40% or greater sequence identity, whereas in subfamilies the sequence identity is about 55% or more. Accordingly, the human genome contains 18 CYP families and 41 subfamilies that encode the 57 enzyme isoforms (Nebert *et al.* 2013). CYP enzymes are expressed in all tissues of the body, but are most abundant in the liver. Xenobiotic metabolism is mainly associated with 12 members of the CYP1, CYP2 and CYP3 families (Table 1). Those members contribute to more than 90% of reactions on xenobiotics (Rendic and Guengerich 2015). The isoforms have large differences in their ligand selectivity. Many substrates are also catalyzed by several CYP enzymes. In drug metabolism, five isoforms 1A2, 2C9, 2C19, 2D6, and 3A4 have a dominant role, and they account for close to 70% of drug metabolism reactions (Rendic and Guengerich 2015). The role of the isoforms is shifted in carcinogen activation, as six isoforms 1A1, 1A2, 1B1, 2A6, 2E1, and 3A4 account for 77% of the reactions (Rendic and Guengerich 2012).

TABLE 1 CYPs in xenobiotic metabolism, based on Rendic and Guengerich (2015).

CYP isoform	Contribution to all CYP-mediated reactions (%)			Main factors of interindividual variation ³
	Drugs in the market and in development ¹	Environmental and industrial chemicals ¹	Carcinogen activation ²	
1A1	5	11	20	Induction
1A2	9	15	17	Induction
1B1	1	6	11	Polymorphism, disease
2A6	2	5	8	Polymorphism, induction
2B6	4	6	NS	Induction, polymorphism
2C8	5	3	NS	Induction
2C9	10	7	NS	Induction, polymorphism
2C19	9	6	NS	Polymorphism, induction
2D6	13	8	NS	Polymorphism
2E1	3	8	11	Induction, inflammation, disease
3A4	27	13	10	Induction, sex, inflammation
3A5	6	2	NS	Induction, sex, inflammation
Other	6	10	23	

NS: Not specified in the source literature.

¹ Rendic and Guengerich (2015)

² Rendic and Guengerich (2012)

³ Zanger and Schwab (2013)

Differences in the ligand selectivity of CYP isoforms arise from their molecular structure. The overall structure of CYP enzymes is conserved (Fig. 1A) (Otyepka *et al.* 2007, Guengerich *et al.* 2016). The catalytic heme cofactor is positioned in the buried binding site next to the highly conserved I helix (Otyepka *et al.* 2007). The binding site is very divergent (Fig. 1B) (Otyepka *et al.* 2007, Guengerich *et al.* 2016). The shape, size and malleability of the binding site is linked to the substrate selectivity of the CYP enzyme (Guengerich *et al.* 2016). Ligands and water molecules can enter the binding site via a multitude of access channels that are found in the areas of the F and G helices, the F/G loop, and the B/C loop (Cojocararu *et al.* 2007, Otyepka *et al.* 2007). The F/G loop can contain short F' and G' helices, likewise to a short B' helix in the B/C loop (Fig. 1A) (Otyepka *et al.* 2007). The amino acid composition and flexibility of these areas have a large impact on the binding site and the composition of the access channels (Otyepka *et al.* 2007). Variations in the size, topology, electrostatics, and malleability of the binding site, access channel composition, and flexibility in the region of the F and G helices and the F/G loop account for different substrate specificities of CYP enzymes (Cojocararu *et al.* 2007, Skopalík *et al.* 2008, Hendrychová *et al.* 2011, Hendrychova *et al.* 2012, Urban *et al.* 2018). Isoforms such as CYP3A4 that have a large binding site and express high flexibility at the binding site and the region of the F and G helices and the F/G loop can accommodate a significantly wider array of substrates than the more restricted isoforms like CYP1A2 and CYP2A6. In addition, if the substrate is significantly smaller than the CYP binding site, the intrinsic properties of the substrate likely have a greater impact on the resulting metabolites than the binding interactions with the CYP enzyme (Cruciani *et al.* 2013). Lastly, certain CYP enzymes have evidence of dual occupancy or, in other words, cooperative ligand binding with two ligands simultaneously in their binding site (Guengerich *et al.* 2016).

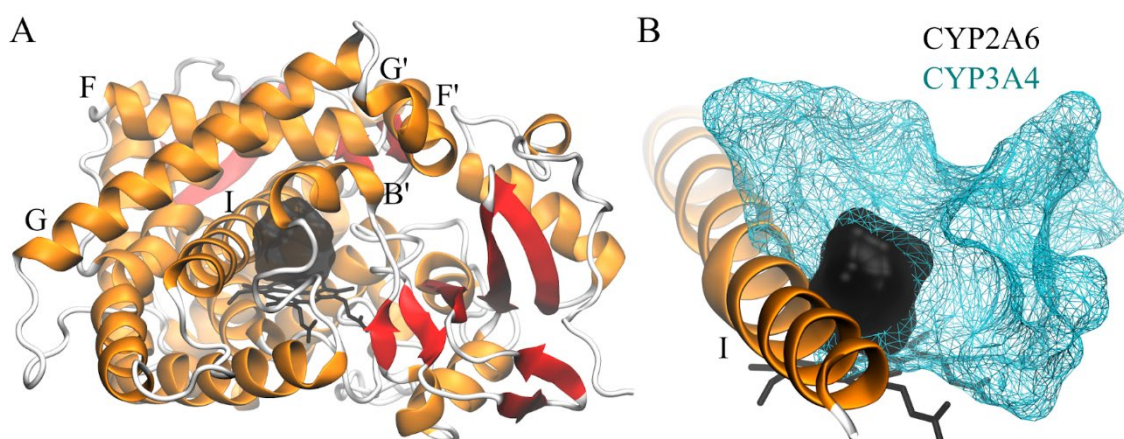


FIGURE 1 The structure of CYP enzymes. (A) The CYP structure is represented as secondary structure elements of CYP2A6 crystal structure (PDB code 1Z10) (Yano *et al.* 2005). (B) Comparison of CYP2A6 and CYP3A4 (PDB code 5TE8) (Sevrioukova and Poulos 2017) binding site topology. Key secondary structures are named. Black stick model: heme; solid and wireframe surface: binding site based on negative image of the binding site created with Panther (Niinivehmas *et al.* 2015). The images were generated in VMD (Humphrey *et al.* 1996).

The reactions catalyzed by CYP enzymes are diverse, but the majority of reactions are oxygenations (Guengerich 2001). The catalytic reaction occurs at the heme cofactor. The overall catalytic cycle is well established, and it begins with the binding of the substrate to the proximity of the heme (step 1) (Fig. 2) (Guengerich 2001). In short, this is followed by a reduction (step 2), binding of molecular oxygen (step 3), again a reduction (step 4), a protonation (step 5), and the scission of the O-O bond, which forms a complex denoted as FeO^{3+} (step 6). Most of the typical oxygenation reactions on CYP substrates can be rationalized with the reactive FeO^{3+} (Guengerich 2001, Isin and Guengerich 2007, Guengerich and Munro 2013). However, the depicted catalytic cycle (Fig. 2) is a simplification, and many other reactions and mechanisms are also possible depending on the nature of the substrate (Guengerich 2001, Isin and Guengerich 2007, Guengerich and Munro 2013). After the formation of the FeO^{3+} (step 6), this complex abstracts a hydrogen atom or an electron from the substrate, or forms a sigma complex with the substrate (step 7). Finally, the product is generated (step 8) and released (step 9) (Fig. 2) (Guengerich 2001). The electrons usually come from the NADPH-P450 reductase, but other electron donors are also possible (Guengerich 2001). Basic reaction endpoints include carbon hydroxylation, heteroatom oxygenation, dealkylation and epoxide formation (Isin and Guengerich 2007). Reactions that are catalyzed by CYP enzymes and have been associated with carcinogen activation include, for example, epoxidation and carbon hydroxylation reactions (Rendic and Guengerich 2012).

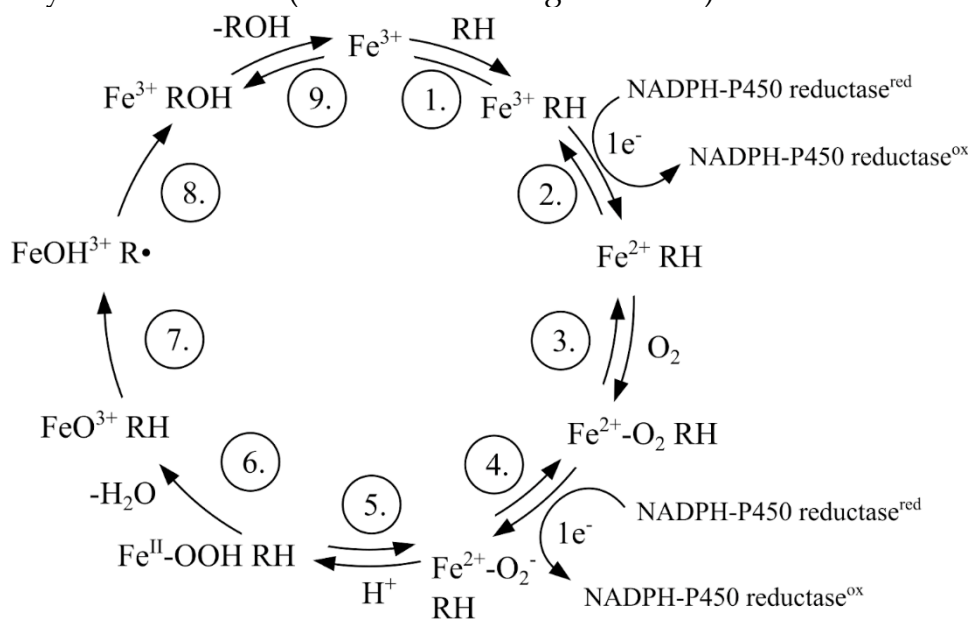


FIGURE 2 A simplified depiction of the CYP catalytic cycle. Adapted from literature (Scheme 1 of Guengerich 2001). Fe: iron atom of the CYP heme; RH: substrate; ROH: product; red/ox: reduced/oxidated state of the reductase.

Issues that arise from CYP metabolism in the clinical setting are generally related to interindividual differences in the efficiency of metabolism and drug-drug interactions that can arise from metabolism (Sikka *et al.* 2005, Lynch and Price 2007). The variation of metabolic efficiency of CYP enzymes between individuals

is affected by several factors, including genetic polymorphisms, diseases, sex, age, and induction or inhibition of the enzymes by both xenobiotics and endogenous compounds (Table 1) (Zanger and Schwab 2013). Based on genetic polymorphisms, individuals can be categorized to poor, extensive, or ultrarapid metabolizer phenotypes (Sikka *et al.* 2005, Zanger and Schwab 2013). In case an administered parent drug is therapeutically active, poor metabolizers may be at increased risk of drug toxicity, whereas the therapeutic effect can be suboptimal in fast metabolizers. Drug molecules that are activated in CYP metabolism have the opposite effect, as poor metabolizers may not gain a therapeutic response (Sikka *et al.* 2005, Zanger and Schwab 2013). From another perspective, the induction and inhibition of CYP enzymes by xenobiotics, in this scope drugs, is a major source of drug-drug interactions (Lynch and Price 2007). There are multiple mechanisms involved, namely induction of the enzyme synthesis, competitive and noncompetitive inhibition, and mechanism-based inactivation (Lynch and Price 2007, Deodhar *et al.* 2020). Xenobiotic-metabolizing CYP enzymes also have wide ligand selectivities, which can lead to several drugs being dependent on the same enzyme(s) for clearance (Sikka *et al.* 2005). Accordingly, the inhibition or induction of a certain CYP enzyme by one drug can cause the accumulation or poor bioavailability of another, which can result in adverse effects or reduced therapeutic response (Sikka *et al.* 2005, Lynch and Price 2007). Finally, in addition to the inhibition and induction of CYP enzymes by xenobiotics, chemical toxicity induced by CYP enzymes is mainly the result of bioactivation of carcinogenic compounds and the formation of reactive products that damage cellular structures (Guengerich 2008). However, lead compounds with such effects should generally be dismissed already in the preclinical phase of drug development.

In preclinical drug development, the optimization of lead compound metabolism, together with other ADMET properties, is a key process to improve the efficacy and safety of the compounds (Issa *et al.* 2017, Zhang and Tang 2018). *In vivo* ADMET testing on animals is still required for drug approval as studies on whole organisms provide the most comprehensive information of ADMET properties and the interplay of different organs to the final effects of the drug candidate (Issa *et al.* 2017). However, there is wide interest to substitute and complement animal-based models, firstly for ethical and economic reasons, and secondly for large interspecies differences especially in metabolism, which challenge the extrapolation of animal *in vivo* results to humans. In addition, the importance of evaluating ADMET properties already at the early stages of drug discovery and development has been widely recognized in the industry in order to reduce the high amount of attrition rates related to them (Wu *et al.* 2020). *In vitro* and *in silico* tools allow the early utilization of human-specific models to predict the effects of metabolism to the lead compounds in human (Issa *et al.* 2017). Accordingly, *in vitro* and *in silico* methods have the potential to produce information to filter or optimize compounds with poor metabolism profiles early on in the drug development process before they reach the *in vivo* or clinical tests. The development and use of *in silico* tools has gained increased attention as

computational methods could be applied on large compound libraries with reduced time and costs as compared to *in vivo* and *in vitro* testing (Wu *et al.* 2020).

In vitro and *in silico* methods can answer more specific questions of CYP metabolism than *in vivo* testing (Issa *et al.* 2017). Human liver microsomes-based *in vitro* assays provide a platform to analyze the compound clearance, rate of metabolism, and inhibition of CYP enzymes, and have the potential to also indicate of *in vivo* interindividual differences of metabolism (Issa *et al.* 2017). In turn, liver cell-based models are at their best for hepatotoxicity assessment, although cell-based systems are also emerging to model multi-organ effects of metabolism. Mass spectrometry and nuclear magnetic resonance methods are used to analyze the structures of metabolites (Kirchmair *et al.* 2012). In specific cases where CYP inhibition has been identified as a key issue, X-ray crystal structures of the ligand-CYP complexes can be used to aid the drug design process (Brändén *et al.* 2014). As discussed in the next section, *in silico* tools can be used to predict a specific objectives in CYP metabolism such as enzyme selectivity, sites of metabolism (SOM) of substrates, and as a derivation of SOM prediction, the resulting metabolites (De Groot and Ekins 2002, Crivori and Poggesi 2006, de Groot 2006, Kirchmair *et al.* 2012, Olsen *et al.* 2015, Raunio *et al.* 2015, Tyzack and Kirchmair 2019). Prediction of enzyme selectivity is of special interest in the light of metabolic stability and drug-drug interactions (Tyzack and Kirchmair 2019). In turn, SOM and metabolite prediction can complement experimental methods in the identification of metabolites (Cruciani *et al.* 2005, 2013, Kirchmair *et al.* 2012). Overall, computational methods can reveal information of the structural and physicochemical basis of CYP metabolism (Kirchmair *et al.* 2012). There are also a wide array of *in silico* tools to predict other ADMET properties, and those are mostly based on structural alerts or statistical data modelling approaches (Wu *et al.* 2020).

2.2 Computational prediction and analysis of CYP metabolism

Computational methods for CYP metabolism prediction can be objected to (1) predict the binding modes and (2) SOMs of substrates, (3) predict metabolites (4) predict substrate (or inhibitor) selectivity among CYP isoforms and (5) screen novel substrates/inhibitors or classify small molecules as substrates, inhibitors and inactive molecules. A vast number of methods have been applied to these objectives (De Groot and Ekins 2002, Crivori and Poggesi 2006, de Groot 2006, Kirchmair *et al.* 2012, Olsen *et al.* 2015, Raunio *et al.* 2015, Tyzack and Kirchmair 2019). Methods to predict CYP induction and rate of metabolism also exist, but it should be noted that the induction pathways arise from interactions of the xenobiotics with transcription factors and not CYP enzymes themselves (Crivori and Poggesi 2006). The prediction of inhibition has been considered more challenging than the prediction of SOMs (Brändén *et al.* 2014, Raunio *et al.* 2015). In SOM prediction, substrates have same principle in common that the SOM needs to be adequately reactive and accessible to the heme in order for the

reaction to occur. In turn, there are several mechanisms for inhibition and inactivation. CYP inhibitors can bind either close to the heme or to a distant site in the protein, multiple ligands can bind simultaneously, or an inactivator can bind covalently to the protein (Brändén *et al.* 2014, Raunio *et al.* 2015). Metabolite prediction is usually a derivation of SOM prediction, as the SOM predictions are used in combination with experimental data to predict the most likely metabolites (Cruciani *et al.* 2005, 2013). In many cases, methods to predict CYP selectivity are not able to differentiate substrates and inhibitors as the experimental data usually contains only the IC₅₀ value without knowledge of whether the ligand is a substrate, inhibitor, or an inactivator (Olsen *et al.* 2015). The CYP metabolism prediction methods often concentrate on a single objective, but they can be combined into wider workflows (Fig. 3) and certain tools have been developed with that goal in mind (Cruciani *et al.* 2005, 2013, Vedani *et al.* 2015, Djoumbou-Feunang *et al.* 2019). Here, the discussion concerns mainly the binding mode and SOM prediction of CYP substrates, but other views are also shortly communicated. The discussion here does not provide an exhausted analysis of all previously applied tools for CYP metabolism prediction, but an overview and examples of the methods. Excellent reviews on the subject have been made previously (Crivori and Poggesi 2006, Kirchmair *et al.* 2012, Olsen *et al.* 2015, Raunio *et al.* 2015, Tyzack and Kirchmair 2019).

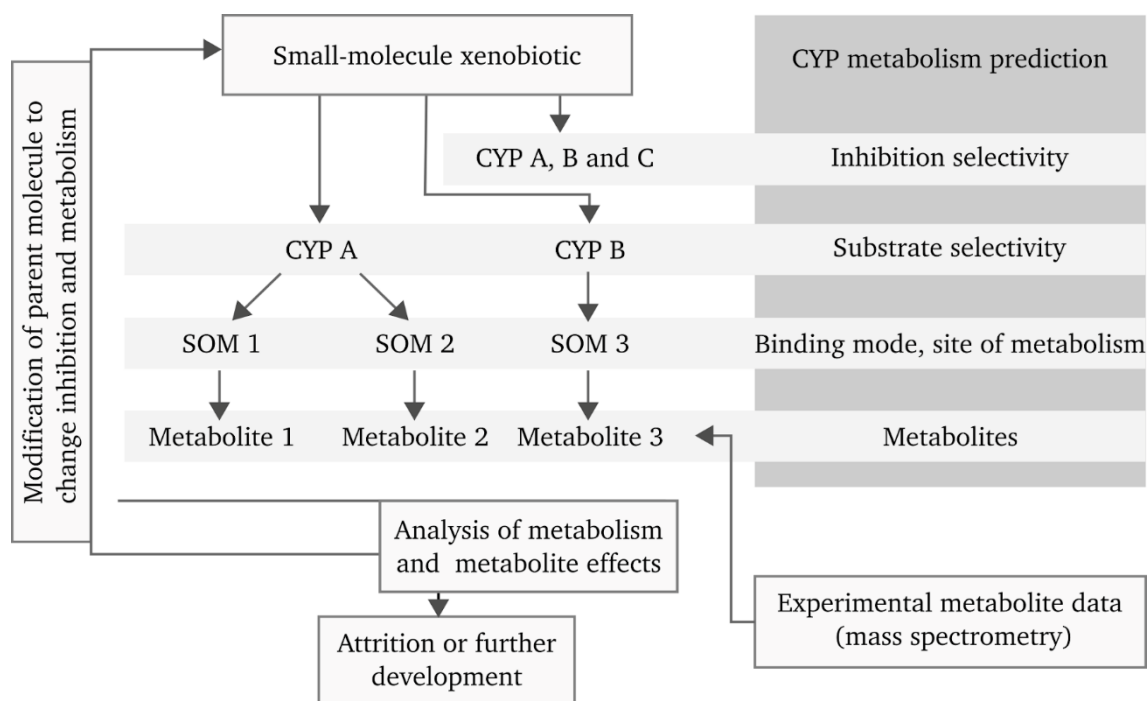


FIGURE 3 A theoretical scheme for combining computational CYP metabolism prediction methods in drug development.

As the enzyme and reaction regioselectivity of CYP substrates are affected by both ligand-CYP binding interactions and the intrinsic chemical nature of the small molecule, a multitude of different approaches have been applied for

computational SOM prediction. The methods can be roughly categorized to 1) enzyme structure-based, 2) ligand-based and 3) combined methods that utilize both structure and ligand-based approaches (Crivori and Poggesi 2006, Kirchmair *et al.* 2012, Olsen *et al.* 2015, Raunio *et al.* 2015, Tyzack and Kirchmair 2019). Another classification can be built upon whether the method approaches SOM selectivity from the view of 1) the reactivity or 2) accessibility of the substrate sites, 3) knowledge-based data mining or as a 4) multi-parameter problem to be solved by machine learning (ML) (Tyzack and Kirchmair 2019).

The generally used metric to measure the success of a SOM prediction method indicates whether a top 1-3 prediction includes one or more true SOMs of a substrate. The top metric is reported as the percentage of substrates with a correct SOM prediction in the top predicted sites. A further analysis of the true positive against false positive predictions within the top metric provides a more detailed view of the effectiveness of the prediction (Zaretski *et al.* 2012). An averaged Spearman metric has also been proposed, which reports the success rate at substrate site level rather than substrate-wise (Huang *et al.* 2013). SOM prediction methods do not attempt to predict the rate of metabolism, which is partly a result of the experimental data used for validation. The data may not contain the kinetic information or the rates might not be comparable between different sources (Sheridan *et al.* 2007, Zaretski *et al.* 2012). Instead, usually the experimentally determined SOM of an individual substrate is characterized as primary, secondary or tertiary SOM. Thus, the rate of metabolism at the primary SOM may differ vastly between substrates.

2.2.1 Enzyme structure-based methods

Enzyme structure-based methods predict the stable binding mode of a substrate or inhibitor in the CYP binding site. As X-ray crystal structures are now available for all major xenobiotic-metabolizing CYP forms, the structure-based methods can be widely applied across different phase I metabolism pathways. The orientation of a ligand in the enzyme binding site depends on the shape and electrostatics complementarity between the ligand and the enzyme. Many of the evaluated structure-based methods rely on molecular docking but also fingerprint matching and MD simulations are used (Table 2) (Tyzack and Kirchmair 2019). Structure-based methods are mostly used to investigate specific ligand-CYP interactions as the flexibility, complex water interactions and the hydrophobic binding sites of CYP enzymes pose challenges to these approaches, especially molecular docking (Tyzack and Kirchmair 2019). In addition, they are computationally expensive and often require expert knowledge for the setup and analysis of the results. Consequently, the methods have been usually tested on just few CYP isoforms and relatively small datasets (Table 2). However, structure-based methods offer interpretable and precise information of the atomic ligand-CYP interactions that define the ligand orientation in the CYP active site. The predictions are also isoform-specific by default as they are based on the 3D structure of a specific CYP enzyme. In addition to binding mode and

SOM prediction, the obtained structural information can be used to rationalize experimental results or to help rational molecule design.

TABLE 2 Enzyme structure-based methods for SOM prediction of CYP substrates.

Method/ reference	Description	Targeted CYPs	SOM prediction rate ¹ (Evaluation set size) ²
(Zamora <i>et al.</i> 2003)	Distance-based 2D fingerprints to match ligand and CYP binding site.	2C9	Top1 over 50%, Top3 90% (87 reactions)
MetaSite (Cruciani <i>et al.</i> 2005, 2013)	2D (Zamora <i>et al.</i> 2003) and later 3D fingerprint matching combined to ligand-based reactivity.	1A2, 2C9, 2C19, 2D6, 3A4	Top2 89-90% (110-222)
(Hritz <i>et al.</i> 2008)	CYP structures from MD simulations for docking.	2D6	Top1 71% 1 structure, 80% decision tree or 90% ensemble of 3 structures (65)
(Vasanthanathan <i>et al.</i> 2009a)	Inclusion of crystal water in docking. SOM prediction, virtual screening and ligand classification.	1A2	Top1 70% (20)
(Santos <i>et al.</i> 2010)	MD simulations with a specific ligand to derive CYP hydration sites and structures for docking.	2D6	Top1 62.3-100% depending on substrate type and CYP structure (5-53)
(Sheng <i>et al.</i> 2014)	CYP structures from MD simulations for docking.	2A6	Top1 57.3%, Top3 65.6% (96)
(Bello <i>et al.</i> 2014, Panneerselvam <i>et al.</i> 2015, Sato <i>et al.</i> 2017, Watanabe <i>et al.</i> 2017, Jandova <i>et al.</i> 2019, Juvonen <i>et al.</i> 2020)	A combination of MD simulations with slightly different objectives to sample binding modes, SOMs and inhibition modes, mostly on one or a couple of ligands.	1A1, 1A2, 1B1, 2C9, 2C11, 2E1, 3A4	-

¹: Prediction rates are not comparable due to differences in evaluation sets.

²: The number of substrates in the evaluation set with the exception of Zamora *et al.* (2003), where the number of reactions, instead of substrates, was reported.

Top1-3: Number of substrates that have a correct prediction among the top 1-3 predictions.

In the case of substrate binding mode prediction, the likely SOM(s) of the substrate can be derived from the predicted binding mode(s). A likely SOM should be accessible for oxidation by the heme, i.e. lie relatively close to the heme

iron with no other substrate atoms to shield the reaction. However, there should still be space for an oxygen to bind to the iron. In docking and MD simulation approaches, a binding mode prediction is considered correct if at least one SOM lies within 6 Å of the heme iron and is thus accessible for the reaction (Hritz *et al.* 2008, Vasanthanathan *et al.* 2009a, Panneerselvam *et al.* 2015, Sato *et al.* 2017, Jandova *et al.* 2019). Such a distance-based approach is reasonable as it leaves space for the oxygen. However, multiple substrate positions can lie at the proximity of the heme iron, and thus more than one SOM prediction is possible from the acquired binding pose (Raunio *et al.* 2015). Accordingly, SOM prediction with the 6 Å rule is specific to a region rather than an atom in the substrate. In a few approaches where either tethered docking or distance-based fingerprints are used to match the substrate with the CYP enzyme, the prediction is precise as each potential SOM is subjected to the proximity of the heme iron and thus gains an individual score (Zamora *et al.* 2003, Cruciani *et al.* 2005, 2013, Tyzack *et al.* 2013).

The consideration of the CYP binding site flexibility is crucial to find binding modes for substrates of varying size and shape. The available crystal structures do not necessarily represent CYP conformations that would reasonably accommodate the studied ligands. Accordingly, relaxation of the enzyme structure in MD simulations prior to docking can significantly improve the prediction success of molecular docking (Hritz *et al.* 2008, Sheng *et al.* 2014). The utilization of more than one CYP conformation has also been demonstrated highly successful (Hritz *et al.* 2008). Docked ligand poses can also be further subjected to MD simulations where the enzyme can adjust to the new ligand (Bello *et al.* 2014, Panneerselvam *et al.* 2015, Sato *et al.* 2017, Juvonen *et al.* 2020). A largely diverging approach from docking is to utilize less explicit 2D or 3D distance-based fingerprints for binding mode evaluation as the fingerprints do not define the atomic interactions as strictly as traditional molecular docking (Zamora *et al.* 2003, Cruciani *et al.* 2005, 2013).

Water-mediated ligand-CYP interactions can be taken into account in both molecular docking and MD simulations. In docking algorithms, crystal structure water molecules can be included in the protein 3D structure (Zhou *et al.* 2006, Vasanthanathan *et al.* 2009a). Other approaches are to predict the hydration sites computationally (De Graaf *et al.* 2005) or derive water positions from hydration sites observed in MD simulations of the CYP enzyme (Santos *et al.* 2010). However, the effect of including fixed water molecules in docking varies between different substrates and enzyme conformations as the water positions may not be optimal for all ligand-CYP complexes (Vasanthanathan *et al.* 2009a, Santos *et al.* 2010). In MD simulations, waters are an innate part of the method as they are carried out in an explicit solvent. In MD simulations, water networks have been shown to differ from one ligand to another in CYP1A2 (Watanabe *et al.* 2017). Simulations of isoforms 2A6, 2B4, 2C8, 2C9, 2D6, 2E1 and 3A4 have demonstrated that water molecules at the CYP binding site can readily exchange with the bulk solvent in MD simulations, the rate depending on the flexibility of the CYP isoform (Rydberg *et al.* 2007, Hendrychova *et al.* 2012).

Molecular docking takes only into account the energetic but not the dynamic stability of the substrate-binding modes. MD simulations naturally provide a view of both energetic and dynamic substrate stability. The simulated ligand poses can be ranked by binding energy estimations (Bello *et al.* 2014, Sato *et al.* 2017, Juvonen *et al.* 2020). Dynamic stability can be considered either by a manual/visual analysis or by automatic clustering different ligand poses that are observed during the simulations, consequently evaluating the occurrence rates of the different poses (Bello *et al.* 2014, Panneerselvam *et al.* 2015, Sato *et al.* 2017, Juvonen *et al.* 2020).

Combining ligand-based reactivity descriptors with binding mode-based SOM prediction can make the prediction more accurate and adds the crucial effect of the chemical nature of the ligand to the prediction (Cruciani *et al.* 2005, 2013, Tyzack *et al.* 2013, Sato *et al.* 2017). As the role of ligand-CYP interactions for SOM selectivity increases for larger substrates and smaller CYP binding sites, or vice versa for ligand-based reactivity, the weight of structure-based binding mode prediction and ligand-based reactivity can be adjusted based on those factors (Cruciani *et al.* 2013).

2.2.2 Ligand-based methods

Ligand-based methods use the structure and physicochemical properties of the ligand to predict CYP selectivity or the SOM(s) of a CYP substrate. As opposed to most of the purely structure-based methods, ligand-based SOM predictions are atom-wise. One of the most considered substrate property is the reactivity of substrate sites, as the reaction is more likely to occur at substrate positions with lower activation energy (Tyzack and Kirchmair 2019). It is depicted as activation energy which is the energy difference between the parent substrate structure and the reaction transition state (Jones *et al.* 2002, Olsen *et al.* 2006). As in enzyme structure-based methods, the accessibility of the substrate positions to the CYP heme iron, and thus catalysis, is another main factor considered in ligand-based methods (Tyzack and Kirchmair 2019). Over time, the ligand-based methods have evolved from pharmacophore models (De Groot and Ekins 2002, de Groot 2006) and the quantum mechanical (QM) calculation of activation energies (Jones *et al.* 2002, Olsen *et al.* 2006, Shaik *et al.* 2010) to ML models (Zaretski *et al.* 2011, 2012, 2013, Huang *et al.* 2013) (Table 3). Pharmacophore and 3D quantitative structure-activity relationship (3D-QSAR) models have been used earlier to predict ligand binding to CYP enzymes, and have been particularly useful in the absence of X-ray crystal structures of CYP enzymes (De Groot and Ekins 2002, Crivori and Poggesi 2006, de Groot 2006). Ligand-based methods include also many examples of knowledge-based and data mining models (Kirchmair *et al.* 2012, Olsen *et al.* 2015, Raunio *et al.* 2015, Tyzack and Kirchmair 2019). As ligand-based models are often computationally efficient, many of them have been made readily available to the larger research and industrial community with fast and easy-to-use web interfaces and downloadable software libraries.

At the most simple level, the activation energy and accessibility of substrate sites provide a fine basis for SOM prediction. The highly cited SMARTCyp

method incorporates these to a simple scoring function (Rydberg *et al.* 2010, 2013). Instead of new QM calculations on each new substrate, the activation energies are pre-calculated on fragments and are matched to the substrate of interest conveniently with 2D fingerprints. The method is especially successful for substrates of CYP3A4, which has a large binding site that can adapt a vast number of different types of substrates. On certain CYP isoforms, the enzyme-substrate interactions have a larger impact on regioselectivity. In some of these cases, the scoring function has been augmented with isoform or subfamily-specific corrections. These define pharmacophoric features that have been identified to highly affect the substrate orientation in the binding sites of these specific CYP enzymes (Rydberg and Olsen 2012a, b, Rydberg *et al.* 2013).

TABLE 3 Ligand-based methods for SOM prediction of CYP substrates.

Method/ reference	Description	Targeted CYPs	SOM prediction rate ¹ (Evaluation set size) ²
(Sheridan <i>et al.</i> 2007)	Isoform-specific random forest ML models that utilize structural descriptors.	2C9, 2D6, 3A4	Top2 72-77% (92-316)
MetaPrint2D (Boyer <i>et al.</i> 2007, Carlsson <i>et al.</i> 2010)	Structural fingerprints to match likelihood of catalysis, based on data mining. Predictions for human, rat, dog or all species.	General Phase I	Top3 87% (30)
SMARTCyp (Rydberg <i>et al.</i> 2010, 2013)	2D fingerprint-based matching of reactivity and accessibility descriptors. Specialized pharmacophore descriptors for CYP2D6 and 2C subfamily	1A2, 2A6, 2B6, 2C8, 2C9, 2D6, 2C19, 2E1, 3A4	Top1 64.1-72.4% Top2 76.8-85.8% (105-475)
RS-Predictor (Zaretski <i>et al.</i> 2011, 2012)	Isoform-specific multiple-instance ranking ML models that utilize 148 topological and 392 quantum mechanical descriptors and SMARTCyp reactivity.	1A2, 2A6, 2B6, 2C19, 2C8, 2C9, 2D6, 2E1, 3A4	Top2 82.1-86.2% (105-475)
DR-Predictor (Huang <i>et al.</i> 2013)	Multiple-instance ranking ML models that combine ligand reactivity and molecular docking-based descriptors.	1A2, 2A6	Top1 65-71%, Top2 82-86% (100-261)
XenoSite (Zaretski <i>et al.</i> 2013)	Isoform-specific and uniform neural networks ML models with RS-Predictor and additional molecule-level descriptors.	1A2, 2A6, 2B6, 2C8, 2C9, 2C19, 2D6, 2E1, 3A4	Top2 83.4-89.0% (105-475)

¹: Prediction rates are not comparable due to differences in evaluation sets.

²: The number of substrates in the evaluation set with the exception of Zamora *et al.* (2003), where the number of reactions, instead of substrates, was reported.

Top1-3: Number of substrates that have a correct prediction among the top 1-3 predictions.

ML is increasingly utilized in the problem solving of CYP metabolism. The methods can utilize a vast number of different types of molecule-level, substructure and atomic descriptors or fingerprints (Table 3) (Zaretski *et al.* 2011, 2012, 2013, Huang *et al.* 2013). The models have also been demonstrated to have high top 2 prediction rates (Table 3). A disadvantage of ML is that it can obscure causal connections, and the end-user might not be able to understand the mechanism behind the obtained results. ML models are also dependent on the available data to train the models, and may thus be restricted in their application domain, for example, to a certain chemical space or CYP isoform. However, the incremental development of ML models has revealed or confirmed many crucial physicochemical or topological substrate and SOM properties, and also relationships between those properties. For example, the addition of SMARTCyp reactivity values to the original topological and QM atomic and substructure descriptors in RS-predictor (Zaretski *et al.* 2011) increased the SOM prediction rates (Zaretski *et al.* 2012), confirming the previously acknowledged importance of reactivity to the catalytic regioselectivity. The addition of molecule-level descriptors further improved the predictions, which suggests that molecular properties such as size, solubility and flexibility are important factors in SOM selectivity and are interrelated to atom-level descriptors (Zaretski *et al.* 2013). This was and can be considered logical as, for example, smaller substrates are likely to bind the CYP binding site in more ways than large ones. Thus, the atom and substructure-level properties might play a bigger role in SOM selectivity in smaller substrates. ML methods have also been used to combine ligand-based reactivity to molecular docking-based binding energy and geometry with equivalent or improved SOM prediction success as compared to other ML models (Huang *et al.* 2013).

2.2.3 Integrative tools, isoform selectivity and metabolite prediction

Many computational methods for CYP metabolism prediction concentrate on binding mode and SOM prediction of CYP substrates, but a wider perspective is relevant when incorporating them with other workflows in drug development and safety assessment. Methods for binding mode and SOM prediction usually assume that the investigated molecules are substrates. Thus, identification of CYP isoform selectivity in both metabolism and inhibition is needed to find relevant SOMs (Fig. 3). Identification of metabolites is also crucial for assessing the potential effects of metabolism. Contrarily, a detailed enzyme-specific metabolism prediction may not be necessary for all circumstances and a more general assessment can be used. Lastly, tools are also available that combine many of the above objectives and integrate them into other ADMET predictions.

Metabolic enzyme selectivity can be a crucial part of the metabolism prediction workflow, but might not be necessary in all situations. One of the latest tools called CypReact offers CYP isoform-specific and uniform ML models for nine CYP isoforms to classify small molecules to substrates/nonsubstrates (Tian *et al.* 2018). The metabolism suite of ADMET Predictor^R (Simulations Plus, Inc., Lancaster, California, USA) offers substrate/nonsubstrate prediction for the

same CYP isoforms, and among other tools, the classification of inhibitors/noninhibitors for five CYP isoforms. In one comparison, ML methods were more successful in the classification task as compared to docking (Vasanthanathan *et al.* 2009a, b). The isoform selectivity prediction of MetaSite suggests the most likely isoforms to mediate a metabolic reaction of a molecule (Cruciani *et al.* 2005, 2013). In cases where a wider metabolic perspective is needed, uniform models can be utilized. MetaPrint2D and FAsT METabolizer predict SOMs considering all phase I, and FAsT METabolizer also phase II, reactions in human, rat and dog either uniformly or by these categories (Boyer *et al.* 2007, Carlsson *et al.* 2010, Kirchmair *et al.* 2013).

Integrative tools offer pre-built modules that combine many steps of metabolism and ADMET prediction. For example, MetaSite combines CYP isoform selectivity, SOM and metabolite prediction and also other metabolism pathways (Cruciani *et al.* 2005, 2013) (Molecular Discovery Ltd., Borehamwood, Hertfordshire, UK). ADMET Predictor^R provides a wide array of models from computational metabolism, including CYP SOM, isoform-selectivity and kinetic models and phase II models, to the prediction of other ADMET properties and compound toxicity (Simulations Plus, Inc., Lancaster, California, USA). BioTransformer has wide metabolism and biodegradation modules, including metabolite identification using provided mass spectrometry data (Djoumbou-Feunang *et al.* 2019). OpenVirtualToxLab estimates endocrine and metabolic disruption, carcinogenicity and cardiotoxicity by modelling compound binding to certain protein targets involved in these pathways (Vedani *et al.* 2015). The types of methods utilized in these integrative tools are diverse, including, for example, molecular docking, ML and data mining models.

2.2.4 Method of choice

There are a great number of tools that can be used for computational prediction of CYP mediated metabolism. The objective defines the types of methods that fit the case-specific needs. The possible computational demand may be limited by the relations of the data set size, available time frame and computational resources. For the analysis of large molecular libraries, many ligand-based methods for SOM and enzyme selectivity offer a fast way to assess the most likely CYP metabolism pathways. Integrative tools may be a convenient option to be incorporated into wider drug development and safety assessment workflows. They combine aspects of metabolism prediction, and can provide tools for other ADMET analysis as well. Enzyme structure-based molecular docking and MD simulations are excellent tools when the aim is to shed light on the underlying mechanisms of enzyme and SOM selectivity. In this thesis, enzyme structure-based methods are utilized for evaluating CYP isoform-selectivity, binding modes and substrate SOMs of novel CYP ligands.

2.3 Virtual screening

Virtual screening (VS) is used to find bioactive compounds to a target protein from large virtual molecular databases. It is widely used in drug discovery as it offers a powerful tool to enrich most potent molecules to the top fraction of the results. Thus, the burden of testing a vast number of compounds experimentally to find the most potent hit compounds can be eased by filtering molecular databases first by VS (Fig. 4) (Gimeno *et al.* 2019). As is the case with computational prediction of CYP mediated metabolism, the number of VS tools is vast, and the methods diverse with both protein structure and ligand-based approaches, and many of the utilized methods overlap. The computational demands of the tools are also diverse. Accordingly, methods with different computational demands can be streamlined into a filtering workflow, where the fastest methods are used for the initial filtering of the database, and more demanding methods are used to cherry-pick the most potent compounds amongst the pre-filtered library (Homeyer *et al.* 2014, Gimeno *et al.* 2019).

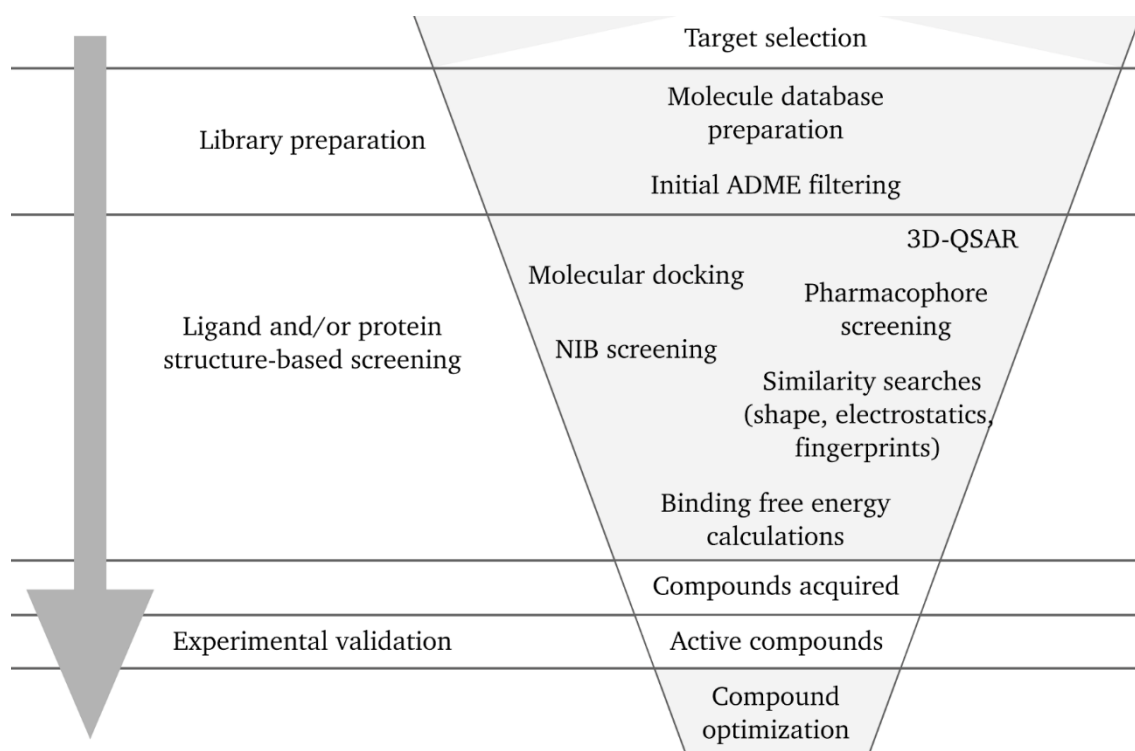


FIGURE 4 General scheme for virtual screening. Adapted from literature (Fig. 1 of Gimeno *et al.* 2019).

Ligand-based VS methods utilize existing structure-activity data and physicochemical properties of known ligands to identify crucial features for activity against a protein target, and as has been discussed, structure-based methods evaluate the interactions of potent molecules with the protein. Ligand-based methods are generally computationally highly efficient, but their

ability to find truly novel ligand structures is somewhat limited due to their dependence on the knowledge of known ligands. Ligand-based methods include approaches such as 2D fingerprint matching (Duan *et al.* 2010), similarity search (Kumar and Zhang 2018), 2D and 3D pharmacophore models (Qing *et al.* 2014, Schaller *et al.* 2020) and 3D quantitative structure-activity relationship (3D-QSAR) methods (Verma *et al.* 2010). Molecular docking is one of the most used structure-based methods for structure-based VS (Maia *et al.* 2020). Other methods include structure-based pharmacophores (Qing *et al.* 2014, Schaller *et al.* 2020) and negative image-based (NIB) screening (Lee *et al.* 2009, Virtanen and Pentikäinen 2010, Niinivehmas *et al.* 2011, 2015, Lee and Zhang 2012) and rescoring (R-NIB) (Kurkinen *et al.* 2018, 2019). In lead optimization and final phases of VS, computationally more demanding methods such as binding free energy calculations can be used to cherry-pick the most potent molecules (Homeyer *et al.* 2014). The choice of the VS method is case-specific and a comparison of different approaches may be useful (Warren *et al.* 2006, McGaughey *et al.* 2007, Cross *et al.* 2009, Duan *et al.* 2010, Homeyer *et al.* 2014, Niinivehmas *et al.* 2016).

The computational validation process of VS methods is generally performed by utilizing libraries of active ligand molecules and decoy compounds (Gimeno *et al.* 2019). These can be derived from general chemical bioactivity databases such as ChEMBL (Mendez *et al.* 2019) or from specialized libraries such as the Database of Useful Decoys (DUD) (Huang *et al.* 2006) and DUD-Enhanced (DUD-E) (Mysinger *et al.* 2012). Ligands are compounds that have been experimentally confirmed to be highly active towards the target protein (Gimeno *et al.* 2019). Decoys resemble the ligands by structure and physicochemical properties but have not been determined to possess activity towards the target. A number of metrics can be used for the validation (Gimeno *et al.* 2019, Maia *et al.* 2020). For example, the enrichment factor (EF) depicts the proportion of active molecules found after the application of a certain filter, for example the acquisition of a certain percentage of top-scored molecules (EF X%). In other words, the EF describes how well the method could, in theory, enrich bioactive molecules from a virtual database to experimental testing in a certain percentage of top-scored molecules. The area under curve (AUC) value of the characteristic operator curve (ROC) describes the overall performance of the VS method. The ROC curve visualizes the performance of a VS method by plotting the true positive rate of ligands against the false positive rate of decoy molecules, and the AUC value depicts the probability of a ligand to be scored better than a decoy compound. During the development of a VS tool, it is also beneficial to evaluate the performance of the method with a diverse set of both protein targets and small molecules (Mysinger *et al.* 2012). The topology and physicochemical nature of ligands varies from target to target, and thus utilizing a structurally and functionally diverse set of target proteins helps avoid bias towards a specific category of chemicals. The same applies for the chemical diversity of the ligand and decoy molecules. For example, the DUD-E benchmarking sets have been built for 102 different protein targets, including nuclear receptors, ion channels, kinases, proteases, and a wide array of other enzymes (Mysinger *et al.* 2012).

2.3.1 Negative image-based screening with Panther

NIB screening builds on the concept that the target protein's ligand binding site is represented as a negative image of the cavity, the similarity of which can be compared to small molecules (Lee *et al.* 2009, Virtanen and Pentikäinen 2010, Niinivehmas *et al.* 2011, 2015, Lee and Zhang 2012). The approach combines the high computational efficiency of ligand-based methods and the structural information of the protein target. NIB methods define the protein binding cavity and its complementarity to a ligand more loosely than traditional docking (Lee and Zhang 2012, Niinivehmas *et al.* 2015). Instead of atom-wise evaluation of the ligand-protein interactions, they are based on the global similarity of electrostatics (Niinivehmas *et al.* 2015) or chemical features (Lee and Zhang 2012) and the shape of the ligand and the binding cavity. In a comparison between AutoDock molecular docking (Morris and Huey 2009) and BSP-SLIM (Binding Site Prediction with Shape-based Ligand Matching with binding pocket) NIB docking, the difference between the level of strictness was considered to result in better performance of the NIB method on low-resolution protein structures (Lee and Zhang 2012).

The priorly developed NIB VS method, based on atomic Panther NIB models, is a fast structure-based approach for rigid docking and VS (Niinivehmas *et al.* 2015). In this approach, the 3D NIB model is created using Panther (Niinivehmas *et al.* 2015), and the 3D shape and electrostatics comparison and scoring are performed with ShaEP (Vainio *et al.* 2009). The NIB method can be applied for VS as is with excellent early enrichment performance (Niinivehmas *et al.* 2015). As with other docking methods, the utilization of MD simulations to generate the protein structures for the NIB model creation may be useful (Virtanen and Pentikäinen 2010). Due to the simple atomic representation of the Panther NIB model, molecular fragments can be incorporated to the model in order to define desired properties of the screened molecules more precisely (F-NIB) (Jokinen *et al.* 2019). Alternatively, the NIB methodology can be utilized with great success for rescoring or consensus scoring of flexible molecular docking results (R-NIB) (Kurkinen *et al.* 2018, 2019). Although the R-NIB approach is slower than the basic Panther NIB VS due to utilization of flexible docking, the resulting binding poses may be more realistic in R-NIB especially in protein targets with a small binding cavity.

In this thesis, the different steps of Panther NIB VS are discussed and a detailed workflow has been provided together with an updated release of the Panther software to be utilized by both experts in the field and by users new to structure-based VS. The demonstrative workflow was performed with the cyclooxygenase-2 (COX-2) benchmarking set from the DUD and DUD-E databases (Huang *et al.* 2006, Mysinger *et al.* 2012). COX-2 is an established drug target for the treatment of inflammation and pain, and the marketed drugs include many non-steroidal anti-inflammatory drugs such as aspirin, ibuprofen and naproxen (Pasero and McCaffery 2001, Kasturi *et al.* 2019).

3 AIMS OF THE STUDY

In this study, protein structure-based methods were used for computational analysis and prediction of CYP mediated metabolism and VS. Molecular modelling, docking and MD simulations were used to evaluate the mechanisms of isoform-selectivity of CYP ligands, ligand binding modes and substrate SOMs. The aims were to develop MD-based protocol for CYP ligand binding mode and substrate SOM prediction, develop novel profluorescent tool molecules with good CYP isoform-selectivity, and to predict/evaluate isoform-selectivity of the reactions. Panther NIB docking, VS and rescoring were explored. Detailed description and workflow for the methodology have been provided. The aim was to provide a discussion and tutorial of the method to be utilized by both experts and users new to structure-based NIB VS.

4 MATERIAL AND METHODS

4.1 Databases (I-V)

Protein 3D crystal structures (I-V) were acquired from the Protein Data Bank (Berman *et al.* 2000) (www.rcsb.org/pdb) and amino acid sequences (I, III) from the UniProt database (The UniProt Consortium 2019). Ligand and decoy molecules for VS benchmarking (V) were acquired from the DUD (Huang *et al.* 2006) and DUD-E (Mysinger *et al.* 2012) libraries.

4.2 Ligand preparation (I-V)

For docking, small-molecule 3D structures, protonization, partial charges and tautomers were generated (I-V). Further low-energy conformer ensembles were generated for the rigid NIB methodology (III, V). These steps were performed using mainly LigPrep and ConfGen (Watts *et al.* 2010) in the Schrödinger modelling environment (Schrödinger, LLC, New York, NY). For the evaluation of the NIB methodology (V), a set of alternative ligand preparation workflows was applied utilizing Open Babel (O'Boyle *et al.* 2011), RDKit, Molconvert in Marvin (ChemAxon), CXCALC in Instant JChem (ChemAxon) and MayaChemTools (Sud 2016). The PLANTS docking results for NIB rescoring (V) were taken from a previous study (Kurkinen *et al.* 2018). For parametrization for MD simulations, ligands were subjected to quantum-mechanical geometry optimization and calculation of electrostatic potential at the HF/6-31+G* level using the polarizable continuum model in Gaussian (Gaussian Inc. Wallingford CT), and the atomic point charges were derived with the RESP method (Bayly *et al.* 1993) (I, II, IV).

4.3 Protein comparison and preparation (I-V)

For purposes of protein sequence comparison and homology modelling, protein sequences were aligned with structure-based matrix using Malign (Johnson and Overington 1993) in the Bodil modelling environment (Lehtonen *et al.* 2004) (I, III). Protein 3D structure superimpositions were done with Vertaa in Bodil (I-V). When the protein crystal structure was not available or the structures required refinement such as filling of missing loops homology modelling was utilized using Modeller (Šali and Blundell 1993) (I) or Nest (Petrey *et al.* 2003) (III). Protein structure protonation was performed using Reduce (Word *et al.* 1999) (I-V).

4.4 Molecular docking and virtual screening (I-V)

Molecular docking was performed with PLANTS docking algorithm and ChemPLP scoring function (Korb *et al.* 2007, 2009) (I, II, IV, V). The scoring function, f_{CHEMPLP} , is empirical and uses the following formula:

$$f_{\text{CHEMPLP}} = f_{\text{plp}} + f_{\text{chem-hb}} + f_{\text{tors-lig}} + f_{\text{clash-lig}} + 0.3 \cdot f_{\text{score-prot}} - 20.0$$

where f_{plp} considers the steric and $f_{\text{chem-hb}}$ the hydrogen bonding and metal-acceptor interactions between the ligand and the protein. The intramolecular ligand interactions are accounted by torsional potential and clash terms $f_{\text{tors-lig}}$ and $f_{\text{clash-lig}}$, and the intramolecular protein interactions by $f_{\text{score-prot}}$.

Panther (Niinivehmas *et al.* 2015) and ShaEP (Vainio *et al.* 2009) were used for NIB docking (III), VS, and rescoring of flexible docking results (Kurkinen *et al.* 2018, 2019) (V). The scoring function in ShaEP produces a similarity score for the shape and electrostatic similarity of two small molecules or other atomic structures, the latter of which the Panther NIB models represent.

Rocker (Lätti *et al.* 2016) was used for receiver operating characteristic (ROC) curves and to calculate EF values and area under curve (AUC) metrics for VS benchmarking (V). The EF values were calculated as true positive rates when 1 or 5% (EFd 1% or EFd 5%) of the decoys were found.

4.5 Molecular dynamics simulations (I, II, IV)

4.5.1 Preparation

Tleap of AMBER (Case *et al.* 2005) was used to prepare ligand-protein structures for MD simulations. The ligand-protein complexes were solvated with rectangular boxes filled with transferable intermolecular potential three-point (TIP3P) waters (Jorgensen *et al.* 1983). The protein was applied with the ff14SB

force field (Maier *et al.* 2015), atomic parameters for six-coordinated iron were used for the CYP heme (Giammona *et al.*, Giammona 1984), and general Amber force field (GAFF) parameters (Wang *et al.* 2004) with the RESP-derived partial charges (Bayly *et al.* 1993) were used for ligands. Hydrogens were added. When applicable, the systems were neutralized with appropriate Na⁺ or Cl⁻ counter ions.

4.5.2 Simulation

The MD simulations were performed in NAMD (Phillips *et al.* 2005). The atoms of the simulated molecules move according to the Newtonian equations of motion, where the movement is defined by the mass, position and the total potential energy $U_{potential}$ of the atom that depends on all atomic positions in the simulated system. The potential energy of an atom is defined by a common potential energy function:

$$U_{potential} = U_{bond} + U_{angle} + U_{dihedral} + U_{vdW} + U_{Coulomb}$$

where the U_{bond} , U_{angle} and $U_{dihedral}$ account for bonded interactions and U_{vdW} and $U_{Coulomb}$ for non-bonded van der Waals and electrostatic interactions.

The MD simulations were performed in four steps (III), or with an additional minimization step after the production run (I, II). The four-step protocol and setup was based on priorly published MD simulations (Ylilauri and Pentikäinen 2013). The systems were minimized using the default conjugate gradient algorithm, first with the protein alpha carbon atoms restricted (5 kcal/mol) for 15,000 steps and second without restrictions for 15,000 steps. A 180,000 step (I, II) or 1,200,000 step (IV) equilibration MD simulation in NVT ensemble was run with the alpha carbon atoms restricted (5 kcal/mol). Finally, a production simulation in NPT ensemble without restrictions was performed using either 2.4 ns (I, II) or 24.0 ns (IV) time frame. Alternatively, the production run snapshots were further minimized in 15,000 steps without constraints (I, II). The MD simulations were conducted using periodic boundary conditions and the particle-mesh Ewald method (Darden *et al.* 1993) for long-range electrostatic interactions. Time step of 2.0 fs was applied as the hydrogens were restrained using the SHAKE algorithm (Ryckaert *et al.* 1977). Cutoff and switching distances of 12.0 Å and 10.0 Å, respectively, were applied for van der Waals and short-range electrostatic interactions. Non-bonded interactions were calculated every time step and the full electrostatic interactions every third step. The temperature was adjusted to 300 K with Langevin dynamics, using 5 ps⁻¹ damping coefficient for all non-hydrogen atoms. The pressure was adjusted to 1 atm using the Langevin piston Nosé-Hoover method with oscillation time scale of 200 fs and damping scale of 100 fs.

4.5.3 Analysis

Binding free energy estimations for the ligand-protein complexes were calculated using the molecular mechanics generalized Born surface area (MMGBSA) (Genheden and Ryde 2015) or Nwat-MMGBSA method (Maffucci and Contini 2013, 2016, Maffucci *et al.* 2018). The calculations were carried out using MMPBSA.py (Miller *et al.* 2012) and the available GB models igb1 (Tsui and Case 2000), igb2 (I, II) and igb5 (I, II, IV) (Onufriev *et al.* 2004). The general formula for calculating the binding energy of ligand-protein complexes with MMGBSA is the following:

$$\Delta G_{bind} = G_{comp} - G_{prot} - G_{lig}$$

where ΔG_{bind} is the binding free energy, G_{comp} , G_{prot} and G_{lig} are the free energies of the complex, protein and ligand, respectively. The free energies are calculated with the equation:

$$G = E_{bnd} + E_{el} + E_{vdW} + G_{pol} + G_{np} - TS$$

where the first three terms are molecular mechanics terms of bonded, electrostatic and van der Waals interactions in vacuum. G_{pol} and G_{np} are the polar and non-polar contributions to the solvation free energy. The polar component is calculated according to the GB model. The last terms are the temperature T multiplied by the solute entropy S . The Nwat-MMGBSA approach uses the same framework, but a specified number N of explicit water molecules closest to the ligand molecule in the MD trajectory are considered as part of the protein.

Cpptraj in AMBER (Case *et al.* 2005) was used for calculating atomic distances, root mean square deviation (RMSD) values (I, II, IV) and the counts of immediate ligand-water interactions (IV). RMSD values of MD snapshots to relevant crystal structures (II) were calculated with the rmsd.py script in the Schrödinger platform (Schrödinger, LLC, New York, NY).

4.6 Visualization and figure preparation (I-V)

Visual analyses were performed in the Bodil modelling environment (Lehtonen *et al.* 2004). Molecular figures were prepared using MOLSCRIPT (Kraulis 1991), Raster3D (Merritt and Murphy 1994) and VMD (Humphrey *et al.* 1996). Rocker (Lätti *et al.* 2016) was used for ROC curves.

5 REVIEW OF THE RESULTS

5.1 Finding substrate binding mode and site of metabolism (I, II)

The prediction of small-molecule binding mode and SOM is a widely considered part of CYP metabolism prediction. Enzyme structure-based methods provide insight into the atomic interactions of ligand-protein complexes. Here, MD simulations and binding free energy calculations using MMGBSA were utilized for binding mode and SOM prediction of seven cases of ligand-CYP enzyme complexes (Table 4). First, on the simpler approach, only the MMGBSA binding energy was used to select the most favoured binding pose. Atomic distances of the ligands to the heme iron were used to predict the SOM. As shortly discussed, the MD/MMGBSA method was also tested on two other protein target cases to evaluate the method on the recognition of crystal structure-like ligand poses and on the correlation of MMGBSA with experimentally determined IC₅₀ values. On the second approach, the binding energy-based binding mode and SOM prediction of CYP substrates were augmented with enhanced stability and atomic distance analysis, and the method was experimented with two CYP substrates.

Four molecular docking poses of each small molecule were subjected to short 2.4 ns MD simulations. Twenty snapshots of each simulation were analyzed as is (II) and/or further minimized (I, II). For each pose, the binding energy was calculated. For the CYP ligands, the atomic distances of the ligands to the catalyzing heme iron were calculated. The stabilities of the poses were analyzed visually (I) or, in addition, using ligand and heme-based RMSD_{LH} and the standard deviation (STD) of the atomic ligand-iron distances (II).

Binding mode prediction of CYP ligands based on MMGBSA values was successful in four out of seven cases (Table 4). The second approach, with the incorporation of the enhanced stability and accessibility analysis, could predict the binding mode and SOM correctly for both applied cases, one of which failed in the binding energy-based prediction (Table 4). Thus, the dynamic stability and accessibility of potential SOMs were crucial to consider in binding mode and SOM prediction in addition to the binding energy. Although the simulations

were relatively short, it was found that a single binding mode can be obtained from multiple different docking poses in the MD simulations. Consequently, the correct predictions required also manual analysis. A post-minimization of the simulation snapshots did not enhance the prediction.

TABLE 4 Binding mode and SOM prediction based on MD metrics.

Ligand	CYP isoform	Experimentally determined SOMs or metabolites	Predicted SOMs Top 1 (Top 2)	Utilized MD metrics
6-methyl-coumarin (6MC)	2A6	C7	C7 (C5)	1*
			C7 (C4/C5)	2*
	2A5	C7	C7	1*
7-methyl-coumarin (7MC)	2A6	Tautomer (7-methylene-7H-chromen-2-ol), C3/C4, MI	7-methyl/tautomer (C4/C5)	1*
	2A5	7-methyl, C3/C4	7-methyl (C3/C4)	1*
7-formyl-coumarin (7FC)	2A6	MI	7-formyl	1*
	2A5	MI	-	1*
Coumarin	2A6	C7	C5 (C7)	1*
			C7 (C5)	2*

MI: Mechanism-based inactivator

1*: Binding mode prediction based on MMGBSA binding energy, SOM prediction based on atomic distances of substrate positions to heme iron. In addition, binding mode stability evaluated visually.

2*: Binding mode and SOM prediction based on MMGBSA binding energy, RMSD_{LH} atomic distances of substrate positions to heme iron and the atomic distance stability (STD).

5.1.1 Binding mode prediction based on MMGBSA (I, II)

The binding modes of 6MC, 7MC and 7FC in complex with CYP2A6 and 2A5 (I), and coumarin in complex with CYP2A6 (II), were attempted to be predicted based on calculated MMGBSA binding energy from 2.4 ns MD simulations of four initial docking poses of each ligand. The computational prediction was compared to experimental results.

The metabolites of 6MC were determined experimentally only for 7-hydroxylation, and the 7MC metabolites are tentative as no standards were available for the acquired mass spectrometry data. 6MC is converted to fluorescent 7-hydroxy-6-methylcoumarin by both CYP2A6 and CYP2A5 with similar rate to coumarin 7-hydroxylation by CYP2A6. 7MC was found to be a mechanism-based

inactivator for CYP2A6 but not for CYP2A5. CYP2A6 converts 7MC to the tautomer of the molecule and hydroxylates the molecule at positions 3 and/or 4. CYP2A5 hydroxylates the molecule at 7-methyl and at position(s) 3 and/or 4. 7FC was determined to be a mechanism-based inactivator for both CYP2A6 and 2A5, but possible metabolites were not determined experimentally. (I)

The MMGBSA binding energy-based prediction of a single binding mode of 6MC and 7MC in complex with CYP2A6 and CYP2A5 was in accordance with experimental results (Table 4). Other SOM(s) than the experimentally confirmed ones were suggested by the MD simulations of 6MC and 7MC in complex with CYP2A6. The MMGBSA binding energy of the energetically preferred ligand pose was often within error limits of at least one other pose. In addition, it was common that a ligand could acquire an identical binding pose in the simulations from multiple differing docking poses. The binding mode of 7FC in CYP2A6 and 2A5 could not be predicted as the binding energy values of the poses were very close and the SOM(s) or metabolite(s) of 7FC were not determined experimentally.

5.1.1.1 Successful primary predictions

Selection of a single 6MC binding pose based on MMGBSA binding energy was in accordance with the experimental result of 6MC 7-hydroxylation by both CYP2A6 and 2A5. In the MD simulations of 6MC in complex with both enzymes, the energetically preferred pose had the position 7 and 6-methyl closest to the heme iron (I Fig. 2 B). The poses were also the most stable ones based on visual analysis. In addition, in the CYP2A5 simulations, the position 7 is closest to the heme iron in two of the most preferred binding poses (I Fig. 2 B). Both poses are stable by visual analysis and the binding energies are within error limits of each other.

The simulations of 6MC in complex with CYP2A6 suggested that other than the experimentally determined 7-hydroxylated metabolite could be possible. The MMGBSA values of two poses are within error limits of the most favored pose. In one of these two poses, the position 5 stays close to the heme iron and is thus available for oxidation. However, the experimental studies tested 6MC only for 7-hydroxylation and thus a metabolite catalyzed at the position 5 has not been experimentally confirmed.

The top binding pose from the 7MC simulations in complex with CYP2A6 and 2A5 agrees with experimentally determined metabolites. In addition, the comparison of the CYP2A6 and 2A5 simulations indicated a difference in the compound's binding to these enzymes, which could explain the mechanism-based inactivation of CYP2A6 by 7MC. The pose in which the 7-methyl is the closest position to the heme iron is favored energetically and by stability in both CYP2A6 and 2A5. The same pose was acquired in three out of four docking poses in the CYP2A5 simulations, and in all there is space available for oxygen to bind the heme iron (I Fig. 2 D, F). Accordingly, a metabolite hydroxylated at the 7-methyl was indicated by the experimental results. In contrast to the acquired 7MC-CYP2A5 complexes, the 7-methyl group lies at a very close proximity to the CYP2A6 heme iron and leaves no space for oxygen to bind the iron (I Fig. 2 C, F).

This could explain the mechanism-based inactivation of CYP2A6 by 7MC. The reaction mechanism is outside the scope of MD simulations, but a hypothesis was derived based on the coordinates of the favored binding mode. The low distance between the 7-methyl and the heme iron could lead to formation of a 7-methylene-7H-chromen-2-ol tautomer, which the experimental data suggests for CYP2A6 but not for CYP2A5. The formed tautomer could bind tightly with the iron by the tautomer's pi-electrons or react irreversibly with the binding site environment in an unidentified way.

The other simulated poses of 7MC in complex with CYP2A6 and 2A5 suggested also other metabolites for the compound. In CYP2A6, other SOMs for 7MC could be the positions 4 and 5, but the experimental results suggested a 3- and/or 4-hydroxylated product. In CYP2A5, the single simulation where the 7-methyl was not closest to the heme, positions 3 and 4 lie close to the heme. Although the pose was energetically clearly worst, it showed great stability and could thus be considered a secondary binding mode of 7MC in CYP2A5. This is in line with the experimental indication of a 3- and/or 4-hydroxylated product of 7MC by CYP2A5.

5.1.1.2 Wrong or ambiguous predictions

The prediction of coumarin binding mode, based on MMGBSA binding energies, did not agree with experimentally determined 7-hydroxylation by CYP2A6. The molecular docking yielded coumarin poses, where the closest sites to the heme iron are (1) 2-carbonyl, (2) position 7, (3) 2-carbonyl and position 3 and (4) positions 5 and 6 (II Fig. 1 B). The calculated MMGBSA values are within error limits of each other in the poses (II Table 1). The pose 4 is the most preferred, followed by pose 2, 3 and 1. Accordingly, the binding energy estimations and the atomic distances suggest that position 5 would be the most preferred SOM, although the correct pose 2 is also within error limits of the top pose. From four differing docking poses, two general coumarin orientations were acquired in the simulations where either the position 7 or 5 is closest to the heme iron (II Table 1).

The mechanism-based inactivation of CYP2A6 and 2A5 by 7FC could not be deduced from the MD simulations. Based on the binding energy, the preferred binding mode of 7FC in complex with CYP2A6 and 2A5 is not clear as the MMGBSA values of the poses are close and steadily within error limits of each other. However, the 7-formyl of 7FC orientates to very close proximity of the CYP2A6 heme iron at the end of the simulation of the pose 4 (I Fig. 2 H). This could indicate that the 7-formyl group plays a role in the mechanism-based inactivation, which was backed up by literature of commonly observed mechanism-based inactivation of CYP enzymes by aldehydes.

5.1.2 Enhanced stability and distance analysis (II)

Since the MMGBSA binding energies of different CYP substrate poses were in many of the above cases within error limits of each other, it was reasonable to take a closer look into other variables of the simulated poses. In order to

investigate some of the options to analyze the energetics and stability of substrate poses, the already discussed MD simulations of four initial docking poses of coumarin and 6MC in complex in CYP2A6 were examined. Both coumarin and 6MC are 7-hydroxylated by CYP2A6 with similar rate (I). Other metabolites of 6MC were not determined (I) and the literature does not suggest other metabolites for coumarin.

A set of simulation-derived metrics was suggested for predicting the preferred binding mode and SOM of a CYP substrate. The binding energy comparison of the simulated substrate poses was incorporated with a simple calculation of the binding pose stability and the atomic distances the substrate to the heme iron. Namely, for each simulation, the RMSD of the substrate and the CYP2A6 heme were calculated together (RMSD_{LH}) in order to consider the stability of the substrate pose in relation to the first frame of the simulation. On one hand, the exclusion of the CYP amino acid residues from the RMSD analysis and superimposition removes the effect of the protein macromovement to the substrate superimposition. This allows a more delicate analysis of the substrate stability. On the other hand, when the heme is included, the RMSD_{LH} indicates of the stability and orientation of the simulated pose in relation to the binding site. Atomic distances and stabilities, the latter indicated by the STD of each distance, of the substrate positions to the CYP heme iron were calculated for each simulation. The closer substrate positions to the heme iron are more likely to be oxidized. The closest substrate position should also be well stabilized at the supposed reaction coordinates, which is indicated by the STD of the mean distance. The distance should be low enough for the position to be available for oxidation, but leave space for the reactive oxygen.

In both coumarin and 6MC simulations, the combination of MMGBSA and the above metrics of ligand stability and atomic distances resulted in correct binding mode and SOM prediction. However, especially in the case of coumarin, this required a manual analysis of the ligand trajectories in the individual poses. Similar or close to identical binding poses were acquired from several simulations although the simulations of both compounds were initiated from four notably differentiating docking poses.

5.1.2.1 Coumarin

Combining the information from MMGBSA binding energy, RMSD_{LH} and the atomic distances together, the coumarin position 7 is preferred at the proximity of the CYP2A6 heme iron, thus in agreement with experimentally determined 7-hydroxylation. The prediction relied partly on manual analysis of the simulations as the orientation of coumarin changed during the individual trajectories. The pose is energetically the second-preferred, but it is the most stable and the position 7 is closer to the heme iron than position 5 in the other binding poses. The preferred pose is also closest to the crystal structure of coumarin in complex with CYP2A6. The second-preferred binding pose, where the coumarin position 5 is closest to the heme iron, could also be considered as a naturally occurring binding mode as the calculated descriptors are within error limits of the top

binding pose. However, coumarin metabolites catalyzed at the position 5 by CYP2A6 are not found in the literature.

5.1.2.2 6-methylcoumarin

The prediction of the 6MC binding mode and SOM agree with the experimentally determined 7-hydroxylation by CYP2A6. Combining the information together, the preferred binding mode of 6MC orients the 6-methyl and position 7 closest to the heme iron. The MMGBSA binding energy is the best for this pose and the positions 6-methyl and 7 are closer to the heme iron and more stable than the position 5 in pose 4, which is second-ranked by MMGBSA and top-ranked by RMSD_{LH} . In the preferred pose 1, the 6-methyl and position 7 are accessible for oxidation. In this pose, difference between the preference of oxidation of the position 6-methyl and 7 cannot be made based on the applied metrics. Another binding mode where the position 5 (pose 4) or 4 (pose 3) is oriented towards the heme is also possible based on the MD simulations. Although the MMGBSA, position 5 distance to the heme iron, and the distance STD are slightly inferior to those of pose 1, the values are very close. However, only data for the 7-hydroxylation of 6MC by CYP2A6 is available and thus the predicted second-preferred binding mode and SOM are not verified experimentally.

5.1.3 MMGBSA in other applications (II)

In VS and molecular docking, it is important that the method recognizes a true binding mode of ligands and that the scores correlate with experimental results. The ability of molecular docking and MD/MMGBSA to accomplish these objectives was investigated with twelve androgen receptor (AR) crystal structure ligands and 152 phosphodiesterase 4B (PDE4B) inhibitors with experimentally determined IC_{50} values. With AR, the MD/MMGBSA method did not generally improve the recognition of the crystal structure-like ligand pose compared to docking. In the case of PDE4B, the correlation of experimental IC_{50} values with MMGBSA binding energies was significantly higher than with docking scores.

5.1.4 The effect of post-minimization (II)

The effect of minimization of the MD simulation production run snapshots to the MD/MMGBSA approach was investigated in the cases of CYP2A6 in complex with coumarin and 6MC, AR and PDE4B. In the case of CYP2A6 substrates coumarin and 6MC, it was found that the post-minimization procedure does not improve the binding mode and SOM prediction in these two cases. The ranking of the simulated binding poses was generally unchanged after the minimization. The MMGBSA and RMSD_{LH} values of the different poses are within error limits (STD) of each other similarly as they are in the non-minimized MD simulations. However, post-minimization brings coumarin closer to the crystal structure and the distance of position 7 is closer to the heme iron, a similar distance as for a typical distance seen in CYP2A6 crystal structures. In the case of AR, the post-minimization slightly improved the crystal structure-like ligand pose

recognition. The post-minimization did not have a significant effect on the correlation of MMGBSA and IC₅₀ values of PDE4B inhibitors.

5.2 Profluorescent tool molecules – one binding mode of interest (III, IV)

Profluorescent substrates can be used to determine catalytic activity and inhibition of CYP enzymes. There are many such tool molecules available, but they often have poor selectivity as they are catalyzed by multiple CYP enzymes. Coumarin-based molecules are abundant for this purpose as nonfluorescent coumarin derivatives can be metabolized to a fluorescent 7-hydroxylated metabolite in a typical CYP reaction (III Fig. 1). The coumarin core offers a wide array of options for chemical functionalization and thus potential for varying the selectivity profile of the 7-hydroxylation reaction by CYP enzymes.

Previously published and new 3-phenylcoumarin derivatives (III Fig. 2, IV Fig. 1) were computationally modelled (Fig. 5) and experimentally tested for 7-hydroxylation by 13 human xenobiotic-metabolizing CYP enzymes. The CYP enzymes are hepatic except for CYP1A1 and 1B1. The CYP1 family members was identified as the most suitable target proteins to accommodate the 3-phenylcoumarin core and subsequently catalyze the 7-hydroxylation reaction. Experimental results confirmed that 19 out of 21 tested 3-phenylcoumarin derivatives were 7-hydroxylated with measurable activity by either or by both CYP1A1 and 1A2. Other isoforms to frequently catalyse the reaction were found to be CYP1B1, 2A6, 2D6 and 2C19 (III Fig. 6, Table 1, IV Fig. 2). The interactions of the 3-phenylcoumarin derivatives with selected CYP isoforms were studied with docking and 24.0 ns MD simulations in the binding pose that was hypothesized to be the most prominent to facilitate the 7-hydroxylation reaction. The computational modelling suggested key ligand-enzyme interactions and properties of the CYP enzymes that affect the preference of the 7-hydroxylation reaction. Some conclusions may also be made of the general properties and key differences of the CYP1 family based on the computational modelling.

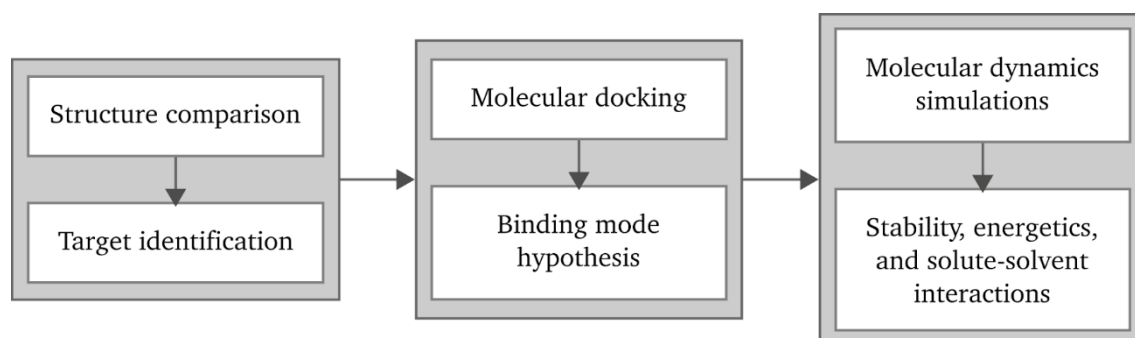


FIGURE 5 Molecular modelling workflow to study the 7-hydroxylation selectivity of 3-phenylcoumarin derivatives by CYP enzymes.

5.2.1 Identification of target isoforms

The comparison of the CYP 3D structures (III Table S1) revealed that the CYP1 family and CYP2A6 would be most suitable to accommodate the 3-phenylcoumarin core to their respective binding sites for 7-hydroxylation. Both the CYP1 family and CYP2A6 have binding sites that are well suited for hydrophobic and planar ligands. However, the CYP2A6 binding site is smaller than those of the CYP1 family, and is likely not able to accommodate a wide array of 3-phenylcoumarin derivatives. The 3-phenylcoumarin core represents alpha-naphthoflavone that is co-crystallized with the CYP1 family enzymes. Both small molecules are planar, have three to four closely attached ring structures and a single carbonyl group. The CYP2A6 is co-crystallized with coumarin which is obviously highly similar but slightly smaller than 3-phenylcoumarin. In conclusion, the binding sites of the CYP1 family enzymes and CYP2A6 have excellent topology to bind 3-phenylcoumarins.

5.2.2 The CYP1A subfamily and CYP2A6

In the CYP1A subfamily and CYP2A6, the binding poses from docking suggested that 3-phenylcoumarin 2-carbonyl could form a hydrogen bond (H-bond) with Ser122, Thr124 and Asn297 of the 1A1, 1A2 and 2A6 isoforms, respectively (Fig. 6 A, III Fig. 4 A, B and D and S, IV). In this pose, the position 7 can be oriented towards the catalyzing heme. The H-bond from the 2-carbonyl could be sufficient to stabilize the 3-phenylcoumarins to this binding mode. Accordingly, other H-bonding substituents might not be required at the 3-phenylcoumarin core. The experimental results showed that 19 out of 21 tested 3-phenylcoumarins were indeed 7-hydroxylated by either or by both CYP1A1 and 1A2 with measurable activity (III Fig. 6, Table 1, IV Fig. 2, Table 1). The 7-hydroxylated derivatives include a large variety of H-bonding and hydrophobic substituents, which suggests that the 2-carbonyl H-bond and hydrophobic interactions would indeed suffice for the substrate stabilization. An exception in the hypothesized binding mode was made on one compound where 6,8-chlorine shields the position 7. The compound core was supposed to be flipped 180 degrees such that the 2-carbonyl points towards Asp320 and Thr497 of CYP1A1 or Asp320 and Thr498 of CYP1A2 in order for the position 7 to be accessible for oxidation (Fig. 6 B, IV Fig. 3D-E).

As the CYP2A6 binding site is smaller than that of CYP1A1 and 1A2, the 7-hydroxylation reaction were catalyzed mainly on the smallest 3-phenylcoumarin derivatives by CYP2A6 (III Fig. 2 and 6, Table 1). Surprisingly, also slightly larger compounds 20 and 22 with a acetoxy group at position 3' or 4' are also 7-hydroxylated by CYP2A6 (IV Fig. 2). Hypothetically, the group might open a channel in the CYP2A6 binding site and find an H-bonding donor there, but this option was not studied with molecular modelling.

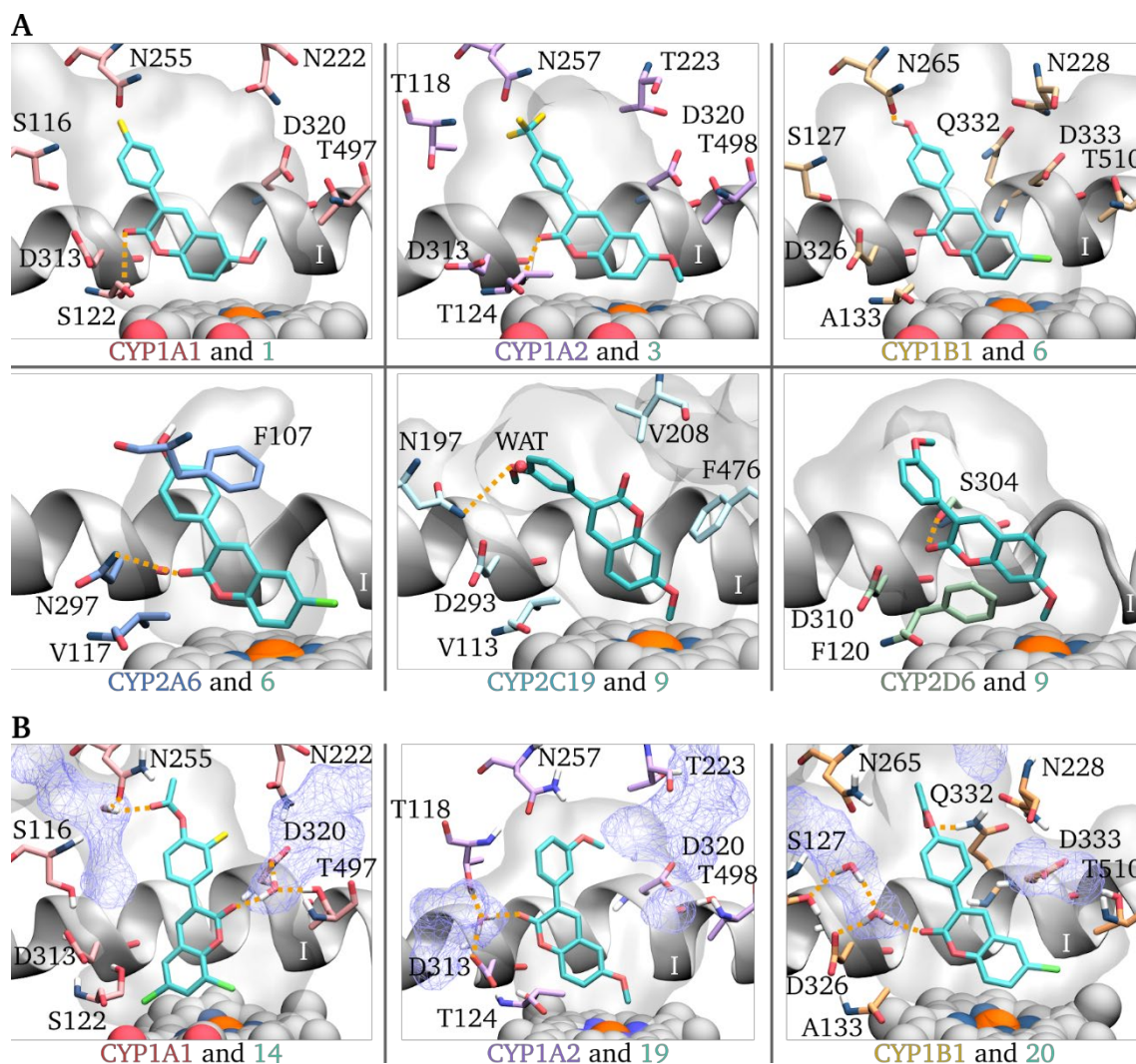


FIGURE 6 Binding poses of 3-phenylcoumarin derivatives in CYP binding sites. A) Docking poses that could allow the catalysis of the 7-hydroxylation reaction. B) Binding poses from MD simulations. Stick models: amino acids, ligands and key water molecules; van der Waals model: heme; orange dotted lines: hydrogen bonds; transparent surface: binding site surface based on a negative image generated with Panther (Niinivehmas *et al.* 2015); wireframe surface: surface of water molecules that are connected to the binding site and are among 20 closest water molecules to the ligand. The images were generated in VMD (Humphrey *et al.* 1996).

The MD simulations of 3-phenylcoumarins in complex with the CYP1A isoforms support the role of the Ser122 H-bond on CYP1A1, but not on the Thr124 H-bond on CYP1A2. The H-bond from the 2-carbonyl to CYP1A1 Ser112 is found in 5/10 of the simulations where the H-bond was assumed to exist (IV Table 3). Furthermore, the presence of the Ser122 H-bond does not automatically indicate of high 7-hydroxylation efficiency (IV Table 1). In CYP1A2, the H-bond from 2-carbonyl to Thr124 is not found (IV Table 3). Instead of the Ser122/Thr124 H-bond, a water-mediated H-bond to Asp313 is found in both CYP1A1 and 1A2 simulations (IV Fig. 3 A, B, G and H). In the differing binding mode of compound 14, a water-mediated H-bond is instead found from 2-carbonyl to Asp320 and Thr497 of CYP1A1 (Fig. 6 B), but not to the corresponding Asp320 and Thr498 of

CYP1A2 (IV Fig. 3D-E). Straight or water-mediated H-bonds with the enzymes were also found to be formed from H-bonding substituents at the 3-phenyl group (Fig. 6 B, IV Fig. 3D, F-I).

5.2.3 CYP1B1

As the topology of CYP1B1 is highly similar to CYP1A1 and 1A2, the most favourable 3-phenylcoumarin binding mode for 7-hydroxylation represents the same general orientation as that in the CYP1A subfamily (Fig. 6, III Fig. 4 A-C, IV Fig. 3). However, CYP1B1 lacks an evident H-bond donor for the 2-carbonyl in this binding mode. The molecular docking poses indicated that H-bonding substituents would be required at the 3-phenyl ring as they could bond with the H-bonding residues at the CYP1B1 binding site opposite to the heme (Fig. 6 A, III Fig. 4C and S1, IV Fig. 3 I). Accordingly, among the tested 3-phenylcoumarin derivatives, mainly those with a H-bonding group at the 3-phenyl positions 3' or 4' were 7-hydroxylated by CYP1B1 (III Fig. 2 and 6, Table 1, IV Fig. 2, Table 1). However, even more hydrophobic derivatives such as the compound 19 can be catalyzed to the 7-hydroxylated metabolite with high efficiency (IV Table 1). In total, 8/21 3-phenylcoumarins were 7-hydroxylated by CYP1B1 with measurable activity (III Table 1, IV Table 1). As in the CYP1A subfamily, MD simulations suggested that the substrates can be stabilized by a water-mediated H-bond from 2-carbonyl to CYP1B1 Asp326 (Fig. 6 B, IV Fig. 3 C, F and I).

The 7-hydroxylation efficiency of certain 3-phenylcoumarins by CYP1B1 is exceptionally high. These compounds 6 (III) and 20 (IV) possess a 6-chlorine and a H-bonding hydroxyl (compound 6) or acetoxy group (compound 20) at position 4'. Compared to their close analogs, compounds 4 and 22, where the corresponding H-bonding group is at position 3', the compounds 6 and 20 have significantly higher 7-hydroxylation efficiency. The MD simulations of compound 20 (Fig. 6 B) and 22 suggest that the delicate difference in the position of the H-bonding group has crucial influence on binding. Both compounds form an H-bond from the 3' or 4'-acetoxy to the enzyme at the same location of the binding site. However, the compound 22 3'-acetoxy tilts the molecule in the binding site such that the water-mediated H-bond to Asp326 is not formed as it is with the compound 20 4'-acetoxy. The rightly-placed H-bonding group at the position 4' can remarkably improve the substrate-enzyme interactions and thus boost the 7-hydroxylation activity of 3-phenylcoumarins by CYP1B1.

The CYP1B1 binding site is the smallest in the CYP1 family and thus the catalytic activity of CYP1B1 is likely more sensitive to the substrate shape and size. The binding site topology is similar to CYP1A1, but the volume is roughly 80 Å³ smaller in CYP1B1 (Walsh *et al.* 2013). The key differences in the H-bonding amino acids of CYP1A1/1B1 are the Ser122/Ala133 and Phe319/Gln332 pairs. In CYP1B1 the water-mediated Asp326 H-bond is the only available H-bond donor at this side of the binding site, as compared to the available Ser122/Thr124 in CYP1A1/1A2. Consequently, substrate binding modes that would benefit from this H-bond donor for high catalytic efficiency need to accommodate the water molecule next to Asp326. The effect of this H-bond and a slight change in

substrate shape to 3-phenylcoumarin 7-hydroxylation activity was demonstrated in the MD simulations of compound 20 and 22 in complex with CYP1B1. A switch of a 4'-acetoxy to position 3' prevents a more stable orientation where the 2-carbonyl can form a water-mediated H-bond to CYP1B1 Asp326. This is likely a major contributor in the large difference in the 7-hydroxylation efficiency of these two compounds (IV Table 1).

5.2.4 CYP2D6 and 2C19

A few 3-phenylcoumarin derivatives were found to be readily 7-hydroxylated also by CYP2D6 and 2C19 (III Fig. 6, Table 1, IV Fig. 2). Some of these were examined with molecular docking (Fig. 6 A, III). In CYP2D6, the 2-carbonyl could form a H-bond with Ser304, and large substituents at the 3-phenyl ring position 3' could orientate towards the substrate access channel that is found in the crystal structure (III Fig. 4 E and S1). Based on the experimental results and the suggested binding mode, the 7-methoxy group of the 7-hydroxylated compounds is likely crucial for the molecule to reach the reaction coordinates near the heme. In CYP2C19, the 3-phenylcoumarin 2-carbonyl is likely to remain unbound and instead a H-bond acceptor 3'-methoxyl at the 3-phenyl ring could replace a crystal structure water and form a H-bond with Asn107 (III Fig. 4 F and S1). Accordingly, the CYP2C19 catalyzes the 7-hydroxylation mainly of derivatives with a H-bonding group at the position 3'.

5.2.5 Novel tool molecules

An array of novel profluorescent substrates were found for CYP enzymes (Table 5). A new selective substrate for CYP1A2, 6-methoxy-3-(4-trifluoromethylphenyl)coumarin (compound 3), could be used for fluorescence-based inhibition assays of CYP1A2 in liver microsomes. Compound 14, 3-(3-fluoro-4-acetoxyphenyl)coumarin, was suggested to be used as selective substrate for CYP1A1 in tissues with low CYP3A4/5 expression. The remaining novel CYP substrates could be used in recombinant enzyme assays. One compound, 3-(3-methoxyphenyl)-6-methoxycoumarin (compound 19), was found to be efficiently converted to the fluorescent product by the CYP1 family enzymes. Two compounds, 3-(4-hydroxyphenyl)-6-chlorocoumarin (compound 6) and 3-(4-acetoxyphenyl)-6-chlorocoumarin (compound 20), were oxidized to the fluorescent product with very high efficiency by CYP1B1. Finally, 3-(3-methoxyphenyl)-7-methoxycoumarin (compound 9) was efficiently 7-hydroxylated by CYP2C19 and 2D6.

TABLE 5 Novel profluorescent tool molecules for CYP enzymes with good selectivity or efficiency of fluorescence-producing 7-hydroxylation of 3-phenylcoumarin derivatives. Selected binding poses for the molecules are shown in Fig. 6.

CYP isoform	Compound	K_m	V_{max}	$V_{max} K_m^{-1}$
1A1	14	15.6	2.5	0.16
	19	0.96	24.2	25.2
1A2	3	3.2	7.9	2.5
	19	0.27	8.2	30.4
1B1	6	0.24	11.7	48.8
	19	0.43	9.3	21.6
	20	0.095	5.1	53.0
2D6	9	1.9	4.6	2.4
2C19	9	1.0	9.1	9.1

5.2.6 Indicators and contributors of catalytic efficiency

As reviewed above, the molecular docking and MD simulations of 3-phenylcoumarin derivatives 1-10 (III) and 13-23 (IV) provided insights to the characteristics and interactions of the compounds and the CYP enzymes that affect the fluorescence-producing 7-hydroxylation activity and enzyme selectivity. Insightful observations were gathered with the investigation of simply a single binding pose that was hypothesized to be most favourable for 7-hydroxylation in the CYP enzymes.

Within the CYP1 family, a detailed comparison was performed on the interactions of the novel profluorescent substrates and the enzymes (IV). The differences of the 7-hydroxylation activity of selected 3-phenylcoumarins by the three CYP1 forms were in accordance with the ligand-enzyme interactions observed in MD simulations. In short, the energetics, position 7 accessibility and stability of the selected compounds in the simulated binding modes with the CYP1 enzymes seemed to correlate with the experimentally determined 7-hydroxylation activities. These are the same metrics as used in the binding mode predictions (II). The example compounds 19, 14 and 20 present different 7-hydroxylation profiles among the CYP1 enzymes. In both compounds 19 and 14, each metric of binding energy, stability and accessibility of the position 7 to the heme iron pointed to the CYP1 enzyme that catalyzed the 7-hydroxylation most efficiently. The same trend was followed in the simulations of the two other CYP1 enzymes. For compound 20, it was suggested that the observed high stability of the compound in complex with CYP1B1 is an important contributor in the 7-hydroxylation efficiency, as the other metrics did not indicate a clear preference of the binding mode by CYP1B1 as compared to CYP1A1 and 1A2.

It must be kept in mind that other binding modes for the compounds may exist in addition to the investigated poses. Firstly, other binding modes might be

more favored over the modelled binding pose, which can lead to decreased activity at the measured SOM. Secondly, at least three general binding poses were found to be favorable for the 3-phenylcoumarin 7-hydroxylation in the CYP1 enzymes. In the first two, the 2-carbonyl either forms a H-bond straight to Ser122 of CYP1A1 (III Fig. 4, IV Fig. 3 G), or via water to Asp313 of CYP1A1 and 1A2 or Asp326 of CYP1B1 (IV Fig. 3A–C, G–I). In the third pose, simulated only for compound 14, the 2-carbonyl H-bonds via water with Asp320 and Thr497 of CYP1A1 or Asp333 and Thr510 of CYP1B1 (IV Fig. 3D–F). On one hand, the alternative binding pose of compound 14 could be favorable also for the other 3-phenylcoumarins at least in CYP1A1 and 1B1. On the other hand, the binding pose simulated for most of the compounds could be feasible also for compound 14 as the 3-phenylcoumarins were able to adopt an upright orientation in the CYP1 binding sites due to the water-mediated H-bond to Asp313 of CYP1A1 and 1A2 or Asp326 of CYP1B1. Thus, the position 7 could be accessible for oxidation by CYP1 enzymes also in this binding pose. In addition, many other factors such as substrate recognition at the enzyme surface or the rate of substrate ingress and egress can affect the catalytic efficiency.

5.2.7 Effects of channels and solvent interactions in the CYP1 family

The MD simulations of 3-phenylcoumarin derivatives in complex with the CYP1 family indicated that waters enter and substrate access channels open readily to the CYP1 binding sites. Water molecules enter to the proximity of the ligands and water-ligand H-bonds are formed in most of the complexes (IV Table 2). Water molecules enter to both sides of the ligands (IV Fig. 3) and they both stabilize and waver the simulated substrate binding poses. In general, CYP enzymes are well-known to possess channels that open from the binding site to the enzyme surface (Cojocaru *et al.* 2007). Water molecules are found at the binding site or at its immediate proximity also in the crystal structures of the CYP1 enzymes (Sansen *et al.* 2007, Wang *et al.* 2011, Walsh *et al.* 2013). In CYP1A2, a single water molecule mediates a H-bond between the ligand and the enzyme (Sansen *et al.* 2007). The Channels database (Pravda *et al.* 2018) reports also three reviewed channels for the CYP1A1 (Walsh *et al.* 2013) and 1B1 (Wang *et al.* 2011) crystal structures, namely the 2ac, 3 and solvent channels (Cojocaru *et al.* 2007, Pravda *et al.* 2018).

Water-mediated H-bonds were a common finding between the 3-phenylcoumarins and CYP1 enzymes (Fig. 6 B). Thus, water molecules likely have an important role in ligand binding to these enzymes. A water-mediated H-bond to Asp313/326 (CYP1A/1B1) seems to have an essential role in the 3-phenylcoumarin stabilization to the binding mode that could allow 7-hydroxylation in all of the three CYP1 enzymes. In CYP1A1 and CYP1B1, it is likely that the compounds can also form a water-mediated H-bond from the 2-carbonyl to Asp320 and Thr497 of CYP1A1 and Asp333 and Thr510 of CYP1B1. Among the 3-phenylcoumarins, water-mediated H-bonds to the enzymes were observed also at the H-bonding substituents at the 3-phenyl ring, but these did not show such high stability.

CYP1A2 seems to be the most suitable to accommodate 3-phenylcoumarins for 7-hydroxylation in general. As water molecules emerge readily to the CYP1 binding sites, the optimal match of the shape and size of the ligand and the binding site is crucial for the ligand stabilization. Among the tested 3-phenylcoumarins, CYP1A2 was found to catalyze the 7-hydroxylation reaction of more compounds and with higher efficiency than CYP1A1 and 1B1 as counted from the V_{\max}/K_m values (III Table 1, IV Table 1). In the simulations, the amount of water molecules at the ligand proximity is lowest for the CYP1A2 complexes although ligand-water H-bonds occur in similar numbers across the three enzymes (IV Table 2). Thus, crucial water molecules can enter the binding site and mediate the ligand-enzyme H-bonds, while a smaller amount of water molecules disrupt the simulated binding mode. This is likely partly due to the account that the CYP1A2 binding site is of the medium size in the CYP1 family, the volumes being 524, 469 and 441 Å³ in CYP1A1, 1A2 and 1B1, respectively (Walsh *et al.* 2013). Thus, the CYP1A1 binding site might allow more water molecules at the binding site, while in CYP1B1 the larger substituents in the tested 3-phenylcoumarins might extrude more frequently to binding site channels and thus expose the ligands to the solvent. As discussed below, a differing channel composition of the three enzymes can also affect the substrate and SOM selectivity and water-mediated ligand-CYP interactions observed in the simulations. Flexibility of the enzymes might also have an effect on the selectivity, but this was not evaluated in these simulations.

The observed water channels differ in CYP1A2 in comparison to CYP1A1 and 1B1 (Fig. 6 B). This might have a major impact on the differences of substrate and SOM preference in the CYP1 family. Channels 2ac, 3 and the solvent channel are found in both CYP1A1 and 1B1 crystal structures (Wang *et al.* 2011, Walsh *et al.* 2013). Channels that most likely correspond the channels 2ac and 3 are also observed in the MD simulations of CYP1A1 and 1B1 (IV Fig. 3 A, D, G, C, F and I). The channel 3 can also be observed in the CYP1A2 simulations (IV Fig. 3 B and H). However in contrast to the 2ac channel in CYP1A1 and 1B1, the most frequently observed channel on the corresponding side of the CYP1A2 binding site opens between Thr118 and Asp313, which likely continues either as the 2e or the water channel (Cojocar *et al.* 2007) to the enzyme surface. Based on the MD simulations, the most evident effect of the differing channel composition was that water molecules emerge from a different direction to this side of the CYP1 binding sites (IV Fig. 3). This resulted in different hydration sites at the CYP1 binding sites and thus differing ligand-water interactions that either stabilized or destabilized the simulated 3-phenylcoumarin binding poses.

5.3 Finding active molecules with negative image-based screening (V)

VS offers a way of finding novel bioactive molecules from large databases. Here, Panther NIB docking, VS and rescoring was explored using the example case of cyclooxygenase-2 (COX-2) DUD and DUD-E benchmarking sets. The practical aspects of the NIB docking and rescoring methodology were discussed. A detailed workflow for NIB screening and rescoring with command line inputs and scripts was provided together with a new release of Panther (Niinivehmas *et al.* 2015). The tools used in the provided inputs and scripts are available either free or with an academic free license. The effect of ligand 3D conformer generation to the NIB screening was investigated using different commercial, academic free and freely available tools for the step.

5.3.1 The screening workflow

The general steps of NIB docking and VS are (1) the selection and preparation of the protein target 3D structure, (2) preparation of ligand 3D structures, (3) selection of the protein binding site centroid, (4) generation of the negative image of the binding site, (5) shape and/or charge comparison of the negative image and ligand 3D structures, and finally (6) either evaluation of the model and the workflow with benchmarking sets or investigation and selection of screened molecules for experimental testing (V Fig. 1).

The ligand 3D structure preparation step (2) is of high importance as the Panther/ShaEP NIB screening uses rigid structures of the ligands in the shape/charge comparison step. The ligand 3D structures may be prepared with a number of software and workflows and the ligands can be in either single or multiconformer sets. Four ligand preparation workflows with commercial, academic free or free software were found to produce vast differences in both the benchmarking results (V Tables 2 and 3) and the number of ligands that survive through both the ligand preparation (2) and screening (5) steps (V Table 1). The use of single conformations of the ligands can greatly increase the speed of the ligand preparation and screening phase (V Fig. 3) depending on the size of the multiconformer set. Surprisingly, in this COX-2 benchmarking example, the single conformer sets also fared better than multiconformer sets, although the effect was clearly case-specific (V Tables 2 and 3). However, the observation may be specific for the particular COX-2 benchmarking example and the settings used in the ligand preparation workflows. Even so, it might prove beneficial in NIB screening benchmarking to compare different ligand preparation workflows and the use of single versus multiconformer ligand 3D structures especially in the case of suboptimal results in the first rounds of benchmarking.

The selection and preparation of the protein target 3D structure in step (1) defines the frame for the NIB model. The quality of the protein structure and its binding cavity affect the shape and charge properties of the NIB model and how well it represents the target. The binding site geometry (V Fig. 5C), H-bonding

groups (V Fig. 1, 4 A, 5 B) and possible cofactors, ligands (V Fig. 1 and 4D-E) or water molecules can all be considered in the model generation. Protonation can be considered rigidly if the protons are added to the protein prior to the Panther NIB model generation, or when applicable, alternative rotations of protons are considered in the absence of protonation (V Fig. 5 B). The benchmarking demonstrated that the screening yields vary between NIB models created with different settings and NIB models of identical settings from the two structures (V Tables 2 and 3), the latter being a phenomenon that is common in molecular docking and structure-based VS.

Creating the initial NIB model with Panther is fairly simple in steps (3) and (4), and there are many options to modify and optimize the model. It was demonstrated with a few settings that varying the settings can affect the screening yield case-specifically (V Fig. 4). For example, the NIB model can be restricted to the volume of the bound ligand in the used protein structure, which can shape the NIB model more alike the ligand (V Fig. D-E). Changing the packing method (V Fig. 4G-H) or cavity detection radius (V Fig. 5 E) can also result in a different shape of the model as the model may reach different nooks in the binding cavity. One of the advantages of NIB Panther models is that the definition of the binding cavity can be very specific if the user wants to target a precisely defined area of the protein binding cavity or surface pocket (V Fig. 5A). As the pocket representation is atomic, the model can also be manually augmented with fragments of small molecules in order to define more precisely the desired properties of the screened compounds (Jokinen *et al.* 2019).

The shape and charge comparison in step (5), in other words docking and screening or rescoring, can be performed using ligand conformers created ab initio with a separate ligand preparation workflow or from a prior molecular docking run. Here, the rigid NIB docking and screening using ab initio ligand conformers produced consistently better AUC values than prior flexible docking (Kurkinen *et al.* 2018) using PLANTS (Korb *et al.* 2007, 2009) (V Tables 3 and 4). However, a combination of the two approaches using NIB rescoring (R-NIB) or consensus scoring of ligand conformers from PLANTS docking is even more successful than either NIB or PLANTS screening alone (V Tables 1-3) as shown also by prior studies (Kurkinen *et al.* 2018).

The utilized workflow from the ligand and protein structure preparation to NIB screening and rescoring was provided as command line inputs and help scripts in the supplementary material of the original publication. The example workflow is based on the DUD benchmarking set for COX-2. The provided workflow utilizes freely available Open Babel (O'Boyle *et al.* 2011), Panther (Niinivehmas *et al.* 2015), ShaEP (Vainio *et al.* 2009) and Rocker (Lätti *et al.* 2016) for ligand preparation, NIB model generation, docking/screening and VS benchmarking calculation/visualization steps, respectively. The Open Babel ligand preparation did not produce the best results from the benchmarking (V Tables 2 and 3) and, accordingly, it may be necessary to use another ligand preparation workflow for actual VS studies. However, the workflow is excellent for demonstrative or tutorial purposes as it is performed with open and relatively easy-to-use tools. Ligand conformers of previous (Kurkinen *et al.* 2018) PLANTS

(Korb *et al.* 2007, 2009) docking are also included for R-NIB rescoring and consensus scoring. Together with the thorough discussion of the NIB methodology, the provided workflow inputs can provide a starting point for NIB VS for anyone new to the method.

6 DISCUSSION

Computational protein structure-based methods were applied to evaluate and predict CYP mediated metabolism. The application of docking and MD simulations on small data sets of small molecules provided insight on the structural determinants of substrate and SOM selectivity on various CYP enzymes, and even offered a glimpse of the tentative structural basis of the differing inhibition mode of one ligand on two similar CYP enzymes. Metrics of 1) binding free energy using MMGBSA, 2) ligand site accessibility to the heme iron using atomic distances, and 3) ligand stability using the STDs of the atomic distances are suggested for future studies of MD-based CYP ligand binding mode and substrate SOM prediction. A detailed MD-based protocol is not provided as the predictions here were partly based on manual analysis of the simulations due to large changes of the binding poses during the simulations. Novel profluorescent tool molecules for CYP enzymes were discovered, with two of them being isoform-selective in certain tissues. Molecular modelling aided in the identification of the most potent target CYPs for the tool molecules. Docking offered a view of the likely interactions that would facilitate the reaction leading to the fluorescent product. MD simulations explained differences in the catalytic activity of the fluorescence-producing reaction of the compounds with the aid of the metrics proposed for binding mode and SOM prediction. Finally, the MD simulations suggested that water interactions and access channel composition have an essential role in ligand binding in the CYP1 family.

MMGBSA offered an adequate frame for the prediction of ligand binding poses and substrate SOMs in CYP enzymes. The model systems of CYP2A6 and 2A5 in complex with small coumarin derivatives offered insights into how the MD/MMGBSA method fares on a data set where the enzymes and ligands are highly similar. However, it was demonstrated that binding energy estimation alone does not necessarily predict a metabolically active binding mode and thus a correct SOM prediction. The binding mode with the best interaction energetics might not be metabolically active as also the chemical nature, 3D location and the general orientation of the molecule also affect whether a reaction occurs in a certain binding mode (Cruciani *et al.* 2005, 2013, Huang *et al.* 2013, Tyzack *et al.*

2013). MD simulations and MMGBSA or the corresponding Poisson-Boltzmann approach MMPBSA have also been previously used for CYP ligand binding mode and CYP selectivity prediction (Bello *et al.* 2014, Sato *et al.* 2017, Juvonen *et al.* 2020).

Energetics, accessibility and stability metrics using MMGBSA, atomic distances to the heme iron and their STDs, are suggested for the analysis and prediction of CYP ligand binding modes and substrate SOMs. The analysis of binding pose stability and substrate accessibility were crucial additions to the MMGBSA-based binding mode and SOM prediction workflow. This combination of metrics was also applied with good performance for analyzing the isoform selectivity of 7-hydroxylation of novel profluorescent 3-phenylcoumarin-based tool molecules by CYP1 enzymes. Both the stability and accessibility were depicted by the atomic distances of the ligand to the heme iron. Another approach for stability analysis would be clustering the binding poses from multiple MD simulation trajectories (Sato *et al.* 2017). This would also be a more automated method for the binding pose comparison. Ligand binding poses can diverge drastically from the starting poses during the simulations (Bello *et al.* 2014). This was also the case in the simulations here, and thus a partly manual analysis was required for the correct binding mode and SOM prediction. Accordingly, binding mode clustering would likely enhance the predictions with the suggested metrics. Incorporating the MD-derived metrics with a ligand-based reactivity descriptor would likely further enhance the methodology (Sato *et al.* 2017) as the intrinsic properties of the ligand also affect SOM selectivity.

Novel profluorescent tool compounds were identified for CYP enzymes, and computational approaches provided insights to the isoform-selectivity of the fluorescence-producing reaction. The most potent CYPs, the CYP1 family and CYP2A6, for catalyzing a specific fluorescence-producing 7-hydroxylation reaction of 3-phenylcoumarin derivatives were identified with a simple comparison of CYP binding sites. All 21 compounds were indeed 7-hydroxylated by at least one of the CYP1 family members and the smallest compounds by CYP2A6, although other isoforms catalyzed the reaction as well. Rigid NIB docking provided clues for the ligand-CYP interactions and binding modes that would facilitate the 7-hydroxylation reaction in CYP isoforms 1A1, 1A2, 1B1, 2A6, 2D6 and 2C19. In MD simulations of 3-phenylcoumarins in complex with the CYP1 family enzymes, the binding modes differed from the initial docking-based hypotheses as the enzymes could relax and water molecules could emerge to the binding sites to mediate ligand-enzyme interactions. The difference between the docking and MD simulations results supports the concept that considering CYP flexibility in ligand binding mode analysis can greatly affect the obtained results (Hritz *et al.* 2008, Sheng *et al.* 2014).

In the CYP1 family, water interactions and access channels to the binding site are suggested to have an important role in substrate and SOM selectivity. In the MD simulations here, water molecules mediated ligand-CYP interactions in all CYP1 forms and the access channel compositions differed between the isoforms. Crystal structures of the CYP1 forms all include water molecules inside or at the immediate proximity of the binding site, and a water molecule has been

reported to mediate H-bond between CYP1A2 and the co-crystallized ligand (Sansen *et al.* 2007, Wang *et al.* 2011, Walsh *et al.* 2013). In previous MD simulations, water molecules have been shown to readily exchange between the binding site and bulk solvent through access channels across xenobiotic-metabolizing CYP enzymes of varying flexibility (Rydberg *et al.* 2007, Hendrychova *et al.* 2012). The binding site water networks of CYP1A2 have also been identified to differ from one ligand to another (Watanabe *et al.* 2017). Here, the access channel composition varied between the CYP1 enzymes, which also affected the water networks. Access channel composition has been suggested to affect CYP substrate recognition by many prior studies (Urban *et al.* 2018). A more detailed analysis of the access channel composition and water networks in the CYP1 family with a series of substrates would be beneficial. On one hand, it could provide more information about the effect of the access channel and water network composition to substrate and SOM selectivity. On the other hand, the bound substrate can also have an impact on the access channels and water networks. Such investigation could be useful in shedding light to the structural mechanisms of CYP mediated metabolism and thus aid in future predictions of CYP mediated metabolism. The variation and importance of the hydration sites in the binding site could be especially useful for binding mode and SOM predictions.

The workflows of molecular modelling, docking, and MD simulations applied to CYP enzymes were fairly simple, but the results offer ideas for utilizing the methods in computational cytochrome P450 mediated metabolism. Compared to docking, MD simulations can provide additional information about the ligand binding pose stability, and insights to the protein flexibility and solvent interactions. The MD simulations of CYP2A6 and 2A5 in complex with small coumarins, and the comparison of 3-phenylcoumarin derivative binding modes in CYP1 enzymes demonstrated how small differences in the highly similar substrates CYP binding sites could affect the catalytic activity and both substrate and SOM selectivity of these enzymes. The MD-based approaches and metrics for CYP mediated metabolism prediction here and in previous studies (Bello *et al.* 2014, Panneerselvam *et al.* 2015, Sato *et al.* 2017, Watanabe *et al.* 2017, Juvonen *et al.* 2020) could be applied on a larger set of known CYP isoforms and ligands. It would be beneficial to evaluate the method with a diverse data set, and even an automated workflow could be built. For now, due to their computational demands, the MD/MMGBSA or MMPBSA studies to predict or evaluate CYP selectivity, binding modes and SOMs have been usually performed on a few example cases (Bello *et al.* 2014, Panneerselvam *et al.* 2015, Sato *et al.* 2017, Watanabe *et al.* 2017, Juvonen *et al.* 2020). In addition to metabolism prediction, MD simulations have been widely applied to analyze the uniform and differing characteristics of CYP enzymes such as flexibility, channel composition and behaviour in an aqueous solvent or lipid membranes (Rydberg *et al.* 2007, Hendrychová *et al.* 2011, Hendrychova *et al.* 2012, Berka *et al.* 2013, Jeřábek *et al.* 2016).

Depending on the available computational resources and the number of hit or lead compounds, the hit-to-lead or lead optimization phase of drug discovery

(Hughes *et al.* 2011) may be most suitable for the utilization of MD simulations in the optimization of CYP mediated metabolism of the compounds in development. At these stages, the number of compounds have already been filtered with other methods and include only the most potent compound series (Hughes *et al.* 2011). MD simulations could be especially useful in optimization cases where a drug lead compound is desired to be metabolized at a specific site, or the formation of a certain metabolite is not wanted. As is the case with other computational methods for the prediction of CYP metabolism (Brändén *et al.* 2014), the application of MD simulations may not be practical in cases where CYP inhibition is the main issue. This is because the mechanisms of inhibition are diverse, including competitive inhibition, binding to an allosteric site, or mechanism-based inactivation (Brändén *et al.* 2014, Raunio *et al.* 2015). Issues related to CYP induction should also be assessed with other methods because the induction pathways are not related to ligand-CYP interactions but to other proteins that act as transcription factors (Crivori and Poggesi 2006).

The Panther NIB methodology for rigid docking, VS and rescoring of molecular docking results is well-established and has demonstrated high early enrichment rates in VS applications (Niinivehmas *et al.* 2015, Kurkinen *et al.* 2018, 2019, Jokinen *et al.* 2019). Here, the different aspects of the method protocol were discussed and a practical workflow has been provided to be used by both experts and new users in the field of NIB VS. The provided workflow in the original publication is excellent for demonstrative purposes as it utilizes free or academically free software, although the utilized ligand preparation workflow did not produce the best results amongst the compared software for the step. In the study, it was demonstrated that the VS success is affected by the model creation settings the used protein 3D structure. The effects of the protein conformation to NIB VS have also been demonstrated in studies utilizing protein structures from MD simulations (Virtanen and Pentikäinen 2010) and is a common phenomenon across different docking approaches. The performance of ligand preparation software in reproducing experimental conformers and probing the conformational space have been studied previously (Ebejer *et al.* 2012, Friedrich *et al.* 2017). Here, the ligand 3D conformer generation was found to greatly affect the NIB VS performance, and special attention should be paid for the chosen protocol. Considering the excellent performance and speed of NIB docking and rescoring in VS (Niinivehmas *et al.* 2015, Kurkinen *et al.* 2018, 2019, Jokinen *et al.* 2019) and the detailed discussion and workflow provided for the method, the NIB Panther methodology is a great option for structure-based VS. Thanks to its speed, the NIB Panther VS rigid docking may be used for initial VS of large molecular databases, or as a rescoring method in combination with flexible docking.

7 CONCLUSIONS

Computational prediction of CYP mediated metabolism and VS have wide attention in drug and chemical development. The utilized computational tools for these objectives are diverse, including fast ligand-based methods and protein structure-based methods that, in turn, provide mechanistic insights into ligand-protein interactions. Here, structure-based methods were used for computational prediction and analysis CYP metabolism and VS. MD simulations were used for CYP ligand binding mode and SOM prediction, and to shed light on the isoform-selectivity of novel inhibitors, substrates and profluorescent tool molecules. Compared to docking, MD simulations provided an important view to the enzyme flexibility, ligand stability and water interactions in ligand-CYP complexes. Metrics of binding free energy, substrate accessibility and binding pose stability were found to be useful in the scope of binding mode and SOM prediction of small CYP2A6 and CYP2A5 ligands. They also showed good performance in the evaluation of reaction isoform-selectivity of 3-phenylcoumarin-based ligands in the CYP1 family. In the following studies, the metrics could be incorporated into a more straightforward binding mode and SOM prediction protocol with, for example, ligand-based reactivity and binding mode clustering. The MD simulations suggested that water interactions and channel composition have an impact on substrate and SOM selectivity in the CYP1 family. In the scope of VS, the priorly developed highly fast structure-based NIB Panther VS methodology was explored. Crucial notes were found and discussed regarding the effects of the used protein structure, options of NIB model generation and ligand 3D conformer generation. A detailed workflow for the NIB method has been provided to be utilized by new users to the protocol. The reviewed methods and protocols are potent tools to be used for the computational prediction and analysis of CYP mediated metabolism and VS in future applications.

Acknowledgements

This work was carried out at the University of Jyväskylä, Department of Biological and Environmental Science and Nanoscience Center. The thesis work was funded by the Jenny and Antti Wihuri foundation, and the Emil Aaltonen foundation. The computational resources were provided by CSC – IT Center for Science.

First of all, I wish to acknowledge my supervisors and the follow-up group. Professor Olli Pentikäinen, thank you tremendously for all the inspiration, support, and encouragement you have given me throughout the years. I always gain new perspectives from our discussions. I am grateful for the time that I have got to work in your research group and to grow as a researcher. Docent Pekka Postila, thank you especially for the time that we shared in close collaboration, and for showing me some of your secrets to efficient writing. Thanks to my follow-up group, Professor Perttu Permi and Professor Gerrit Groenhof, for your valuable advice on my PhD journey, and Perttu for accepting to be my local supervisor for the final stretch of my PhD.

Thanks to the thesis examination panel. Docent Maija Lahtela-Kakkonen and Professor Jukka Hakkola, your keen preliminary examination and insightful comments on the manuscript truly helped me to level up the thesis. Thanks to Docent Tuomo Laitinen who kindly accepted the invitation to act as my opponent. I appreciate the time and effort you all put into the examination.

I would like to express my gratitude to all co-authors and collaborators. Above all, thanks to the key authors Professor Risto Juvonen and Professor Hannu Raunio for your work and insights on the cytochrome P450 enzymes, and Docent Juhani Huuskonen for the work on chemical synthesis. Special thanks to Risto, who has been the creative mind behind many of the projects. I am grateful to Professor Phil Biggin for the inspiration and perspectives I gained during my visit to SBCB and the University of Oxford.

My warmest thanks to everyone at the research group, at the department and the Nanoscience center who has helped me along the way and shared the journey with me. Thank you Dr. Sanna Niinivehmas for your endless kindness and support, for teaching me to take it easy, and for making the research group feel like home. Sakari Lätti, it was fun to begin my journey with you. I enjoy your detailed scribbles and explanations of the most complex things. Thank you Dr. Sanna Rauhamäki for our shared journey in the team, the valuable peer support, and the hilarious paths we imagined for ourselves. Thanks to Sami Kurkinen for your rigorous work in our shared publications, and Elmeri Jokinen for the time we worked together. Dr. Heli Lehtivuori, Jaakko Mastomäki, and Kalle Kansanen, thank you for the numerous laughs and discussions that we had at the office.

Finally, I am thankful for the constant support of my closest ones. Matti, Emil, and the baby, thank you for your love and the life that we live together. You keep me grounded and constantly remind me of the most important things in life. Thanks to my parents, siblings, and your families for your support and all the moments in your company.

YHTEENVETO (RÉSUMÉ IN FINNISH)

Laskennallinen sytokromi P450 –välitteinen metabolia ja virtuaaliseulonta

Biokemiallisten ilmiöiden laskennallinen mallinnus muodostaa olennaisen osan lääkeaineiden kehitysprosessia. Laskennallisten työkalujen avulla voidaan vähentää kehityksessä vaadittavien laboratoriokokeiden käyttöä ja siten kustannuksia, jotka ovat lääkeainekehityksessä merkittävän korkeita ja heijastuvat myös markkinoille tulevien lääkkeiden hintaan. Laskennalliset menetelmät täydentävät kokeellisia tutkimuksia sekä tarjoavat niille vaihtoehtoja. Menetelmien kehitys on erityisesti roolissa, kun kemikaalien turvallisuustestauksessa käytettävälle eläinkokeille etsitään vaihtoehtoja. Tähän tähtääviä säädöksiä ovat muun muassa Euroopan unionin REACH-asetus kemikaalien rekisteröinnistä, arvioinnista, lupamenettelyistä ja rajoituksista, sekä kosmetiikka-asetus, jonka mukaisesti eläinkokeet on kielletty kosmetiikan ainesosien testauksessa.

Pienmolekyylin, kuten lääke- tai muun vierasaineen, vaikutus syntyy, kun se sitoutuu biologiseen makromolekyyliin eli useimmiten proteiiniin ja joko lisää tai estää sen toimintaa. Sitoutuvan, bioaktiivisen pienmolekyylin eli ligandin sitoutumispaikkaa proteiinirakenteessa kutsutaan sitoutumistaskuksi. Ligandin ja sitoutumistaskun koon ja muodon yhteensopivuus sekä fysikaalis-kemialliset ominaisuudet, kuten eri kohtien sähkövaraus, vaikuttavat siihen, kuinka tehokkaasti ligandi sitoutuu. Laskennalliset työkalut voidaan jaotella pienmolekyylin rakenteeseen perustuviin eli ligandipohjaisiin menetelmiin sekä proteiinin ja ligandin vuorovaikutuksiin perustuviin rakennepohjaisiin menetelmiin, joista molempia käytetään laajasti sekä laskennallisessa sytokromi P450 (CYP) –välitteisen metabolian ennustuksessa että virtuaaliseulonnassa.

Metabolia on lääkeaine- ja kemikaalikehityksessä tärkeässä roolissa, sillä metabolisten entsyymiproteiinien katalysoimat reaktiot muuttavat vierasainemolekyylin rakennetta ja sitä kautta sen toimintaa. Metabolia on osa vierasaineen ADMET-ominaisuuksia (imeytyminen, jakautuminen, metabolia, erittyminen ja toksisuus), jotka vaikuttavat molekyylin soveltuvuuteen lääkeaineeksi. Useimmiten metaboliareaktiot tekevät molekyylistä inaktiivisen, minkä seurauksena lääkeainekandidaatti saattaa menettää terapeuttisen vaikutuksensa liian nopeasti. Toisaalta reaktiot voivat johtaa myös toksisiin ja reaktiivisiin tuotteisiin, ja metabolia on usein lääkkeiden ei-toivottavien yhteisvaikutusten taustalla. CYP-entsyymit ovat yksi metabolian tärkeä tutkimuskohde, sillä ihmisellä ne osallistuvat lääkeaineista sekä kaikista vierasaineista yli 90 %:n metaboliaan ja yli 60 %:iin toksisten molekyyliden aktivaatioista. CYP-entsyymit ovat runsaimmillaan maksassa, joskin niitä löytyy kaikista kehon kudoksista. Laskennallisen metabolian työkaluilla voidaan esimerkiksi arvioida, mihin entsyymeihin vierasaineet sitoutuvat (entsyymiselektiivisyys), missä pienmolekyylin atomipositioissa reaktiot tapahtuvat (metaboliakohta), sekä millaisia metaboliatuotteet ovat rakenteeltaan.

Virtuaaliseulontaa käytetään uusien bioaktiivisten molekyyliden etsintään laajoista virtuaalisista molekyylitietokannoista. Tavoitteena on rikastaa bioaktiivisten molekyyliden osuutta kokeellisissa tutkimuksissa, jolloin kehityksessä

vaadittavien laboratoriotutkimusten määrää voidaan vähentää. Bioaktiivisten molekyylien etsinnän lisäksi virtuaaliseulonnan eri vaiheissa voidaan hyödyntää laskennallista ADMET-ominaisuuksien ennustusta.

Tässä väitöskirjassa käytettiin laskennallisia rakennepohjaisia menetelmiä CYP-entsyymien metabolian tutkimiseen ja ennustukseen sekä virtuaaliseulontaan. Menetelmissä hyödynnetään ligandien ja proteiinien 3D-rakenteita, jotka voidaan hakea erilaisista internetin tietokannoista tai rakentaa laskennallisilla molekyylihallinnusmenetelmillä. Tavoitteena oli kehittää molekyylidynamiikkaan (MD) perustuva protokolla CYP-ligandien sitoutumisasennon ja metaboliakohdan ennustukseen, kehittää uusia CYP-alatyypiselektiivisiä työkalumolekyylejä kokeellisiin tutkimuksiin sekä arvioida metaboliareaktioiden CYP-selektiivisyyttä. Virtuaaliseulontaan oli tavoitteena tarjota käytännönläheinen kuvaus sekä tutustumiseen soveltuva protokolla aiemmin kehitetylle Panther-ohjelmaan perustuvalla menetelmällä.

CYP-ligandien sitoutumisasennon ja substraattien metaboliakohtien ennustukseen esitettiin molekyylidynamiikkaan (MD) perustuvia metriikoita, jotka kuvaavat ligandi-CYP-kompleksin sitoutumisenergiaa, ligandin läheisyyttä CYP-reaktiokeskukseen sekä ligandin asennon stabiilisuutta CYP-entsyymin sitoutumistaskussa. MD-simulaatioissa mallinnetaan ligandi-proteiinikompleksien liikettä atomitarkkuudella nanosekuntien aikaskaalassa. Sitoutumisasento ennustettiin aluksi neljän telakoinnilla tuotetun vaihtoehdon joukosta laskennallisesti arvioidun sitoutumisenergian perusteella (I, II). Pelkkä sitoutumisenergian käyttö ennustuksessa ei tuottanut täysin toivottua tulosta. Toisessa lähestymistavassa (II) tärkeimpänä metriikkana sitoutumisenergian rinnalla toimi ligandin atomipositioiden etäisyys CYP-entsyymin reaktiokeskuksesta sekä stabiilisuuden arviointi kunkin etäisyyden vaihtelun perusteella. Näiden yhdistäminen sitoutumisenergian laskentaan tuotti onnistuneen ennustuksen käytetyille esimerkkitapauksille. Täysin selkeää protokollaa MD-pohjaiseen sitoutumisasennon ja metaboliakohdan ennustukseen ei pystytty esittämään, sillä ligandin sitoutumisasento CYP-entsyymissä saattoi merkittävästi muuttua simulaation aikana ja ennustukset vaativat täten myös manuaalista analyysiä. Protokollan automatisoinnissa ja tarkennuksessa voitaisiin käyttää muussa kirjallisuudessa esitettyjä menetelmiä, kuten samankaltaisten sitoutumisasentojen yhdistämistä useista eri simulaatioista sekä ligandin reaktiivisuuden arviointia.

CYP-entsyymeille kehitettiin uusia työkalumolekyylejä, jotka muuttuvat fluoresoiviksi, kun CYP-entsyymin katalysoima reaktio tapahtuu molekyylin tietyssä atomipositiossa (III, IV). Molekyylit perustuivat tunnettuun ligandirakenteeseen, johon liitettiin erilaisia kemiallisia ryhmiä. Osa molekyyleistä oli julkaistu aiemmissä tutkimuksissa ja osa oli uusia. CYP-entsyymialatyypien 3D-rakenteiden ja sitoutumistaskujen vertailu visuaalisesti osoitti neljä parasta kohdeentsyymiä näille molekyyleille. Kokeelliset tulokset osoittivat, että näistä etenkin kaksi CYP1-perheen jäsentä katalysoivat fluoresoivaan tuotteeseen johtavaa reaktiota, joskin yhteensä kuudelle CYP-alatyypille esitettiin potentiaalisia työkalumolekyylejä. Telakoinnin tuloksena molekyyleille löydettiin eri CYP-alatyypeissä vuorovaikutuksiltaan suotuisat sitoutumisasennot, jossa fluoresoivaan tuotteeseen johtava reaktio voisi tapahtua. Kahdelle CYP-alatyypille löydettiin tietyissä

kudoksissa selektiivinen työkalumolekyyli. Näitä työkalumolekyyliä voisi käyttää kokeellisissa kudospohjaisissa tutkimuksissa, joissa samassa koeputkessa on useita eri CYP-alatyyppejä. Muut profluoresoivat molekyylit eivät olleet yhtä selektiivisiä, mutta nekin voisivat olla hyödyllisiä eristettyjen CYP-alatyypin kokeellisissa tutkimuksissa.

Telakoiduista profluoresoivista molekyyleistä osa simuloitiin kolmen eri CYP1-entsyymin kanssa, ja MD-tulokset selittivät fluoresoivan reaktion entsyymiselektiivisyyttä (IV). CYP-metabolian MD-pohjaiseen ennustukseen esitetyt metriikat (I, II) toimivat hyvin myös uusien profluoresoivien työkalumolekyylien entsyymiselektiivisyyden arvioinnissa (IV). Lisäksi havaittiin, että vesimolekyylit ja entsyymien sisällä oleviin sitoutumistaskuihin johtavat kanavat vaikuttaisivat merkittävästi tutkittujen työkalumolekyylien sitoutumiseen CYP1-perheessä (IV). Toisin kuin telakointi, MD-simulaatiot mallinnetaan vesiympäristössä sekä nimensä mukaisesti dynaamisesti, joten vastaavia havaintoja ei voitu tehdä telakoinnissa. Simulaatioissa sitoutumistaskuun tulleet vesimolekyylit toimivat ligandien ja CYP1-entsyymien välisissä sidoksissa. CYP1-entsyymeillä kanavien sijainti oli toisistaan hieman erilainen, mikä vaikutti osaltaan vesimolekyylien sijaintiin ja täten ligandi-CYP-vuorovaikutuksiin. Aiemmissa laskennallisissa ja kokeellisissa tutkimuksissa on havaittu, että vesimolekyylit voivat toimia ligandi-CYP-vuorovaikutusten välittäjinä, ja että CYP-entsyymeissä olevilla kanavilla on vaikutuksia ligandiselektiivisyyteen. Esitetyt havainnot CYP1-perheen MD-simulaatioista vahvistavat näitä teorioita.

Väitöskirjassa tarjottiin käytännönläheistä tietoa aiemmin kehitetyn Panther-ohjelmaan perustuvan virtuaaliseulontamenetelmän keskeisistä työvaiheista (V). Menetelmä on aiemmissa tutkimuksissa osoitettu olevan nopea molekyylitietokantojen seulonnassa sekä kykenevän tunnistamaan tehokkaasti bioaktiivisia molekyylejä eri kohdeproteiineihin. Menetelmässä kohdeproteiinin 3D-rakenteen sitoutumistaskusta rakennetaan negatiivikuva, joka vastaa sitoutumistaskun muotoa ja sähköstaattisia ominaisuuksia. Negatiivikuvan samankaltaisuutta pienmolekyylien kanssa verrataan laskennallisesti, ja saatujen pisteytysten perusteella molekyylit voidaan asettaa paremmuusjärjestykseen. Väitöskirjassa tehdyssä tutkimuksessa osoitettiin, kuinka proteiimirakenteen valinta, negatiivikuvan rakennuksessa käytetyt asetukset sekä pienmolekyylien 3D-rakenteiden rakennukseen käytetty ohjelma vaikuttavat virtuaaliseulontatuloksiin. Alkuperäisen artikkelin julkaisun yhteydessä julkaistiin myös Panther-ohjelman päivitetty versio sekä protokolla ja komentoriviohjeet tähän virtuaaliseulontamenetelmään tutustumiseen.

Väitöskirjassa käytetyt ja esitetyt menetelmät – metriikat ja menetelmät CYP-metabolian ennustukseen, virtuaaliseulontamenetelmä sekä uudet työkalumolekyylit CYP-entsyymeille – tarjoavat sekä valmiita työkaluja että ideoita tuleviin tutkimuksiin ja menetelmäkehitykseen.

REFERENCES

- Bayly C.C.I., Cieplak P., Cornell W.D. & Kollman P. a. 1993. A well-behaved electrostatic potential based method using charge restraints for deriving atomic charges: the RESP model. *J. Phys. Chem.* 97: 10269–10280.
- Bello M., Mendieta-Wejebe J.E. & Correa-Basurto J. 2014. Structural and energetic analysis to provide insight residues of CYP2C9, 2C11 and 2E1 involved in valproic acid dehydrogenation selectivity. *Biochem. Pharmacol.* 90: 145–158.
- Berka K., Paloncýová M., Anzenbacher P. & Otyepka M. 2013. Behavior of human cytochromes p450 on lipid membranes. *J. Phys. Chem. B* 117: 11556–11564.
- Berman H.M., Westbrook J., Feng Z., Gilliland G., Bhat T.N., Weissig H., Shindyalov I.N. & Bourne P.E. 2000. The protein data bank. *Nucleic Acids Res.* 28: 235–242.
- Boyer S., Arnby C.H., Carlsson L., Smith J., Stein V. & Glen R.C. 2007. Reaction site mapping of xenobiotic biotransformations. *J. Chem. Inf. Model.* 47: 583–590.
- Brändén G., Sjögren T., Schnecke V. & Xue Y. 2014. Structure-based ligand design to overcome CYP inhibition in drug discovery projects. *Drug Discov. Today* 19: 905–911.
- Bruno R.D. & Njar V.C.O. 2007. Targeting Cytochrome P450 Enzymes: A New Approach in Anti-cancer Drug Development. *Bioorg. Med. Chem.* 15: 5047–5060.
- Carlsson L., Spjuth O., Adams S., Glen R.C. & Boyer S. 2010. Use of historic metabolic biotransformation data as a means of anticipating metabolic sites using MetaPrint2D and Bioclipse. *BMC Bioinformatics* 11: 362–368.
- Case D.A., Cheatham III T.E., Darden T., Gohlke H., Luo R., Merz JR K.M., Onufriev A., Simmerling C., Wang B. & Woods R.J. 2005. The Amber biomolecular simulation programs. *J. Magn. Reson.* 26: 1668–1688.
- Cojocaru V., Winn P.J. & Wade R.C. 2007. The ins and outs of cytochrome P450s. *Biochim. Biophys. Acta* 1770: 390–401.
- Crivori P. & Poggesi I. 2006. Computational approaches for predicting CYP-related metabolism properties in the screening of new drugs. *Eur. J. Med. Chem.* 41: 795–808.
- Cross J.B., Thompson D.C., Rai B.K., Baber J.C., Fan K.Y., Hu Y. & Humblet C. 2009. Comparison of several molecular docking programs: Pose prediction and virtual screening accuracy. *J. Chem. Inf. Model.* 49: 1455–1474.
- Cruciani G., Baroni M., Benedetti P., Goracci L. & Fortuna C.G. 2013. Exposition and reactivity optimization to predict sites of metabolism in chemicals. *Drug Discov. Today Technol.* 10: e155–e165.
- Cruciani G., Carosati E., Boeck B. De, Ethirajulu K., Mackie C., Howe T. & Vianello R. 2005. MetaSite: Understanding metabolism in human cytochromes from the perspective of the chemist. *J. Med. Chem.* 48: 6970–6979.
- Darden T., York D. & Pedersen L. 1993. Particle mesh Ewald: An $N \log(N)$ method for Ewald sums in large systems. *J. Chem. Phys.* 98: 10089–10092.

- Deodhar M., Rihani S.B. Al, Arwood M.J., Darakjian L., Dow P., Turgeon J. & Michaud V. 2020. Mechanisms of cyp450 inhibition: Understanding drug-drug interactions due to mechanism-based inhibition in clinical practice. *Pharmaceutics* 12: 1–18.
- Djoumbou-Feunang Y., Fiamoncini J., Gil-de-la-Fuente A., Greiner R., Manach C. & Wishart D.S. 2019. BioTransformer: A comprehensive computational tool for small molecule metabolism prediction and metabolite identification. *J. Cheminform.* 11: 1–25.
- Duan J., Dixon S.L., Lowrie J.F. & Sherman W. 2010. Analysis and comparison of 2D fingerprints: Insights into database screening performance using eight fingerprint methods. *J. Mol. Graph. Model.* 29: 157–170.
- Ebejer J.P., Morris G.M. & Deane C.M. 2012. Freely available conformer generation methods: How good are they? *J. Chem. Inf. Model.* 52: 1146–1158.
- Friedrich N.O., Bruyn Kops C. De, Flachsenberg F., Sommer K., Rarey M. & Kirchmair J. 2017. Benchmarking Commercial Conformer Ensemble Generators. *J. Chem. Inf. Model.* 57: 2719–2728.
- Genheden S. & Ryde U. 2015. The MM/PBSA and MM/GBSA methods to estimate ligand-binding affinities. *Expert Opin. Drug Discov.* 10: 449–461.
- Giammona D.A. 1984. Force field modifications for united atom heme plus flexible water. PhD thesis, University of California, Davis.
- Giammona D.A., Case D. & Bayly C. (n.d.). Force field modifications for all-atom heme. <http://research.bmh.manchester.ac.uk/bryce/amber/> (7.10.2020)
- Gimeno A., Ojeda-Montes M.J., Tomás-Hernández S., Cereto-Massagué A., Beltrán-Debón R., Mulero M., Pujadas G. & Garcia-Vallvé S. 2019. The light and dark sides of virtual screening: What is there to know? *Int. J. Mol. Sci.* 20: 1375–1399.
- Graaf C. De, Pospisil P., Pos W., Folkers G. & Vermeulen N.P.E. 2005. Binding mode prediction of cytochrome P450 and thymidine kinase protein-ligand complexes by consideration of water and rescoring in automated docking. *J. Med. Chem.* 48: 2308–2318.
- Groot M.J. de. 2006. Designing better drugs: predicting cytochrome P450 metabolism. *Drug Discov. Today* 11: 601–606.
- Groot M.J. De & Ekins S. 2002. Pharmacophore modeling of cytochromes P450. *Adv. Drug Deliv. Rev.* 54: 367–383.
- Guengerich F.P. 2001. Common and uncommon cytochrome P450 reactions related to metabolism and chemical toxicity. *Chem. Res. Toxicol.* 14: 611–650.
- Guengerich F.P. 2008. Cytochrome P450 and Chemical Toxicology. *Chem. Res. Toxicol.* 21: 70–83.
- Guengerich F.P. 2011. Mechanisms of drug toxicity and relevance to pharmaceutical development. *Drug Metab. Pharmacokinet.* 26: 3–14.
- Guengerich F.P. & Munro a. W. 2013. Unusual Cytochrome P450 Enzymes and Reactions. *J. Biol. Chem.* 288: 17065–17073.
- Guengerich F.P., Waterman M.R. & Egli M. 2016. Recent Structural Insights into Cytochrome P450 Function. *Trends Pharmacol. Sci.* 37: 625–640.
- Hendrychová T., Anzenbacherová E., Hudeček J., Skopalík J., Lange R., Hildebrandt P., Otyepka M. & Anzenbacher P. 2011. Flexibility of human

- cytochrome P450 enzymes: Molecular dynamics and spectroscopy reveal important function-related variations. *Biochim. Biophys. Acta - Proteins Proteomics* 1814: 58–68.
- Hendrychova T., Berka K., Navratilova V., Anzenbacher P. & Otyepka M. 2012. Dynamics and Hydration of the Active Sites of Mammalian Cytochromes P450 Probed by Molecular Dynamics Simulations. *Curr. Drug Metab.* 13: 177–189.
- Homeyer N., Stoll F., Hillisch A. & Gohlke H. 2014. Binding Free Energy Calculations for Lead Optimization: Assessment of Their Accuracy in an Industrial Drug Design Context. *J. Chem. Theory Comput.* 10: 3331–3344.
- Hritz J., Ruitter A. De & Oostenbrink C. 2008. Impact of plasticity and flexibility on docking results for cytochrome P450 2D6: A combined approach of molecular dynamics and ligand docking. *J. Med. Chem.* 51: 7469–7477.
- Huang N., Shoichet B.K. & Irwin J.J. 2006. Benchmarking sets for molecular docking. *J. Med. Chem.* 49: 6789–6801.
- Huang T.W., Zaretski J., Bergeron C., Bennett K.P. & Breneman C.M. 2013. DR-Predictor: Incorporating flexible docking with specialized electronic reactivity and machine learning techniques to predict CYP-mediated sites of metabolism. *J. Chem. Inf. Model.* 53: 3352–3366.
- Hughes J.P., Rees S.S., Kalindjian S.B. & Philpott K.L. 2011. Principles of early drug discovery. *Br. J. Pharmacol.* 162: 1239–1249.
- Humphrey W., Dalke A. & Schulten K. 1996. VMD: visual molecular dynamics. *J. Mol. Graph.* 14: 33–38.
- Insin E.M. & Guengerich F.P. 2007. Complex reactions catalyzed by cytochrome P450 enzymes. *Biochim. Biophys. Acta - Gen. Subj.* 1770: 314–329.
- Issa N.T., Wathieu H., Ojo A., Byers S.W. & Dakshanamurthy S. 2017. Drug Metabolism in Preclinical Drug Development: A Survey of the Discovery Process, Toxicology, and Computational Tools. *Curr. Drug Metab.* 18: 556–565.
- Jandova Z., Gill S.C., Lim N.M., Mobley D.L. & Oostenbrink C. 2019. Binding Modes and Metabolism of Caffeine. *Chem. Res. Toxicol.* 32: 1374–1383.
- Jeřábek P., Florián J. & Martínek V. 2016. Lipid molecules can induce an opening of membrane-facing tunnels in cytochrome P450 1A2. *Phys. Chem. Chem. Phys.* 18: 30344–30356.
- Johnson M.S. & Overington J.P. 1993. A structural basis for sequence comparisons: An evaluation of scoring methodologies. *J. Mol. Biol.* 233: 716–738.
- Jokinen E.M., Postila P.A., Ahinko M., Niinivehmas S. & Pentikäinen O.T. 2019. Fragment- and negative image-based screening of phosphodiesterase 10A inhibitors. *Chem. Biol. Drug Des.* 94: 1799–1812.
- Jones J.P., Mysinger M. & Korzekwa K.R. 2002. Computational models for cytochrome P450: A predictive electronic model for aromatic oxidation and hydrogen atom abstraction. *Drug Metab. Dispos.* 30: 7–12.
- Jorgensen W.L., Chandrasekhar J., Madura J.D., Impey R.W. & Klein M.L. 1983. Comparison of simple potential functions for simulating liquid water. *J. Chem. Phys.* 79: 926–935.
- Juvonen R.O., Jokinen E.M., Javaid A., Lehtonen M., Raunio H. & Pentikäinen O.T. 2020. Inhibition of human CYP1 enzymes by a classical inhibitor α -

- naphthoflavone and a novel inhibitor N-(3, 5-dichlorophenyl)cyclopropanecarboxamide: An in vitro and in silico study. *Chem. Biol. Drug Des.* 95: 520–533.
- Kasturi J., Palla P.R., Bakshi V. & Boggula N. 2019. Non Steroidal Anti Inflammatory Drugs-An Overview. *J. Drug Deliv. Ther.* 9: 442–448.
- Kirchmair J., Williamson M.J., Afzal A.M., Tyzack J.D., Choy A.P.K., Howlett A., Rydberg P. & Glen R.C. 2013. FASt MEtabolizer (FAME): A rapid and accurate predictor of sites of metabolism in multiple species by endogenous enzymes. *J. Chem. Inf. Model.* 53: 2896–2907.
- Kirchmair J., Williamson M.J., Tyzack J.D., Tan L., Bond P.J., Bender A. & Glen R.C. 2012. Computational prediction of metabolism: Sites, products, SAR, P450 enzyme dynamics, and mechanisms. *J. Chem. Inf. Model.* 52: 617–648.
- Korb O., Stützle T. & Exner T.E. 2007. An ant colony optimization approach to flexible protein–ligand docking. *Swarm Intell.* 1: 115–134.
- Korb O., Stützle T. & Exner T.E. 2009. Empirical scoring functions for advanced Protein-Ligand docking with PLANTS. *J. Chem. Inf. Model.* 49: 84–96.
- Kraulis P.J. 1991. MOLSCRIPT: a program to produce both detailed and schematic plots of protein structures. *J. Appl. Crystallogr.* 24: 946–950.
- Kumar A. & Zhang K.Y.J. 2018. Advances in the development of shape similarity methods and their application in drug discovery. *Front. Chem.* 6: 1–21.
- Kurkinen S.T., Lätti S., Pentikäinen O.T. & Postila P.A. 2019. Getting Docking into Shape Using Negative Image-Based Rescoring. *J. Chem. Inf. Model.* 59: 3584–3599.
- Kurkinen S.T., Niinivehmas S., Ahinko M., Lätti S., Pentikäinen O.T. & Postila P.A. 2018. Improving Docking Performance Using Negative Image-Based Rescoring. *Front. Pharmacol.* 9: 1–15.
- Lätti S., Niinivehmas S. & Pentikäinen O.T. 2016. Rocker: Open source, easy-to-use tool for AUC and enrichment calculations and ROC visualization. *J. Cheminform.* 8: 1–5.
- Lee H.S., Lee C.S., Kim J.S., Kim D.H. & Choe H. 2009. Improving virtual screening performance against conformational variations of receptors by shape matching with ligand binding pocket. *J. Chem. Inf. Model.* 49: 2419–2428.
- Lee H.S. & Zhang Y. 2012. BSP-SLIM: A Blind Low-Resolution Ligand-Protein Docking Approach Using Predicted Protein Structures. *Proteins* 80: 93–110.
- Lehtonen J. V, Still D.-J., Rantanen V.-V., Ekholm J., Björklund D., Iftikhar Z., Huhtala M., Repo S., Jussila A., Jaakkola J., Pentikäinen O., Nyrönen T., Salminen T., Gyllenberg M. & Johnson M.S. 2004. BODIL: a molecular modeling environment for structure-function analysis and drug design. *J. Comput. Aided. Mol. Des.* 18: 401–419.
- Lynch T. & Price A. 2007. The effect of cytochrome P450 metabolism on drug response, interactions, and adverse effects. *Am. Fam. Physician* 76: 391–396.
- Maffucci I. & Contini A. 2013. Explicit ligand hydration shells improve the correlation between MM-PB/GBSA binding energies and experimental activities. *J. Chem. Theory Comput.* 9: 2706–2717.

- Maffucci I. & Contini A. 2016. Improved Computation of Protein-Protein Relative Binding Energies with the Nwat-MMGBSA Method. *J. Chem. Inf. Model.* 56: 1692–1704.
- Maffucci I., Hu X., Fumagalli V. & Contini A. 2018. An efficient implementation of the Nwat-MMGBSA method to rescore docking results in medium-throughput virtual screenings. *Front. Chem.* 6: 1–14.
- Maia E.H.B., Assis L.C., Oliveira T.A. de, Silva A.M. da & Taranto A.G. 2020. Structure-Based Virtual Screening: From Classical to Artificial Intelligence. *Front. Chem.* 8: 343.
- Maier J.A., Martinez C., Kasavajhala K., Wickstrom L., Hauser K.E. & Simmerling C. 2015. ff14SB: Improving the Accuracy of Protein Side Chain and Backbone Parameters from ff99SB. *J. Chem. Theory Comput.* 11: 3696–3713.
- McGaughey G.B., Sheridan R.P., Bayly C.I., Culberson J.C., Kreamsoulas C., Lindsley S., Maiorov V., Truchon J.F. & Cornell W.D. 2007. Comparison of topological, shape, and docking methods in virtual screening. *J. Chem. Inf. Model.* 47: 1504–1519.
- Mendez D., Gaulton A., Bento A.P., Chambers J., Veij M. De, Félix E., Magariños M.P., Mosquera J.F., Mutowo P., Nowotka M., Gordillo-Marañón M., Hunter F., Junco L., Mugumbate G., Rodriguez-Lopez M., Atkinson F., Bosc N., Radoux C.J., Segura-Cabrera A., Hersey A. & Leach A.R. 2019. ChEMBL: Towards direct deposition of bioassay data. *Nucleic Acids Res.* 47: D930–D940.
- Merritt E.A. & Murphy M.E.P. 1994. Raster3D Version 2.0. A program for photorealistic molecular graphics. *Acta Crystallogr. Sect. D Biol. Crystallogr.* 50: 869–873.
- Miller B.R., McGee T.D., Swails J.M., Homeyer N., Gohlke H. & Roitberg A.E. 2012. MMPBSA.py: An efficient program for end-state free energy calculations. *J. Chem. Theory Comput.* 8: 3314–3321.
- Morris G. & Huey R. 2009. AutoDock4 and AutoDockTools4: Automated docking with selective receptor flexibility. *J. Comput. Chem.* 30: 2785–2791.
- Mysinger M.M., Carchia M., Irwin J.J. & Shoichet B.K. 2012. Directory of useful decoys, enhanced (DUD-E): Better ligands and decoys for better benchmarking. *J. Med. Chem.* 55: 6582–6594.
- Nebert D.W., Wikvall K. & Miller W.L. 2013. Human cytochromes P450 in health and disease. *Philos. Trans. R. Soc. Lond. B. Biol. Sci.* 368: 20120431.
- Niinivehmas S.P., Manivannan E., Rauhamäki S., Huuskonen J. & Pentikäinen O.T. 2016. Identification of estrogen receptor a ligands with virtual screening techniques. *J. Mol. Graph. Model.* 64: 30–39.
- Niinivehmas S.P., Salokas K., Lätti S., Raunio H. & Pentikäinen O.T. 2015. Ultrafast protein structure-based virtual screening with Panther. *J. Comput. Aided. Mol. Des.* 29: 989–1006.
- Niinivehmas S.P., Virtanen S.I., Lehtonen J. V., Postila P.A. & Pentikäinen O.T. 2011. Comparison of virtual high-throughput screening methods for the identification of phosphodiesterase-5 inhibitors. *J. Chem. Inf. Model.* 51: 1353–1363.
- O'Boyle N.M., Banck M., James C.A., Morley C., Vandermeersch T. & Hutchison G.R. 2011. Open Babel: An Open chemical toolbox. *J. Cheminform.* 3: 1–14.

- Olsen L., Oostenbrink C. & Jørgensen F.S. 2015. Prediction of cytochrome P450 mediated metabolism. *Adv. Drug Deliv. Rev.* 86: 61–71.
- Olsen L., Rydberg P., Rod T.H. & Ryde U. 2006. Prediction of Activation Energies for Hydrogen Abstraction by Cytochrome P450. *J. Med. Chem.* 49: 6489–6499.
- Onufriev A., Bashford D. & Case D.A. 2004. Exploring Protein Native States and Large-Scale Conformational Changes with a Modified Generalized Born Model. *Proteins Struct. Funct. Genet.* 55: 383–394.
- Otyepka M., Skopalík J., Anzenbacherová E. & Anzenbacher P. 2007. What common structural features and variations of mammalian P450s are known to date? *Biochim. Biophys. Acta - Gen. Subj.* 1770: 376–389.
- Panneerselvam S., Yesudhas D., Durai P., Anwar M., Gosu V. & Choi S. 2015. A Combined Molecular Docking/Dynamics Approach to Probe the Binding Mode of Cancer Drugs with Cytochrome P450 3A4. *Molecules* 20: 14915–14935.
- Pasero C. & McCaffery M. 2001. Selective COX-2 inhibitors. *Am. J. Nurs.* 101: 655–683.
- Petrey D., Xiang Z., Tang C.L., Xie L., Gimpelev M., Mitros T., Soto C.S., Goldsmith-Fischman S., Kernytsky A., Schlessinger A., Koh I.Y.Y., Alexov E. & Honig B. 2003. Using Multiple Structure Alignments, Fast Model Building, and Energetic Analysis in Fold Recognition and Homology Modeling. *Proteins* 53: 430–435.
- Phillips J.C., Braun R., Wang W., Gumbart J., Tajkhorshid E., Villa E., Chipot C., Skeel R.D., Kale L. & Schulten K. 2005. Scalable molecular dynamics with NAMD. *J. Comput. Chem.* 26: 1781–1802.
- Pravda L., Sehnal D., Svobodová VaEková R., Navrátilová V., Toušek D., Berka K., Otyepka M. & Koca J. 2018. ChannelsDB: Database of biomacromolecular tunnels and pores. *Nucleic Acids Res.* 46: D399–D405.
- Qing X., Lee X.Y., Raeymaeker J. De, Tame J.R., Zhang K.Y., Maeyer M. De & Voet A.R. 2014. Pharmacophore modeling: Advances, Limitations, And current utility in drug discovery. *J. Receptor. Ligand Channel Res.* 7: 81–92.
- Raunio H., Kuusisto M., Juvonen R.O. & Pentikänen O.T. 2015. Modeling of interactions between xenobiotics and cytochrome P450 (CYP) enzymes. *Front. Pharmacology* 6: 1–14.
- Rendic S. & Guengerich F.P. 2012. Contributions of human enzymes in carcinogen metabolism. *Chem. Res. Toxicol.* 25: 1316–1383.
- Rendic S. & Guengerich F.P. 2015. Survey of Human Oxidoreductases and Cytochrome P450 Enzymes Involved in the Metabolism of Xenobiotic and Natural Chemicals. *Chem. Res. Toxicol.* 28: 38–42.
- Ryckaert J.P., Ciccotti G. & Berendsen H.J.C. 1977. Numerical integration of the cartesian equations of motion of a system with constraints: molecular dynamics of n-alkanes. *J. Comput. Phys.* 23: 327–341.
- Rydberg P., Gloriam D.E., Zaretski J., Breneman C. & Olsen L. 2010. SMARTCyp: A 2D method for prediction of cytochrome P450-mediated drug metabolism. *ACS Med. Chem. Lett.* 1: 96–100.
- Rydberg P. & Olsen L. 2012a. Predicting Drug Metabolism by Cytochrome P450 2C9: Comparison with the 2D6 and 3A4 Isoforms. *ChemMedChem* 7: 1202–1209.

- Rydberg P. & Olsen L. 2012b. Ligand-based site of metabolism prediction for cytochrome P450 2D6. *ACS Med. Chem. Lett.* 3: 69–73.
- Rydberg P., Rod T.H., Olsen L. & Ryde U. 2007. Dynamics of water molecules in the active-site cavity of human cytochromes P450. *J. Phys. Chem. B* 111: 5445–5457.
- Rydberg P., Rostkowski M., Gloriam D.E. & Olsen L. 2013. The contribution of atom accessibility to site of metabolism models for cytochromes P450. *Mol. Pharm.* 10: 1216–1223.
- Šali A. & Blundell T.L. 1993. Comparative protein modelling by satisfaction of spatial restraints. *J. Mol. Biol.* 234: 779–815.
- Sansen S., Yano J.K., Reynald R.L., Schoch G.A., Griffin K.J., Stout C.D. & Johnson E.F. 2007. Adaptations for the oxidation of polycyclic aromatic hydrocarbons exhibited by the structure of human P450 1A2. *J. Biol. Chem.* 282: 14348–14355.
- Santos R., Hritz J. & Oostenbrink C. 2010. Role of water in molecular docking simulations of cytochrome P450 2D6. *J. Chem. Inf. Model.* 50: 146–154.
- Sato A., Yuki H., Watanabe C., Saito J.I., Konagaya A. & Honma T. 2017. Prediction of the site of CYP3A4 metabolism of tolterodine by molecular dynamics simulation from multiple initial structures of the CYP3A4-tolterodine complex. *Chem-Bio Informatics J.* 17: 38–52.
- Schaller D., Šribar D., Noonan T., Deng L., Nguyen T.N., Pach S., Machalz D., Bermudez M. & Wolber G. 2020. Next generation 3D pharmacophore modeling. *Wiley Interdiscip. Rev. Comput. Mol. Sci.* 10: 1–20.
- Sevrioukova I.F. & Poulos T.L. 2017. Structural basis for regiospecific midazolam oxidation by human cytochrome P450 3A4. *Proc. Natl. Acad. Sci.* 114: 486–491.
- Shaik S., Cohen S., Wang Y., Chen H., Kumar D. & Thiel W. 2010. *P450 enzymes: their structure, reactivity, and selectivity-modeled by QM/MM calculations.*
- Sheng Y., Chen Y., Wang L., Liu G., Li W. & Tang Y. 2014. Effects of protein flexibility on the site of metabolism prediction for CYP2A6 substrates. *J. Mol. Graph. Model.* 54: 90–99.
- Sheridan R.P., Korzekwa K.R., Torres R. a. & Walker M.J. 2007. Empirical regioselectivity models for human cytochromes P450 3A4, 2D6, and 2C9. *J. Med. Chem.* 50: 3173–3184.
- Sikka R., Magauran B., Ulrich A. & Shannon M. 2005. Bench to Bedside: Pharmacogenomics, adverse drug interactions, and the cytochrome P450 system. *Acad. Emerg. Med.* 12: 1227–1235.
- Skopalík J., Anzenbacher P. & Otyepka M. 2008. Flexibility of human cytochromes P450: molecular dynamics reveals differences between CYPs 3A4, 2C9, and 2A6, which correlate with their substrate preferences. *J. Phys. Chem. B* 112: 8165–8173.
- Sud M. 2016. MayaChemTools: An Open Source Package for Computational Drug Discovery. *J. Chem. Inf. Model.* 56: 2292–2297.
- Testa B., Pedretti A. & Vistoli G. 2012. Reactions and enzymes in the metabolism of drugs and other xenobiotics. *Drug Discov. Today* 17: 549–560.
- The UniProt Consortium. 2019. UniProt: A worldwide hub of protein knowledge. *Nucleic Acids Res.* 47: D506–D515.

- Tian S., Djoumbou Y., Greiner R. & Wishart D.S. 2018. CypReact: A Software Tool for in silico Reactant Prediction for Human Cytochrome P450 Enzymes. *J. Chem. Inf. Model.* 58: 1282–1291.
- Tsui V. & Case D.A. 2000. Theory and applications of the Generalized Born solvation model in macromolecular simulations. *Biopolymers* 56: 275–291.
- Tyzack J.D. & Kirchmair J. 2019. Computational methods and tools to predict cytochrome P450 metabolism for drug discovery. *Chem. Biol. Drug Des.* 93: 377–386.
- Tyzack J.D., Williamson M.J., Torella R. & Glen R.C. 2013. Prediction of cytochrome P450 xenobiotic metabolism: Tethered docking and reactivity derived from ligand molecular orbital analysis. *J. Chem. Inf. Model.* 53: 1294–1305.
- Urban P., Lautier T., Pompon D. & Truan G. 2018. Ligand access channels in cytochrome P450 enzymes: A review. *Int. J. Mol. Sci.* 19: 1617–1638.
- Vainio M.J., Puranen J.S. & Johnson M.S. 2009. ShaEP: Molecular overlay based on shape and electrostatic potential. *J. Chem. Inf. Model.* 49: 492–502.
- Vasanthanathan P., Hritz J., Taboureau O., Olsen L., Jørgensen F.S., Vermeulen N.P.E. & Oostenbrink C. 2009a. Virtual screening and prediction of site of metabolism for cytochrome P450 1A2 ligands. *J. Chem. Inf. Model.* 49: 43–52.
- Vasanthanathan P., Taboureau O., Oostenbrink C., Vermeulen N.P.E., Olsen L. & Jørgensen F.S. 2009b. Classification of cytochrome P450 1A2 inhibitors and noninhibitors by machine learning techniques. *Drug Metab. Dispos.* 37: 658–664.
- Vedani A., Dobler M., Hu Z. & Smieško M. 2015. OpenVirtualToxLab-A platform for generating and exchanging in silico toxicity data. *Toxicol. Lett.* 232: 519–532.
- Verma J., Khedkar V. & Coutinho E. 2010. 3D-QSAR in Drug Design - A Review. *Curr. Top. Med. Chem.* 10: 95–115.
- Virtanen S.I. & Pentikäinen O.T. 2010. Efficient virtual screening using multiple protein conformations described as negative images of the ligand-binding site. *J. Chem. Inf. Model.* 50: 1005–1011.
- Walsh A.A., Szklarz G.D. & Scott E.E. 2013. Human cytochrome P450 1A1 structure and utility in understanding drug and xenobiotic metabolism. *J. Biol. Chem.* 288: 12932–12943.
- Wang A., Savas U., Stout C.D. & Johnson E.F. 2011. Structural characterization of the complex between alpha-naphthoflavone and human cytochrome P450 1B1. *J. Biol. Chem.* 286: 5736–5743.
- Wang J.M., Wolf R.M., Caldwell J.W., Kollman P. a & Case D. a. 2004. Development and testing of a general amber force field. *J. Comput. Chem.* 25: 1157–1174.
- Warren G.L., Andrews C.W., Capelli A.M., Clarke B., LaLonde J., Lambert M.H., Lindvall M., Nevins N., Semus S.F., Senger S., Tedesco G., Wall I.D., Woolven J.M., Peishoff C.E. & Head M.S. 2006. A critical assessment of docking programs and scoring functions. *J. Med. Chem.* 49: 5912–5931.
- Watanabe Y., Fukuyoshi S., Kato K., Hiratsuka M., Yamaotsu N., Hirono S., Gouda H. & Oda A. 2017. Investigation of substrate recognition for cytochrome P450 1A2 mediated by water molecules using docking and molecular dynamics simulations. *J. Mol. Graph. Model.* 74: 326–336.

- Watts K.S., Dalal P., Murphy R.B., Sherman W., Friesner R.A. & Shelley J.C. 2010. ConfGen: A conformational search method for efficient generation of bioactive conformers. *J. Chem. Inf. Model.* 50: 534–546.
- Word J.M., Lovell S.C., Richardson J.S. & Richardson D.C. 1999. Asparagine and glutamine: using hydrogen atom contacts in the choice of side-chain amide orientation. *J. Mol. Biol.* 285: 1735–1747.
- Wu F., Zhou Y., Li L., Shen X., Chen G., Wang X., Liang X., Tan M. & Huang Z. 2020. Computational Approaches in Preclinical Studies on Drug Discovery and Development. *Front. Chem.* 8.
- Yano J.K., Hsu M.H., Griffin K.J., Stout C.D. & Johnson E.F. 2005. Structures of human microsomal cytochrome P450 2A6 complexed with coumarin and methoxsalen. *Nat. Struct. Mol. Biol.* 12: 822–823.
- Ylilauri M. & Pentikäinen O.T. 2013. MMGBSA as a tool to understand the binding affinities of filamin-peptide interactions. *J. Chem. Inf. Model.* 53: 2626–2633.
- Zamora I., Afzelius L. & Cruciani G. 2003. Predicting drug metabolism: A site of metabolism prediction tool applied to the cytochrome P450 2C9. *J. Med. Chem.* 46: 2313–2324.
- Zanger U.M. & Schwab M. 2013. Cytochrome P450 enzymes in drug metabolism: Regulation of gene expression, enzyme activities, and impact of genetic variation. *Pharmacol. Ther.* 138: 103–141.
- Zaretski J., Bergeron C., Rydberg P., Huang T.W., Bennett K.P. & Breneman C.M. 2011. RS-predictor: A new tool for predicting sites of cytochrome P450-mediated metabolism applied to CYP 3A4. *J. Chem. Inf. Model.* 51: 1667–1689.
- Zaretski J., Matlock M. & Swamidass S.J. 2013. XenoSite: Accurately predicting cyp-mediated sites of metabolism with neural networks. *J. Chem. Inf. Model.* 53: 3373–3383.
- Zaretski J., Rydberg P., Bergeron C., Bennett K.P., Olsen L. & Breneman C.M. 2012. RS-predictor models augmented with SMARTCyp reactivities: Robust metabolic regioselectivity predictions for nine CYP isozymes. *J. Chem. Inf. Model.* 52: 1637–1659.
- Zhang Z. & Tang W. 2018. Drug metabolism in drug discovery and development. *Acta Pharm. Sin. B* 8: 721–732.
- Zhou D., Afzelius L., Grimm S.W., Andersson T.B., Zauhar R.J. & Zamora I. 2006. Comparison of Methods for the Prediction of the Metabolic Sites for CYP3A4-Mediated Metabolic Reactions. *Drug Metab. Dispos.* 34: 976–983.



ORIGINAL PAPERS

I

INHIBITORY EFFECTS AND OXIDATION OF 6-METHYLCOUMARIN, 7-METHYLCOUMARIN AND 7-FORMYLCOUMARIN VIA HUMAN CYP2A6 AND ITS MOUSE AND PIG ORTHOLOGOUS ENZYMES

by

Juvonen R.O., Kuusisto M., Fohrgrup C., Pitkänen M.H., Nevalainen T.J., Auriola S.,
Raunio H., Pasanen M. & Pentikäinen O.T., 2016

Xenobiotica 46: 14-24

DOI 10.3109/00498254.2015.1048327

Reproduced with kind permission by Taylor & Francis.

Inhibitory effects and oxidation of 6-methylcoumarin, 7-methylcoumarin and 7-formylcoumarin via human CYP2A6 and its mouse and pig orthologous enzymes

Risto O. Juvonen¹, Mira Kuusisto^{1,2}, Carolin Fohrgrup¹, Mari H. Pitkänen¹, Tapio J. Nevalainen¹, Seppo Auriola¹, Hannu Raunio¹, Markku Pasanen¹, Olli T. Pentikäinen²,

1 School of Pharmacy, Faculty of Health Sciences, University of Eastern Finland, Box 1627, 70211 Kuopio, Finland.

2 University of Jyväskylä, Department of Biological and Environmental Science & Nanoscience Center, P.O.Box 35, 40014 University of Jyväskylä, Finland

Corresponding author: Risto O. Juvonen, School of Pharmacy, Faculty of Health Sciences, University of Eastern Finland, Box 1627, 70211 Kuopio, Finland, tel 358 40 728 2699, e-mail: risto.juvonen@uef.fi

Key terms: cytochrome P450, coumarin derivative, metabolism, enzyme assay, fluorescence

Abstract

1. Information about the metabolism of compounds is essential in drug discovery and development, risk assessment of chemicals and further development of predictive methods.
2. In vitro and in silico methods were applied to evaluate the metabolic and inhibitory properties of 6-methylcoumarin, 7-methylcoumarin and 7-formylcoumarin with human CYP2A6, mouse CYP2A5 and pig CYP2A19.
3. 6-Methylcoumarin was oxidized to fluorescent 7-hydroxy-6-methylcoumarin by CYP2A6 (K_m : 0.64 – 0.91 μM ; V_{max} : 0.81 – 0.89 min^{-1}) and by CYP2A5 and CYP2A19. The reaction was almost completely inhibited at 10 μM 7-methylcoumarin in liver microsomes of human and mouse, but in pig only 40 % inhibition was obtained with the anti-CYP2A5 antibody or with methoxsalen and pilocarpine. 7-Methylcoumarin was a mechanism-based inhibitor for CYP2A6, but not for the mouse and pig enzymes. 7-Formylcoumarin was a mechanism-based inhibitor for CYP2As of all species.
4. Docking and molecular dynamics simulations of 6-methylcoumarin and 7-methylcoumarin in the active sites of CYP2A6 and CYP2A5 demonstrated a favorable orientation of the 7-position of 6-methylcoumarin toward the heme moiety. Several orientations of 7-methylcoumarin were possible in CYP2A6 and CYP2A5.
5. These results indicate that the active site of CYP2A6 has unique interaction properties for ligands and differs in this respect from CYP2A5 and CYP2A19.

Introduction

Although there are many xenobiotic metabolizing enzymes, the cytochrome P450 (CYP) enzymes are particularly important, because they are abundant in liver and catalyze the elimination reactions of all kinds of organic compounds within molecular weights 32 and 1203 g/mol (Sevior, Pelkonen & Ahokas 2012, Testa, Pedretti & Vistoli 2012, Zanger, Schwab 2013). It would be a great advantage if the role of CYPs in biokinetics could be predicted rapidly and reliably during drug discovery and development programmes as well as in risk assessment of chemicals, since detailed experimental studies of large numbers of molecules are both time-consuming and expensive.

Numerous methods are available to evaluate CYP-mediated metabolism *in vivo*, *in vitro*, and more recently, *in silico*. The fluorescence-based *in vitro* assays are standard methods used in competitive inhibition screens, since they enable rapid identification of potential CYP substrates or inhibitors. Many coumarin derivatives have proved to be especially useful in fluorescence based *in vitro* assays (Foti, Wienkers & Wahlstrom 2010, Makaji et al. 2009, Turpeinen et al. 2006). Several different kinds of *in silico* models have also been developed to predict the structure-activity relationship of CYP enzymes, the latest models aim to predict both the site(s) of metabolism and which metabolites will be formed (Cruciani 2013, Kirchmair et al. 2012, Long 2013). Although these *in silico* techniques have become quite reliable, there is still much scope for further refinement.

While there is known to be some cross-species conservation of CYP enzyme function, CYP-mediated metabolism often differs substantially between humans and other mammalian species (Bogaards et al. 2000, Dalgaard 2015). In the CYP2A subfamily, the amino acid sequence identity between human CYP2A6, mouse CYP2A5, and pig CYP2A19 is more than 82 % all of these enzymes can catalyze the coumarin 7-hydroxylation reaction. However, very few studies have compared the characteristics of these orthologous enzymes. Site-directed mutagenesis studies of CYP2A5 and CYP2A6 as well as identification of genetic CYP2A6 variants have revealed the nature of the amino acid residues important for the specificity and function of these enzymes (Pelkonen et al. 2000, Raunio, Rahnasto-Rilla 2012). Even minute structural differences in CYP ligands can alter their oxidation rate, metabolism patterns and inhibition potencies (Stepan et al. 2011). Since the

elimination rate can be changed and reactive metabolites can be formed, small structural changes in the substrates can greatly affect the pharmacological and toxicological effects of compounds. Therefore, it is vital for decision making during drug discovery and development and toxicological risk assessment of chemicals that we have reliable structure-activity relationship information about CYPs, their substrates and their inhibitors (DeLisle, Otten & Rhodes 2011). This kind of data input is also important when refining the novel in silico techniques.

A wide range of in silico methods have been applied for the prediction of CYP catalyzed small molecule metabolism, for example docking, quantum chemistry based reactivity calculations etc. (Cruciani 2013, Kirchmair et al. 2012, Long 2013). One of the key in silico methods used to estimate the binding modes and energetics in drug discovery is the post-docking characterization from molecular dynamics simulations with binding energy estimation obtained from molecular mechanics - generalized Born - surface area (MMGBSA) calculations (Tsui, Case 2000).

Although case specific, MMGBSA has proven to be a reliable tool both for protein-small molecule (Rastelli et al. 2010, Niinivehmas et al. 2011, Hou et al. 2011, Ylilauri, Pentikäinen 2012) and protein-protein interactions (Gohlke, Case 2004, Ylilauri, Pentikäinen 2013) but it has not been applied in the prediction of SOMs, perhaps due to its computational cost.

The main aim of this study was to obtain new structure-activity relationship data about the human CYP2A6, mouse CYP2A5 and pig CYP2A19 enzymes. We took both in vitro and in silico approaches to evaluate, how three structurally similar compounds, 7-methylcoumarin, 7-formylcoumarin and 6-methylcoumarin, would interact with the CYP2A6, CYP2A5 and CYP2A19 enzymes. The results provide detailed insight into both common and distinctive features of the catalytic properties of these three orthologous CYPs.

Materials and methods

Chemicals and reagents: All chemicals were of the highest purity available from their commercial suppliers. Tris-HCl, MnCl₂, MgCl₂, reduced glutathione (GSH), isocitric acid and isocitric acid dehydrogenase were purchased from Sigma-Aldrich (Steinheim, Germany), KCl from J.T. Baker, NADPH and NADP from Roche Diagnostics (Mannheim, Germany), 6-methylcoumarin and 7-methylcoumarin from Aldrich Inc., 7-hydroxy-6-methylcoumarin from Ryan Scientific Inc., USA. 200 mL NADPH regenerating system contained 178.5 mg NADP (nicotinamide adenine

dinucleotide phosphate), 645 mg isocitric acid, 340 mg KCl, 240 mg MgCl₂, 0.32 mg MnCl₂ and 15 U isocitric acid dehydrogenase.

Reagents and solvents for the synthesis of 7-formylcoumarin were purchased from Sigma-Aldrich and were used without further purification. Reactions were monitored by thin-layer chromatography (TLC) using aluminum sheets coated with silica gel F245 (60 Å, 40-63 µm, 230-400 mesh) with suitable UV visualization. Purification was carried out by flash chromatography (FC) on J. T. Baker's silica gel for chromatography (pore size 60 Å, particle size 50 nm). The petroleum ether (PE) used for chromatography was from fraction 40–60°C. ¹H NMR was recorded on a Bruker Avance AV 500 (Bruker Biospin, Switzerland) spectrometer operating at 500.1 MHz using tetramethylsilane (TMS) as an internal standard. Chemical shifts are reported in ppm on the δ scale from an internal standard of solvent (CDCl₃ 7.26). The spectra were processed from the recorded FID files with TOPSPIN 2.1 software. The following abbreviations are used: s, singlet; d, doublet. Coupling constants are reported in Hz. ESI-MS spectra were acquired using a LCQ quadrupole ion trap mass spectrometer equipped with an electrospray ionization source (Thermo LTQ, San Jose, CA, USA).

7-Methylcoumarin (500 mg, 3.12 mmol) in 1, 4-dioxane (10 mL) in a microwave reaction vial was added with SeO₂ (519 mg, 4.68 mmol). The reaction vial was capped and the mixture was heated in a microwave at 200°C for 60 min. The reaction mixture was diluted with DCM, filtered, washed with water and NaHCO₃-solution. The reaction mixture was concentrated and the resulting material was purified by column chromatography (silica gel) using a EtOAc /petroleum ether (1:10) as the eluent, providing the desired product as a pale yellow solid (217 mg, 40%). ¹H NMR (CDCl₃): δ 6.68 (1H, d, J = 9.5 Hz, H-3), 7.66 (1H, d, J = 8.8 Hz, H-5), 7.76 (1H, d, J = 9.5 Hz, H-4), 7.80 (1H, d, J = 1.6 Hz, H-8), 8.07 (1H, dd, J = 7.3, 1.6 Hz, H-6), 10.09 (1H, s, CHO); ESI-MS 175.0 [M+H]⁺.

Biological material: The human livers used in this study were obtained from the University of Oulu Hospital as surplus from kidney transplantation donors. The collection of the surplus tissue was approved by the Ethics Committee of the Medical Faculty of the University of Oulu. After surgical excision, the liver samples were immediately transferred to ice, cut into pieces, snap frozen in liquid nitrogen and stored at -80°C until the microsomes prepared. Pig liver samples were from female control pigs used for practicing surgical procedures, Kuopio University. DBA/2N/Kuo

mice and Wistar rats were obtained from the National Laboratory Animal Centre, Kuopio University. Rats were given i.p. 0.5 mL 0.9 % saline/kg/day for four days. Mice were given i.p. 0.1 mL 0.9 % saline/10 g/day for four days, pyrazole in saline (150 mg/kg) for three days or i.p. 80 mg/kg phenobarbital on the first morning and then 40 mg/kg on four consecutive morning. Animals were killed 24 h after the last treatment. Liver microsomes were prepared as described previously (Lang, Gielen & Nebert 1981). The microsomal protein concentration was determined by the Bradford method. The mice and rat had unrestricted access to water and standard chow (Lactamin R36, Lactamin AB, Södertälje, Sweden). The Ethics Committee for Animal Experiments, University of Kuopio, approved these experiments. Baculovirus-insect cell-expressed human CYP1A1, 1A2, 2A6, 2B6, 2C8, 2C9, 2C19, 2D6, 2E1, 3A4, 3A5 and 3A7 were purchased from BD Biosciences Discovery Labware (Woburn, MA, USA) and used according to the manufacture's instructions. The preparation and characteristics of anti-CYP2A5 antibody have been described earlier (Raunio et al. 1998).

Incubations and fluorescence assays: Excitation and emission fluorescence spectra of 1 μ M 6-methylcoumarin and 7-hydroxy-6-methyl coumarin in 100 mM Tris-HCl pH 7.4 were measured with a Shimadzu spectrophotofluorometer RF5000.

Oxidation of 6-methylcoumarin: 0 – 100 μ M 6-methylcoumarin was incubated in 100 mM Tris-HCl buffer pH 7.4 containing 5 mM $MgCl_2$, 10 nM recombinant CYP or 0 – 0.2 g/L microsomal protein and 0.5 mM NADPH at 37°C for 20 min or indicated time. The reaction was stopped with 3 % trichloroacetic acid and the fluorescence measured with an EnVision2104 multilabel, a Perkin Elmer reader using ex 380 and em 460 nm in 1 M glycine-NaOH buffer pH 10.4. Incubation without 6-methylcoumarin, enzyme or NADPH was used as blank reaction. Standards of 0 – 1 μ M 7-hydroxy-6-methylcoumarin were used to calculate the amounts of product formed. In samples for analysis by HPLC-fluorescence detector and HPLC/MS a total of 10 μ M 6-methylcoumarin was incubated under the above conditions for 40 min, the reaction stopped by adding triple the volume of acetonitrile, centrifuged at 10 000 x g for 5 min and the supernatant analyzed.

Inhibition of 6-methylcoumarin 7-hydroxylation: the incubation mixture contained 100 mM Tris-HCl pH 7.4, 10 μ M 6-methylcoumarin, 50 mg/L microsomal protein, 20 % NADPH regenerating system and inhibiting agent of 0 – 10 μ M methoxsalen, 0 – 1.25 mM pilocarpine or 0 – 0.5 g/L anti-CYP2A5 antibody. Blank reactions did not

contain NADPH or enzyme. The reaction was stopped after 20 min incubation by addition of 1 M glycine-NaOH pH 10.4 and the fluorescence measured by Victor 1420 multilabel reader, Perkin Elmer using ex 350 nm and em 450 nm.

Inhibition of coumarin 7-hydroxylation: the incubation mixture contained 100 mM Tris-HCl pH 7.4, 10 μ M coumarin, 20 mg/L microsomal protein, 20 % NADPH regenerating system and 0 – 10 μ M methoxsalen, 0 -1.25 mM pilocarpine or 0 – 0.5 g/L anti-CYP2A5 antibody. Blank reactions did not contain NADPH or enzyme. The reactions were stopped after 20 min incubation by addition of 3 % trichloroacetic acid, followed 1 M glycine-NaOH pH 10.4 and the fluorescence measured by Victor multilabel reader, Perkin Elmer using ex 350 nm and em 450 nm.

When the effect of preincubation on coumarin 7-hydroxylation was studied, 0 – 500 μ M concentrations of 7-methylcoumarin or 7-formylcoumarin were first incubated in 100 μ L 100 mM Tris-HCl buffer pH 7.4 containing 0.5 mM NADPH, 5 mM $MgCl_2$ and 200 mg/l microsomal protein or 100 nM CYP2A6 for 0 – 30 min. Secondly, 10 μ L sample was taken from this mixture to the final volume of 200 μ L containing 100 mM Tris-HCl buffer pH 7.4, 5 mM $MgCl_2$, 100 μ M coumarin and 0.5 mM NADPH. After 20 min incubation, the reaction was stopped by adding 20 μ L 30 % trichloroacetic acid, and then 140 μ L 1.6 M glycine-NaOH pH 10.4 was added into the 110 μ L incubation sample and the fluorescence measured as described above.

In the metabolism experiments, 7-methylcoumarin was incubated in 50 mM phosphate buffer pH 7.4 containing 0 – 1 mg/L microsomal protein or 5 nM CYP2A6, 20 % NADPH regenerating system with or without 1 mM reduced glutathione at 37°C for 5 – 60 min. A total of 0.5 mg/L anti-CYP2A5 antibody was used in the inhibitory experiments. Blank reactions did not contain enzyme, NADPH regenerating system or 7-methylcoumarin. The reaction was stopped by a triple volume of methanol, centrifuged 10 000 g for 10 min, the supernatant was evaporated in a vacuum centrifuge and stored at -20°C.

HPLC-fluorescence and MS analysis: A Shimadzu liquid chromatograph system was used to analyze the 6-methylcoumarin incubation sample. The system contained an LC10A0Vp Shimadzu liquid chromatograph controller, LC-20AP prominence UFLC pumps, Zorbax C18 SB-Aq 3.5 μ m particle size 30 x 150 mm column and SPD-10A XL Shimadzu fluorescence detector. The initial mobile phase was 90 % A (water) and 10 % B (50 % acetonitrile and 50 % methanol). This was kept constant for 1 minute and then B was increased linearly to 100 % in 10 minutes

and run for 2 min. Then, the column was allowed to re-equilibrate at 10 % B for 5 minutes prior to next injection. The fluorescence detector was used with excitation 330 nm and emission 450 nm.

The analyses of 7-methylcoumarin metabolites were performed with high performance liquid chromatography mass spectrometer (LC-MS/MS) Agilent 1200 HPLC coupled with a Finnigan LTQ system (Thermo Electron, San Jose, CA, USA) with an electrospray ionization (ESI) source. Full scan and dependent MS/MS was used in the characterization of the metabolites. The data was acquired by Xcalibur 1.4 SRI software (Thermo electron corporation, San Jose, CA, USA). The compounds were separated using reversed-phase column Zorbax C18 SB-Aq 30 x 150 mm column, particle size 3.5 μm . The initial mobile phase was 85% A (0.1% formic acid in water) and 15 % B (acetonitrile), then B was increased linearly to 30 % in 5 minutes, and to 80 % in 2 minutes and kept there for 2 minutes. Then, the column was allowed to re-equilibrate at 15% B for 4 minutes prior to the next injection. Flow rate was 0.2 ml per min and injection volume 5 μl .

The quantitative analysis of 7-methylcoumarin was performed using selected reaction monitoring and coumarin as the internal standard. The transition was for 7-methylcoumarin m/z 161 \rightarrow 117, and calibration standards were 0.5 μM , 2 μM , 5 μM , 10 μM , 30 μM and 50 μM .

The analysis of glutathione conjugates formed in the incubation of 7-methylcoumarin was performed using the same system, but the initial mobile phase was 95 % A (0.1% formic acid in water) and 5 % B (acetonitrile), then B was increased linearly to 80 % in 8 minutes. The identification of coumarin derivative metabolites was based on MS/MS fragmentation studies by Concannon et al. 2000, Morreel et al. 2010, and Timonen et al. 2013.

In silico analysis: Optimization and parametrization of ligands: Parametrization of ligands were performed as follows: The 3D structures of CYP2A6 substrates were optimized by quantum mechanical techniques with GAUSSIAN09 (Gaussian, Inc., Wallingford, CT) at the HF/6-31+G* level using a polarizable continuum model. The RESP method (Bayly et al., 1993) was used to calculate the atom-centered point charges from the electrostatic potentials. Only the most likely tautomer and ionization state at pH 7.4 was used for each ligand.

Homology modeling of CYP2A5: The sequence alignment between the crystal structure of CYP2A6 (PDB-code: 1Z10 (Yano et al. 2005) and rat CYP2A5

sequence was produced with Malign in Bodil (Lehtonen et al. 2004) by employing structure-based matrix (Johnson, Overington 1993) with gap-formation penalty of 40. Based on the produced sequence alignment, the model of rat CYP2A5 was built with the Modeller version 9.13 (Sali, Blundell 1993). Side chain conformations at the catalytic site were visually inspected.

Molecular docking: The CYP2A6 structure (PDB-code: 1Z10 (Yano et al. 2005) was prepared for docking. Hydrogens were added with Reduce (Word et al. 1999) and the atom types in the heme were corrected. The sixth coordination position that could be occupied by an oxygen was left unoccupied to enable inhibitory ligand conformations that are close to iron and could directly coordinate to it. Furthermore, since the energetically optimal conformation for substrate binding would be the transition state, whose structural details are not known, the unoccupied coordination position can reasonable be used to study substrates as well. Nevertheless, the possible space for oxygen at the reaction center was also analyzed in each case. The molecules were docked into the structure of CYP2A6 with Plants (Korb, Stützle & Exner 2009) using the Chemplp scoring method. Four binding mode predictions with RMSD threshold of 2.0 Å were generated for each molecule to ensure that the conformational space between CYPs and bound ligand is enough for detailed analysis. Same four docking results were used for both CYP2A6 and CYP2A6, which were superimposed with Vertaa in Bodil (Lehtonen et al. 2004). Rationality of the binding conformations was visually inspected.

Molecular dynamics simulations and analysis: Tleap in Antechamber (Wang, Wang & Kollman 2001) was used to: (1) generate force field parameters for protein and combined protein-ligand parameterizations; (2) add hydrogen atoms; and (3) solvate the system with a rectangular box of transferable intermolecular potential three-point (TIP3P) water molecules extending 13 Å in all dimensions around the solute. Parameters suitable for six-coordinate iron were used for the heme group (Giammmona, 1984).

Molecular dynamics (MD) simulations were performed with NAMD 2.9 (Phillips et al., 2005) as described earlier (Ylilauri, Pentikäinen 2012)); in short, five steps were used: (1) 15,000 steps of energy minimization where Ca-atoms were restrained with 5 kcal/mol; (2) 15,000 steps of energy minimization without restraints; (3) 180,000 steps of MD where C^α-atoms were restrained with 5 kcal/mol; (4) 1,200,000 steps (2.4 ns; time step: 2 fs) of MD without restraints; (5) snapshot structures (20) from

the 2.4 ns MD simulation were minimized without restraints in 15,000 steps for more reliable MMGBSA analysis.

Superimposition of protein-ligand complexes was performed with Vertaa in Bodil (Lehtonen et al. 2004).

All MD trajectory manipulations were made with Cpptraj (Roe, Cheatham 2013).

MMGBSA analyses were performed with MMPBSA.py (Miller III et al. 2012) script implemented in Antechamber by using three IGB-models: igb1 (Tsui, Case 2000), igb2, and igb5 (Onufriev, Bashford & Case 2004), however, since all methods gave very similar results, only the igb1-values are shown.

Results

Oxidation of 6-methylcoumarin to 7-hydroxy-6-methylcoumarin. 6-

Methylcoumarin is non-fluorescent, but when incubated with liver microsomes in the presence of NADPH, it is converted to the fluorescent metabolite, 7-hydroxy-6-methylcoumarin which has two excitation maximum values at 353 nm and 388 nm (310 – 400 nm) and an emission maximum at 455 nm (430 – 500 nm) (Fig. 1A). The increase of fluorescence intensity was also dependent on both the time and amount of oxidizing enzyme (Fig. 1B). No other fluorescent metabolites were detected when the incubate was analyzed by HPLC using a fluorescent detector set at ex 330 nm and em 450 nm (Fig. 1C and D).

When examining the recombinant human CYPs, only CYP2A6 was able to catalyze the reaction at a high rate, whereas CYPs 1A1, 2B6, 2C8, 2C9, 2C19, 2D6, 2E1, and 3A4 were inactive and CYPs 1A2, 3A5 and 3A7 had very low activity (Fig. 1E). The 6-methylcoumarin 7-hydroxylation reaction rate was clearly higher in human, pig and mouse than in rat liver microsomes (Fig. 1F). The 6-methylcoumarin K_m value was smaller for human and mouse than for pig liver microsomes (Table 1). The 6-methylcoumarin K_m was less than 1 μ M in the recombinant CYP2A6 catalyzed reaction.

The anti-CYP2A5 antibody inhibited 6-methylcoumarin 7-hydroxylation by 100 % in pyrazole-induced mouse and by 90 % in human liver microsomes, but only by 40-50 % in pig liver microsomes. Methoxsalen and pilocarpine, well known chemical inhibitors of CYP2A enzymes, inhibited also completely 6-methylcoumarin 7-hydroxylation in pyrazole-treated mouse liver microsomes. However, the inhibition was incomplete against the reaction in human (90 % inhibition) and pig (50 % inhibition) microsomes (data not shown).

Docking of 6-methylcoumarin into the CYP2A6 enzyme yielded four conformations (Fig. 2) where the closest ligand positions to the heme iron were: (1) position 6-methyl and position 7; (2) positions 3 and 4; (3) carbonyl oxygen atom; and (4) position 6-methyl and position 5. Furthermore, in all complexes there was reasonable space available to accommodate oxygen needed for the reaction. According to the MD simulations, conformation 1 was clearly the most stable one. The estimations of binding energy, done by using MMGBSA, indicated that conformation 1 was energetically preferred (conf1: -30.0 ± 1.0 kcal/mol; conf2: -22.7 ± 1.4 kcal/mol; conf3: -28.9 ± 1.0 kcal/mol; conf4: -29.2 ± 1.8 kcal/mol). However, it should be noted that the binding energy estimations for conformations 3 and 4 were always within the error limits of conformation 1, while conformation 2 was the least favored. Summary, the stability and binding energy estimations indicated that the primary site for metabolism in 6-methylcoumarin would be at position 7 (Fig 2B). Furthermore, the space around the iron and position 7 of 6-methylcoumarin was sufficiently large to accommodate oxygen, either as O or O₂, which is necessary for the oxidation reaction, similarly as seen in the crystal structure of CYP2A6 with bound coumarin. However, in particular, the close proximity of iron to position 5 in conformation 4 suggested that other metabolites might also exist.

In mouse CYP2A5 the starting conformations for MD simulations of 6-methylcoumarin were the same as in CYP2A6. Here, conformations 1 and 3 showed excellent stability, and they were also energetically clearly preferred within the error limits (Fig 2B), whereas conformations 2 and 4 were disfavored. Conformation 3 had always lower energy than conformation 1. In conformation 1, position 7 of 6-methylcoumarin was located optimally to allow it to be oxidized similarly to the situation encountered with human CYP2A6. However, in contrast to CYP2A6, conformation 3 had also position 7 towards the iron already during the energy minimization. Accordingly, both of these stable and energetically most favorable conformations had ligand position 7 facing towards the iron and it could be estimated that hydroxylation of position 7 of 6-methylcoumarin would also be preferred by CYP2A5.

Taken together, 6-methylcoumarin was oxidized to 7-hydroxy-6-methylcoumarin by human CYP2A6 and mouse CYP2A5: (1) the formation of 7-hydroxy-6-methylcoumarin from 6-methylcoumarin could be measured, (2) the oxidative reaction occurred only when 6-methylcoumarin, CYP2A6 and NADPH were all

present, (3) anti-CYP2A5 antibody and chemical CYP2A inhibitors prevented efficiently the oxidation in human and mouse liver microsomes, and (4) MD simulation suggested that the most preferred binding conformation was such that position 7 was facing towards the heme iron. Pig CYP2A19 was also able to catalyze the reaction, but pig liver microsomes seemed to express also other catalyzing enzyme(s).

Inhibition of coumarin 7-hydroxylation by 7-methylcoumarin and 7-formylcoumarin. The inhibition characteristics of 7-methylcoumarin and 7-formylcoumarin were determined for human, mouse and pig CYP2A-mediated coumarin 7-hydroxylation (Table 2). When there was no preincubation the 7-methylcoumarin IC_{50} value was smaller (35 – 50 %) in mouse and pig than in human liver microsomes or recombinant CYP2A6. However, if 7-methylcoumarin was incubated for 30 min, this led to 2 – 5 fold increase in IC_{50} with the pig and mouse microsomes but to a decrease by 80 % with the human liver microsomes and recombinant CYP2A6. The decrease in IC_{50} value due to preincubation was both time and concentration dependent (Fig. 3) indicating that 7-methylcoumarin is a mechanism-based inhibitor for human CYP2A6. The maximum inactivation rate in human liver microsomes and CYP2A5 was $0.09 - 0.15 \text{ min}^{-1}$ indicating that about 1 % of CYP2A6 was inactivated in one minute, with half maximal inactivation being reached at $10 \mu\text{M}$ 7-methylcoumarin (Table 3).

The binding of 7-methylcoumarin was simulated with MD with four different conformations in the CYP2A6 and CYP2A5 binding sites (Figure 2E). Interestingly, the most stable conformation was conformation 4, which was also energetically the most attractive one (conf1: $-25.5 \pm 0.8 \text{ kcal/mol}$, conf2: $-27.6 \pm 1.8 \text{ kcal/mol}$, conf3: $-23.1 \pm 1.0 \text{ kcal/mol}$, conf4: $-28.8 \pm 0.9 \text{ kcal/mol}$). The simulation of conformation 4 placed the 7-methyl group in very close proximity to the heme iron of CYP2A6 (Figure 2F). The distance was clearly shorter than the distance between the heme iron and position 7 in 6-methylcoumarin (6-methylcoumarin: $3.8 \pm 0.2 \text{ \AA}$; 7-methylcoumarin $2.7 \pm 0.2 \text{ \AA}$). Furthermore, iron, methyl and oxygen at the binding cavity could not orientate similarly as in the CYP2A6 - 6-methylcoumarin complex and accordingly, the reaction coordinate differ from those with coumarin and 6-methylcoumarin. In contrast, although the 7-methyl was closest to the heme iron also in CYP2A5 (the most stable and energetically preferred conformation), the distance and orientation were similar to that of position 7 in 6-methylcoumarin (Figure 2F). It

was also notable that 7-methyl ended up in close proximity to iron from three starting conformations.

The results of different reaction coordinates of 7-methylcoumarin in human CYP2A6 and mouse CYP2A5 indicated that the effect and reaction mechanism could be different in these two orthologs. For example, in the case of CYP2A6 the close proximity of methyl to iron could permit the ligand to take another tautomer, i.e. 7-methylene-7H-chromen-2-ol, which again could interact favorably with iron via its pi-electrons or react with its environment through some currently unknown mechanism. In CYP2A5 the predominant reaction would likely be hydroxylation of the 7-methyl group. Furthermore, from the three starting conformations of 7-methylcoumarin with CYP2A6, the ligand would be predicted to adopt the conformation where position C5 (or C5 and C4) would be closest to iron, suggesting that the hydroxylation of those positions is also possible. In addition to 7-methyl, for CYP2A5 a relatively stable binding conformation was obtained from starting conformation 1, where C3 was closest to iron, followed by C4 or carbonyl oxygen atom. Accordingly, this suggests that also positions C3 and C4 could be hydroxylated by CYP2A5.

In CYP2A5, the predominant reaction of 7-methylcoumarin would likely be hydroxylation of 7-methyl group. On the energetically favored conformation 2 (conf1: -23.1 ± 1.3 , conf2: -29.7 ± 1.4 , conf3: -25.8 ± 2.3 , conf4: -27.6 ± 0.5 kcal/mol), the 7-methyl group is oriented to close proximity of the heme iron already during minimization, and the new conformation is maintained throughout the simulation. In addition, the 7-methyl group is maintained on the same position in conformation 4 as in conformation 2, and conformation 3 adopts similar coordinates at the end of the simulation. The great conformational change of conformation 3 is the CYP2A5 active site decreases the average estimated binding energy from $-24.1 \pm$ kcal/mol to 28.4 ± 0.9 kcal/mol. 7-methyl hydroxylation is clearly preferred for 7-methylcoumarin since the 7-methyl group is the most favored position at the proximity of the heme iron, and the corresponding conformations are also energetically favored. In addition to 7-methyl hydroxylation, positions C3 and C4 could also be hydroxylated by CYP2A5 based on the simulation of conformation 1. Although the binding energy of conformation 1 is low due to lack of hydrogen bond between 7-methylcoumarin and Asn297 residue, positions C3 and C4 stay close to the heme iron within the simulation.

For 7-formylcoumarin, three major results were obtained (Table 2): (1) 7-methylcoumarin was a more potent inhibitor than 7-formylcoumarin in all three species indicating that presence of aldehyde group decreased inhibitory potency. (2) The 7-formylcoumarin IC₅₀ value was decreased when preincubated with NADPH and hepatic microsomes from all species. However, the preincubation did not affect the IC₅₀ value of 7-formylcoumarin with recombinant CYP2A6. (3) The effect of preincubation of 7-methylcoumarin on IC₅₀ values differed between species, as IC₅₀ was decreased to 10 % in mouse, 20 % in human and 50 % in pig liver microsomes during the preincubation. The decrease of IC₅₀-value in response to preincubation suggested that 7-formylcoumarin was a mechanism-based inhibitor for coumarin 7-hydroxylation in human, mouse and pig liver microsomes.

7-formylcoumarin was docked to achieve four different starting conformations for MD simulation and MMGBSA analysis (Fig 2G). The binding energy estimations between different starting conformations varied clearly less than the standard deviations; thus, the exact binding conformation for 7-formylcoumarin cannot be predicted from these simple binding energy estimations (CYP2A6/CYP2A5: conf1: $-24.8 \pm 1.2/-24.5 \pm 1.5$ kcal/mol, conf2: $-27.6 \pm 1.8/-24.2 \pm 2.1$ kcal/ml, conf3: $-26.5 \pm 1.6/-27.9 \pm 1.6$ kcal/mol, conf4: $-28.4 \pm 2.7/-25.9 \pm 1.6$ kcal/mol). However, similarly as the 7-methyl group in 7-methylcoumarin with CYP2A6, the formyl group of 7-formylcoumarin orients itself in close proximity to heme iron at the end of the MD simulation from starting conformation 2 (average distance between 2.0-2.4 ns: 3.5 ± 0.2 Å; Figure 2H).

Oxidation of 7-methylcoumarin. 7-methylcoumarin metabolites were characterized based on the m/z values of their protonated molecules and on their MS/MS fragmentation (Table 4.). Authentic standards were not available for the metabolites, and thus 7-methylcoumarin and 7-methyl-6-hydroxycoumarin was used for comparison. 7-methylcoumarin was oxidized most efficiently by pig liver microsomes followed by human, mouse and rat. A concentration of 10 μM 7-methylcoumarin took less than 5 min to decrease the activity by 50 % in pig liver microsomes, 5 min in human and 20 min in mouse but longer than 120 min in rat liver microsomes when 0.8 mg/ml protein was used in 100 mM phosphate buffer containing a NADPH regenerating system. Four different metabolites (1-4) were detected from the incubations with mouse and pig liver microsomes, but metabolite 3 was not formed in human and rat liver microsomes (Fig. 4, Table 4). Metabolites 1 and 3 and 7-methyl-6-hydroxylcoumarin indicated a typical loss of CO₂ from the protonated molecule.

Ions of m/z 105 and 121 of metabolites 1 and 3 are typical hydroxyl metabolites of coumarins (Concannon et al. 2000). Metabolite 1 indicated m/z ions 147 and 157 explained by the loss of formaldehyde from the side chain and water, respectively (Morreel et al. 2010). It was the most abundant according to the peak area. Metabolite 2 peak area accounted for 60 % of the total whereas metabolite 4 amounted 5 % (Fig. 4A). If GSH was present in the incubation, three different glutathione conjugates were formed (Fig. 4B). The presence of the antibody against CYP2A5 completely abolished metabolite 4 formation in microsomes from all species and metabolite 2 formation in human microsomes and recombinant CYP2A6 (Fig. 4C). Furthermore the antibody partially inhibited metabolite 1 formation. Anti-CYP2A5 antibody increased the formation of glutathione conjugation in incubations containing microsomes.

Discussion

This study adds novel information to the earlier CYP2A structure-activity relationship studies. 6-Methylcoumarin was a high affinity substrate for human CYP2A6 and mouse CYP2A5, and it was oxidized to the fluorescent 7-hydroxy-6-methylcoumarin via these CYPs. This reaction was catalyzed also by pig CYP2A19. In silico analyses confirmed that 6-methylcoumarin could be efficiently 7-hydroxylated by both CYP2A6 and 2A5. However, the exact orientation of 7-methylcoumarin differed between the CYP2A6 and CYP2A5 active sites. 7-Methylcoumarin was oxidized to 3 - 4 metabolites by human, mouse, pig and rat liver microsomes. It appeared to be a mechanism-based inhibitor for human CYP2A6, but not for the mouse and pig CYP2A enzymes. The MD simulations found evidence that this could be due to the different orientations of 7-methylcoumarin in the active sites of these enzymes. In contrast, 7-formylcoumarin was a mechanism-based inhibitor of all of the studied enzymes.

6-Methylcoumarin, 7-methylcoumarin and 7-formylcoumarin are novel ligands for CYP2A6, expanding the list of known ligands such as lactones (Juvonen et al. 2000) and derivatives of naphthalene, quinolone (Rahnasto et al. 2005), benzothiophene, thienopyridine, benzofuran (Rahnasto et al. 2011, Tani et al. 2014) indole and nicotine type compounds (Yano et al. 2006, Raunio, Rahnasto-Rilla 2012). The docking and MD simulations confirmed that the 7-carbon of 6-methylcoumarin was oriented toward the heme moiety and there was sufficient space for oxygen to coordinate to heme iron in the CYP2A6 active site. The orientations of carbons 3, 4,

5 or 6 in the coumarin ring towards heme were less stable than those of the 6-methyl and 7-carbon. The 6-methyl substitution did not change the affinity i.e. K_m values of coumarin and 6-methylcoumarin in their 7-hydroxylation reactions by CYP2A6 were equivalent (Soucek 1999). Therefore there is space for the 6-methyl substitution in its active site, which agrees with the data obtained when CYP2A6 has been co-crystallized with coumarin (Yano et al. 2005) and is observed in the present docking models. The orientation of 7-methylcoumarin in the active site of CYP2A6 differed from that of 6-methylcoumarin, as the 7-methyl group was localized closer to iron in heme than the 7-carbon of 6-methylcoumarin.

Interestingly, 7-methylcoumarin proved to be a mechanism-based inhibitor for CYP2A6; this may be due to its peculiar orientation in the enzyme active site. 7-Methylcoumarin was transformed to at least two metabolites, 7-hydroxymethylcoumarin and its own tautomer 7-methylene-7H-chromene-2-ol. The tautomer is reactive and could be a candidate reactive metabolite causing the observed mechanism-based inhibition of CYP2A6. The formation of this metabolite was completely inhibited in human liver microsomes by the antibody against CYP2A5, only partially in pig and not at all in mouse liver microsomes, indicating that CYP2A6 is the major catalyzing enzyme in human, but CYP2A19 and CYP2A5 do not catalyze its formation in pig and mouse. Another possibility could be that the orientation of 7-methylcoumarin in the active site CYP2A6 enabled oxidation to produce an epoxide in the lactone ring with subsequent inactivation of the enzyme. In the rat coumarin is not oxidized to 7-hydroxycoumarin but instead to the reactive and toxic 3, 4-epoxide coumarin, i.e. there is oxidation in the lactone structure (Lake et al. 1989, Born et al. 2000). 7-Formylcoumarin was also a mechanism-based inhibitor for CYP2A6 due to its aldehyde character (Raner et al. 1997, Rahnasto et al. 2003). Therefore the 7-formyl group must be oriented toward the heme of CYP2A6, which was also deduced in the *in silico* analyses.

The 7-hydroxylation activity of 6-methylcoumarin could be measured conveniently in a multi-well plate set up, as the metabolite 7-hydroxy-6-methylcoumarin had distinctive fluorescence properties. This activity varied in hepatic microsomes between the studied species. Human microsomes had the highest reaction rate followed by pig and mouse, finally the rate in rat microsomes was only 0.2 % of the human rate. This resembled the rates of coumarin 7-hydroxylation in these species (Kaipainen, Koivusaari & Lang 1985). The hepatic CYP2A enzyme expression

patterns explain this difference, as CYP2A6 is expressed in human liver, CYP2A5 in mouse and CYP2A19 in pig liver, whereas CYP2A3 is not expressed in rat liver (Skaanild 2006). However, this study indicated that there is another CYP enzyme present in pig liver which possesses significant catalytic activity for this reaction, as the anti-CYP2A5 antibody and chemical CYP2A inhibitors inhibited only partially the hydroxylation reaction. We did not determine if 6-methylcoumarin was oxidized to other metabolites by these microsomes.

There were also species differences in the oxidation of 7-methylcoumarin, as in pig and mouse it was oxidized to four metabolites whereas in human and rat only three metabolites could be detected and furthermore the formation rate of these metabolites varied between the species. In pig and human microsomes, 7-methylcoumarin was oxidized faster than in mouse and rat microsomes. In addition, 7-methylcoumarin inhibited human CYP2A6 differently from mouse CYP2A5 and pig CYP2A19. It proved to be a mechanism-based inhibitor in human but not in mouse and pig liver microsomes. This reveals that the orientation of 7-methylcoumarin in the active site of CYP2A6 is different from its orientation in CYP2A5 and CYP2A19. However, there were no species differences observed in the ways that 7-formylcoumarin inhibited coumarin 7-hydroxylation.

Conclusions

6-Methylcoumarin and 7-methylcoumarin are novel substrates for human CYP2A6 and its homologous enzymes, mouse CYP2A5 and pig CYP2A19. 6-Methylcoumarin was oxidized to a fluorescent metabolite, 7-hydroxy-6-methylcoumarin, which could be conveniently measured with a fluorometer. 6-Methylcoumarin is comparable to coumarin as a substrate for CYP2A substrate. The orientation of 6-methylcoumarin is similar in the active sites of CYP2A6, CYP2A5 and CYP2A19 enzymes. Since 7-methylcoumarin is a mechanism-based inhibitor for CYP2A6 but not for CYP2A5 and CYP2A19, its orientation in the active site of CYP2A6 differed from that in CYP2A5 and CYP2A19. 6-Methylcoumarin and 7-methylcoumarin were oxidized efficiently by liver microsomes from humans, pigs and mice but very poorly by rat liver microsomes. These results indicate that the position of the methyl substitution profoundly affects the properties of these coumarin derivatives as CYP2A ligands.

Acknowledgements

We thank Mrs Hannele Jaatinen for her laboratory expertise. CSC - IT Center for Science is acknowledged for generous computational resources (OTP; project Nos. jyy2516 and jyy2585).

Declaration of Interest

This study was supported by Academy of Finland project number 137589. The authors report no declarations of interest.

References

- Bogaards, J.J.P., Bertrand, M., Jackson, P., Oudshoorn, M.J., Weaver, R.J., Van Bladeren, P.J. & Walther, B. 2000, "Determining the best animal model for human cytochrome P450 activities: A comparison of mouse, rat, rabbit, dog, micropig, monkey and man", *Xenobiotica*, vol. 30, no. 12, pp. 1131-1152.
- Born, S.L., Caudill, D., Smith, B.J. & Lehman-McKeeman, L.D. 2000, "In vitro kinetics of coumarin 3,4-epoxidation: Application to species differences in toxicity and carcinogenicity", *Toxicological Sciences*, vol. 58, no. 1, pp. 23-31.
- Concannon S., Ramachandran V.N. & Smyth W.F. 2000, "A study of the electrospray ionization of selected coumarin derivatives and their subsequent fragmentation using an ion trap mass spectrometer", *Rapid Communication of Mass Spectrometry*, vol. 14, no. 14, pp. 1157- 1166.
- Cruciani, G. 2013, "Metabolites: Structure determination and prediction", *Drug Discovery Today: Technologies*, vol. 10, no. 1, pp. e145-e146.
- Dalgaard, L. 2015, "Comparison of minipig, dog, monkey and human drug metabolism and disposition", *Journal of pharmacological and toxicological methods*, <http://dx.doi.org/10.1016/j.vascn.2014.12.005>.
- DeLisle, R.K., Otten, J. & Rhodes, S. 2011, "In silico modeling of P450 substrates, inhibitors, activators, and inducers", *Combinatorial Chemistry and High Throughput Screening*, vol. 14, no. 5, pp. 396-416.
- Foti, R.S., Wienkers, L.C. & Wahlstrom, J.L. 2010, "Application of cytochrome P450 drug interaction screening in drug discovery", *Combinatorial Chemistry and High Throughput Screening*, vol. 13, no. 2, pp. 145-158.
- Giammona D.A. 1984, Ph.D. thesis, University of California, Davis
- Gohlke, H. & Case, D.A. 2004, "Converging Free Energy Estimates: MM-PB(GB)SA Studies on the Protein-Protein Complex Ras-Raf", *Journal of Computational Chemistry*, vol. 25, no. 2, pp. 238-250.

- Hou, T., Wang, J., Li, Y. & Wang, W. 2011, "Assessing the performance of the MM/PBSA and MM/GBSA methods. 1. The accuracy of binding free energy calculations based on molecular dynamics simulations", *Journal of Chemical Information and Modeling*, vol. 51, no. 1, pp. 69-82.
- Johnson, M.S, Overington, J. 1993, "A structural basis for sequence comparisons. An evaluation of scoring methodologies", *Journal of Molecular Biology*, vol 233, no. 4, pp. 716-738.
- Juvonen, R.O., Gynther, J., Pasanen, M., Alhava, E. & Poso, A. 2000, "Pronounced differences in inhibition potency of lactone and non-lactone compounds for mouse and human coumarin 7-hydroxylases (CYP2A5 and CYP2A6)", *Xenobiotica*, vol. 30, no. 1, pp. 81-92.
- Kaipainen, P., Koivusaari, U. & Lang, M. 1985, "Catalytic and immunological comparison of coumarin 7-hydroxylation in different species", *Comparative Biochemistry and Physiology. Part C, Comparative*, vol. 81, no. 2, pp. 293-296.
- Kirchmair, J., Williamson, M.J., Tyzack, J.D., Tan, L., Bond, P.J., Bender, A. & Glen, R.C. 2012, "Computational prediction of metabolism: Sites, products, SAR, P450 enzyme dynamics, and mechanisms", *Journal of Chemical Information and Modeling*, vol. 52, no. 3, pp. 617-648.
- Korb, O., Stützel, T. & Exner, T.E. 2009, "Empirical scoring functions for advanced Protein-Ligand docking with PLANTS", *Journal of Chemical Information and Modeling*, vol. 49, no. 1, pp. 84-96.
- Lake, B.G., Gray, T.J.B., Evans, J.G., Lewis, D.F.V., Beamand, J.A. & Hue, K.L. 1989, "Studies on the mechanism of coumarin-induced toxicity in rat hepatocytes: Comparison with dihydrocoumarin and other coumarin metabolites", *Toxicology and applied pharmacology*, vol. 97, no. 2, pp. 311-323.
- Lang, M.A., Gielen, J.E. & Nebert, D.W. 1981, "Genetic evidence for many unique liver microsomal P-450-mediated monooxygenase activities in heterogeneic stock mice", *Journal of Biological Chemistry*, vol. 256, no. 23, pp. 12068-12075.
- Lehtonen, J.V., Still, D.-., Rantanen, V.-., Ekholm, J., Björklund, D., Iftikhar, Z., Huhtala, M., Repo, S., Jussila, A., Jaakkola, J., Pentikäinen, O., Nyrönen, T., Salminen, T., Gyllenberg, M. & Johnson, M.S. 2004, "BODIL: A molecular modeling environment for structure-function analysis and drug design", *Journal of computer-aided molecular design*, vol. 18, no. 6, pp. 401-419.
- Long, A. 2013, "Drug metabolism in silico-the knowledge-based expert system approach. Historical perspectives and current strategies", *Drug Discovery Today: Technologies*, vol. 10, no. 1, pp. e147-e153.
- Makaji, E., Trambitas, C.S., Shen, P., Holloway, A.C. & Crankshaw, D.J. 2009, "Effects of cytochrome P450 inhibitors on the biotransformation of fluorogenic substrates by adult male rat liver microsomes and cDNA-expressed rat

- cytochrome P450 isoforms", *Toxicological Sciences*, vol. 113, no. 2, pp. 293-304.
- Miller III, B.R., McGee, T.D., Swails, J.M., Homeyer, N., Gohlke, H. & Roitberg, A.E. 2012, "MMPBSA.py: An efficient program for end-state free energy calculations", *Journal of Chemical Theory and Computation*, vol. 8, no. 9, pp. 3314-3321.
- Morreel K., Kim H., Lu F., Dima O., Akiyama T., vanholme R. Niculaes C. Goeminne G., Inze D. Messens E., Ralph J. & Boerjan W. 2010, "Mass spectrometry-based fragmentation as an identification tool in lignomics", *Analytical Chemistry* vol. 89, no. 19, pp. 8095-8105.
- Niinivehmas, S.P., Virtanen, S.I., Lehtonen, J.V., Postila, P.A. & Pentikäinen, O.T. 2011, "Comparison of virtual high-throughput screening methods for the identification of phosphodiesterase-5 inhibitors", *Journal of Chemical Information and Modeling*, vol. 51, no. 6, pp. 1353-1363.
- Onufriev, A., Bashford, D. & Case, D.A. 2004, "Exploring Protein Native States and Large-Scale Conformational Changes with a Modified Generalized Born Model", *Proteins: Structure, Function and Genetics*, vol. 55, no. 2, pp. 383-394.
- Pelkonen, O., Rautio, A., Raunio, H. & Pasanen, M. 2000, "CYP2A6: A human coumarin 7-hydroxylase", *Toxicology*, vol. 144, no. 1-3, pp. 139-147.
- Rahnasto, M., Raunio, H., Poso, A. & Juvonen, R.O. 2003, "More potent inhibition of human CYP2A6 than mouse CYP2A5 enzyme activities by derivatives of phenylethylamine and benzaldehyde", *Xenobiotica*, vol. 33, no. 5, pp. 529-539.
- Rahnasto, M., Raunio, H., Poso, A., Wittekindt, C. & Juvonen, R.O. 2005, "Quantitative structure-activity relationship analysis of inhibitors of the nicotine metabolizing CYP2A6 enzyme", *Journal of medicinal chemistry*, vol. 48, no. 2, pp. 440-449.
- Rahnasto, M.K., Raunio, H.A., Wittekindt, C., Salminen, K.A., Leppänen, J., Juvonen, R.O., Poso, A. & Lahtela-Kakkonen, M.K. 2011, "Identification of novel CYP2A6 inhibitors by virtual screening", *Bioorganic and Medicinal Chemistry*, vol. 19, no. 23, pp. 7186-7193.
- Raner, G.M., Chiang, E.W., Vaz, A.D.N. & Coon, M.J. 1997, "Mechanism-based inactivation of cytochrome P450 2B4 by aldehydes: Relationship to aldehyde deformylation via a peroxyhemiacetal intermediate", *Biochemistry*, vol. 36, no. 16, pp. 4895-4902.
- Rastelli, G., Del Rio, A., Degliesposti, G. & Sgobba, M. 2010, "Fast and accurate predictions of binding free energies using MM-PBSA and MM-GBSA", *Journal of Computational Chemistry*, vol. 31, no. 4, pp. 797-810.
- Raunio, H., Juvonen, R., Pasanen, M., Pelkonen, O., Pääkkö, P. & Soini, Y. 1998, "Cytochrome P4502A6 (CYP2A6) expression in human hepatocellular carcinoma", *Hepatology*, vol. 27, no. 2, pp. 427-432.

- Raunio, H. & Rahnasto-Rilla, M. 2012, "CYP2A6: Genetics, structure, regulation, and function", *Drug metabolism and drug interactions*, vol. 27, no. 2, pp. 73-88.
- Roe, D.R. & Cheatham, T.E. 2013, "PTRAJ and CPPTRAJ: Software for processing and analysis of molecular dynamics trajectory data", *Journal of Chemical Theory and Computation*, vol. 9, no. 7, pp. 3084-3095.
- Sali, A. & Blundell, T.L. 1993, "Comparative protein modelling by satisfaction of spatial restraints", *Journal of Molecular Biology*, vol. 234, no. 3, pp. 779-815.
- Sevior, D.K., Pelkonen, O. & Ahokas, J.T. 2012, "Hepatocytes: The powerhouse of biotransformation", *International Journal of Biochemistry and Cell Biology*, vol. 44, no. 2, pp. 257-261.
- Skaanild, M.T. 2006, "Porcine cytochrome P450 and metabolism", *Current pharmaceutical design*, vol. 12, no. 11, pp. 1421-1427.
- Soucek, P. 1999, "Expression of cytochrome P450 2A6 in Escherichia coli: Purification, spectral and catalytic characterization, and preparation of polyclonal antibodies", *Archives of Biochemistry and Biophysics*, vol. 370, no. 2, pp. 190-200.
- Stepan, A.F., Walker, D.P., Bauman, J., Price, D.A., Baillie, T.A., Kalgutkar, A.S. & Aleo, M.D. 2011, "Structural alert/reactive metabolite concept as applied in medicinal chemistry to mitigate the risk of idiosyncratic drug toxicity: A perspective based on the critical examination of trends in the top 200 drugs marketed in the United States", *Chemical research in toxicology*, vol. 24, no. 9, pp. 1345-1410.
- Tani, N., Juvonen, R.O., Raunio, H., Fashe, M., Leppänen, J., Zhao, B., Tyndale, R.F. & Rahnasto-Rilla, M. 2014, "Rational design of novel CYP2A6 inhibitors", *Bioorganic and Medicinal Chemistry*, vol. 22, no. 23, pp. 6655-6664.
- Testa, B., Pedretti, A. & Vistoli, G. 2012, "Reactions and enzymes in the metabolism of drugs and other xenobiotics", *Drug discovery today*, vol. 17, no. 11-12, pp. 549-560.
- Timonen J., Romppanen R., Aulaskari P. & Jänis J. 2013, " Low-energy collision-induced dissociation tandem mass spectrometry of 7-acetyloxycoumarins", *Rapid Communication of Mass Spectrometry*, vol. 27., no. 23, pp. 2665-2675.
- Tsui, V. & Case, D.A. 2000, "Theory and applications of the Generalized Born solvation model in macromolecular simulations", *Biopolymers*, vol. 56, no. 4, pp. 275-291.
- Turpeinen, M., Korhonen, L.E., Tolonen, A., Uusitalo, J., Juvonen, R., Raunio, H. & Pelkonen, O. 2006, "Cytochrome P450 (CYP) inhibition screening: Comparison of three tests", *European Journal of Pharmaceutical Sciences*, vol. 29, no. 2, pp. 130-138.

- Wang, J.M., Wang, W. & Kollman, P.A. 2001., "Antechamber: an accessory software package for molecular mechanical calculations. Abstracts of papers of the American Chemical Society, 222, U403.
- Word, J.M., Lovell, S.C., Richardson, J.S. & Richardson, D.C. 1999, "Asparagine and glutamine: Using hydrogen atom contacts in the choice of side-chain amide orientation", *Journal of Molecular Biology*, vol. 285, no. 4, pp. 1735-1747.
- Yano, J.K., Denton, T.T., Cerny, M.A., Zhang, X., Johnson, E.F. & Cashman, J.R. 2006, "Synthetic inhibitors of cytochrome P-450 2A6: Inhibitory activity, difference spectra, mechanism of inhibition, and protein cocrystallization", *Journal of medicinal chemistry*, vol. 49, no. 24, pp. 6987-7001.
- Yano, J.K., Hsu, M.-., Griffin, K.J., Stout, C.D. & Johnson, E.F. 2005, "Structures of human microsomal cytochrome P450 2A6 complexed with coumarin and methoxsalen", *Nature Structural and Molecular Biology*, vol. 12, no. 9, pp. 822-823.
- Ylilauri, M. & Pentikäinen, O.T. 2013, "MMGBSA as a tool to understand the binding affinities of filamin-peptide interactions", *Journal of Chemical Information and Modeling*, vol. 53, no. 10, pp. 2626-2633.
- Ylilauri, M. & Pentikäinen, O.T. 2012, "Structural Mechanism of N-Methyl-D-Aspartate Receptor Type 1 Partial Agonism", *PLoS ONE*, vol. 7, no. 10.
- Zanger, U.M. & Schwab, M. 2013, "Cytochrome P450 enzymes in drug metabolism: Regulation of gene expression, enzyme activities, and impact of genetic variation", *Pharmacology and Therapeutics*, vol. 138, no. 1, pp. 103-141.

Tables and table legends

Table 1. Kinetics of 7-hydroxylation of 6-methylcoumarin.

	Km for 6-methylcoumarin [μM]	Vmax [nmol/(min * g)]	Vmax/Km [mL/(min * g prot)]
Human	0.21 (0.15-0.27)	59 (56-62)	280
CYP2A6	0.78 (0.64-0.91)	0.85 (0.81-0.88)	1,1
Mouse control	0.26 (0.17-0.35)	18 (17-19)	69
Pig	4.4 (3.1-5.6)	29 (26-32)	6,6
	6.2 (4.5-7.9)	38 (33-42)	6,1

Table 2. IC₅₀ values of 7-methylcoumarin and 7-formylcoumarin for human, mouse, pig and recombinant CYP2A6 coumarin 7-hydroxylation. Liver microsomal coumarin 7-hydroxylation was inhibited by increasing concentrations of both compounds without (NO) and with inhibitor (Yes) after 30 min preincubation.

		IC ₅₀ (95 % confidence interval)[μM]			
7-x coumarin	Preincubation	Human	Pig	Mouse	CYP2A6
7-Methylcoumarin	NO	20 (15 – 25)	8.4 (6.5 -10.3)	6.9 (4.9 – 8.9)	18 (11-26)
7-Methylcoumarin	Yes	3.5 (2.8 - 4.3)	20 (12 – 28)	35 (9 – 62)	2.0 (1.7 – 2.2)
7 - Formylcoumarin	NO	180 (67 - 280)	170 (29 – 300)	550 (0 – 2300)	25 (17 - 37)
7 - Formylcoumarin	Yes	39 (19 – 59)	89 (25 – 150)	56 (14 -98)	25 (19 – 30)

Table 3. K_i and k_{inact} values of 7-methylcoumarin for human coumarin 7-hydroxylation.

	K _i [μM]	k _{inact} [1/min]
Human liver microsomes	14 (0 – 29)	0.149 (0.082 – 0.211)
Recombinant CYP2A6	4.5 (0 – 11)	0.091 (0.053 – 0.129)

Table 4. Metabolites of oxidized 7-methylcoumarin.

Compound	m/z	MS/MS fragments	Tentative structure
7-Methylcoumarin	161	115, 117 (-CO ₂)	
7-(hydroxy)-6-methylcoumarin	177	105, 121, 133 (-CO ₂), 157	
Metabolite 1	177	105, 133 (-CO ₂), 147 (-H ₂ CO), 157, 159 (-H ₂ O)	7-(hydroxymethyl)-coumarin
Metabolite 2	161	141, 150	7-methylene-7H-chromen-2-ol
Metabolite 3	177	105, 121, 133 (-CO ₂), 150, 157	x-hydroxyl-7-methylcoumarin
Metabolite 4	179	158, 166	3- or 4-hydroxy-7-methylchroman-2-one

Figures and figure legends

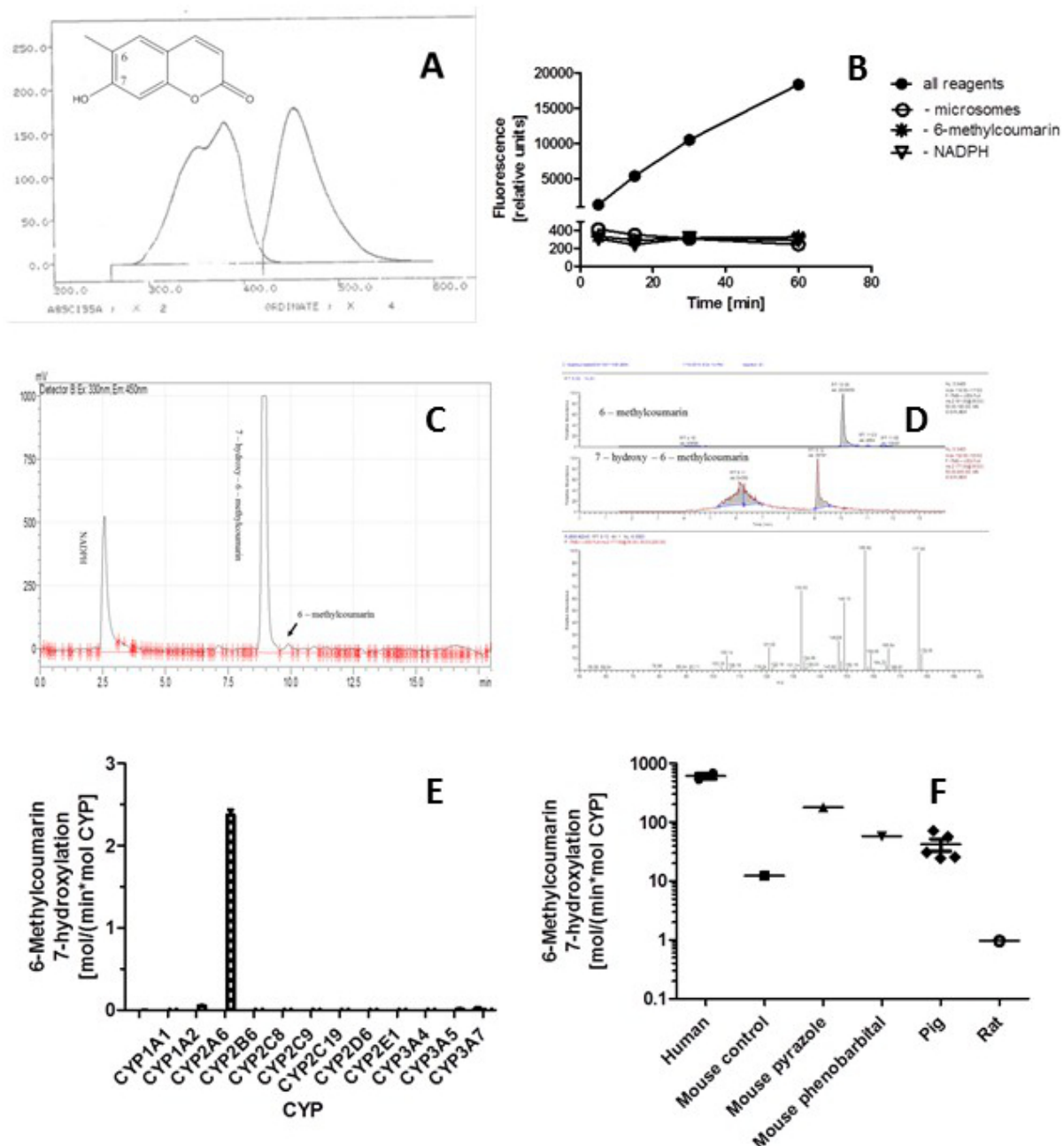


Figure 1. Formation of the fluorescent metabolite, 7-hydroxy-6-methylcoumarin. Panel A shows the emission and excitation spectra of 7-hydroxy-6-methylcoumarin. Fluorescence increased when the reaction mixture contained hepatic microsomes, NADPH and 6-methylcoumarin, but no fluorescence was formed if one of these components was missing (panel B). Panel C shows an HPLC chromatogram obtained with ex 330 nm and em 450 nm; panel D is a chromatogram and MS spectrum from a 60-min incubation with all reagents. Panel E shows the

hydroxylation rate of 6-methylcoumarin in recombinant human CYPs and panel F illustrates the rate in different species.

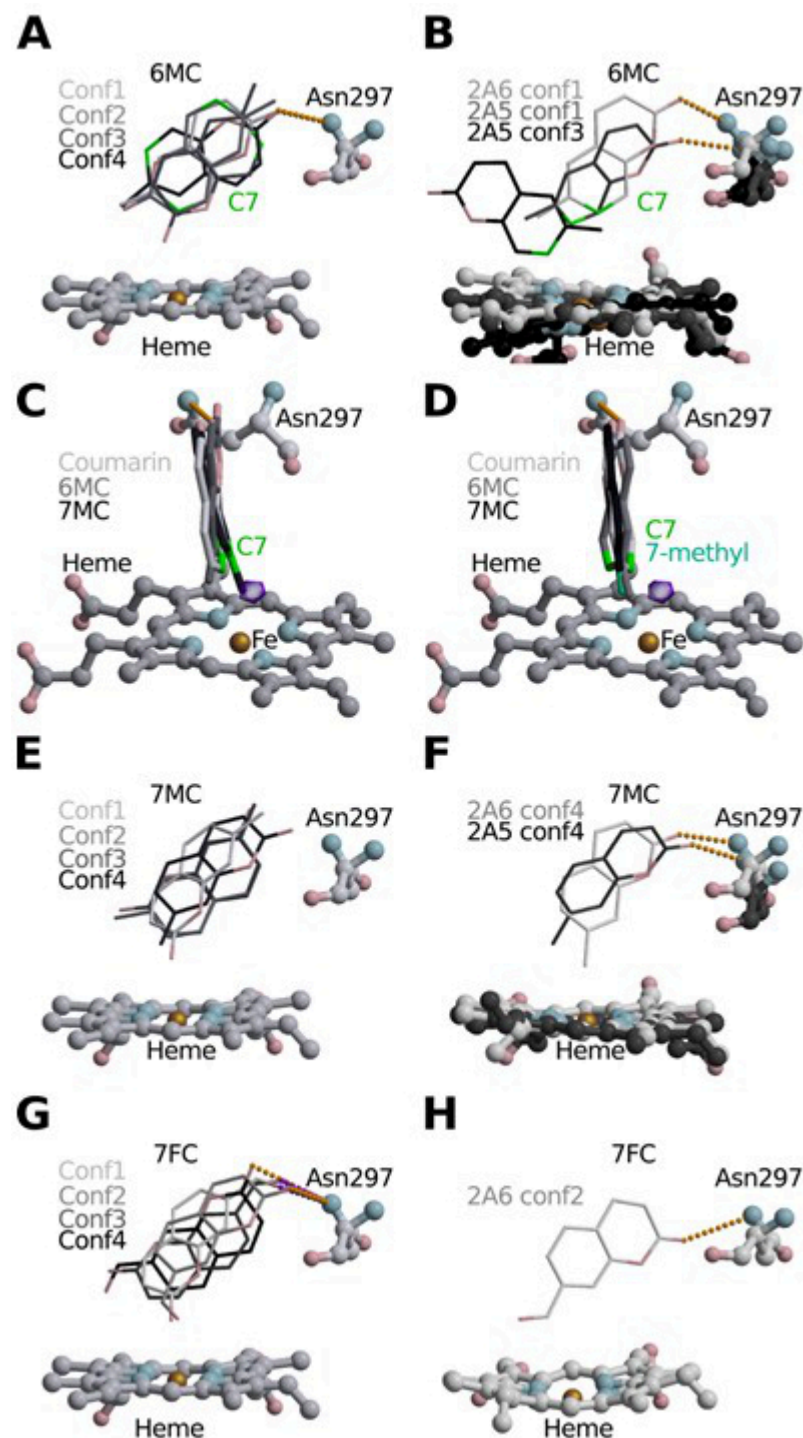


Figure 2. Binding of 6-methylcoumarin (6MC), 7-methylcoumarin (7MC), and 7-formylcoumarin (7FC) within CYP2A6 and CYP2A5 based on docking and molecular dynamics simulations. Panels (A), (E), and (G) show the four starting conformations for MD simulations for 6MC, 7MC, and 7FC, respectively. These conformations 1-4 were obtained with molecular docking, and are distinguished by different coloring of

carbon atoms. Panels (B), (F), and (H) show the most stable and energetically preferred conformations for 6MC, 7MC, and 7FC, respectively, again separated with different coloring of carbon atoms. In panels (C) and (D) electron density of the CYP2A6 – coumarin crystal structure ($|F_0| - |F_c|$ 0.11 e/Å³, deep purple surface) in the vicinity of iron (orange sphere) and C7 of coumarin (green), which could be occupied by an oxygen needed for the oxidation reaction. With CYP2A6, oxygen could be located in the exactly same same position with bound 6-methylcoumarin (C) (medium gray carbon atoms and green C7) but not with 7-methylcoumari (darkest gray carbon atoms). With CYP2A6 both 6- and 7-methylcoumarin can accommodate the oxygen (D). The likely oxidation position (C7) of 6MC is highlighted in green (A, B) and is always the closest atom to iron (shown as an orange sphere) in heme with the most stable and energetically preferred conformations. The most stable and energetically preferred conformations of 7MC have the 7-methyl group closest to iron (E, F). The binding energy estimations of 7FC cannot be used in the selection of the most likely conformation (G, H), however, from starting conformation 2 (G) the distance to iron is optimized for catalytic activity (H). Hydrogen bonds between Asn297 and ligands are shown in orange (carbonyl oxygen atom at coumarin-part at all ligands) and purple (aldehyde of 7FC) dotted line, when formed.

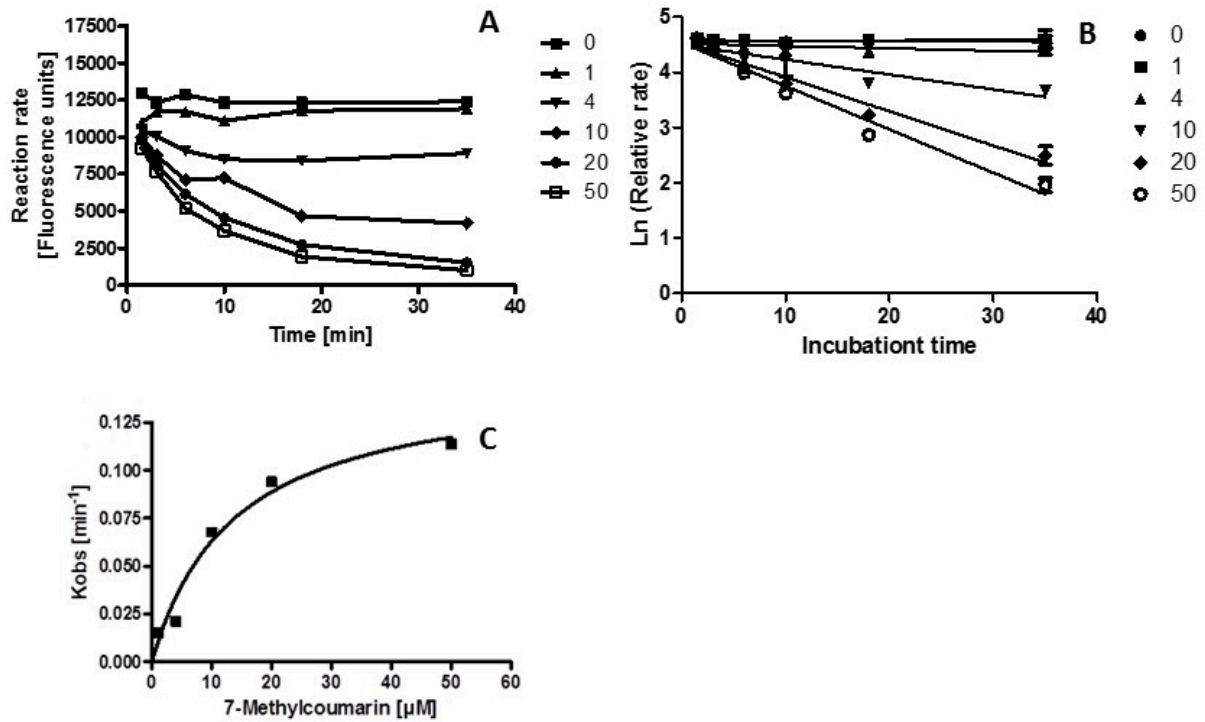


Figure 3. Time and concentration dependent inhibition of human coumarin 7-hydroxylation by 7-methylcoumarin. Different 7-methylcoumarin concentrations (0 – 50) were first incubated for various times with human liver microsomes and NADPH in 100 mM Tris-HCl pH 7.4, from which 5 μl samples were taken into 100 μl 100 mM Tris-HCl pH 7.4 containing 100 μM coumarin to determine coumarin 7-hydroxylation activity. Panel A shows the decrease in the fluorescence of 7-hydroxycoumarin at the indicated 7-methylcoumarin concentrations, panel B shows the relative activities derived from the data of panel A and panel C the dependency of inactivation rate of coumarin 7-hydroxylation (k_{obs} -values) at every 7-methylcoumarin concentration derived from the panel B.

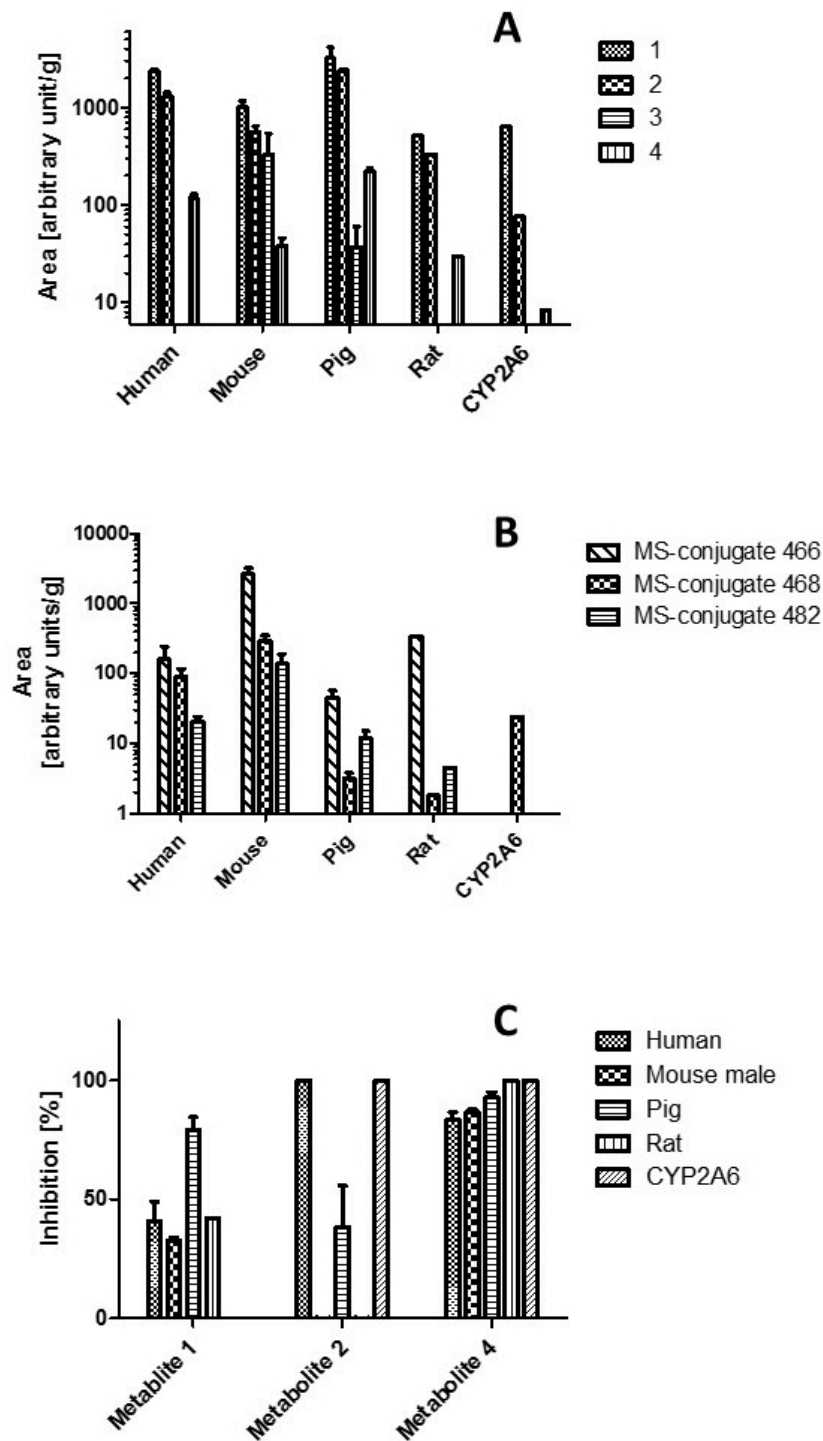


Figure 4. Metabolism of 7-methylcoumarin in different species. Ten μM 7-methylcoumarin was incubated for 60 min at 37°C in 100 mM Tris-HCl buffer pH 7.4 containing microsomes and a NADPH regenerating system. The reaction was stopped by addition of methanol and the supernatant analyzed by HPLC/MS (A). Numbers 1 – 4 refer to metabolites 1 - 4. In panel B, the samples contained 2 mM glutathione and were incubated for 30 min. Panel C shows the inhibition of metabolism after inclusion of anti-CYP2A5 antibody into the mixture.



II

SUITABILITY OF MMGBSA FOR THE SELECTION OF CORRECT LIGAND BINDING MODES FROM DOCKING RESULTS

by

Ahinko M.*, Niinivehmas S.*, Jokinen E. & Pentikäinen O.T., 2019
* Equal contribution

Chemical Biology & Drug Design 93: 522–538

DOI 10.1111/cbdd.13446

Reproduced with kind permission by John Wiley and Sons.

Article type : Research Article

Suitability of MMGBSA for the Selection of Correct Ligand Binding Modes from Docking Results

Mira Ahinko^{1‡}, Sanna Niinivehmas^{1,2‡}, Elmeri Jokinen², Olli T. Pentikäinen^{1,2*}

¹ University of Jyväskylä, MedChem.fi, Department of Biological and Environmental Science & Nanoscience Center, University of Jyväskylä, P.O. Box 35, FI-40014 University of Jyväskylä, Finland

² University of Turku, MedChem.fi, Institute of Biomedicine, Integrative Physiology and Pharmacology, Kiinamyllynkatu 10, Medisiina C6, FI-20520 Turku, Finland

* Corresponding author: e-mail: olli.pentikainen@utu.fi; ‡ Equal contribution

The estimation of the correct binding mode and affinity of a ligand into a target protein using computational methods is challenging. However, docking can introduce poses from which the correct binding mode could be identified using other methods. Here, we analyzed the reliability of binding energy estimation using the molecular mechanics-generalized Born surface area (MMGBSA) method without and with energy minimization to identify the likely ligand binding modes within docking results. MMGBSA workflow (1) outperformed docking in recognizing the correct binding modes of androgen receptor ligands and (2) improved the correlation coefficient of computational and experimental results of rescored docking poses to phosphodiesterase 4B. Combined with stability and atomic distance analysis, MMGBSA helped to (3) identify the binding modes and sites of metabolism of cytochrome P450 2A6 substrates. The standard deviation of estimated binding energy within one simulation was lowered by minimization in all three example cases. Minimization improved the identification of the correct binding modes of androgen receptor ligands. Although only three case studies are shown, the results are analogous and indicate that these behaviors could be generalized. Such identified binding modes could be further used, for example, with free energy perturbation methods to understand binding energetics more accurately.

Introduction

Being able to accurately calculate differences in the binding free energies of protein–ligand and protein–protein interactions is essential in applications related to drug discovery [1,2]. A wide variety of methods have been developed to rank ligands based on their binding affinities. Molecular docking algorithms are the least computationally demanding but lack accuracy in the approximation of ligand binding affinity [3–9]. Methods based on molecular dynamics (MD) or Monte Carlo simulations consume more computational resources, with the aim of producing rigorous estimations of binding

This article has been accepted for publication and undergone full peer review but has not been through the copyediting, typesetting, pagination and proofreading process, which may lead to differences between this version and the Version of Record. Please cite this article as doi:

10.1111/cbdd.13446

This article is protected by copyright. All rights reserved.

free energies. In principle, the most accurate predictions are generated by the alchemical free energy methods, such as free energy perturbation (FEP), which require intensive computational effort due to the sampling of unphysical intermediate states between the initial and final state of the system [10]. A less time-consuming MD-based option is offered by the molecular mechanics generalized Born or Poisson–Boltzmann surface area (MMGBSA or MMPBSA) methods that analyze only the free and bound states of the system [11].

The MMGBSA/MMPBSA methods have been widely used in the identification of active ligands and their affinities and binding modes [12]. With MMGBSA, protein–ligand and protein–protein interaction energies can be estimated relatively quickly when compared with alchemical free energy methods. Several studies have shown that MMGBSA generally outperforms the scoring functions of docking algorithms in terms of accuracy in ranking ligands by their binding affinity [13,14]. Reported correlations between experimental and MMGBSA-derived binding affinities range from excellent to poor, indicating that the performance of MMGBSA/MMPBSA methods is highly case-specific [15–18]. Because of this variance, the careful selection of essential parameters—such as the length of the MD simulation, dielectric constants, and whether to include or exclude the entropy term—has been advised, as such parameters can greatly influence the precision of the method [19]. Significant correlations between experimental and computational binding free energies have been obtained both by averaging the binding free energy over multiple protein–ligand complexes derived from MD simulation snapshots and by running an MMGBSA analysis on a single minimized snapshot [13,14,20,21]. Still, FEP has been shown to be generally more capable of identifying active ligands and their correct binding modes than MMGBSA, making it the preferable method for the final binding free energy estimation [22]. In general, MMGBSA method enables rapid estimation of binding affinity but only with the cost of crude approximations. Especially the lack of conformational entropy and free energy of solvent binding cause significant standard error of estimation, which again limits the applicability of the method in drug discovery [12].

The difficulty of adequately sampling the relevant ligand binding modes has traditionally been one of the major limitations of FEP and other alchemical free energy methods [23]. Especially in cases of multiple possible binding modes, this inability may cause a substantial decrease in the precision of the free energy calculation [24,25]. Generally, considering different ligand binding modes requires the utilization of multiple calculations, which significantly increases the computational cost of the protocol. This has constrained the use of alchemical free energy methods in many applications, such as virtual screening, where computational efficiency is one of the main priorities [26]. The problem has been addressed by utilizing methods, such as replica exchange with solute tempering (REST) and accelerated MD, that aim to enable consideration of multiple ligand binding modes during a single calculation by lowering the energetic barriers between them [27–33]. Another possible way to tackle the issue is to decrease the number of necessary calculations by identifying the biologically relevant binding modes with computationally less demanding methods prior to using the free energy methods. The reported good performance of MMGBSA indicates the usefulness of this method in filtering irrelevant ligand binding modes to facilitate the completion of the computationally more intensive alchemical free energy analysis.

Here, we have used MD simulations together with MMGBSA analysis to rescore docking results. Specifically, we have studied the stability of both formed complexes and binding energies using MD simulation snapshots without and with energy minimization. Three protein targets that we have studied also previously [15,34–37]—cytochrome P450 type 2A6 (CYP2A6), androgen receptor (AR), and phosphodiesterase 4B (PDE4B)—were utilized to evaluate the performance of MMGBSA in identifying ligand binding modes. CYP2A6 has a relatively small binding site for ligands, and thus, it is an important player in the oxidation of the smallest xenobiotics [38]. It is also an excellent model enzyme because its binding cavity is limited in size and has easily definable sites for polar interactions.

AR belongs to nuclear receptors and is a traditional target for the discovery of prostate cancer treatments [39]. PDE4B belongs to a large family of PDE-enzymes that degrade cAMP and cGMP by catalyzing the breakage of their phosphodiester bond. PDE4 has many implications in drug discovery, and it has been suggested that PDE4B inhibitors could act as therapeutic agents e.g. against depression and schizophrenia [40] and chronic obstructive pulmonary disease [41].

Materials and methods

Protein structures: Protein structures were acquired from the Protein Data Bank (PDB; www.rcsb.org) [42,43]. The coumarin-bound structure was used for CYP2A6 (PDB-code: 1Z10 [44]). Twelve crystal structures for AR were chosen: 1GS4 [45], 1Z95 [46], 2AM9 [47], 2AMB [47], 2HVC [48], 2IHQ [49], 2OZ7 [50], 2PNU [51], 3B66 [52], 3RLL [53], 4OHA [54], 5V8Q [55]. In structure selection, the structural variability of the crystallized ligands and the resolution of the crystal structure were emphasized. For PDE4B we used crystal structure of PDE4B with bound inhibitor (PDB-code: 4W5E [56]) for two reasons: 1) it contains also the additional part to many other structures, which forms a lid into the inhibitor-binding site in PDE4B, and 2) due it is easier to compare the results to our previous results [37]. Hydrogens were added to protein structures using reduce 3.23 [57].

Ligand preparation: For CYP2A6, two known substrates, coumarin and 6-methylcoumarin, were selected. Both compounds are 7-hydroxylated in CYP2A6 oxidation [36,58]. For AR, ligands were separated from the chosen protein crystal structures. In the case of PDE4B, we used 152 previously published PDE4B inhibitors that have been measured with comparable methods [59–64]. Three-dimensional molecules for CYP2A6 and PDE4B were obtained by using LigPrep in Maestro 2017-4 (Schrödinger Inc, Portland, OR, USA), with following options: (1) OPLS2005 force field, (2) protonization at physiological pH 7.4±0.0, where ligands were ionized with Epik, (3) tautomers were generated, (4) specific chiralities were retained, (5) maximum number of tautomers and chiralities was set to 32/ligand. For tautomers and chiralities only one low energy conformation was kept. For AR, bonds and stereochemistry of ligands were checked to comply with that given in PDB. Hydrogens and partial charges were added using OPLS2005 force field in Maestro (Schrödinger Inc, Portland, OR, USA).

Molecular docking: Molecular docking for CYP2A6, AR, and PDE4B was performed with Plants v.1.2 [65] with chemplp scoring function to produce four binding modes for each ligand that differ significantly (RMSD = 2.5 Å (AR/PDE4B) or 2.0 Å (CYP2A6)). The docking area was set to the center of the binding cavity defined by the bound ligand in each protein structure. In the case of AR, the ligands separated from the protein crystal structures were cross-docked back to the different crystal structures. In all used three examples the ligand binding site does not contain large cavities to surrounding solvent, and accordingly, the docking area was relatively easy to define, and all of the docked ligand poses were located at the defined binding sites.

Parametrization of ligands: Parametrization of ligands for MD simulations were performed with two different methods: (1) the 3D structures of CYP2A6 substrates were optimized quantum mechanically with GAUSSIAN09 (Gaussian, Inc., Wallingford, CT) at the HF/6-31+G* level using a polarizable continuum model. The RESP method [66] was used to calculate the atom-centered point charges from the electrostatic potentials; (2) AR ligands and PDE4B inhibitors were optimized and parametrized with Antechamber [67] method utilizing charge method AM1-bcc.

Preparations for MD: Tleap in Antechamber 17 [68] was used to: (1) generate force field parameters for protein and combine protein-ligand parametrizations; (2) add hydrogen atoms; and (3) solvate the system with a rectangular box of transferable intermolecular potential three-point (TIP3P) water molecules [69] extending 13 Å in every dimensions around the solute. The ff14SB force field [70] was

used for the protein structures. For CYP2A6, parameters suitable for heme with a six-coordinate iron were used [71] (<https://personalpages.manchester.ac.uk/staff/Richard.Bryce/amber/index.html>).

MD simulations and MMGBSA: MD simulations were performed with NAMD 2.9 [72] in four steps: (1) 15,000 steps of energy minimization where Ca-atoms were restrained with 5kcal/mol; (2) 15,000 steps of energy minimization without restraints; (3) 180,000 steps of MD where Ca-atoms were restrained with 5kcal/mol; (4) 1,200,000 steps (2.4 ns) of MD without restraints. The energy minimization of snapshot structures from the MD simulation was performed for 15,000 steps without constraints. Otherwise all parameters were kept similar as in our previous study [17]. All energy minimizations were performed using the default conjugate gradient energy minimization method. Superpositioning of protein-ligand complexes was performed with Vertaa in Bodil [73]. All MD trajectory analysis were made with Cpptraj [74]. RMSD calculations in relation to crystal structures were conducted with rmsd.py script in Schrödinger release 2017-4 (Schrödinger Inc, Portland, OR, USA). MMGBSA analyses were performed with MMPBSA.py script [75] implemented in Antechamber. For generalized Born calculations, three different igb-models, namely igb1, igb2, and igb5, were employed. Shortly, the main difference between these three igb-models is that the original description of solute boundaries in term of effective radii (igb1) have been rescaled in igb2 and igb5 to mimic primarily the computationally more demanding Poisson-Boltzmann model.

Results and discussion

The general aim of this research was to study the ability of MMGBSA to identify the biologically relevant binding modes of small molecules in various target proteins. First, a key challenge in drug discovery is understanding the metabolism, and especially the consequent metabolites for the developed molecules. Accordingly, we studied the possible binding modes of coumarin and 6-methylcoumarin into CYP2A6 to determine whether their site of metabolism (SOM) can be predicted using MMGBSA. Second, the identification of biologically relevant binding modes is an essential quality in computational methods. As such, we used AR to study the binding modes that are verifiable from the protein crystal structures. Last, we tested the effect of ligand binding pose selection using MMGBSA for the correlation coefficient between experimental and computational data with PDE4B. Short (2.4 ns) MD simulations with relatively fast MMGBSA-analysis were employed, although, longer simulations could expose to larger conformational changes and the usage of implicit solvation model has significant drawback in case the solvent molecules form explicit hydrogen-bond network in order to stabilize the ligand binding. From these two possible problems, the short simulation time was compensated with the usage of multiple starting poses from docking. Another issue is the rather limited number of study cases. However, it has been previously shown that a small number of study cases can demonstrate the usability of the method, although more cases are needed to draw broad conclusions. For example, it has been shown that ensemble docking for only two [76] or three study cases, one of which was AR,[77] was enough to indicate the applicability of the method. In addition to that, with molecular docking and MD, promising results have been obtained in studying the binding of AR ligands in detail to predict agonism and antagonism [78], and MD combined with MMGBSA showed success in studying interaction mechanism ARs with only one specific compound [79].

CYP2A6: Identification of the SOM

The recognition of the correct SOM(s) is crucial in drug discovery because it can act as the first step in identifying the formed metabolites of new molecules and thus understanding their possible toxicity effects in living organisms. Because MMGBSA has been used somewhat successfully in the prediction of binding affinities, our aim was to study whether the most likely binding mode for CYP2A6 substrates can be recognized solely by using MMGBSA. All calculations were directly performed using MD simulation snapshots and energy minimized snapshots.

Coumarin is the most used reference compound with CYP2A6 because the catalysis of coumarin to fluorescent 7-hydroxylcoumarin is specific to the 2A6 form in the array of human CYP enzymes. The crystal structure of CYP2A6 in complex with coumarin [44] explains, at the structural level, the likely mechanism of catalysis. The carbonyl oxygen atom of coumarin accepts a hydrogen bond from Asn297 (Figure 1A: orange dotted line), and position 7 (C7) locates towards the heme iron (Figure 1A). Furthermore, there is a small electron density in the vicinity of the iron and C7 of coumarin, where oxygen (O, O2, OH, etc.) could be placed for the catalysis to occur (Figure 1A).

MD simulations with coumarin: The MD simulations were started from four coumarin docking poses, of which the pose 2 is closest to the crystal structure binding mode (Figure 1B). Twenty snapshots with their minimized correspondents from each MD trajectory were used in the binding energy estimation with MMGBSA. A comparison of the numerical MMGBSA values from the simulation snapshots without and with minimization (Table 1) reveals that all four binding poses, with all three igb-models, give a clearly lower energy value with the minimized snapshots (igb1: -3.7 ± 0.4 ; igb2: -4.7 ± 0.4 ; igb5: -5.8 ± 0.3) and that the standard deviations of the values are also clearly lower (igb1: -0.7 ± 0.2 ; igb2: -0.7 ± 0.1 ; igb5: 0.7 ± 0.3). The difference is highest with igb5, which seems to be very sensitive to hydrogen bond distances and angles. In the binding poses without minimization, the large variations in the igb5 energies are highly in accordance with the variation of the distance and angle of the interaction of Asn297 with the carbonyl oxygen atom of coumarin.

Table 1. Docking scores and binding energy estimations (MMGBSA; kcal/mol) with different generalized Born models (igb1, 2, and 5) for four coumarin and 6-methylcoumarin binding poses (#1-4) within CYP2A6.

Molecule	Pose	Docking	Without minimization			RMSD1	RMSD20	Minimized			RMSD1	RMSD20
			igb1	igb2	igb5			igb1	igb2	igb5		
coumarin	1	-71.0	-20.8±1.6	-20.5±1.7	-22.9±1.9	2.31	2.67	-24.9±0.9	-25.4±1.0	-28.7±1.4	2.23	2.52
	2	-70.4	-21.7±1.6	-21.4±1.8	-23.9±2.1	0.62	0.98	-25.6±0.8	-26.3±0.9	-30.0±1.1	0.59	1.11
	3	-70.4	-21.3±3.6	-21.0±4.0	-23.3±4.1	4.30	0.71	-24.9±3.1	-25.6±3.5	-29.4±3.3	4.36	1.00
	4	-67.4	-22.4±1.9	-22.3±1.9	-25.2±2.1	2.63	2.71	-25.5±1.1	-26.4±1.3	-30.5±1.6	2.46	2.63
6-methyl-coumarin	1	-77.8	-25.8±1.7	-25.9±1.9	-28.4±2.2	-	-	-30.0±1.0	-31.2±1.2	-34.9±1.5	-	-
	2	-73.9	-19.4±1.6	-18.4±1.6	-20.9±1.9	-	-	-22.7±1.3	-22.5±1.4	-26.2±2.0	-	-
	3	-70.1	-24.4±1.8	-23.9±1.8	-26.1±1.8	-	-	-28.9±1.8	-29.5±1.9	-32.9±2.0	-	-
	4	-68.6	-24.4±1.3	-23.8±1.5	-26.1±1.8	-	-	-29.2±1.8	-29.8±2.0	-33.6±2.2	-	-

Underline: Original docking pose that resembles crystal structure binding mode (coumarin) or is in agreement with other experimental results (6-methylcoumarin); bold: The best binding energy and the lowest RMSD value of the molecule's binding poses within the MMGBSA method; ±: Standard deviation in MD snapshots. RMSD1=RMSD value to the crystal structure from the beginning of the MD simulation (the first frame). RMSD20=RMSD value to the crystal structure from the end of the MD simulation (the last frame).

The MMGBSA binding energies rank the coumarin pose 4 highest both without with minimization in igb2 and igb5, while docking ranked the initial pose the lowest (Table 1). The MMGBSA-based order of the poses stayed the same between snapshots without/with minimization in igb2 and igb5, and they changed only slightly in the igb1 energies. Only the igb1 energy from minimized snapshots rank the crystal structure-like pose 2 the highest. The comparison of energy values between the binding poses shows that in the snapshots without minimization, the difference between the most favorable and the worst pose is much higher than in the minimized snapshots (igb1: 0.8; igb2: 0.8; igb5: 0.5). In addition, without minimization, the differences between the best and the second-best poses are approximately three to ten times those of the corresponding minimized snapshots (without/with minimization: igb1: 0.74/0.08; igb2: 0.90/0.09; igb5: 1.27/0.51). However, as the standard deviations are also clearly higher for the coumarin binding poses without minimization, the MMGBSA values for all poses are within the error limits of each other. The gain in binding energy from minimization is similar in all coumarin poses with each igb model (e.g. igb1 pose 1: -4.1; pose 2: -3.9; pose 3; -3.6; pose 4: -3.1). This results from, firstly, the above-mentioned observation that the improvement of hydrogen bonding interactions is clearly a significant factor for lowering the MMGBSA value in minimization, and secondly, that all binding poses of coumarin eventually formed a hydrogen bond to CYP2A6 during the MD simulations (see below) that could be improved in the minimization step. As the MMGBSA values of the coumarin binding poses are within error limits of each other, the binding energy estimations alone cannot be used to identify the most likely binding mode for coumarin.

Examining the coumarin orientation in simulations from the four different starting poses, it is notable that from each, the substrate rotates in such way that the carbonyl oxygen accepts a hydrogen bond from Asn297 (Table 2), which is the only polar residue in the vicinity of the coumarin binding site. Furthermore, from two starting poses (poses 2 and 3), C7 is or becomes the closest to the heme iron (Table 2; average distance without/with minimization 3.6/3.4 Å) and the whole ligand pose is or becomes similar to the crystal structure based on both visual and RMSD analysis (Table 1). Simultaneous to the C7 flip towards the heme in pose 3, the energy of the complex drops notably as the coumarin forms the hydrogen bond with Asn297 (without/with minimization: igb1: -7.6/-6.7; igb2: -8.5/-7.4; igb5: -8.6/-6.9). From the other two starting poses (poses 1 and 4), position 5 (C5) is or becomes closest to the iron, but the distance of the C5 is farther than that of the C7 in poses 2 and 3 (Table 2; average distance without/with minimization 3.9/3.8 Å). When considering the typical distances of the groups closest to the iron in the crystal structures of CYP2A6 (e.g., coumarin: 3.2 Å; methoxsalen (PDB-code:1Z11 [44]): 3.3 Å), the C7 of the minimized binding modes, 2 and 3 are at a similar optimal distance to typical values, while the C5 of poses 1 and 4 are slightly farther compared to typical values. The variations in the distances are also clearly lower when C7 is the closest to iron (without minimization: 0.38 vs. 0.59; minimized: 0.23 vs. 0.45). In both the simulations without and with minimization, conformation 2 is the most stable based on the RMSD from both the ligand and the heme, but it is within the error limits of binding modes 1 and 4 (Table 2).

Table 2. The stability, closest carbon atom to heme iron, and Asn297 side chain nitrogen distance (Å) to the carbonyl group of coumarin and 6-methylcoumarin binding poses (#1-4) with CYP2A6 in simulations without and with minimization.

Molecule	Pose	Without minimization					Minimized				
		RMSD _L	RMSD _{LH}	CX	d	d (N-O)	RMSD _L	RMSD _{LH}	CX	d	d (N-O)
coumarin	1	0.16±0.03	1.19±0.20	C5	4.0±0.8	3.0±0.4	0.02±0.01	1.03±0.17	C5	3.8±0.7	2.9±0.0
	2	0.20±0.04	1.04±0.18	C7	3.7±0.4	2.9±0.2	0.04±0.02	0.96±0.17	C7	3.4±0.3	2.8±0.0
	3	0.14±0.04	2.34±0.40	C7	4.0±1.2	4.5±2.8	0.04±0.01	2.29±0.34	C7	4.0±1.3	4.5±1.0
	4	0.14±0.03	1.17±0.15	C5	3.8±0.4	3.0±0.3	0.04±0.02	1.07±0.16	C5	3.7±0.3	2.9±0.0
6-methyl-coumarin	1	0.60±0.17	1.20±0.07	C7 6M	3.9±0.3 3.9±0.4	2.9±0.1	0.60±0.20	1.1±0.05	C7 6M	3.8±0.2 3.9±0.2	2.9±0.0
	2	0.53±0.21	1.70±0.19	C4	3.4±0.7	10.8±0.9	0.51±0.24	1.77±0.16	C4	3.5±0.7	10.3±0.8
	3	0.53±0.26	2.04±0.10	C4	6.2±0.7	3.2±1.6	0.56±0.24	1.83±0.07	C4	5.7±0.5	3.1±1.1
	4	0.59±0.19	1.05±0.13	C5	4.4±0.4	3.0±0.2	0.43±0.27	0.94±0.18	C5	4.2±0.3	2.9±0.0

Underline: Original docking pose that resembles crystal structure binding mode (coumarin) or is in agreement with other experimental results (6-methylcoumarin); RMSD: Root mean square deviation of ligand (L) or ligand and heme (LH) in relation to the first snapshot; bold: the lowest RMSD of ligand and heme; ±: Standard deviation in MD snapshots; CX: The closest substrate carbon to the heme iron on average; d: The distance of the closest carbon atom to the heme iron on average; d (N-O): The distance of Asn297 side chain nitrogen to coumarin carbonyl; 6M: 6-methyl.

While the binding energy or the stability alone do not strictly differentiate the preference of coumarin hydroxylation for C7 over C5, the distance and variation of the closest substrate carbon atom to the heme iron does suggest that C7 is more susceptible for oxidation by CYP2A6, which is in line with experimental data [58]. Altogether, the combination of MMGBSA binding energy estimation, stability calculation, and considering the distance (together with its variations) of the coumarin's atomic positions to the heme iron form an *in silico* protocol that gives detailed insight into the binding mode of coumarin and provides an *in silico* workflow for the prediction of the SOM, in this case the hydroxylation of position 7, of coumarin.

MD simulations with 6-methylcoumarin: The docking of 6-methylcoumarin into CYP2A6 yielded four starting poses for MD simulations (Figure 1C), where the closest ligand positions to the heme iron are as follows: (1) position 6-methyl and position 7; (2) positions 4 and 6; (3) positions 3 and 4; and (4) position 6-methyl and 5. In the MD simulations, poses 1 and 4 were clearly the most stable ones, based on the RMSD of the ligand and the heme group (Table 2), and in pose 1, the C7 and 6-methyl groups are in close proximity to the heme iron (Table 2). There was still enough space to accommodate the catalytic oxygen needed for oxidation in pose 1, as seen with coumarin in the crystal structure (Figure 1A). In addition, the distance of C7 from the iron remained low enough for catalysis, although not as low as it was for C7 in the coumarin simulations (Table 2). The estimations of binding energy, done using MMGBSA, indicated that the pose 1 was energetically preferred (Table 1). As opposed to the case of coumarin where MMGBSA recognized the native binding mode better than docking,

MMGBSA and docking ranked the same 6-methylcoumarin pose 1 highest (Table 1). However, the MMGBSA binding energy estimations for poses 3 and 4 were always within the error limits of pose 1, while pose 2 was clearly worse, as it was the only pose that did not rotate in the catalytic site to accept a hydrogen bond from Asn297 during the simulation. Pose 2 also gained the least in binding energy in minimization due to the lack of a hydrogen bond with the enzyme (e.g. igb1 pose 1: -4.2; pose 2: -3.3; pose 3: -4.5; pose 4: -4.8). In the case of 6-methylcoumarin, there is no difference between the MD snapshots without and with minimization for the selection of the preferred binding mode. The ligand-heme RMSD- and the MMGBSA-based order of the poses stayed generally the same from both without and with minimization. Altogether, the stability, the distance of the closest carbon to the heme iron, and the binding energy estimations suggested that the primary SOM in 6-methylcoumarin would be C7 in pose 1 (Tables 1 and 2). This result, where C7 is the preferred SOM, correlates with the experimental results, which show that the primary metabolite is hydroxylated at C7 [36].

Identifying the correct binding mode and SOM: Although the simulation times were short, from a catalytic point of view it is crucial to understand how well the substrate is stabilized into favorable reaction coordinates. As a simple measurement, the RMSD of docked substrate and substrate plus the heme was calculated from the simulation trajectories (Table 2). In the case of two rigid substrates, the substrate-only RMSD values originate mainly from slight variations in bond distances and methyl group rotation in 6-methylcoumarin, and accordingly, it is highly beneficial to calculate the RMSD together with the heme. Adding the heme to the RMSD calculation brings forward the bigger shifts in the substrate's orientation in relation to the catalytic site. With coumarin, binding poses 1, 2 and 4 were again within error of the measurement of this RMSD value, although pose 2, in which the C7 is towards the heme, has a slightly lower RMSD. With 6-methylcoumarin, the most stabilized substrate and heme positions are for poses 1 and 4. The minimization step did not bring added value to either MMGBSA or RMSD analysis, but it stabilized the substrate positions that were towards the heme iron a little closer to the distances seen in crystal structures. Using both the ligand and heme-based RMSD and the distance of the substrate atoms to the heme iron to analyze the stabilization of the substrate to the favorable reaction coordinates is suggested to be an essential addition to MMGBSA binding energy estimations for finding the active binding modes (i.e., those binding modes in which the substrate is truly oxidized) and SOM(s) for CYP substrates.

When considering both the predicted binding energy and the stabilization of the reaction coordinates (Tables 1 and 2), it would be logical to suggest that for coumarin, the most favored binding mode is either pose 2 or 4, and for 6-methylcoumarin, it is pose 1. The results suggest that it is possible that coumarin has two favorable SOMs instead of just one, while 6-methylcoumarin has one clearly favorable site for CYP2A6 catalyzed oxidation. Altogether, this is in line with typical phenomena among xenobiotic-metabolizing CYP enzymes. A single CYP form can quite often oxidize the same substrate from multiple sites, as can be found in databases of SOMs for substrates of different CYP enzymes [80,81]. The malleability of the catalytic sites allows the substrate to orient into several binding modes in the site, resulting in the ability of the enzyme to oxidize various positions of the small molecule. Even in the relatively small and rigid catalytic site of CYP2A6, the variations in the shape of the catalytic site can play a major role in determining the success of structure-based regioselectivity prediction of the enzyme's substrates [82].

The flexibility of xenobiotic-metabolizing CYP enzymes and the multitude of possible binding modes for substrates create a challenge for finding the active binding mode(s) of CYP substrates. Furthermore, finding the active binding mode from multiple possible equally stable and energetically favorable ones is complicated by the fact that the substrate may also have an inhibiting binding mode. For instance, pilocarpine that is a competitive inhibitor of CYP2A6 [83,84] has been crystallized in the inhibiting binding mode, where its lone-pair nitrogen is coordinated with the heme iron [85]. However, it is also oxidized by CYP2A6 at its position 3 [86], which, in the crystal structure, is further

away from the usual reaction coordinates that lie near the heme iron. This is where, for instance, the SOM C7 of coumarin is placed in the crystal structure complex with CYP2A6 (Figure 1A) [44]. The inhibiting effect can occur when a non-reactive group faces the heme (i.e., the substrate is stabilized into an orientation where oxidation cannot occur efficiently), or when the CYP mediated catalysis results in a reactive metabolite that can irreversibly inhibit the enzyme. Finding both the active and inhibitive compounds and their binding modes in different CYP forms using *in silico* methods can be a helpful step in the risk assessment of new molecules [87]. Altogether, projecting the simulations here to a larger context, the workflow and observations can provide a plausible starting point into following studies for gaining a more detailed view of the defining interactions between small molecules and CYP enzymes.

AR: Identification of binding modes

Docking: For virtual screening purposes, it is important that the docking protocol can utilize any protein structure to produce biologically relevant and reliable binding poses for variable compounds [6,7]. In general, molecular docking identifies “correct” (i.e., crystal structure-like) binding mode for AR ligands very well. In cross-docking, with ten ligands out of twelve, the best ranked docking pose resembles the crystal structure ligand binding mode and is thus considered correct. Also, with the two “failed” docking results (i.e., for which crystal structure-like pose is not the best ranked pose), the correct binding mode is among the four saved poses (Table 3). One of the failed docking structures, the 3RLL ligand, was cross-docked into the 3B66 protein structure. In the 3B66 protein, Met745 turns towards the binding pocket, and thus, the binding pocket is not favorable for 3RLL ligand binding (Figure 2A). In addition, the original 3RLL protein has a Thr877Ala mutation in the binding site; however, the absence of this mutation should not affect the docking result much because it does not restrict the binding area. In self-docking, the 3RLL ligand repeats the crystal structure binding pose. The 5V8Q ligand was docked into the 2AMB protein. In the 2AMB protein, the position of Thr877 is altered in the binding area, but this does not affect the usable binding area. However, the docking scores for different poses of the 5V8Q ligand are relatively similar (-81.5 – -77.6; -78.9 for the crystal structure-like pose; Table 3). In self-docking, the crystal structure-like pose of the 5V8Q ligand is identified as the best pose. It is notable that, in self-docking, the scale of the docking scores is very different than that of the scores in cross-docking (-118.5 vs. -102.4 for 3RLL and -90.6 vs. -78.9 for 5V8Q). All in all, molecular docking seems to be a reasonable way to relatively quickly identify biologically relevant binding modes, at least in cases where there is some prior knowledge about the binding site. However, here, only ligands that are known to bind to AR were cross-docked into varying protein conformations.

[Table 3. Docking scores, binding energy estimations (MMGBSA; kcal/mol) with different generalized Born models (igb1, 2, and 5) and RMSD values for twelve cross-docked AR ligands.

Molecule	Pose	Docking	Without minimization			RMSD1	RMSD20	Minimized			RMSD1	RMSD20
			igb1	igb2	igb5			igb1	igb2	igb5		
1GS4	1	-87.4	-47.7± 2.1	-46.1± 2.1	-52.1± 2.3	0.63	0.63	-53.8± 1.5	-54.4± 1.9	-62.6± 2.1	0.83	0.83
	2	-78.9	-45.3± 2.5	-43.2± 2.8	-46.7± 3.2	7.39	7.42	-51.7± 1.8	-51.7± 2.3	-57.2± 2.7	7.40	7.39
	3	-76.5	-44.2± 2.2	-43.0± 2.8	-49.2± 3.8	3.03	3.28	-51.1± 2.8	-51.8± 3.7	-60.5± 5.0	3.02	3.34
	4	-63.3	-46.8± 2.6	-45.6± 3.0	-50.6± 3.8	7.12	7.07	-54.6± 2.1	-55.0± 2.3	-61.5± 3.0	7.07	7.11
1Z95	1	-79.7	-53.8± 2.4	-50.7± 2.6	-55.1± 3.1	1.30	1.32	-60.3± 0.9	-58.7± 1.0	-64.5± 1.5	1.25	1.27
	2	-78.0	-47.1± 2.1	-42.4± 2.3	-45.5± 2.5	2.56	3.00	-54.4± 1.5	-51.2± 1.9	-55.7± 2.4	2.79	3.05
	3	-72.7	-46.2± 2.5	-40.2± 2.6	-40.3± 3.0	7.34	7.96	-53.6± 2.7	-48.4± 2.6	-49.4± 3.2	7.42	7.86
	4	-72.4	-43.8± 2.8	-38.5± 2.9	-40.6± 3.0	7.93	7.82	-50.7± 1.2	-46.5± 1.0	-49.9± 0.9	8.10	7.95
2AM9	1	-91.6	-45.4± 2.0	-48.5± 2.0	-58.0± 1.7	0.49	0.49	-51.9± 0.9	-57.1± 1.1	-68.3± 1.4	0.30	0.23
	2	-83.1	-43.5± 2.9	-46.0± 2.9	-54.3± 2.9	3.02	3.19	-49.4± 2.0	-54.3± 1.8	-64.7± 1.6	2.99	3.10
	3	-73.8	-43.0± 2.7	-46.4± 3.1	-54.9± 3.4	6.70	6.80	-49.6± 2.4	-55.1± 3.0	-65.4± 4.0	6.71	6.71
	4	-68.3	-41.7± 2.9	-44.8± 3.1	-53.3± 3.1	6.64	6.71	-48.2± 2.6	-53.5± 2.6	-64.0± 2.6	6.63	6.74

				3.2	3.4				3.2	3.8		
2AMB	1	-107.6	-52.6± 2.0	-54.7± 2.4	-63.9± 2.9	0.43	0.41	-60.1± 0.8	-64.7± 1.0	-76.5± 1.2	0.39	0.41
	2	-77.2	-44.9± 2.6	-46.4± 3.1	-53.9± 3.4	6.82	6.87	-51.2± 1.0	-55.3± 1.3	-65.1± 1.6	6.79	6.84
	3	-74.4	-44.9± 2.2	-44.5± 2.2	-49.8± 2.2	3.24	3.60	-51.4± 2.0	-52.8± 2.2	-60.2± 2.4	3.31	3.65
	4	-68.4	-44.8± 2.6	-45.1± 2.8	-51.3± 3.2	3.40	3.46	-52.8± 1.5	-55.4± 1.9	-64.6± 2.7	3.42	3.54
2HVC	1	-97.4	-50.4± 2.6	-46.1± 3.0	-49.4± 3.6	0.59	0.90	-58.4± 1.3	-55.0± 1.1	-58.7± 1.3	0.71	0.81
	2	-89.4	-40.2± 2.0	-36.6± 2.4	-40.2± 2.9	3.28	3.27	-46.9± 1.5	-44.1± 1.7	-48.5± 1.8	3.16	3.33
	3	-88.6	-37.7± 1.9	-34.4± 2.1	-37.6± 2.5	6.77	7.06	-44.3± 0.9	-42.0± 1.1	-45.9± 1.5	6.83	6.87
	4	-84.7	-41.2± 1.7	-37.5± 1.7	-40.2± 1.9	6.33	6.36	-47.5± 1.2	-44.7± 1.7	-48.2± 2.3	6.25	6.33
2IHQ	1	-77.1	-44.7± 1.8	-41.3± 1.7	-43.7± 1.7	0.43	0.96	-50.1± 1.0	-47.3± 1.0	-50.6± 1.0	0.38	0.64
	2	-70.8	-39.2± 2.1	-36.1± 2.2	-39.0± 2.3	2.90	2.84	-44.5± 1.0	-42.4± 1.2	-46.7± 1.5	2.84	2.86
	3	-67.0	-42.5± 1.9	-38.3± 2.2	-40.9± 2.5	2.08	2.20	-47.8± 0.9	-44.5± 1.0	-48.4± 1.2	2.07	2.06
	4	-64.3	-39.0± 2.4	-36.0± 2.7	-38.9± 3.2	6.59	6.67	-45.6± 1.1	-43.2± 1.5	-46.9± 2.1	6.61	6.63
2OZ7	1	-62.3	-59.7± 1.8	-58.6± 2.0	-61.5± 2.5	0.79	0.88	-68.0± 1.1	-68.1± 1.2	-71.6± 1.3	0.84	0.82
	2	-60.0	-54.1± 2.6	-52.4± 4.1	-53.9± 9.1	7.37	7.45	-61.3± 1.5	-60.5± 5.1	-62.5± 5.1	7.42	7.40

				2.7	3.0				1.4	1.5		
	3	-45.3	-55.4± 2.4	-55.1± 2.6	-59.0± 3.3	4.03	4.00	-61.7± 1.4	-63.1± 1.8	-68.3± 2.3	4.10	4.02
	4	-45.0	-50.3± 2.4	-47.2± 2.4	-46.2± 2.4	8.98	9.87	-55.8± 1.6	-53.2± 1.2	-52.2± 1.3	9.16	9.98
2PNU	1	-127.0	-66.7± 2.7	-70.4± 2.9	-83.1± 3.3	0.50	0.51	-76.5± 1.3	-83.2± 1.5	-98.1± 1.7	0.47	0.35
	2	-82.6	-66.5± 2.9	-69.9± 3.2	-83.1± 3.6	0.54	0.78	-76.2± 1.3	-82.8± 1.7	-98.4± 2.2	0.63	0.52
	3	-80.8	-58.2± 1.7	-59.3± 1.6	-68.5± 1.6	8.59	8.81	-65.5± 1.2	-68.5± 1.3	-79.5± 1.7	8.65	8.72
	4	-73.7	-66.6± 1.9	-70.8± 2.1	-84.3± 2.8	0.43	0.61	-75.4± 1.6	-82.7± 1.8	-98.2± 2.0	0.46	0.60
3B66	1	-75.6	-54.5± 1.8	-54.6± 2.0	-63.1± 2.2	0.70	0.84	-63.1± 1.2	-65.9± 1.2	-77.3± 1.3	0.53	0.85
	2	-70.7	-51.4± 4.5	-50.3± 4.8	-57.8± 5.1	7.17	6.59	-60.6± 2.8	-61.4± 2.6	-71.6± 2.9	7.60	6.59
	3	-68.2	-47.0± 2.5	-44.6± 2.3	-51.2± 2.5	2.46	2.53	-54.6± 1.3	-54.7± 1.2	-64.6± 1.7	2.42	2.35
	4	-67.7	-50.9± 2.6	-49.0± 2.8	-55.5± 3.2	2.29	2.40	-57.7± 1.8	-57.4± 2.3	-66.3± 3.3	2.26	2.38
3RLL	1	-67.4	-53.2± 3.1	-50.9± 3.3	-54.1± 3.6	6.97	7.07	-61.7± 1.9	-60.6± 1.8	-65.5± 2.1	7.00	6.97
	2	-57.2	-57.3± 3.0	-54.6± 3.0	-58.0± 3.3	0.57	1.00	-64.9± 1.4	-63.5± 1.4	-68.3± 1.8	0.54	0.86
	3	-57.2	-57.2± 1.9	-54.1± 1.9	-56.8± 2.1	3.03	3.13	-64.9± 1.7	-63.2± 2.0	-67.3± 2.4	3.05	3.10
	4	-54.8	-58.7± 2.3	-54.8± 2.8	-57.2± 2.8	7.25	7.49	-65.9± 2.2	-63.4± 2.4	-67.2± 2.8	7.25	7.49

				2.4	2.8				2.5	3.0		
4OHA	1	-81.0	-39.6± 2.2	-37.5± 2.6	-39.2± 2.9	1.55	0.85	-46.5± 1.5	-45.6± 2.0	-48.6± 2.3	1.31	0.49
	2	-77.3	-38.7± 1.9	-35.7± 2.1	-37.1± 2.6	2.90	2.67	-45.8± 1.1	-44.1± 1.6	-46.9± 2.1	2.91	2.62
	3	-63.9	-33.4± 2.6	-30.8± 2.7	-31.5± 2.9	6.77	7.05	-40.3± 1.8	-38.5± 1.7	-39.8± 2.1	6.77	6.96
	4	-63.8	-32.6± 2.4	-29.5± 2.6	-29.3± 2.9	6.28	6.31	-38.0± 1.8	-35.7± 2.0	-36.3± 2.2	6.31	6.29
5V8Q	1	-81.5	-39.5± 2.2	-36.9± 2.3	-39.6± 2.6	2.39	2.45	-46.7± 1.3	-45.4± 1.6	-49.4± 1.8	2.41	2.45
	2	-81.0	-38.9± 1.8	-36.6± 1.9	-39.7± 2.0	3.36	3.19	-45.2± 0.8	-43.9± 1.0	-48.0± 1.2	3.23	3.22
	3	-78.9	-42.3± 2.8	-39.4± 2.9	-41.3± 3.0	0.71	0.80	-48.6± 1.2	-46.9± 1.1	-50.4± 0.9	0.53	0.89
	4	-77.6	-39.8± 1.5	-37.6± 1.8	-39.2± 2.4	6.45	6.33	-44.5± 1.4	-43.1± 1.7	-45.5± 2.4	6.48	6.34

Underline: Docking pose that resembles crystal structure binding mode; bold: The best binding energy and the lowest RMSD value of the molecule's binding poses within the MMGBSA method; ±: standard deviation in MD snapshots.
 RMSD1=RMSD value to the crystal structure from the beginning of the MD simulation (the first frame).
 RMSD20=RMSD value to the crystal structure from the end of the MD simulation (the last frame).

MD simulations and MMGBSA: As mentioned, the general aim of this study was to examine the ability of MMGBSA to identify biologically relevant binding modes of small molecules. The AR ligands seemed to be rather stable during the simulations, and none of the docking poses were drastically changed, which was observed both in visual inspection and by calculated RMSD values (Table 3). This could be partly due to the relatively short MD simulations (2.4 ns). However, we expect that usage of several starting poses with such a short simulation time reflects better the situation than if only one starting pose would be employed. After the minimization of the MD snapshots, the energy values were lower and the standard errors were smaller in all cases (Table 3).

In coarse numerical comparison, MMGBSA without minimization using igb5 recognizes the correct binding mode of cross-docked 3RLL ligand (which failed in docking). After minimization, in addition to igb5, igb2 recognizes the correct binding mode (Figure 2B). This shows that small changes in the protein conformations are crucial for the identification of biologically relevant small molecule

binding modes, at least when identification is based on coarse numerical comparison. When MD simulations and MMGBSA originate from self-docked 3RLL ligand, MMGBSA calculations with and without minimization clearly recognize the correct binding mode as the best pose (data not shown). With 5V8Q (which failed in docking), MMGBSA recognizes the correct binding mode with and without minimization, using all three igbs.

With the 1GS4 ligand, after minimization using igb1 and igb2, pose No. 4 ranks over correct pose No. 1 in coarse numerical comparison (Table 3; Figure 3). However, the differences in the energy estimations are not significant and are clearly within the error ranges (Table 3). The 1GS4 protein is a double mutant (Leu701His, Thr877Ala; Figure 3A); as such, when the 1GS4 ligand is cross-docked into wild type protein structure (2AM9), the reverse binding mode also seems reasonable (Figure 3C). Unfortunately, there is no experimental data or crystal structure of the 1GS4 ligand with wild type protein, so the actual binding mode remains unclear. However, this shows that novel and potentially biologically relevant binding modes can be obtained via computational methods.

With the 2PNU ligand, only igb1 without minimization recognizes the correct binding mode in coarse numerical comparison. After minimization, igb2 also raises the correct binding mode into the first place. The 2PNU ligand is a steroidal ligand with a bulky chain (Figure 4A) directed towards helix 12. This creates a challenge when docking. Basically, the ligand has two more or less reasonable binding modes: crystal structure-like and reversed (Figure 4B). The formation of other poses is sterically hindered, leading to a situation in which three poses (out of four saved) resemble the crystal structure binding mode after MD simulation (Figure 4C). All these binding modes behave similarly, with or without minimization in MMGBSA (Table 3; 2PNU conformations 1, 2, and 4). Different docking poses can be produced by increasing the required RMSD value. However, novel poses created this way are unreasonable and, thus, easily separated from the biologically relevant binding mode, both with docking scores and with MMGBSA energy estimations (data not shown).

In all other cases, MMGBSA with and without minimization identifies the correct binding pose to be the best choice in coarse numerical comparison. The MMGBSA results are clearly over the error limits, with ligands from 1Z95, 2AMB, and 2HVC, with and without minimization, with all igbs; with ligands from 2IHQ and 2OZ7 with minimized igb1 and igb2; and with ligands from 3B66 with minimized igb2 and igb5. In other cases, differences in the biologically relevant binding modes are not over the error limit. For most of the cases, MD/MMGBSA does not bring added value because the method is computationally demanding, and correct binding poses can already be identified in molecular docking. Molecular docking, MD, and MMGBSA have all been previously used to study the binding of AR ligands. For example, molecular docking and MD were used to create antagonist AR structures, which led to a vast improvement in docking AR antagonists and separating them from decoy compounds, [78] and MD/MMGBSA has proven accurate enough to study the interaction mechanism between R-bicalutamide and wildtype/mutant ARs [79]. Also, in this study MD/MMGBSA facilitated the identification of some AR ligands and their relevant binding poses. MD helped to improve two mediocre docking poses into biologically relevant forms, which were identified as correct via MMGBSA (2PNU, pose No. 2, and pose No. 4). One igb model before minimization and two igb models after minimization identified the 3RLL ligand, which failed in docking. 5V8Q also failed in docking but was identified using all igb models, both with and without minimization.

PDE4B

Last, we tested the effect of ligand binding pose selection with MMGBSA to the correlation between experimental and computational data. For this, PDE4B was used as a test case, along with 152 published inhibitors whose inhibition data has been measured using a similar method, enabling a rough assumption about the homogeneity of the biological data. The selected data set is reasonable for

the identification of possible correlation between computed and experimental data, as the pIC₅₀ spreads seven log units (3.4–10.5).

Effect of inhibitor binding pose. All compounds were docked four times into the PDE4B structure, which yielded a total of 488 protein–ligand complexes. The RMSD difference between the acceptable poses was set to 2.5, ensuring that all the binding modes were truly different. All 488 complexes were subjected to short MD simulation with MMGBSA post-processing to determine whether MMGBSA can produce free energy binding estimations that correlate with experimentally obtained IC₅₀ values. Already, igb models have found that the top poses from docking produce R₂ values of 0.64 to 0.71 (Figure 5: blue). This shows that the data used is likely meaningful. When the lowest MMGBSA energy for each molecule is selected, the correlation with experimental results increases significantly, up to 0.77 (Figure 5: red; igb1, with and without energy minimization of snapshots). Interestingly, when the lowest binding energy is sought, the second ranked docking result is most often selected, by a slight margin; however, together, all four results seem highly useful as the ranked docking solutions are roughly selected in a ratio of 25:32:25:18, with only small variation between the different igb models.

Effect of energy minimization of MD in simulation snapshots. Not surprisingly, as with CYP2A6 and AR, the minimized snapshots of protein–ligand complexes yield systematically lower free energy of binding estimations, on average, from 10 kcal/mol (igb1 and igb2) to 13 kcal/mol (igb5) (Figure 5). Furthermore, the average error of the all measurements is lowered by 0.7 kcal/mol, regardless of igb model used. The minimization of the MD snapshots that were used in the MMGBSA calculations barely affects the correlation coefficient (Figure 5).

It is impossible to determine whether the selection of the binding pose for each molecule is correct in large data sets, especially when the structural data is not available. Accordingly, if possible, the methods used in such case should be verified with existing experimental data. In general, for example, docking methods are reasonable for the identification of possible binding modes for each molecule, but the scoring functions associated with them need to compromise between speed and accuracy. Thus, these scoring functions do not recognize the “correct” binding mode as their first option, and their ability to rank active ligands is quite often poor [3,8,35]. Therefore, the choice of the binding pose for each molecule or the identification of active molecules should be done using an alternative scoring function(s) [34,88,89]. In many cases, yet another rapid scoring may help with this; although this is a more time-consuming method, it might give more relevant data, as we show here using MMGBSA, which resulted in a relatively high correlation coefficient between the calculated and experimental data. Whether the selected poses truly represent the biologically relevant complex structure cannot be verified. It is notable that the correlation coefficient for this data set is relatively high and is significantly higher when compared to docking alone (Plants R₂=0.66; Glide SP R₂=0.03), or to the use of the best docking pose with Prime MMGBSA (from Plants poses R₂=0.38; from Glide SP poses R₂=0.25) or all poses from Plants (R₂=0.53) [37]. As in this case, the MMGBSA results clearly show that highly active PDE4B inhibitors (pIC₅₀>7.5) can be identified relatively reliably, suggesting that this combination of methods could be employed in the future studies where novel PDE4B inhibitors are searched.

Conclusions

Here, we have used MMGBSA, with and without the energy minimization of trajectory snapshots, to study whether the correct binding conformation of a small molecule to its target protein can be identified using several docking conformations. To provide a wider perspective, we employed three different types of problems: (1) the identification of a substrate binding mode in CYP2A6

enzyme, (2) the identification of AR ligand binding modes, verified using crystal structures, and (3) the improvement of correlation coefficient between experimental and computational data using a set of PDE4B inhibitors. Not surprisingly, in all cases, the minimization of MD simulation snapshots lowered the free energy of binding estimations. This phenomenon was most profoundly seen with *igb5*, which suggests that *igb5* is the most sensitive for precise distances and angles in interactions. In the case of CYP2A6, it was possible to identify the likely binding mode(s) for the substrates by combining the estimation of free energy of binding to a heme and ligand-based RMSD and atomic distance calculations from MD simulation snapshots. In the case of AR, MMGBSA improved the identification of binding conformations in contrast to docking, and with minimized MD trajectory snapshots, it was possible to identify the correct binding mode within error limits. With PDE4B, the correlation between the experimental and computational results was significantly improved when the docking conformation was selected based on MMGBSA. Although energy minimization helped only in the case of AR, it was obvious that the minimization of MD snapshots tends to lower the errors in the free energy of binding estimation throughout the MD simulation, which often helps in the selection of the best binding pose. The choice of short MD simulations (2.4 ns) was based on previous studies that suggest that longer simulations do not necessarily improve the outcome but already minimization of protein-ligand complexes are quite often enough.[16,19] Obviously, if large conformational changes would be expected, then longer simulation time would be a more reasonable choice.

Acknowledgements: The project was funded by the Jenny and Antti Wihuri Foundation (MA), the Emil Aaltonen Foundation (MA) and the Finnish Cultural Foundation, Varsinais-Suomi Regional fund (EJ). CSC, The Finnish IT Centre for Science is acknowledged for their generous computational grants (O.T.P. projects *jyy2516*, *jyy2585*, and *jyy2586*).

Figure 1. CYP2A6 crystal structure and docked substrate binding modes. (A) Coumarin (orange carbon atoms) binding to CYP2A6 and unassigned electron density (purple) in the crystal structure of the complex (PDB-code: 1Z10 [44]). Binding poses of coumarin (B) and 6-methylcoumarin (C) after docking. Gray carbon atoms=crystal structure Asn297 and heme, blue carbon atoms=conf. No. 1, green carbon atoms=conf. No. 2, pink carbon atoms=conf. No. 3, brown carbon atoms=conf. No. 4. In (A) the numbering scheme for coumarin is shown.

Figure 2. Effect of protein conformation on identification of biologically relevant small molecule binding modes. A) Small changes in protein conformation affect recognition of crystal structure-like ligand poses in docking. For example: 3RLL ligand (turquoise) was docked into 3B66 protein structure (light blue) in which Met745 has turned towards binding pocket. This makes binding pocket unfavorable for 3RLL ligand binding. B) In MD Met745 turns away from the binding pocket (3B66 protein, light blue) and correct binding mode for 3RLL ligand (orange) is recognized with MMGBSA *igb2*. For comparison 3RLL crystal structure complex is shown in grey in both A and B.

Figure 3. Potential binding modes of 1GS4 ligand. A) Original crystal structure (PDB: 1GS4) is a double mutant which may affect binding mode. Original crystal structure ligand binding mode is shown with purple carbon atoms. Binding modes in wildtype protein for B) crystal structure-like pose No.1 (orange carbon atoms) and C) reversed pose No.4 (turquoise carbon atoms). Carbon atoms in amino acids are shown in gray in all panels.

Figure 4. Binding poses for 2PNU ligand after molecular docking and MD simulations. A) Original crystal structure binding mode of 2PNU ligand (purple carbon atoms) and binding mode with the lowest RMSD value (conf. No. 1, blue carbon atoms; RMSD from last MD frame=0.35). B) Binding modes after docking and C) after MD simulations for three correctly identified binding modes. Blue carbon atoms=conf. No. 1, green carbon atoms=conf. No. 2, brown carbon atoms=conf. No. 4.

Figure 5. Effect of choice of ligand pose and energy minimization to correlation coefficient for experimentally measured PDE4B inhibitors. Already the usage of MMGBSA values for the best docking conformation yields meaningful correlation with experimental results (blue) but are clearly better when the best MMGBSA value is used (red). In contrast, the minimization of MD trajectory snapshots does not improve the correlation (right panels) to those without minimization (left panels). The experimental pIC50 values are shown on X-axis and binding energy estimations from MMGBSA are on Y-axis.

Conflict of Interest

The authors declare that they have no conflict of interest.

References

1. Gilson, M.K.; Zhou, H.-X. Calculation of protein-ligand binding affinities. *Annu. Rev. Biophys. Biomol. Struct.* **2007**, *36*, 21–42, doi:10.1146/annurev.biophys.36.040306.132550.
2. Jorgensen, W.L. Efficient Drug Lead Discovery and Optimization. *Acc. Chem. Res.* **2009**, *42*, 724–733, doi:10.1021/ar800236t.
3. Warren, G.L.; Andrews, C.W.; Capelli, A.-M.; Clarke, B.; LaLonde, J.; Lambert, M.H.; Lindvall, M.; Nevins, N.; Semus, S.F.; Senger, S.; Tedesco, G.; Wall, I.D.; Woolven, J.M.; Peishoff, C.E.; Head, M.S. A critical assessment of docking programs and scoring functions. *J. Med. Chem.* **2006**, *49*, 5912–5931.
4. Feliu, E.; Oliva, B. How different from random are docking predictions when ranked by scoring functions? *Proteins* **2010**, *78*, 3376–3385, doi:10.1002/prot.22844.
5. Plewczynski, D.; Lazniewski, M.; Augustyniak, R.; Ginalski, K. Can we trust docking results? Evaluation of seven commonly used programs on PDBbind database. *J. Comput. Chem.* **2011**, *32*, 742–755, doi:10.1002/jcc.21643.
6. Ramírez, D.; Caballero, J. Is It Reliable to Take the Molecular Docking Top Scoring Position as the Best Solution without Considering Available Structural Data? *Molecules* **2018**, *23*.
7. Wang, Z.; Sun, H.; Yao, X.; Li, D.; Xu, L.; Li, Y.; Tian, S.; Hou, T. Comprehensive evaluation of ten docking programs on a diverse set of protein-ligand complexes: the prediction accuracy of sampling power and scoring power. *Phys. Chem. Chem. Phys.* **2016**, *18*, 12964–12975, doi:10.1039/C6CP01555G.
8. Cross, J.B.; Thompson, D.C.; Rai, B.K.; Baber, J.C.; Fan, K.Y.; Hu, Y.; Humblet, C. Comparison of several molecular docking programs: pose prediction and virtual screening accuracy. *J. Chem. Inf. Model.* **2009**, *49*, 1455–1474.
9. McGaughey, G.B.; Sheridan, R.P.; Bayly, C.I.; Culberson, J.C.; Kretsoulas, C.; Lindsley, S.; Maiorov, V.; Truchon, J.-F.; Cornell, W.D. Comparison of topological, shape, and docking methods in virtual screening. *J. Chem. Inf. Model.* **2007**, *47*, 1504–1519, doi:10.1021/ci700052x.
10. Shirts, M.R.; Mobley, D.L.; Chodera, J.D. Chapter 4 Alchemical Free Energy Calculations: Ready for Prime

Time? In; Spellmeyer, D.C., Wheeler, R., Eds.; Annual Reports in Computational Chemistry; Elsevier, 2007; Vol. 3, pp. 41–59.

11. Kollman, P.A.; Massova, I.; Reyes, C.; Kuhn, B.; Huo, S.; Chong, L.; Lee, M.; Lee, T.; Duan, Y.; Wang, W.; Donini, O.; Cieplak, P.; Srinivasan, J.; Case, D.A.; Cheatham, T.E. 3rd Calculating structures and free energies of complex molecules: combining molecular mechanics and continuum models. *Acc. Chem. Res.* **2000**, *33*, 889–897.
12. Genheden, S.; Ryde, U. The MM/PBSA and MM/GBSA methods to estimate ligand-binding affinities. *Expert Opin. Drug Discov.* **2015**, *10*, 449–461.
13. Sun, H.; Li, Y.; Shen, M.; Tian, S.; Xu, L.; Pan, P.; Guan, Y.; Hou, T. Assessing the performance of MM/PBSA and MM/GBSA methods. 5. Improved docking performance using high solute dielectric constant MM/GBSA and MM/PBSA rescoring. *Phys. Chem. Chem. Phys.* **2014**, *16*, 22035–22045, doi:10.1039/c4cp03179b.
14. Hou, T.; Wang, J.; Li, Y.; Wang, W. Assessing the performance of the molecular mechanics/Poisson Boltzmann surface area and molecular mechanics/generalized Born surface area methods. II. The accuracy of ranking poses generated from docking. *J. Comput. Chem.* **2011**, *32*, 866–877, doi:10.1002/jcc.21666.
15. Niinivehmas, S.P.; Virtanen, S.I.; Lehtonen, J. V; Postila, P.A.; Pentikäinen, O.T. Comparison of virtual high-throughput screening methods for the identification of phosphodiesterase-5 inhibitors. *J. Chem. Inf. Model.* **2011**, *51*, 1353–63, doi:10.1021/ci1004527.
16. Virtanen, S.I.; Niinivehmas, S.P.; Pentikäinen, O.T. Case-specific performance of MM-PBSA, MM-GBSA, and SIE in virtual screening. *J. Mol. Graph. Model.* **2015**, *62*, 303–318, doi:10.1016/j.jmgm.2015.10.012.
17. Ylilauri, M.; Pentikäinen, O.T. MMGBSA as a tool to understand the binding affinities of filamin-peptide interactions. *J. Chem. Inf. Model.* **2013**, *53*, doi:10.1021/ci4002475.
18. Sun, H.; Li, Y.; Tian, S.; Xu, L.; Hou, T. Assessing the performance of MM/PBSA and MM/GBSA methods. 4. Accuracies of MM/PBSA and MM/GBSA methodologies evaluated by various simulation protocols using PDBbind data set. *Phys. Chem. Chem. Phys.* **2014**, *16*, 16719–16729, doi:10.1039/c4cp01388c.
19. Hou, T.; Wang, J.; Li, Y.; Wang, W. Assessing the performance of the MM/PBSA and MM/GBSA methods. 1. The accuracy of binding free energy calculations based on molecular dynamics simulations. *J. Chem. Inf. Model.* **2011**, *51*, 69–82.
20. Karami, L.; Saboury, A.A.; Rezaee, E.; Tabatabai, S.A. Investigation of the binding mode of 1, 3, 4-oxadiazole derivatives as amide-based inhibitors for soluble epoxide hydrolase (sEH) by molecular docking and MM-GBSA. *Eur. Biophys. J.* **2017**, *46*, 445–459, doi:10.1007/s00249-016-1188-0.
21. Rastelli, G.; Del Rio, A.; Degliesposti, G.; Sgobba, M. Fast and accurate predictions of binding free energies using MM-PBSA and MM-GBSA. *J. Comput. Chem.* **2010**, *31*, 797–810, doi:10.1002/jcc.21372.
22. Kaus, J.W.; Harder, E.; Lin, T.; Abel, R.; McCammon, J.A.; Wang, L. How To Deal with Multiple Binding Poses in Alchemical Relative Protein–Ligand Binding Free Energy Calculations. *J. Chem. Theory Comput.*

2015, 11, 2670–2679.

23. Chodera, J.D.; Mobley, D.L.; Shirts, M.R.; Dixon, R.W.; Branson, K.; Pande, V.S. Alchemical free energy methods for drug discovery: progress and challenges. *Curr. Opin. Struct. Biol.* **2011**, *21*, 150–160, doi:10.1016/j.sbi.2011.01.011.
24. Mobley, D.L.; Graves, A.P.; Chodera, J.D.; McReynolds, A.C.; Shoichet, B.K.; Dill, K.A. Predicting absolute ligand binding free energies to a simple model site. *J. Mol. Biol.* **2007**, *371*, 1118–1134, doi:10.1016/j.jmb.2007.06.002.
25. Boyce, S.E.; Mobley, D.L.; Rocklin, G.J.; Graves, A.P.; Dill, K.A.; Shoichet, B.K. Predicting ligand binding affinity with alchemical free energy methods in a polar model binding site. *J. Mol. Biol.* **2009**, *394*, 747–763, doi:10.1016/j.jmb.2009.09.049.
26. Homeyer, N.; Stoll, F.; Hillisch, A.; Gohlke, H. Binding Free Energy Calculations for Lead Optimization: Assessment of Their Accuracy in an Industrial Drug Design Context. *J. Chem. Theory Comput.* **2014**, *10*, 3331–3344, doi:10.1021/ct5000296.
27. Liu, P.; Kim, B.; Friesner, R.A.; Berne, B.J. Replica exchange with solute tempering: a method for sampling biological systems in explicit water. *Proc. Natl. Acad. Sci. U. S. A.* **2005**, *102*, 13749–13754, doi:10.1073/pnas.0506346102.
28. Wang, L.; Friesner, R.A.; Berne, B.J. Replica exchange with solute scaling: a more efficient version of replica exchange with solute tempering (REST2). *J. Phys. Chem. B* **2011**, *115*, 9431–9438, doi:10.1021/jp204407d.
29. Moors, S.L.C.; Michielssens, S.; Ceulemans, A. Improved Replica Exchange Method for Native-State Protein Sampling. *J. Chem. Theory Comput.* **2011**, *7*, 231–237, doi:10.1021/ct100493v.
30. Wang, L.; Berne, B.J.; Friesner, R.A. On achieving high accuracy and reliability in the calculation of relative protein-ligand binding affinities. *Proc. Natl. Acad. Sci. U. S. A.* **2012**, *109*, 1937–1942, doi:10.1073/pnas.1114017109.
31. Hamelberg, D.; Mongan, J.; McCammon, J.A. Accelerated molecular dynamics: a promising and efficient simulation method for biomolecules. *J. Chem. Phys.* **2004**, *120*, 11919–11929, doi:10.1063/1.1755656.
32. de Oliveira, C.A.F.; Hamelberg, D.; McCammon, J.A. Coupling Accelerated Molecular Dynamics Methods with Thermodynamic Integration Simulations. *J. Chem. Theory Comput.* **2008**, *4*, 1516–1525, doi:10.1021/ct800160q.
33. Arrar, M.; de Oliveira, C.A.F.; Fajer, M.; Sinko, W.; McCammon, J.A. w-REXAMD: A Hamiltonian Replica Exchange Approach to Improve Free Energy Calculations for Systems with Kinetically Trapped Conformations. *J. Chem. Theory Comput.* **2013**, *9*, 18–23, doi:10.1021/ct300896h.
34. Kurkinen, S.T.; Niinivehmas, S.; Ahinko, M.; Lätti, S.; Pentikäinen, O.T.; Postila, P.A. Improving docking performance using negative image-based rescoring. *Front. Pharmacol.* **2018**, *9*, doi:10.3389/fphar.2018.00260.

35. Virtanen, S.I.; Pentikäinen, O.T. Efficient virtual screening using multiple protein conformations described as negative images of the ligand-binding site. *J. Chem. Inf. Model.* **2010**, *50*, 1005–1011, doi:10.1021/ci100121c.
36. Juvonen, R.O.; Kuusisto, M.; Fohrgrup, C.; Pitkänen, M.H.; Nevalainen, T.J.; Auriola, S.; Raunio, H.; Pasanen, M.; Pentikäinen, O.T. Inhibitory effects and oxidation of 6-methylcoumarin, 7-methylcoumarin and 7-formylcoumarin via human CYP2A6 and its mouse and pig orthologous enzymes. *Xenobiotica* **2016**, *46*, 14–24, doi:10.3109/00498254.2015.1048327.
37. Shubina, V.; Niinivehmas, S.; Pentikäinen, O.T. Reliability of virtual screening methods in prediction of PDE4B-inhibitor activity. *Curr. Drug Discov. Technol.* **2015**, *12*, 117–126.
38. Raunio, H.; Rahnasto-Rilla, M. CYP2A6: Genetics, structure, regulation, and function. *Drug Metabol. Drug Interact.* **2012**, *27*, 73–88.
39. Heinlein, C.A.; Chang, C. Androgen receptor in prostate cancer. *Endocr. Rev.* **2004**, *25*, 276–308, doi:10.1210/er.2002-0032.
40. Maxwell, C.R.; Kanes, S.J.; Abel, T.; Siegel, S.J. Phosphodiesterase inhibitors: A novel mechanism for receptor-independent antipsychotic medications. *Neuroscience* **2004**, *129*, 101–107, doi:10.1016/j.neuroscience.2004.07.038.
41. Brown, W.M. Treating COPD with PDE 4 inhibitors. *Int. J. COPD* **2007**, *2*, 517–533.
42. Berman, H.M.; Westbrook, J.; Feng, Z.; Gilliland, G.; Bhat, T.N.; Weissig, H.; Shindyalov, I.N.; Bourne, P.E. The protein data bank. *Nucleic Acids Res.* **2000**, *28*, 235–242, doi:10.1093/nar/28.1.235.
43. Rose, P.W.; Prlic, A.; Altunkaya, A.; Bi, C.; Bradley, A.R.; Christie, C.H.; Costanzo, L. Di; Duarte, J.M.; Dutta, S.; Feng, Z.; Green, R.K.; Goodsell, D.S.; Hudson, B.; Kalro, T.; Lowe, R.; Peisach, E.; Randle, C.; Rose, A.S.; Shao, C.; Tao, Y.-P.; Valasatava, Y.; Voigt, M.; Westbrook, J.D.; Woo, J.; Yang, H.; Young, J.Y.; Zardecki, C.; Berman, H.M.; Burley, S.K. The RCSB protein data bank: integrative view of protein, gene and 3D structural information. *Nucleic Acids Res.* **2017**, *45*, D271–D281, doi:10.1093/nar/gkw1000.
44. Yano, J.K.; Hsu, M.-H.; Griffin, K.J.; Stout, C.D.; Johnson, E.F. Structures of human microsomal cytochrome P450 2A6 complexed with coumarin and methoxsalen. *Nat. Struct. Mol. Biol.* **2005**, *12*, 822–823, doi:10.1038/nsmb971.
45. Matias, P.M.; Carrondo, M.A.; Coelho, R.; Thomaz, M.; Zhao, X.-Y.; Wegg, A.; Crusius, K.; Egner, U.; Donner, P. Structural basis for the glucocorticoid response in a mutant human androgen receptor (AR(ccr)) derived from an androgen-independent prostate cancer. *J. Med. Chem.* **2002**, *45*, 1439–1446.
46. Bohl, C.E.; Gao, W.; Miller, D.D.; Bell, C.E.; Dalton, J.T. Structural basis for antagonism and resistance of bicalutamide in prostate cancer. *Proc. Natl. Acad. Sci. U. S. A.* **2005**, *102*, 6201–6206, doi:10.1073/pnas.0500381102.
47. Pereira de Jesus-Tran, K.; Côté, P.-L.; Cantin, L.; Blanchet, J.; Labrie, F.; Breton, R. Comparison of crystal structures of human androgen receptor ligand-binding domain complexed with various agonists reveals

- molecular determinants responsible for binding affinity. *Protein Sci.* 2006, 15, 987–999.
48. Wang, F.; Liu, X.; Li, H.; Liang, K.; Miner, J.N.; Hong, M.; Kallel, E.A.; van Oeveren, A.; Zhi, L.; Jiang, T. Structure of the ligand-binding domain (LBD) of human androgen receptor in complex with a selective modulator LGD2226. *Acta Crystallogr. Sect. F Struct. Biol. Cryst. Commun.* 2006, 62, 1067–1071.
49. Sun, C.; Robl, J.A.; Wang, T.C.; Huang, Y.; Kuhns, J.E.; Lupisella, J.A.; Beehler, B.C.; Golla, R.; Sleph, P.G.; Seethala, R.; Fura, A.; Krystek, S.R.J.; An, Y.; Malley, M.F.; Sack, J.S.; Salvati, M.E.; Grover, G.J.; Ostrowski, J.; Hamann, L.G. Discovery of potent, orally-active, and muscle-selective androgen receptor modulators based on an N-aryl-hydroxybicyclohydantoin scaffold. *J. Med. Chem.* 2006, 49, 7596–7599, doi:10.1021/jm061101w.
50. Bohl, C.E.; Wu, Z.; Miller, D.D.; Bell, C.E.; Dalton, J.T. Crystal structure of the T877A human androgen receptor ligand-binding domain complexed to cyproterone acetate provides insight for ligand-induced conformational changes and structure-based drug design. *J. Biol. Chem.* 2007, 282, 13648–13655, doi:10.1074/jbc.M611711200.
51. Cantin, L.; Faucher, F.; Couture, J.-F.; de Jesus-Tran, K.P.; Legrand, P.; Ciobanu, L.C.; Frechette, Y.; Labrecque, R.; Singh, S.M.; Labrie, F.; Breton, R. Structural characterization of the human androgen receptor ligand-binding domain complexed with EM5744, a rationally designed steroidal ligand bearing a bulky chain directed toward helix 12. *J. Biol. Chem.* 2007, 282, 30910–30919, doi:10.1074/jbc.M705524200.
52. Bohl, C.E.; Wu, Z.; Chen, J.; Mohler, M.L.; Yang, J.; Hwang, D.J.; Mustafa, S.; Miller, D.D.; Bell, C.E.; Dalton, J.T. Effect of B-ring substitution pattern on binding mode of propionamide selective androgen receptor modulators. *Bioorg. Med. Chem. Lett.* 2008, 18, 5567–5570, doi:10.1016/j.bmcl.2008.09.002.
53. Duke, C.B.; Jones, A.; Bohl, C.E.; Dalton, J.T.; Miller, D.D. Unexpected binding orientation of bulky-B-ring anti-androgens and implications for future drug targets. *J. Med. Chem.* 2011, 54, 3973–3976, doi:10.1021/jm2000097.
54. Hsu, C.-L.; Liu, J.-S.; Wu, P.-L.; Guan, H.-H.; Chen, Y.-L.; Lin, A.-C.; Ting, H.-J.; Pang, S.-T.; Yeh, S.-D.; Ma, W.-L.; Chen, C.-J.; Wu, W.-G.; Chang, C. Identification of a new androgen receptor (AR) co-regulator BUD31 and related peptides to suppress wild-type and mutated AR-mediated prostate cancer growth via peptide screening and X-ray structure analysis. *Mol. Oncol.* 2014, 8, 1575–1587, doi:10.1016/j.molonc.2014.06.009.
55. Aikawa, K.; Asano, M.; Ono, K.; Habuka, N.; Yano, J.; Wilson, K.; Fujita, H.; Kandori, H.; Hara, T.; Morimoto, M.; Santou, T.; Yamaoka, M.; Nakayama, M.; Hasuoka, A. Synthesis and biological evaluation of novel selective androgen receptor modulators (SARMs) Part III: Discovery of 4-(5-oxopyrrolidine-1-yl)benzotrile derivative 2f as a clinical candidate. *Bioorg. Med. Chem.* 2017, 25, 3330–3349, doi:10.1016/j.bmc.2017.04.018.
56. Goto, T.; Shiina, A.; Murata, T.; Tomii, M.; Yamazaki, T.; Yoshida, K.I.; Yoshino, T.; Suzuki, O.; Sogawa, Y.; Mizukami, K.; Takagi, N.; Yoshitomi, T.; Etori, M.; Tsuchida, H.; Mikkaichi, T.; Nakao, N.; Takahashi, M.; Takahashi, H.; Sasaki, S. Identification of the 5,5-dioxo-7,8-dihydro-6H-thiopyrano[3,2-d]pyrimidine derivatives as highly selective PDE4B inhibitors. *Bioorganic Med. Chem. Lett.* 2014, 24, 893–899,

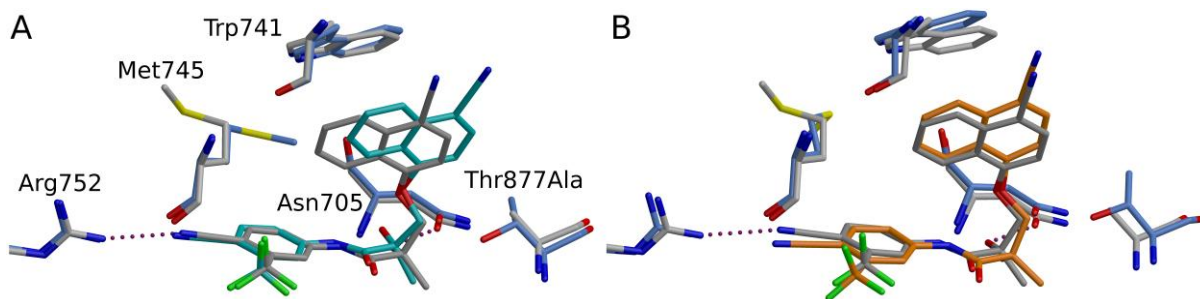
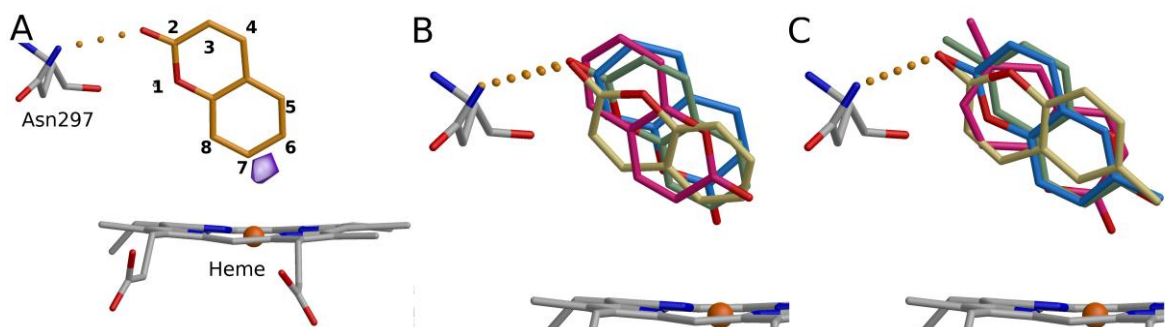
doi:10.1016/j.bmcl.2013.12.076.

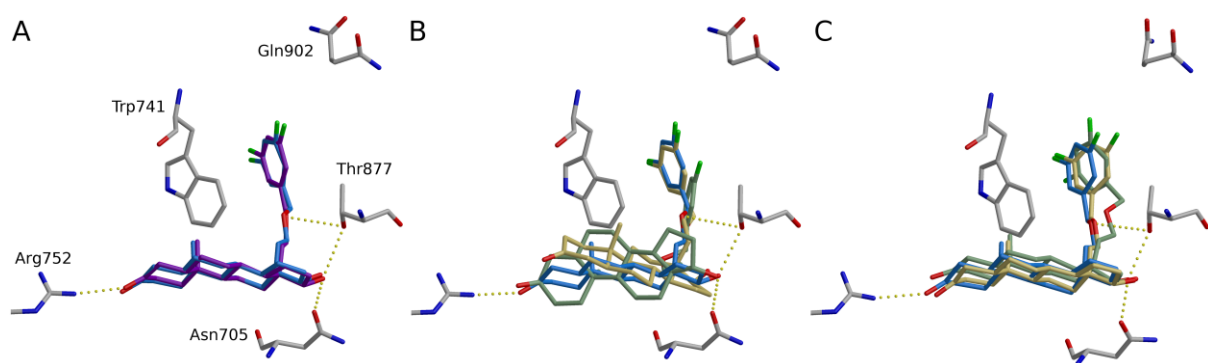
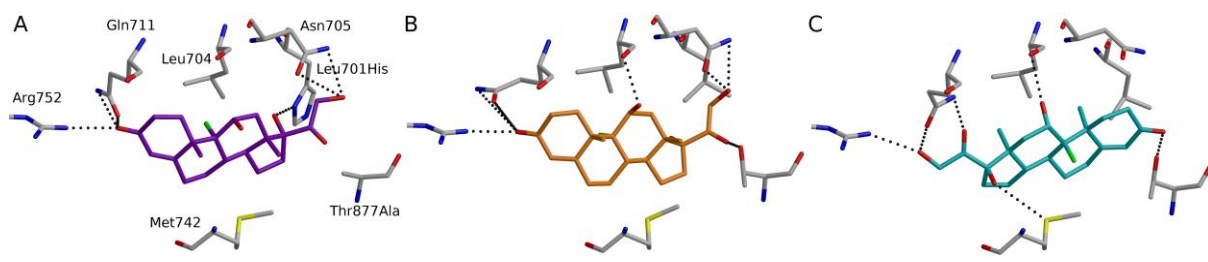
57. Word, J.M.; Lovell, S.C.; Richardson, J.S.; Richardson, D.C. Asparagine and Glutamine: Using Hydrogen Atom Contacts in the Choice of Side-chain Amide Orientation. *J. Mol. Biol.* **1999**, *285*, 1735–1747, doi:10.1006/jmbi.1998.2401.
58. Pelkonen, O.; Rautio, A.; Raunio, H.; Pasanen, M. CYP2A6: A human coumarin 7-hydroxylase. *Toxicology* **2000**, *144*, 139–147.
59. Kuang, R.; Shue, H.J.; Xiao, L.; Blythin, D.J.; Shih, N.Y.; Chen, X.; Gu, D.; Schwerdt, J.; Lin, L.; Ting, P.C.; Cao, J.; Aslanian, R.; Piwinski, J.J.; Prelusky, D.; Wu, P.; Zhang, J.; Zhang, X.; Celly, C.S.; Billah, M.; Wang, P. Discovery of oxazole-based PDE4 inhibitors with picomolar potency. *Bioorganic Med. Chem. Lett.* **2012**, *22*, 2594–2597, doi:10.1016/j.bmcl.2012.01.115.
60. Kuang, R.; Shue, H.J.; Blythin, D.J.; Shih, N.Y.; Gu, D.; Chen, X.; Schwerdt, J.; Lin, L.; Ting, P.C.; Zhu, X.; Aslanian, R.; Piwinski, J.J.; Xiao, L.; Prelusky, D.; Wu, P.; Zhang, J.; Zhang, X.; Celly, C.S.; Minnicozzi, M.; Billah, M.; Wang, P. Discovery of a highly potent series of oxazole-based phosphodiesterase 4 inhibitors. *Bioorganic Med. Chem. Lett.* **2007**, *17*, 5150–5154, doi:10.1016/j.bmcl.2007.06.092.
61. Irvine, M.W.; Patrick, G.L.; Kewney, J.; Hastings, S.F.; MacKenzie, S.J. Rhodanine derivatives as novel inhibitors of PDE4. *Bioorganic Med. Chem. Lett.* **2008**, *18*, 2032–2037, doi:10.1016/j.bmcl.2008.01.117.
62. Allcock, R.W.; Blakli, H.; Jiang, Z.; Johnston, K.A.; Morgan, K.M.; Rosair, G.M.; Iwase, K.; Kohno, Y.; Adams, D.R. Phosphodiesterase inhibitors. Part 1: Synthesis and structure-activity relationships of pyrazolopyridine-pyridazinone PDE inhibitors developed from ibudilast. *Bioorganic Med. Chem. Lett.* **2011**, *21*, 3307–3312, doi:10.1016/j.bmcl.2011.04.021.
63. Ochiai, K.; Takita, S.; Kojima, A.; Eiraku, T.; Iwase, K.; Kishi, T.; Ohinata, A.; Yageta, Y.; Yasue, T.; Adams, D.R.; Kohno, Y. Phosphodiesterase inhibitors. Part 5: Hybrid PDE3/4 inhibitors as dual bronchorelaxant/anti-inflammatory agents for inhaled administration. *Bioorganic Med. Chem. Lett.* **2013**, *23*, 375–381, doi:10.1016/j.bmcl.2012.08.121.
64. Ochiai, K.; Takita, S.; Kojima, A.; Eiraku, T.; Ando, N.; Iwase, K.; Kishi, T.; Ohinata, A.; Yageta, Y.; Yasue, T.; Adams, D.R.; Kohno, Y. Phosphodiesterase inhibitors. Part 4: Design, synthesis and structure-activity relationships of dual PDE3/4-inhibitory fused bicyclic heteroaromatic-4,4-dimethylpyrazolones. *Bioorganic Med. Chem. Lett.* **2012**, *22*, 5833–5838, doi:10.1016/j.bmcl.2012.07.088.
65. Korb, O.; Stützel, T.; Exner, T.E. Empirical scoring functions for advanced protein-ligand docking with PLANTS. *J. Chem. Inf. Model.* **2009**, *49*, 84–96, doi:10.1021/ci800298z.
66. Bayly, C.I.; Cieplak, P.; Cornell, W.; Kollman, P.A. A well-behaved electrostatic potential based method using charge restraints for deriving atomic charges: the RESP model. *J. Phys. Chem.* **1993**, *97*, 10269–10280, doi:10.1021/j100142a004.
67. Wang, J.M.; Wang, W.; Kollman, P.A. Antechamber: An Accessory Software Package for Molecular Mechanical Calculations. *Abstr. Pap. Am. Chem. S.* **2001**, *222*, U403–U403.

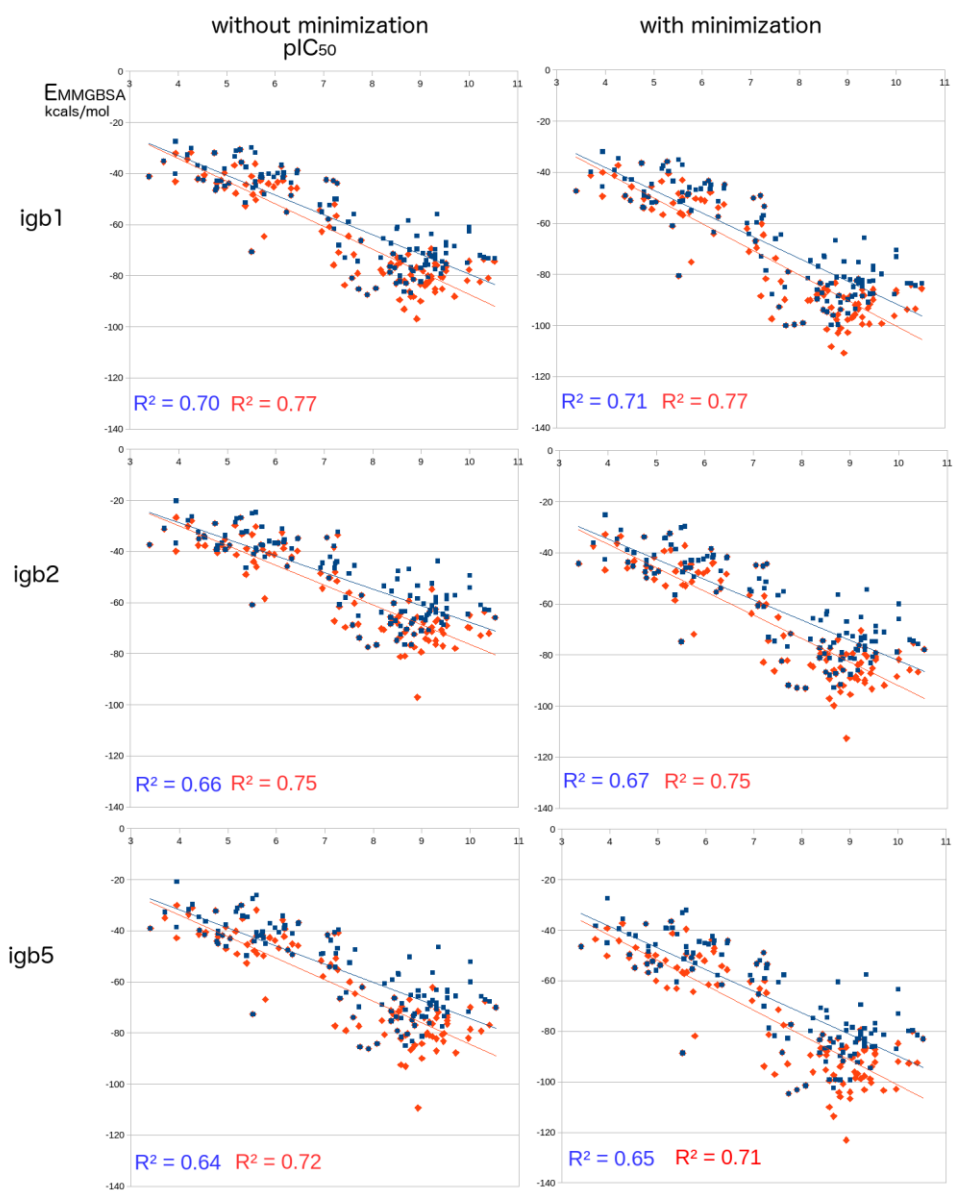
68. Wang, J.; Wang, W.; Kollman, P.A.; Case, D.A. Automatic atom type and bond type perception in molecular mechanical calculations. *J. Mol. Graph. Model.* **2006**, *25*, 247–260.
69. Jorgensen, W.L.; Chandrasekhar, J.; Madura, J.D.; Impey, R.W.; Klein, M.L. Comparison of simple potential functions for simulating liquid water. *J. Chem. Phys.* **1983**, *79*, 926–935, doi:10.1063/1.445869.
70. Maier, J.A.; Martinez, C.; Kasavajhala, K.; Wickstrom, L.; Hauser, K.E.; Simmerling, C. ff14SB: Improving the Accuracy of Protein Side Chain and Backbone Parameters from ff99SB. *J. Chem. Theory Comput.* **2015**, *11*, 3696–3713, doi:10.1021/acs.jctc.5b00255.
71. Giammona, D.A. Force field modifications for united atom heme plus flexible water, University of California, 1984.
72. Phillips, J.C.; Braun, R.; Wang, W.; Gumbart, J.; Tajkhorshid, E.; Villa, E.; Chipot, C.; Skeel, R.D.; Kale, L.; Schulten, K. Scalable molecular dynamics with NAMD. *J. Comput. Chem.* **2005**, *26*, 1781–1802, doi:10.1002/jcc.20289.
73. Lehtonen, J. V.; Still, D.-J.; Rantanen, V.-V.; Ekholm, J.; Björklund, D.; Iftikhar, Z.; Huhtala, M.; Repo, S.; Jussila, A.; Jaakkola, J.; Pentikäinen, O.; Nyrönen, T.; Salminen, T.; Gyllenberg, M.; Johnson, M.S. BODIL: a molecular modeling environment for structure-function analysis and drug design. *J. Comput. Aided. Mol. Des.* **2004**, *18*, 401–419.
74. Roe, D.R.; Cheatham, T.E. 3rd PTRAJ and CPPTRAJ: Software for Processing and Analysis of Molecular Dynamics Trajectory Data. *J. Chem. Theory Comput.* **2013**, *9*, 3084–3095, doi:10.1021/ct400341p.
75. Miller, B.R.; McGee, T.D.; Swails, J.M.; Homeyer, N.; Gohlke, H.; Roitberg, A.E. MMPBSA.py: An Efficient Program for End-State Free Energy Calculations. *J. Chem. Theory Comput.* **2012**, *8*, 3314–3321, doi:10.1021/ct300418h.
76. Motta, S.; Bonati, L. Modeling Binding with Large Conformational Changes: Key Points in Ensemble-Docking Approaches. *J. Chem. Inf. Model.* **2017**, *57*, 1563–1578, doi:10.1021/acs.jcim.7b00125.
77. Swift, R. V.; Jusoh, S.A.; Offutt, T.L.; Li, E.S.; Amaro, R.E. Knowledge-Based Methods to Train and Optimize Virtual Screening Ensembles. *J. Chem. Inf. Model.* **2016**, *56*, 830–842, doi:10.1021/acs.jcim.5b00684.
78. Wahl, J.; Smieško, M. Endocrine Disruption at the Androgen Receptor: Employing Molecular Dynamics and Docking for Improved Virtual Screening and Toxicity Prediction. *Int. J. Mol. Sci.* **2018**, *19*.
79. Liu, H.; Han, R.; Li, J.; Liu, H.; Zheng, L. Molecular mechanism of R-bicalutamide switching from androgen receptor antagonist to agonist induced by amino acid mutations using molecular dynamics simulations and free energy calculation. *J. Comput. Aided. Mol. Des.* **2016**, *30*, 1189–1200, doi:10.1007/s10822-016-9992-2.
80. Sheridan, R.P.; Korzekwa, K.R.; Torres, R. a.; Walker, M.J. Empirical regioselectivity models for human cytochromes P450 3A4, 2D6, and 2C9. *J. Med. Chem.* **2007**, *50*, 3173–3184, doi:10.1021/jm0613471.
81. Zaretski, J.; Rydberg, P.; Bergeron, C.; Bennett, K.P.; Olsen, L.; Breneman, C.M. RS-predictor models

augmented with SMARTCyp reactivities: Robust metabolic regioselectivity predictions for nine CYP isozymes. *J. Chem. Inf. Model.* **2012**, *52*, 1637–1659, doi:10.1021/ci300009z.

82. Sheng, Y.; Chen, Y.; Wang, L.; Liu, G.; Li, W.; Tang, Y. Effects of protein flexibility on the site of metabolism prediction for CYP2A6 substrates. *J. Mol. Graph. Model.* **2014**, *54*, 90–99, doi:10.1016/j.jmglm.2014.09.005.
83. Kimonen, T.; Juvonen, R.O.; Alhava, E.; Pasanen, M. The inhibition of CYP enzymes in mouse and human liver by pilocarpine. *Br. J. Pharmacol.* **1995**, *114*, 832–836, doi:10.1111/j.1476-5381.1995.tb13279.x.
84. Kinonen, T.; Pasanen, M.; Gynther, J.; Poso, A.; Jarvinen, T.; Alhava, E.; Juvonen, R.O. Competitive inhibition of coumarin 7-hydroxylation by pilocarpine and its interaction with mouse CYP2A5 and human CYP2A6. *Br. J. Pharmacol.* **1995**, *116*, 2625–2630.
85. DeVore, N.M.; Meneely, K.M.; Bart, A.G.; Stephens, E.S.; Battaile, K.P.; Scott, E.E. Structural comparison of cytochromes P450 2A6, 2A13, and 2E1 with pilocarpine. *FEBS J.* **2012**, *279*, 1621–1631, doi:10.1111/j.1742-4658.2011.08412.x.
86. Endo, T.; Ban, M.; Hirata, K.; Yamamoto, A.; Hara, Y.; Momose, Y. Involvement of CYP2A6 in the formation of a novel metabolite, 3-hydroxypilocarpine, from pilocarpine in human liver microsomes. *Drug Metab. Dispos.* **2007**, *35*, 476–483, doi:10.1124/dmd.106.013425.
87. Raunio, H.; Kuusisto, M.; Juvonen, R.O.; Pentikänen, O.T. Modeling of interactions between xenobiotics and cytochrome P450 (CYP) enzymes. *Front. Pharmacology* **2015**, *6*, 1–14, doi:10.3389/fphar.2015.00123.
88. Clark, R.D.; Strizhev, A.; Leonard, J.M.; Blake, J.F.; Matthew, J.B. Consensus scoring for ligand/protein interactions. *J. Mol. Graph. Model.* **2002**, *20*, 281–295, doi:10.1016/S1093-3263(01)00125-5.
89. Charifson, P.S.; Corkery, J.J.; Murcko, M.A.; Walters, W.P. Consensus scoring: A method for obtaining improved hit rates from docking databases of three-dimensional structures into proteins. *J. Med. Chem.* **1999**, *42*, 5100–5109, doi:10.1021/jm990352k.









III

DEVELOPMENT OF NEW COUMARIN-BASED PROFLUORESCENT SUBSTRATES FOR HUMAN CYTOCHROME P450 ENZYMES

by

Juvonen R.O., Ahinko M., Huuskonen J., Raunio H. & Pentikäinen O.T., 2019

Xenobiotica 49: 1015–1024

DOI 10.1080/00498254.2018.1530399

Reproduced with kind permission by Taylor & Francis.

Development of New Coumarin-Based Profluorescent Substrates for Human Cytochrome P450 Enzymes

Risto O. Juvonen^{1,*}, Mira Ahinko², Juhani Huuskonen³, Hannu Raunio¹, Olli T. Pentikäinen^{2,4,*}

1 School of Pharmacy, Faculty of Health Sciences, University of Eastern Finland, Box 1627, 70211 Kuopio, Finland

2 University of Jyväskylä, Department of Biological and Environmental Science & Nanoscience Center, P.O. Box 35, FI-40014 University of Jyväskylä, Finland

3 University of Jyväskylä, Department of Chemistry, P.O. Box 35, FI-40014 University of Jyväskylä, Finland

4 Institute of Biomedicine, Faculty of Medicine, Integrative Physiology and Pharmacology, University of Turku, Kiinamylynkatu 10, FI-20520 Turku, Finland

* Corresponding authors: risto.juvonen@uef.fi (in vitro); olli.pentikainen@utu.fi (modeling and synthesis).

Abstract

1. Cytochrome P450 (CYP) enzymes constitute an essential xenobiotic metabolizing system that regulates the elimination of lipophilic compounds from the body. Convenient and affordable assays for CYP enzymes are important for assessing these metabolic pathways.
2. In this study, 10 novel profluorescent coumarin derivatives with various substitutions at carbons 3, 6 and 7 were developed. Molecular modeling indicated that 3-phenylcoumarin offers an excellent scaffold for the development of selective substrate compounds for various human CYP forms, as they could be metabolized to fluorescent 7-hydroxycoumarin derivatives. Oxidation of profluorescent coumarin derivatives to fluorescent metabolites by 13 important human liver xenobiotic-metabolizing CYP forms was determined by enzyme kinetic assays.
3. Four of the coumarin derivatives were converted to fluorescent metabolites by CYP1 family enzymes, with 6-methoxy-3-(4-trifluoromethylphenyl)coumarin being oxidized selectively by CYP1A2 in human liver microsomes. Another set of four compounds were metabolized by CYP2A6 and CYP1 enzymes. 7-Methoxy-3-(3-methoxyphenyl)coumarin was oxidized efficiently by CYP2C19 and CYP2D6 in a nonselective fashion.
4. The advantages of the novel substrates were 1) an excellent signal-to-background ratio, 2) selectivity for CYP1 forms, and 3) convenient multiwell plate measurement, allowing for precise determination of potential inhibitors of important human hepatic forms CYP1A2, CYP2C19 and CYP2D6.

Keywords: drug metabolism, CYP, oxidation, fluorescence, coumarin, derivative, enzyme kinetics

Abbreviations: 3-cyano-7-ethoxycoumarin (CEC), 7-ethoxy-4-trifluoromethylcoumarin (EFC), 7-methoxy-4-trifluoromethylcoumarin (MFC), 7-methoxy-4-aminomethylcoumarin (MAMC) and 7-benzyloxy-4-trifluoromethylcoumarin (BFC)

INTRODUCTION

Cytochrome P450 (CYP) monooxygenases are the most versatile enzymes that metabolize lipophilic exogenous compounds entering the body. This metabolism is an essential mechanism of elimination for both xenobiotics and harmful endogenous compounds (Gonzalez et al., 2018). The CYP enzymes comprise a very large superfamily, with 57 individual human forms identified. Of these CYP forms, approximately 10 members in the families CYP1, CYP2 and CYP3 catalyze the oxidation of xenobiotics to a significant degree (Testa et al., 2012; Guengerich 2017). CYPs are most abundantly expressed in the liver, but they are also present in other barrier tissues such as the gastrointestinal tract, lung, skin, kidney and nose epithelium (Sevior et al., 2012; Zanger and Schwab, 2013).

When new chemical compounds are developed, especially novel pharmaceuticals and pesticides, it is necessary to thoroughly evaluate their metabolic pathways and the enzymes that catalyze them. In particular, the CYP-mediated metabolism needs to be assessed. For pharmaceutical candidates, this ensures that the factors affecting their pharmacokinetics and drug interactions mediated by interference with metabolic pathways are on record (Kirchmair et al., 2015, Zientek and Youdim 2015, Fowler et al., 2017).

Inhibition of CYP enzymes is a major mechanism for metabolism-based drug interactions. Several different kinds of *in vitro* methods have been established to identify and quantitatively measure the type and extent of CYP inhibition. In such experiments, the CYP enzymes can be introduced into the incubation mixture as individual cDNA-expressed CYP forms or as enzyme mixtures, i.e., tissue fractions such as human liver microsomes (Pelkonen et al., 2005; 2013, Knights et al., 2016).

For the measurement of a substrate and its metabolites in *in vitro* assays, the most versatile analytical approaches are liquid chromatography-mass spectrometry (LC-MS) methods. The drawback of these methods is that the equipment is expensive and its use is labor intensive (Tolonen and Pelkonen, 2015). In contrast, using probe substrates that are selective for the CYP forms of interest allows the use of simple analytical methods such as fluorescence detection. High-throughput data acquisition is possible using direct profluorescent CYP substrates in a multiwell plate format. Suitable substrates for the five principal drug-metabolizing enzymes (CYP1A2, CYP2C9, CYP2C19, CYP2D6 and CYP3A4) were reported in the late 1990s (Crespi et al., 1997). Other techniques were subsequently developed, including the commercially available Vivid® fluorescent substrates (Trubetskoy et al., 2005) and

luminogenic assays (Cali et al., 2006). These assays are based on CYP-catalyzed reactions which generate easily detectable products.

Coumarin derivatives can be converted to 7-hydroxycoumarin metabolites in an oxidation reaction typical to CYP enzymes (Figure 1). Substitution of the coumarin scaffold at the 7-position with an electron-donating group yields highly fluorescent molecules (Lavis and Raines, 2014). Thus, many coumarin derivatives are used as profluorescent CYP substrates; these include 7-ethoxycoumarin, 3-cyano-7-ethoxycoumarin (CEC), 7-ethoxy-4-trifluoromethylcoumarin (EFC), 7-methoxy-4-trifluoromethylcoumarin (MFC), 7-methoxy-4-aminomethylcoumarin (MAMC) and 7-benzyloxy-4-trifluoromethylcoumarin (BFC). The shortcoming of these substrates is that they are not selective but are oxidized by several CYP forms (Crespi et al., 1997; Crespi and Stresser, 2000; Rendic 2000; Turpeinen et al., 2006; Waxman and Chang, 2006). Coumarin is an example of a selective substrate, as it is oxidized practically exclusively by human CYP2A6, mouse CYP2A5 and pig CYP2A19 to fluorescent 7-hydroxycoumarin (Pelkonen et al., 2000; Skaanild and Friis, 2005; Raunio and Rahnasto-Rilla, 2012).

Figure 1.

Ideally, selective profluorescent CYP substrates would provide an efficient and low-cost toolbox for studying CYP form-specific metabolism in simple fluorescence-based assays. However, although many profluorescent substrates are available, new selective and sensitive substrates are needed as most human CYP forms are still missing the optimal profluorescent substrate. Diverse options to functionalize the coumarin core provide a wide chemical space to explore and design new CYP substrates. We have previously synthesized a series of coumarin derivatives to be evaluated as ligands for various pharmacologically important targets, including 17 β -hydroxysteroid dehydrogenases, (Niinivehmas et al., 2018) estrogen receptor α (Niinivehmas et al., 2016) and monoamine oxidase B (Rauhamaäki et al., 2018). Some of these derivatives showed marked changes in their fluorescence properties after oxidation. This prompted us to develop novel substrates for human UDP-glucuronosyltransferase (UGT) enzymes based on the loss of fluorescence of the 7-hydroxyl-substituted coumarins upon glucuronidation (Juvonen et al., 2018).

In this study, we expanded the coumarin-based library with 3-substituted derivatives as substrates for CYP enzymes. Novel derivatives with potentially suitable interactions with the key xenobiotic-metabolizing human CYP forms were evaluated by docking them in three-dimensional CYP models. The most promising compounds were tested for their absorbance and fluorescence properties, their CYP form selectivity and their key enzyme kinetic characteristics. Several of the compounds proved to be selective, especially for CYP1A forms. Molecular modeling approaches rationalized the structural features that defined the CYP form selectivity.

MATERIALS AND METHODS

Molecular modeling. The 7-hydroxylation selectivity of the 3-phenylcoumarin derivatives by CYP forms was assessed using structural analysis, docking and multiple sequence alignment of the CYP forms. The 3D structures of the enzymes in the scope of this study were retrieved from the Protein Databank (PDB; www.rcsb.org) (Berman et al., 2000) (Supplementary Table S1), except CYP3A7, whose structure has not yet been solved. Where applicable, the selection of crystal structures was based on the bound ligands so that they would resemble the 3-phenylcoumarin core as closely as possible. However, in many cases such as for CYP3A4 the bound ligands considerably diverged from this requirement. The A chains of the CYP structures were superimposed to the A chain of the CYP1A1 structure with Vertaa in Bodil and were examined visually using Bodil (Lehtonen et al., 2004). The full sequences of all the forms were acquired from the UniProt database (The UniProt Consortium, 2017) (Table S1). The multiple sequence alignment was built on top of the pre-aligned sequences derived from the above mentioned superimposition of CYP2A6 and CYP3A4 to CYP1A1, by using Malign (Wheeler and Gladstein, 1994) in Bodil with structure-based matrix (STRMAT110) (Johnson and Overington, 1993) and gap penalty of 30.

The 3D structures, protonation states, possible tautomers, conformers, and metal-binding states for the 3-phenylcoumarin derivatives at pH 7.4 were prepared using LigPrep and ConfGenX in Schrödinger Release 2017-3 (Schrödinger LLC, New York, NY, USA, 2017). The 3-phenylcoumarin analogs were docked to the CYP1A1, CYP1A2, CYP1B1, CYP2A6, CYP2D6 and CYP2C19 structures using the PANTHER protocol (Niinivehmas et al., 2015), which creates a negative image of the protein binding site, and the shape- and electrostatics-based superimposition of ShaEP (Vainio et al., 2009). Conformations that overlapped with the

corresponding protein structure were removed. Figures were prepared using VMD 1.9.2 (Humphrey et al., 1996).

Chemicals. 7-Benzyloxy-4-trifluoromethylcoumarin (BFC) was from Corning (Corning, NY, USA). Formic acid (99 %) and MgCl₂ were from Honeywell Riedel-de Haen (Bucharest, Romania). Acetonitrile (Ultra gradient HPLC grade), methanol (HPLC gradient grade) and glycine were from Fisher J.T. Baker (Waltham, Massachusetts, USA). Ethanol (≥99.5 %, Etax Aa) was from Altia (Helsinki, Finland). Water was deionized by MilliQ gradient A10. All chemicals were of the highest purity available from their commercial suppliers. Trichloroacetic acid, 7-hydroxy-4-trifluoromethylcoumarin (HFC), Tris-HCl, MnCl₂, MgCl₂, reduced glutathione (GSH), isocitric acid and isocitric acid dehydrogenase were purchased from Sigma-Aldrich (Steinheim, Germany), KCl from J.T. Baker, NADPH and NADP⁺ from Roche Diagnostics (Mannheim, Germany). 200 mL NADPH regenerating system contained 178.5 mg NADP⁺ (nicotinamide adenine dinucleotide phosphate), 645 mg isocitric acid, 340 mg KCl, 240 mg MgCl₂, 0.32 mg MnCl₂ and 15 U isocitric acid dehydrogenase.

Synthesis of coumarin derivatives and reference compounds. Synthesis and experimental data for **1–4** and **7–10** (Figure 2) have been published earlier (Niinivehmas et al., 2018; Rauhamäki et al., 2018). Compound **6** (Figure 2) has been published by another research group (Delogu et al., 2014). BFC (**11**) was used a reference substrate, and the readily fluorescent 7-hydroxy-3-(4-fluorophenyl)coumarin (**12**) was used as a surrogate standard for quantification of metabolite formation (Figure 2).

Figure 2.

A typical procedure (Figure 3.): A mixture of salicylaldehyde derivative (2 mmol) and phenyl acetic acid derivative (2.1 mmol), acetic acid anhydride (0.6 mL) and trimethylamine (TEA) (0.36 mL) were placed in a microwave reactor tube and this mixture was heated at 100–170°C with microwave apparatus for 10–20 min. After cooling, 2 ml of 10% NaHCO₃ solution was added and the precipitate was filtered, dried and recrystallized from ethanol/H₂O or acetone/H₂O mixture. The acetyl group(s) were removed by treating the compound with methanol/NaOH(aq) solution for 30-60 min at room temperature. The solution was acidified

with HCl(aq) and the precipitate was filtered and recrystallized if needed. Based on the elemental analysis and/or ¹H-NMR the purity of compounds was >95%.

Figure 3.

6-Chloro-3-(pyridin-3-yl)coumarin (**5**). Yield 46%, m.p. 220-222°C; ¹H-NMR(d₆-DMSO, 300 MHz): = 7.52 (m, 2H, H-8, H-5'), 7.69 (dd, 1H, J₃ = 8.8 Hz, J₄ = 2.6 Hz, H-7), 7.89 (d, 1H, J₄ = 2.6 Hz, H-5), 8.12 (dd, 1H, J₃ = 8.0 Hz, J₄ = 2.3 Hz, J_{4'} = 1.7 Hz, H-6), 8.33 (s, 1H, H-4), 8.63 (dd, 1H, J₃ = 4.8 Hz, J₄ = 1.8 Hz, H-4'), 8.88 (dd, 1H, J₄ = 2.4, J₅ = 0.8 Hz, H-2'); ¹³C-NMR(d₆-DMSO): = 118.06, 120.71, 123.24, 125.38, 127.69, 128.39, 130.31, 131.61, 136.07, 140.06, 148.94, 149.61, 151.79, 159.21; Elemental analysis for C₁₄H₈ClNO₂·0.25H₂O calc. C% 64.14 H% 3.27 N% 5.34, found C% 64.28 H% 3.20 N% 4.87.

6-Chloro-3-(4-hydroxyphenyl)coumarin (**6**). Yield 77%, m.p. 245-247°C; ¹H-NMR(d₆-DMSO, 300 MHz): = 6.85 (d, J₃ = 7.7 Hz, H-3', H-5'), 7.45 (d, J₃ = 8.8 Hz, H-8), 7.55-7.62 (m, 3H, H-7, H-2', H-6'), 7.85 (d, 1H, J₄ = 2.6 Hz, H-5), 8.10 (s, 1H, H-4), 9.79 (s, 1H, Ph-OH); ¹³C-NMR(d₆-DMSO): = 115.11, 117.74, 121.13, 124.85, 127.22, 127.81, 128.17, 129.88, 130.57, 137.11, 151.22, 158.24, 159.46; Elemental analysis for C₁₅H₉ClO₃·0.5H₂O calc. C% 63.96 H% 3.58, found C% 63.75 H% 3.42.

Biological material. Baculovirus-insect cell-expressed human CYP1A1, CYP1A2, CYP1B1, CYP2A6, CYP2B6, CYP2C8, CYP2C9, CYP2C19, CYP2D6, CYP2E1, CYP3A4, CYP3A5 and CYP3A7 were purchased from BD Biosciences Discovery Labware (Woburn, MA, USA) and used according to the manufacturer's instructions.

The human liver tissue used in this study was obtained from the University of Oulu Hospital as surplus from organ transplantation surgery. The collection of the surplus tissue was approved by the Ethics Committee of the Medical Faculty of the University of Oulu (January 21, 1986). After surgical excision, the liver samples were immediately transferred to ice, cut into pieces, snap frozen in liquid nitrogen and stored at -80°C until microsomes were prepared. Microsomes were prepared as described (Lang et al., 1981).

Spectral measurements. Absorbance spectra of the coumarin derivatives (10 μM) in 100 mM phosphate buffer pH 7.4 were measured from 250 nm to 600 nm with a Hitachi U-2000

spectrophotometer (Tokyo, Japan). Excitation and emission fluorescence spectra of 10 μM compound **12** in 100 mM Tris-HCL pH 7.4 were measured at 466 nm emission and 380 nm excitation, respectively, with a Shimadzu RF-5000 fluorometer (Tokyo, Japan). Compound **12** was used as a surrogate standard to quantify the formed fluorescent metabolites from non-fluorescent parent compounds.

Oxidation assays. The kinetic assays were carried out in 100 μL volume containing 100 mM Tris-HCl buffer pH 7.4, 0–100 μM coumarin derivative, 2.5–25 nM recombinant CYP or 0–0.1 g/L microsomal protein and 20 % NADPH regenerating system. Incubations took place at 37°C in 96-multiwell plates; the fluorescence was measured with a Victor² plate reader (PerkinElmer Life Sciences, Turku, Finland). The reaction was started by adding NADPH and fluorescence measured every second minute for 40 min using excitation 405 nm and emission 460 nm. Incubation without coumarin derivative, enzyme or NADPH was used as blank reaction (negative control). Compound **12** (0–4 μM) was used as the surrogate standard to calculate the amount of product formed. The linear phase of the initial phase of the reactions was used for calculations, if it was non-linear for the whole 40 min. In the endpoint assays the reaction was stopped at 40 min by adding 150 μL 1.6 M glycine-NaOH buffer pH 10.4 and the fluorescence measured using excitation 405 nm and emission 460 nm.

When the oxidation of coumarin derivatives was inhibited by 3.2 nM–20 μM α -naphthoflavone, the same incubation conditions and measurement setup was used. One μL α -naphthoflavone was added from 100% dimethyl sulfoxide stock solution, non-inhibited sample contained 1% dimethyl sulfoxide and negative control did not contain microsomes.

RESULTS

The well-known CYP substrate coumarin, which is oxidized to fluorescent 7-hydroxycoumarin, was used as the starting point in the discovery of novel CYP form-specific substrates. Therefore, interactions between the in-house synthesized 3-phenylcoumarins and the CYP proteins were analyzed by molecular modeling to identify characteristics that support oxidation of substrate candidates to fluorescent 7-hydroxycoumarin derivatives (Figure 1).

General procedure for the selection of coumarin derivatives

Ten 3-substituted coumarin derivatives, **1–10** (Figure 2) were selected for experimental tests based on the modeling results (Figure 4) with the goal of fulfilling three criteria: 1) the molecule should fit in the catalytic site of preferably only one CYP form, 2) the compound's position 7 should either be unsubstituted or have a methoxy group and 3) position 7 should be located

next to the heme moiety, being thus available for CYP oxidation. More detailed modeling data for the substrate selection are given below.

Structural basis for the selection of coumarin derivatives

A structural comparison of the CYP forms identified the CYP1A subfamily as the most ideal for accommodating and orienting position 7 of the 3-phenylcoumarin derivatives towards the heme for 7-hydroxylation. In the CYP1A subfamily, a hydroxyl group (Ser122 in CYP1A1 and Thr124 in CYP1A2) was available to act as a hydrogen bond donor to the coumarin carbonyl group (Figures 4A, 3B and S1). CYP1B1 is highly similar to the CYP1A forms but lacks the above-mentioned hydrogen bond donor, and therefore the 3-phenylcoumarin requires a hydrogen bond donor substituted at the 3-phenyl ring to interact with Asn265, which could orient such coumarin derivatives favorably for 7-hydroxylation (Figures 4C and S1).

Figure 4.

The coumarin core of 3-phenylcoumarins fits excellently into the substrate-binding cavity of CYP2A6 and could be stabilized into a catalyzing orientation with hydrophobic and hydrogen-bonding interactions (Figure 3D: CYP2A6 with docked **6**; Figure S1). To understand selective oxidation by the CYP1 forms and CYP2A6 at position 7, seven coumarin derivatives with various substitutions in positions 6 and 3-phenyl were planned for experimental testing (compounds **1–7**).

Since the models of the CYP1 forms and CYP2A6 suggested that substitution at position 6 was beneficial for binding into the hydrophobic cavity of these enzymes, a compound without any substitution in position 6 was also chosen for experimental studies (**8**). As CYPs can catalyze O-demethylation of non-fluorescent 7-methoxycoumarin derivatives to the corresponding fluorescent 7-hydroxy derivative, compounds **9** and **10** were subjected to experimental testing to fully understand the binding preference of such compounds. Compound **10** also has a bulky substituent at the 3-phenyl ring, which tested whether flexibility of the catalytic sites allowed its entrance and whether other CYP forms with larger binding cavities, such as CYP2Cs and CYP3A4, catalyzed its oxidation to the fluorescent product.

Although the selected compounds were initially directed to the CYP1 family and CYP2A6, the experimental results showed that the compounds **9** and **10** were prominent profluorescent tool

molecules for CYP2D6 and compounds 8 and 9 for CYP2C19 (see below). In CYP2D6, Ser304 can act as a hydrogen bond donor to orient the tested compounds for 7-hydroxylation, while the compound 10 is able to extend towards the substrate access channel (Figures 4E and S1). However, the 7-ethoxy group might be needed for the compounds to reach the reaction coordinates in CYP2D6. The 2'-ethoxy oxygen in compounds 8 and 9 can coordinate with CYP2C19 Asn107 by replacing the water molecule present in the crystal structure (Figures 4F and S1), but in the case of compound 10 this interaction is likely prevented by the additional phenyl group.

Increased fluorescence after CYP mediated oxidation

The absorbance and fluorescence properties of the selected coumarin derivatives (**1–10**) and the reference compounds **11** and **12** were analyzed prior to the oxidation assays. The absorbance maximums of the compounds varied between 287 and 349 nm (Table S2). The positive control **12** was strongly fluorescent at 460 nm using 405 nm excitation due to the 7-hydroxyl substituent, whereas **1–11** lacked the 7-hydroxyl substituent and were non-fluorescent or very weakly fluorescent (Figure 5A).

Compounds **1–10** were incubated in the first experiment with pig liver microsomes and in subsequent experiments with human liver microsomes and recombinant CYPs in the presence of NADPH. The emitted fluorescence at 460 nm emission using excitation 405 nm was measured for 40 min. For all compounds the fluorescence increased during incubation and was dependent on the amount of microsomes. However, if NADPH, the CYP enzyme or the coumarin derivative were missing (blanks), no increase in fluorescence occurred (Figure 5B). When **8** was incubated with three selected CYP forms (CYP1A1, CYP1A2, CYP2A6), the fluorescence intensity (ex 405 nm, em 460 nm) increased time-dependently (Figure 5B).

For all compounds, the signal-to-background fluorescence ratios increased steadily during the 40-min incubation (Figure 5C). The highest oxidation rates for the hydroxylation of position 7 in human liver microsomes were observed with compounds **4–6** and **9**, and the lowest rates were observed with compounds **2**, **3**, **7** and **8** (Figure 5D). Fluorescence was higher at more alkaline pH, such as 10.4, than at neutral pH 7.4, making possible the conventional endpoint measurement (data not shown). Accordingly, it could be assumed that all of the selected coumarin derivatives could act as profluorescent compounds for CYP forms.

Figure 5.

Oxidation of coumarin derivatives by individual CYP forms

A kinetic assay at a fixed substrate concentration (10 μM) was used to determine the oxidation rates of all coumarin derivatives by 13 human CYP forms (Figure 6). Compounds **1–10** exhibited a greater oxidation rate than the reference compound **11** (BFC). The highest rates in recombinant CYPs were observed with compounds **1**, **9** and **10**, and the lowest rates were observed with compounds **2**, **5** and **8**. All compounds were oxidized to some extent by CYP1A1, CYP1A2 or both. Compound **3** showed clear CYP1A selectivity, while **2** had CYP1A2 selectivity and **7** was oxidized by all three CYP1 forms. Compounds **4** and **5** were oxidized preferentially by CYP2A6. Compound **8** was oxidized by CYP2C19, CYP1A2 and CYP2A6, whereas **9** and **10** and the reference compound **12** were oxidized by multiple CYP forms.

Figure 6.

Kinetic parameters

The basic Michaelis-Menten enzyme kinetic parameters were determined for compounds **1–10**, catalyzed by CYP1A1, CYP1A2, CYP1B1, CYP2A6, CYP2C19 and CYP2D6 (Table 1). K_m values varied from 0.15 μM (compound **5**/CYP1A1) to 59 μM (**5**/CYP2A6). V_{\max} values ranged from 0.037 (**8**/CYP1A1) to 35 mol/(min* μmol CYP) (**9**/CYP1A2), and the intrinsic clearance (V_{\max}/K_m) ranged from 0.0017 (**8**/CYP1A1) to 49 L/(min* μmol CYP) (**6**/CYP1B1). The highest intrinsic clearance values (i.e., indicating greatest enzyme efficiency) were observed for compound **5** by CYP1A1, **9** by CYP1A2, **6** by CYP1B1 and CYP2A6, **9** by CYP2C19 and CYP2D6.

Inhibition of 7-hydroxylation by α -naphthoflavone

The 7-hydroxylation reactions of all the new compounds were catalyzed by one or multiple CYP1 forms. Accordingly, the inhibition of the reaction in human liver microsomes by α -naphthoflavone, a potent inhibitor of CYP1 forms, was determined (Figure 7). The

7-hydroxylation of compound **3** was inhibited ~90% at 0.1 μ M α -naphthoflavone; for the other compounds, inhibition ranged from 0% (compound **4**) to 65% (compound **7**).

Figure 7.

DISCUSSION

We developed 10 profluorescent coumarin derivatives, some of which showed selectivity to key human xenobiotic-metabolizing CYP forms. The excellent signal-to-background fluorescence ratio of the metabolites allowed for accurate quantification of the enzyme kinetic parameters. The novel compounds were modified differently from earlier well-known coumarin-based CYP substrates, as the substituents were either at carbon 3 or carbon 6 instead of carbon 4 or alkoxy substitution at carbon 7. These profluorescent substrates are potentially useful for evaluating the CYP inhibition potency of nonfluorescent compounds.

After incubation in conditions supporting CYP oxidation, the change in fluorescence of all the substrates could be measured using excitation 405 nm and emission 460 nm. However, the exact excitation and emission peaks differed somewhat among the compounds. The reference compound **11** (BFC) was oxidized to HFC with an emission maximum at 490 nm. NADPH did not cause interfering fluorescence at these wavelengths, as it was excited at wavelengths < 390 nm. There was little background fluorescence with all compounds. At lower excitation wavelengths, such as 350 nm, the background was increased due to fluorescence of NADPH and the coumarin derivative itself.

The formation of fluorescence was monitored continuously for up to 40 min in the multiwell plate assay. The oxidation rate could be determined from the linear phase of the reaction. The surrogate standard **12** was used to calculate all oxidation rates instead of the specific 7-hydroxyl coumarin derivative formed. This was justified because both the excitation and emission peaks of the coumarin derivatives were broad and intense, and thus the maximum wavelengths did not need to be used. To obtain more precise oxidation rates the authentic 7-hydroxycoumarin derivative standards would be required, but such standards are not presently available. The reaction rate between the substrates varied by more than 100 times, as compound **8** had a V_{\max} of less than 0.1 mol product/(min*mol CYP) catalyzed by CYP1A1, while compounds **1**, **3**, **4**, **6**, **9** and **10** showed a V_{\max} of at least 10 mol product/(min*mol CYP) with several CYP forms.

Similar oxidation rates have been observed previously with other coumarin-based CYP substrates such as coumarin, 6-methylcoumarin, 7-ethoxycoumarin, CEC and BFC (Crespi et al., 2002; Juvonen et al., 2016).

Simple structural comparison of the catalytic sites of the studied enzymes, combined with molecular docking, revealed that the CYP1 forms and CYP2A6, in particular, could be targeted with 3-phenylcoumarins. For the selected compounds **1–9**, possible binding modes were found in one or several of the catalytic sites with the preferred orientation where the 7-position of the coumarin core or the 7-methoxy substitution was toward the heme. Experimental results showed that all 10 novel coumarins were 7-hydroxylated by at least one form in the CYP1 family. The catalytic sites of the available X-ray crystal structures of the CYP1A forms were relatively small and did not provide reasonable volume for deducing binding modes by rigid docking for the larger compound **10**. Crystallization of these forms with larger substrates would be beneficial for understanding the malleability of these CYP forms.

The 3-phenylcoumarin core itself is ideal for 7-hydroxylation by the CYP1A forms. A hydrogen bond from the coumarin carbonyl to Ser122 or Thr124 in CYP1A1 or CYP1A2, respectively, can orient position 7 of the coumarin core towards the heme, while the 3-phenyl interacts with the CYP1 conserved Phe224 (CYP1A1; Figure 4A–B). CYP1B1 7-hydroxylated mainly the 3' and 4'-hydroxyl derivatives **4**, **6** and **7**, which could be favorably oriented in the catalytic site by forming a hydrogen bond to Asn265 (Figure 3C). Compound **3** was the most selective CYP1A substrate, being oxidized by CYP1A1 and CYP1A2 with very low rate occurring via CYP1B1. In human liver microsomes, the oxidation of **3** was completely blocked by α -naphthoflavone, a classical inhibitor of all three CYP1 forms (Sai *et al.* (2000), Rendic (2002)). The CYP1A2-catalyzed V_{\max} of **3** (~8 mol product/(min*mol CYP)) was clearly higher than that reported for the widely used profluorescent substrate 7-ethoxyresorufin (~1 mol product/(min*mol CYP)) (Rendic, 2002; Ghosal et al., 2003). In addition to CYP1A1, CYP1A2 and CYP1B1, 7-ethoxyresorufin was also catalyzed weakly by CYP2B6, a relatively abundant form in human liver (Rendic, 2002). Since CYP1A1 and CYP1B1 are not constitutively expressed in human liver, (Zanger and Schwab, 2013) **3** is a potentially new selective profluorescent model substrate for CYP1A2.

Compound **2** appeared to be CYP1A2 selective with very little oxidation by the other tested hepatic CYP forms. However, α -naphthoflavone inhibited oxidation of **2** by only 60% in human liver microsomes, suggesting that the liver contains other CYP(s) catalyzing the

7-hydroxylation reaction. Compounds **1**, **7** and **9** were oxidized by all CYP1 forms with varying contribution by other forms. Consequently, they were incompletely inhibited by α -naphthoflavone in liver microsomes. The intrinsic clearance of **1**, **3** and **7** by CYP1A forms was ~ 10 times greater than that of **2** by CYP1A2. The intrinsic clearance of **7** by CYP1B1 was the highest among these substrates.

Compounds **4**, **5** and **6** were oxidized rapidly and **8** slowly by CYP2A6. These were the smallest of the selected 3-phenylcoumarins and were thus able to fit into the CYP2A6 catalytic site. Compound **7** was similar in size, but the two hydroxyl groups at positions 6 and 4' were not favored in the hydrophobic catalytic site of CYP2A6. Compounds **4** and **5** showed selectivity for CYP2A6, but the selectivity was not as clear as that of coumarin 7-hydroxylation. Accordingly, coumarin remains the most selective profluorescent substrate for CYP2A6 (Pelkonen et al., 2000; Raunio and Rahnasto-Rilla, 2012). In addition to poorer selectivity, the K_m values of compounds **4**, **5** and **6** were at least 20 times higher than that of coumarin ($K_m \sim 1 \mu\text{M}$) indicating that the co-substitutions at carbons 3 and 6 of the coumarin core decreased the affinity. We reported recently that the K_m of 6-methylcoumarin was equal to that of coumarin and it was oxidized efficiently to a 7-hydroxyl metabolite by CYP2A6; (Juvonen et al., 2016) these results indicated that the catalytic site of CYP2A6 accepts many kinds of coumarin derivatives to be oxidized to fluorescent 7-hydroxyl metabolites.

Although the CYP1 family and CYP2A6 are both optimal enzymes for 3-phenylcoumarins in size and shape, their catalytic sites differ in shape and hydrophobicity. The catalytic site of CYP2A6 is smaller and more hydrophobic than the CYP1 catalytic sites, as CYP2A6 only has Asn297 as a hydrogen bonding residue while CYP1A has several residues that can interact with the coumarin carbonyl and the hydrogen bonding groups at the 3-phenyl ring. Accordingly, major differences in the specificity of the 7-hydroxylation of the 3-phenylcoumarins between the CYP1 family and CYP2A6 are likely to result mainly from the size and hydrophobicity of the compound, with CYP2A6 being more suitable for the smallest and most hydrophobic substrates.

The oxidation of compounds **8** and **9** was catalyzed by CYP2C19, but also by other CYPs. 3-O-methylfluorescein and 7-ethoxy-3-cyanocoumarin are among the current profluorescent CYP2C19 substrates. Both compounds are also catalyzed by several other human CYP forms (Rendic (2002), Ghosal et al. (2003)). The oxidation rate of compound **9** was faster (V_{\max} 4.6 mol/(min*mol CYP)) than the rate reported for 7-ethoxy-3-cyanocoumarin (V_{\max} 0.84

mol/(min* μ mol CYP)) (Ghosal et al., 2003). Compound **9** was also catalyzed by CYP2D6 with a rather high efficiency (V_{\max} 9.1 mol/(min* μ mol CYP), and intrinsic clearance was 9.1 L/(min* μ mol CYP)). CYP2D6 produced fluorescent 7-hydroxyl metabolites only by O-demethylation of the 7-methoxy derivatives (compounds **9** and **10**). Known profluorescent CYP2D6 substrates include 3-[2-(N,N-diethyl-N-methylammonium)-ethyl]-7-methoxy-4-methylcoumarin (AMMC), MFC, MAMC and some 9-N-aminoacridine derivatives, all of which are also catalyzed by several other CYP forms (Chauret et al., 2001; Rendic, 2002; Mayer et al., 2007). However, AMMC exhibits some degree of CYP selectivity, as CYP1A1, 1A2, 1B1 and 2B6 oxidize it only weakly (Chauret et al., 2001). The reported oxidation rate of all these compounds by CYP2D6 is lower than that of **9**, suggesting that **9** is potentially a new profluorescent substrate for measuring CYP2D6 activity. The lack of good selectivity is not a problem when these novel CYP2C19 and CYP2D6 substrates are used with recombinant CYP forms.

These new coumarin derivatives are not at moment commercially available. However, their synthesis is straightforward as described in the Materials and Methods section. In addition, the authors may provide compounds 1-4 and 7-10 in limited amounts upon request.

CONCLUSION

Ten coumarin derivatives were identified as profluorescent substrates for the main human liver CYP enzymes. All of these compounds were oxidized to corresponding fluorescent 7-hydroxycoumarin metabolites, and the oxidation rates by individual CYP forms and the key enzyme kinetic parameters could be determined reliably. The oxidation of all derivatives was catalyzed by the CYP1A forms with varying efficiency. Molecular modeling yielded precise information about the interactions between the compounds and individual CYP enzymes. These novel substrates would be especially suited for simple high-throughput testing of the CYP inhibition properties of nonfluorescent compounds. Our study using modeling, chemical synthesis and enzyme activity measurement of profluorescent coumarin derivatives paves the way for developing new selective or sensitive coumarin-derivative substrates for other key human CYPs. Currently we are focusing on further improving selectivity, especially towards CYP1A forms.

ACKNOWLEDGMENTS

The project was supported by the Jenny and Antti Wihuri Foundation (MA) and the Emil Aaltonen Foundation (MA). CSC, The Finnish IT Center for Science is acknowledged for computational resources (OTP; projects jyy2516 and jyy2585).

DISCLOSURE OF INTEREST

The authors report no conflict of interest.

References

- Berman HM, Westbrook J, Feng Z, *et al.*, (2000). The protein data bank. *Nucleic Acids Res.* 28: 235–242.
- Cali JJ, Ma D, Sobol M, *et al.*, (2006). Luminogenic cytochrome P450 assays. *Expert Opin. Drug Metab. Toxicol.* 2: 629–645.
- Chauret N, Dobbs B, Lackman RL, *et al.*, (2001). The Use of 3- [2- (N , N-Diethyl-N-Methylammonium) Ethyl] -7-Methoxy-4- Methylcoumarin (AMMC) As a Specific Cyp2D6 Probe in Human Liver Microsomes. *Drug Metab. Dispos.* 29: 1196–1200.
- Crespi CL, Miller VP, and Penman BW, (1997). Microtiter plate assays for inhibition of human, drug-metabolizing cytochromes P450. *Anal. Biochem.* 248: 188–190.
- Crespi CL, Miller VP, and Stresser DM, (2002). Design and application of fluorometric assays for human cytochrome P450 inhibition. *Methods Enzymol.* 357: 276–284.
- Crespi CL and Stresser DM, (2000). Fluorometric screening for metabolism-based drug-drug interactions. *J. Pharmacol. Toxicol. Methods* 44: 325–331.
- Delogu GL, Serra S, Quezada E, *et al.*, (2014). Monoamine oxidase (MAO) inhibitory activity: 3-phenylcoumarins versus 4-hydroxy-3-phenylcoumarins. *ChemMedChem* 9: 1672–1676.
- Fowler S, Morcos PN, Cleary Y, *et al.*, (2017). Progress in Prediction and Interpretation of Clinically Relevant Metabolic Drug-Drug Interactions: a Minireview Illustrating Recent Developments and Current Opportunities. *Curr. Pharmacol. Reports* 3: 36–49.
- Ghosal A, Hapangama N, Yuan Y, *et al.*, (2003). Rapid determination of enzyme activities of recombinant human cytochromes P450, human liver microsomes and hepatocytes. *Biopharm. Drug Dispos.* 24: 375–384.
- Gonzalez FJ, Coughtrie M, and Tukey RH, (2018). Drug metabolism. *In*: L.L. Brunton, B.A. Chabner, and B.C. Knollmann, eds. *Goodman & Gilman's The Pharmacological Basis of Therapeutics*. New York: McGraw-Hill, 85–100.
- Guengerich FP, (2017). Intersection of the roles of cytochrome P450 enzymes with xenobiotic and endogenous substrates: Relevance to toxicity and drug interactions. *Chem. Res. Toxicol.* 30: 2–12.

- Humphrey W, Dalke A, and Schulten K, (1996). VMD: visual molecular dynamics. *J. Mol. Graph.* 14: 33–38.
- Johnson MS and Overington JP, (1993). A structural basis for sequence comparisons: An evaluation of scoring methodologies. *J. Mol. Biol.* 233: 716–738.
- Juvonen RO, Kuusisto M, Fohrgrup C, *et al.*, (2016). Inhibitory effects and oxidation of 6-methylcoumarin, 7-methylcoumarin and 7-formylcoumarin via human CYP2A6 and its mouse and pig orthologous enzymes. *Xenobiotica* 46: 14–24.
- Juvonen RO, Rauhamäki S, Kortet S, *et al.*, (2018). Molecular Docking-Based Design and Development of a Highly Selective Probe Substrate for UDP-glucuronosyltransferase 1A10. *Mol. Pharm.* 15: 923–933.
- Kirchmair J, Göller AH, Lang D, *et al.*, (2015). Predicting drug metabolism: Experiment and/or computation? *Nat. Rev. Drug Discov.*
- Knights KM, Stresser DM, Miners JO, *et al.*, (2016). In vitro drug metabolism using liver microsomes. *Curr. Protoc. Pharmacol.* 2016: 7.8.1-7.8.24.
- Lang MA, Gielen JE, and Nebert DW, (1981). Genetic Evidence for Many Unique Liver Microsomal P-450-mediated Monooxygenase Activities in Heterogeneous Stock Mice. *J. Biol. Chem.* 256: 12068–12075.
- Lavis LD and Raines RT, (2014). Bright building blocks for chemical biology. *ACS Chem. Biol.* 9: 855–866.
- Lehtonen J V, Still D-J, Rantanen V-V, *et al.*, (2004). BODIL: a molecular modeling environment for structure-function analysis and drug design. *J. Comput. Aided. Mol. Des.* 18: 401–19.
- Mayer RT, Dolence EK, and Mayer GE, (2007). A real-time fluorescence assay for measuring N-dealkylation. *Drug Metab. Dispos.* 35: 103–109.
- Niinivehmas S, Postila PA, Rauhamäki S, *et al.*, (2018). Blocking oestradiol synthesis pathways with potent and selective coumarin derivatives. *J. Enzyme Inhib. Med. Chem.* 33: 743–754.
- Niinivehmas SP, Manivannan E, Rauhamäki S, *et al.*, (2016). Identification of estrogen receptor a ligands with virtual screening techniques. *J. Mol. Graph. Model.* 64: 30–39.

- Niinivehmas SP, Salokas K, Lätti S, *et al.*, (2015). Ultrafast protein structure-based virtual screening with Panther. *J. Comput. Aided. Mol. Des.* 29: 989–1006.
- Pelkonen O, Rautio A, Raunio H, *et al.*, (2000). CYP2A6: A human coumarin 7-hydroxylase. *Toxicology*.
- Pelkonen O, Turpeinen M, Hakkola J, *et al.*, (2013). Preservation, induction or incorporation of metabolism into the in vitro cellular system - Views to current opportunities and limitations. *Toxicol. Vitro.* 27: 1578–1583.
- Pelkonen O, Turpeinen M, Uusitalo J, *et al.*, (2005). Prediction of drug metabolism and interactions on the basis of in vitro investigations. *In: Basic and Clinical Pharmacology and Toxicology.* 167–175.
- Rauhämäki S, Postila PA, Niinivehmas S, *et al.*, (2018). Structure-Activity Relationship Analysis of 3-Phenylcoumarin-Based Monoamine Oxidase B Inhibitors. *Front. Chem.* 6: 1–18.
- Raunio H and Rahnasto-Rilla M, (2012). CYP2A6: Genetics, structure, regulation, and function. *Drug Metabol. Drug Interact.* 27: 73–88.
- Rendic S, (2002). Summary of information on human CYP enzymes: human P450 metabolism data. *Drug Metab. Rev.* 34: 83–448.
- Reynald RL, Sansen S, Stout CD, *et al.*, (2012). Structural characterization of human cytochrome P450 2C19: Active site differences between P450s 2C8, 2C9, and 2C19. *J. Biol. Chem.* 287: 44581–44591.
- Sai Y, Dai R, Yang TJ, *et al.*, (2000). Assessment of specificity of eight chemical inhibitors using cDNA-expressed cytochromes P450. *Xenobiotica* 30: 327–343.
- Sevior DK, Pelkonen O, and Ahokas JT, (2012). Hepatocytes: The powerhouse of biotransformation. *Int. J. Biochem. Cell Biol.* 44: 257–261.
- Skaanild MT and Friis C, (2005). Porcine CYP2A polymorphisms and activity. *Basic Clin. Pharmacol. Toxicol.* 97: 115–121.
- Testa B, Pedretti A, and Vistoli G, (2012). Reactions and enzymes in the metabolism of drugs and other xenobiotics. *Drug Discov. Today* 17: 549–560.
- The UniProt Consortium, (2017). UniProt: The universal protein knowledgebase. *Nucleic*

Acids Res. 45: D158–D169.

Tolonen A and Pelkonen O, (2015). Analytical challenges for conducting rapid metabolism characterization for QIVIVE. *Toxicology* 332: 20–29.

Trubetskoy O V., Gibson JR, and Marks BD, (2005). Highly miniaturized formats for in vitro drug metabolism assays using Vivid?? fluorescent substrates and recombinant human cytochrome P450 enzymes. *J. Biomol. Screen.* 10: 56–66.

Turpeinen M, Korhonen LE, Tolonen A, *et al.*, (2006). Cytochrome P450 (CYP) inhibition screening: comparison of three tests. *Eur J Pharm Sci* 29: 130–138.

Vainio MJ, Puranen JS, and Johnson MS, (2009). ShaEP : Molecular Overlay Based on Shape and Electrostatic Potential ShaEP : Molecular Overlay Based on Shape and Electrostatic Potential. *Methods* 49: 492–502.

Wang A, Savas U, Hsu M-H, *et al.*, (2012). Crystal Structure of Human Cytochrome P450 2D6 with Prinomastat Bound. *J. Biol. Chem.* 287: 10834–10843.

Waxman DJ and Chang TKH, (2006). Use of 7-Ethoxycoumarin to Monitor Multiple Enzymes in the Human CYP1, CYP2, and CYP3 Families. *In*: I.R. Phillips and E.A. Shephard, eds. *Cytochrome P450 Protocols*. Humana Press, 153–156.

Wheeler WC and Gladstein DS, (1994). MALIGN: A multiple sequence alignment program. *J. Hered.* 85: 410–413.

Zanger UM and Schwab M, (2013). Cytochrome P450 enzymes in drug metabolism: Regulation of gene expression, enzyme activities, and impact of genetic variation. *Pharmacol. Ther.* 138: 103–141.

Zientek MA and Youdim K, (2015). Reaction phenotyping: Advances in the experimental strategies used to characterize the contribution of drug-metabolizing enzymes. *Drug Metab. Dispos.* 43: 163–181.

Tables and table captions

Table 1. The Michaelis-Menten kinetic constants of the 7-hydroxylation of the coumarin derivatives catalyzed by human CYPs. Unit of K_m is μM , V_{\max} mol/(min x mol CYP) and V_{\max}/K_m L/(min * mol CYP).

CYP1A1	1	3	5	6	7	8	9	10
K_m	5.3 (2.7-8.0)	2.8 (1.3-4.4)	0.15 (0.07-0.22)	7.7 (0-20.8)	1.1 (0-2.8)	22 (0-58)	3.3 (1.4-5.3)	5.5 (1.9-9.1)
V_{\max}	15.5 (12.6-18.3)	10.1 (8.3-11.9)	1.1 (1.0-1.3)	25.6 (0-58)	1.7 (1.1-2.2)	0.037 (0.005-0.069)	19.7 (15.7-23.7)	17.6 (11.9-23.2)
V_{\max}/K_m	2.9	3.6	7.3	3.3	1.5	0.0017	6.0	3.2

CYP1A2	1	2	3	5	7	8	9	10
K_m	1.2 (0.8-1.6)	10.3 (3.7-16.7)	3.2 (2.0-4.4)	0.4 (0.29-0.5)	4.9 (4.3-5.5)	0.2 (0-0.46)	2.0 (1.1-2.9)	4.0 (1.8-1.6)
V_{\max}	4.1 (3.8-4.4)	1.21 (0.87-1.55)	7.9 (6.9-9.0)	0.54 (0.5-0.58)	7.1 (6.8-7.4)	0.22 (0.19-0.24)	35.4 (30.9-39.9)	11.5 (8.8-14.3)
V_{\max}/K_m	3.4	0.12	2.5	1.35	1.5	1.1	17.7	2.9

CYP1B1	4	6	7
K_m	1.2 (0.7-1.7)	0.24 (0.13-1.7)	0.39 (0.32-0.46)
V_{\max}	2.1 (1.9-2.3)	11.7 (10.3-13)	5.0 (4.8-5.1)
V_{\max}/K_m	1,8	48.8	12.8

CYP2A6	4	5	6
K_m	53 (36-70)	59 (38-81)	18.4 (16.3-20.4)
V_{\max}	14.5 (11.6-17.4)	8.9 (6.8-11)	9.0 (8.5-9.5)
V_{\max}/K_m	0.27	0.15	0.49

CYP2C19	8	9
K_m	6.5 (0-13)	1.9 (0.9-3)
V_{\max}	0.39 (0.2-0.57)	4.6 (3.8-5.4)
V_{\max}/K_m	0.06	2.4

CYP2D6	9	10
K_m	1.0 (0.55-1.5)	13 (2.3-24)
V_{\max}	9.1 (8.3-9.7)	11.1 (5-17.2)
V_{\max}/K_m	9.1	0.85

Figures and figure captions

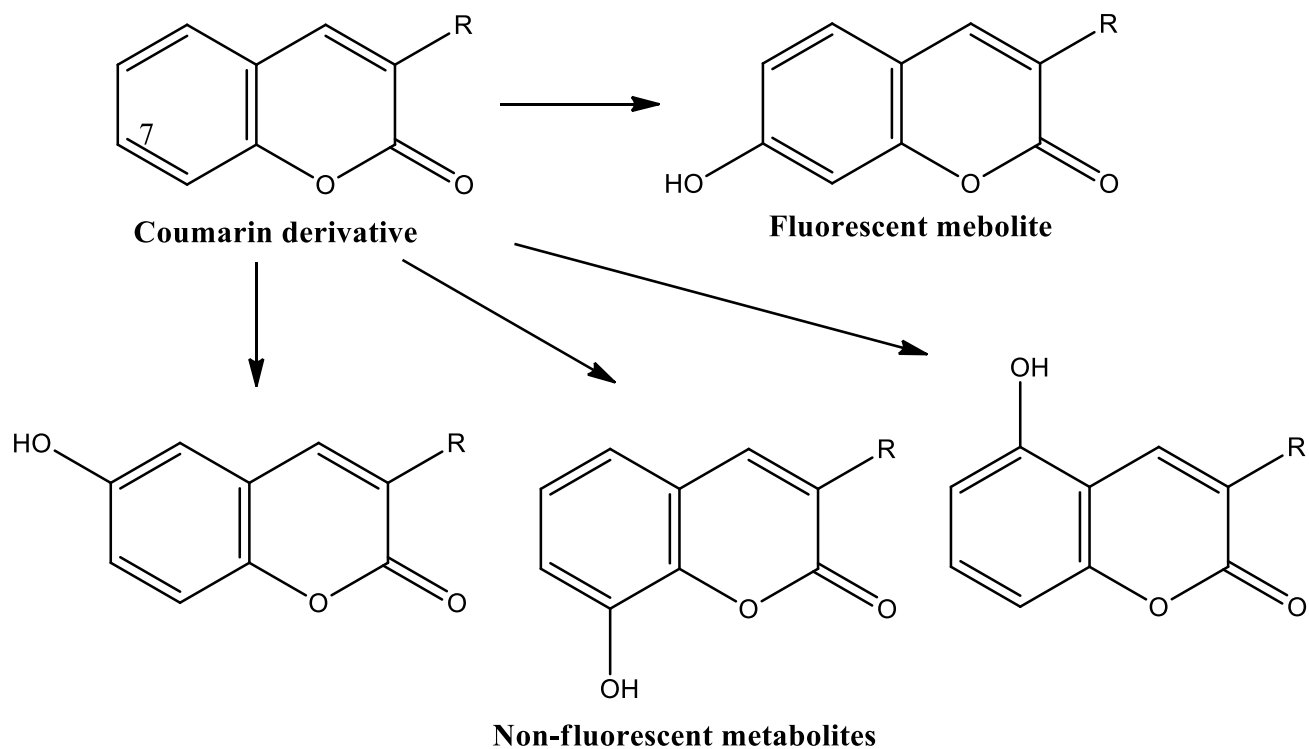


Figure 1. Change in fluorescence of coumarin derivatives upon CYP oxidation. Coumarins are oxidized to fluorescent 7-hydroxy metabolites, while hydroxylation at other positions does not increase fluorescence.

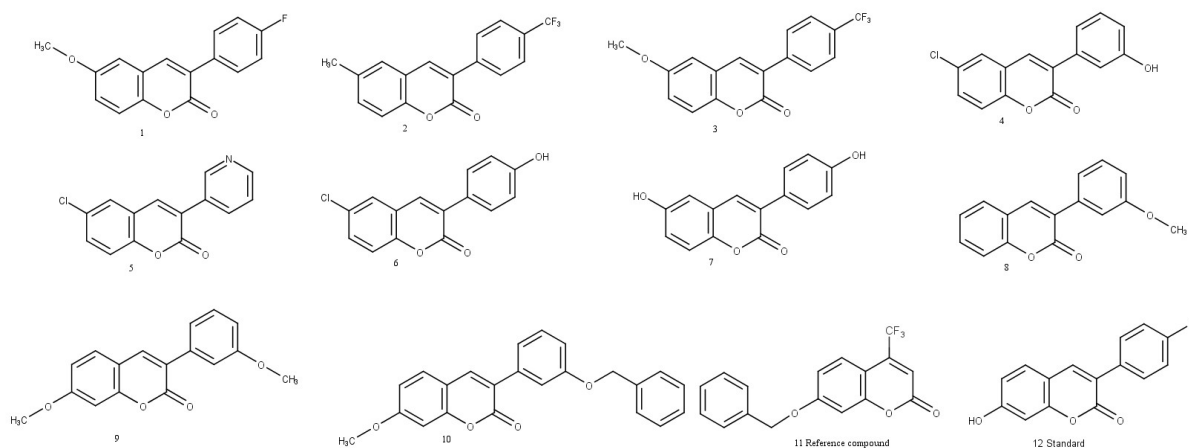


Figure 2. Structures of the studied coumarin derivatives. **1:** 3-(4-fluorophenyl)-6-methoxycoumarin; **2:** 3-(4-trifluoromethylphenyl)-6-methylcoumarin; **3:** 3-(4-trifluoromethylphenyl)-6-methoxycoumarin; **4:** 3-(3-hydroxyphenyl)-6-chlorocoumarin, **5:** 3-pyridyl-6-chlorocoumarin; **6:** 3-(4-hydroxyphenyl)-6-chlorocoumarin; **7:** 3-(4-hydroxyphenyl)-6-hydroxycoumarin; **8:** 3-(3-methoxyphenyl)coumarin; **9:** 3-(3-methoxyphenyl)-7-methoxycoumarin; **10:** 3-(3-benzyloxy)phenyl-7-methoxycoumarin; **11:** 4-trifluoromethyl-7-benzyloxocoumarin; **12:** 3-(4-fluorophenyl)-7-hydroxycoumarin.

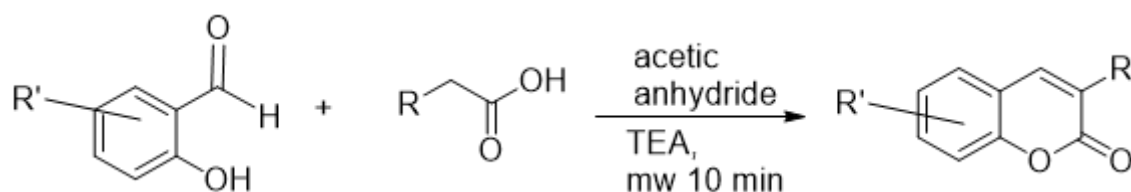


Figure 3. The synthesis of 3-phenylcoumarin analogs.

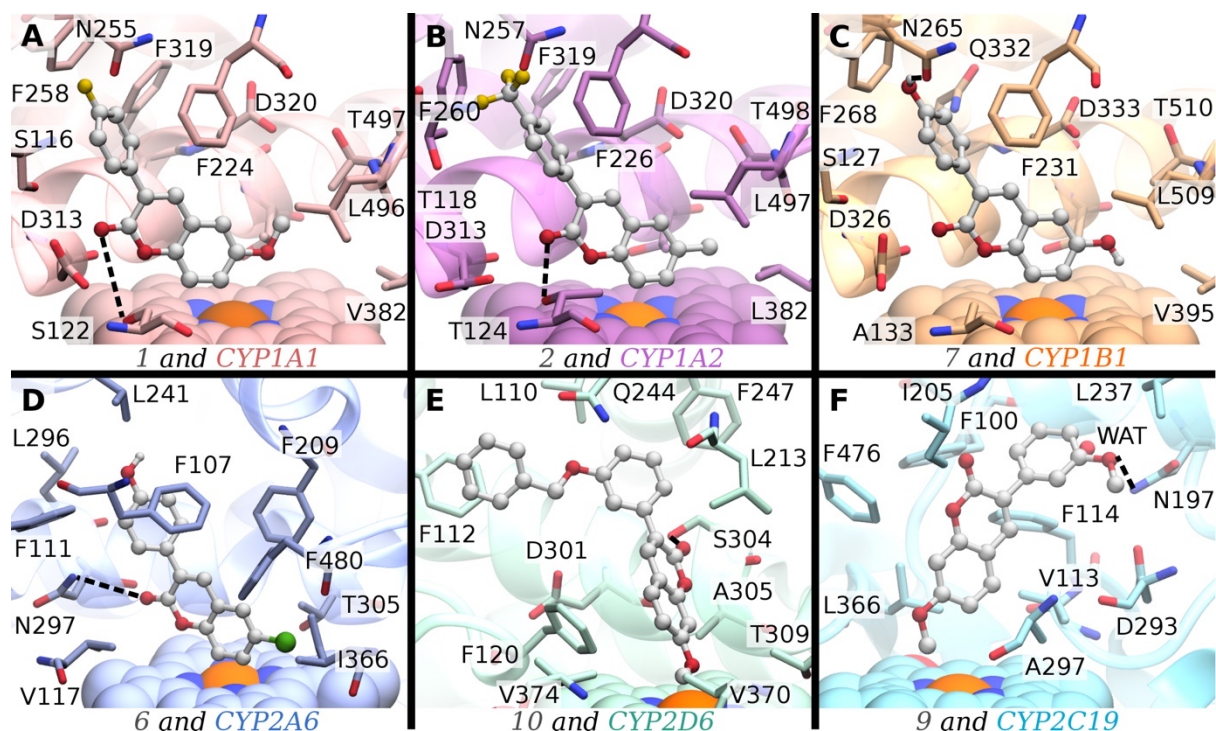


Figure 4. The binding of 3-phenylcoumarins to the CYP forms 1A1, 1A2, 1B1 and 2A6. (A) The docked pose of **1** forms a hydrogen bond from the coumarin carbonyl to the Ser122 hydroxyl group in CYP1A1 (PDB: 4I8V) (Walsh et al., 2013) and points position 7 towards the heme. (B) In CYP1A2 (PDB: 2HI4) (Sansen et al., 2007), the docked pose of compound **2** forms a hydrogen bond with Thr124 and stacks with Phe226. (C) Compound **7** forms a hydrogen bond to Asn265 and stacks with Phe231 in its docked pose to CYP1B1 (PDB: 3PM0) (Wang et al., 2011). The orientation of the 4'-hydroxy hydrogen was manipulated to show the hydrogen bond to Asn265. (D) The docked pose of compound **6** forms a hydrogen bond to Asn297 and packs with Phe107 in the CYP2A6 (PDB: 2FDV) (Yano et al., 2006) catalytic site. (E) Ser304 of CYP2D6 (PDB: 3QM4) (Wang et al., 2012) forms a hydrogen bond with the docked compound **10**. (F) The docked compound **9** replaces the crystal water molecule (WAT) and coordinates with Asn197 in CYP2C19 (PDB: 4GQS) (Reynald et al., 2012). Ball-and-stick: 3-phenylcoumarin derivatives; van der Waals: hemes; cartoon and stick: enzymes.

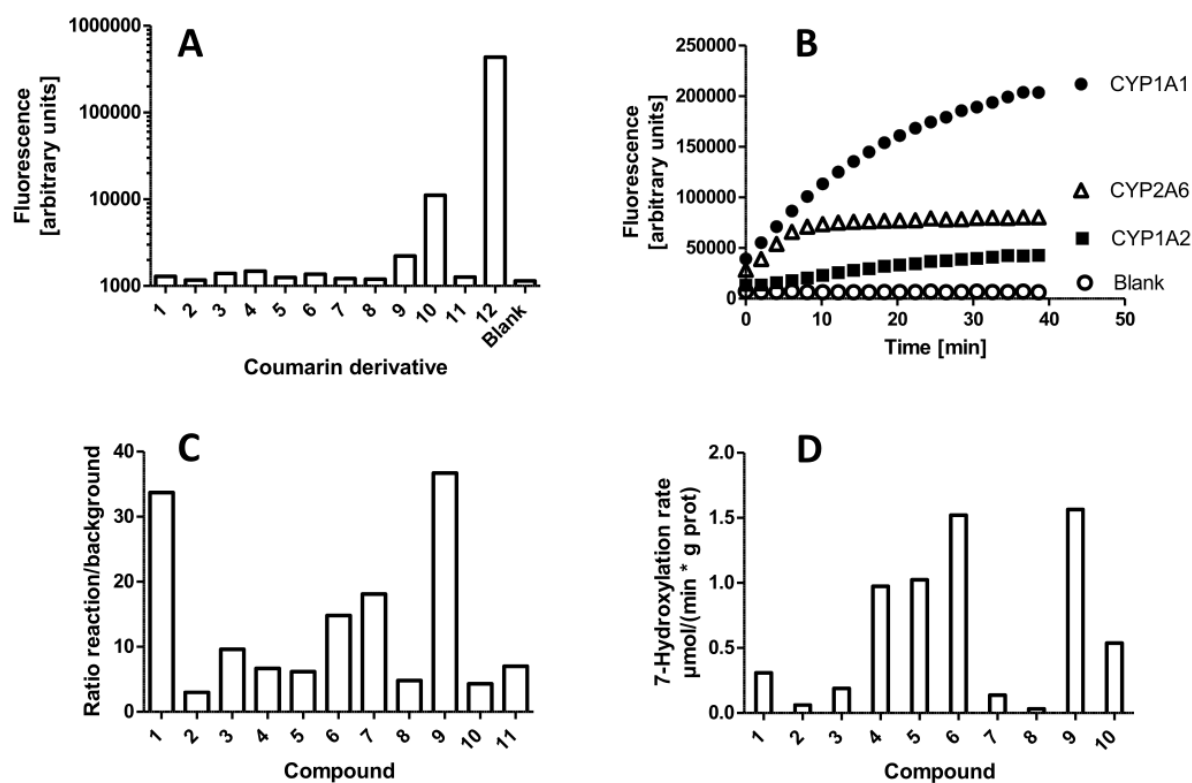


Figure 5. Fluorescence and 7-hydroxylation of the coumarin derivatives. (A) Arbitrary fluorescence intensities of all compounds (1 μM) in 100 mM Tris-HCl pH 7.4 at excitation 405 nm and emission 460 nm. (B) Increase in fluorescence intensity (ex 405 nm, em 460 nm) of compound 8 during incubation with CYP1A1, CYP1A2 and CYP2A6. (C) Signal-to-background ratio of fluorescence after 40 min reaction. (D) Rate of 7-hydroxylation of compounds 1–10 in human hepatic microsomes. The rate is determined from the linear phase of the reaction. The compounds (10 μM) were incubated for 40 min in 100 mM Tris-HCl buffer containing 0.05 g/L microsomal protein or a 25 nM recombinant CYP enzyme and a NADPH regenerating system.

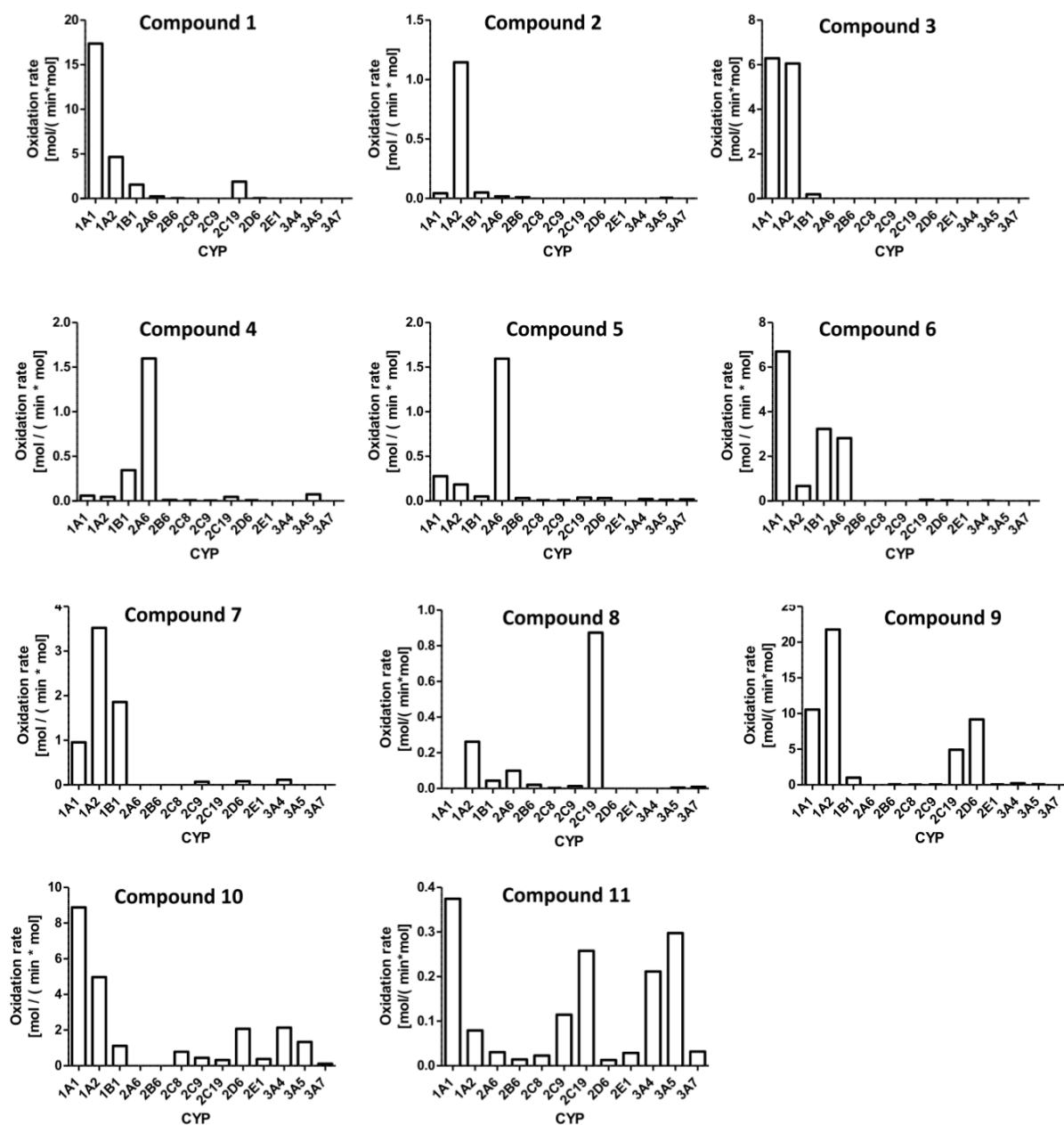


Figure 6. Oxidation of the coumarin derivatives by 13 human CYP forms. Formation of fluorescent metabolites from coumarin derivatives was determined in incubations containing a 25 nM CYP, a 20% NADPH regenerating system and a 10 μ M coumarin-derivative in 100 mM Tris-HCl pH 7.4. The activities were determined from the linear phases of the reactions and do not represent V_{max} values. Note the variation in Y-axis scales.

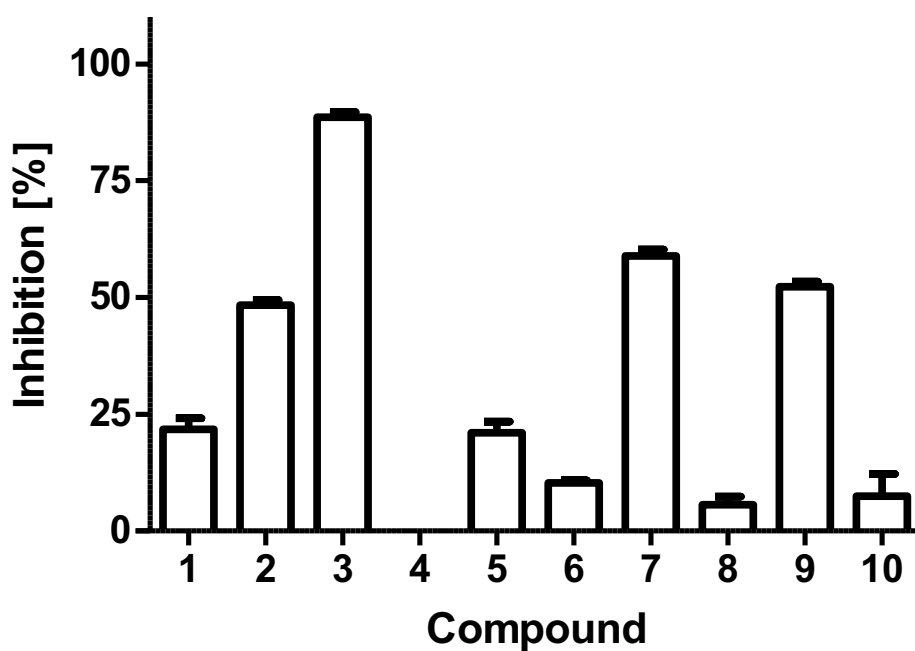


Figure 7. Inhibition of 7-hydroxylation of the coumarin derivatives by α -naphthoflavone in human hepatic microsomes. Inhibition of fluorescent metabolite formation was determined in 100 mM Tris-HCl pH 7.4 containing 55 mg/L microsomal protein, a NADPH regenerating system, a 10 μ M coumarin derivative and 0.1 μ M α -naphthoflavone. The reaction rate was determined from the linear phase of the reaction and inhibition percentage was calculated as $100 \times \text{inhibited rate} / \text{non-inhibited rate}$. Results are given as the average of two separate experiments. The error bars denote SEM.

Supplementary Table 1. Crystal structures and amino acid sequences used in molecular modeling.

CYP form	UniProt entry	PDB ID
1A1	P04798-1	4I8V ^{a,b} (Walsh et al. 2013)
1A2	P05177-1	2HI4 ^a (Sansen et al. 2007)
1B1	Q16678-1	3PM0 ^a (Wang et al. 2011)
2A6	P11509-1	1Z10 (Yano et al. 2005) 2FDV ^{a,b} (Yano et al. 2006)
2B6	P20813-1	3QOA (Shah et al. 2011) 3UA5 (Shah et al. 2012)
2C8	P10632-1	2VN0 (Schoch et al. 2008)
2C9	P11712-1	1OG5 (Williams et al. 2003) 4NZ2 (Brändén et al. 2014) 1R9O (Wester et al. 2004)
2C19	P33261-1	4GQS ^a (Reynald et al. 2012)
2D6	P10635-1	3QM4 ^a (Wang et al. 2012) 4WNW (Wang et al. 2015)
2E1	P05181-1	3T3Z (DeVore et al. 2012)
3A4	P08684-1	3UA1 (Sevrioukova & Poulos 2012) 5TE8 ^b (Sevrioukova & Poulos 2017)
3A5	P20815-1	5VEU (Hsu et al. 2018)
3A7	P24462-1	-

a. Structures used in molecular docking

b. Structures used in structure-based sequence pre-alignment

Supplementary Table 2. The absorbance properties of the coumarin derivatives.

Compound number	A_{max} [nm]	ε_{abs} [cm⁻¹*M⁻¹]
1	287	5 800
2	293	6 200
3	293	5 700
4	294 333	13 100 12 300
5	292	17 900
6	340	7 200
7	349	14 900
8	324	14 800
9	340	17 400
10	349	10 400
12	346	19 300

Supplementary Figure 1. Multiple sequence alignment of the CYP forms. The catalytic sites of the CYP1 family are very conserved (light pink) and have similar amino acids at the positions suggested to be involved in 3-phenylcoumarin binding (pink). The catalytic site amino acids (light blue) and the suggested key residues in 3-phenylcoumarin binding (teal) differ among CYP2A6, CYP2D6 and CYP2C19. The amino acids present in either CYP3A4 or CYP3A5 binding sites (yellow) are conserved among the CYP3 forms. The conserved threonine in the helix I (black) and the heme-binding amino acids (grey) are aligned among all sequences. The alignment was built on top of structure-based pre-alignments of CYP2A6 and CYP3A4 to CYP1A1 from *Vertaa* in Bodil (Lehtonen 2004), and was performed with Malign (Johnson 1993) with structure-based matrix (STRMAT110) (Johnson & Overington 1993) and gap penalty of 30. The structure-based pre-alignments were left out of the figure for clarity. The used structures and sequences are listed in Supplementary Table 1.

	1	10	20	30	40																																											
CYP1A1	M	L	F	P	I	S	M	S	A	T	E	F	-	-	L	L	A	S	V	I	F	C	L	V	F	W	V	I	R	A	-	-	-	-	-	-	-	-	S	R								
CYP1A2	M	A	L	S	Q	S	V	P	F	S	A	T	E	L	L	L	A	S	A	I	F	C	L	V	F	W	V	L	K	G	-	-	-	-	-	-	-	-	-	-	-	L	R					
CYP1B1	M	G	T	S	L	S	P	N	D	P	W	P	-	-	L	N	P	L	S	I	Q	Q	T	T	L	L	L	L	S	V	L	A	T	V	H	V	G	Q	R	L	L							
CYP2A6	M	L	A	S	G	M	L	L	V	A	L	L	-	-	-	-	-	-	-	V	C	L	T	V	M	V	L	M	S	-	-	-	-	-	-	-	-	-	-	-	V	Q						
CYP2B6	M	E	L	S	V	L	L	F	L	A	L	L	-	-	-	-	-	-	-	-	T	G	L	L	L	L	L	S	-	-	-	-	-	-	-	-	-	-	-	-	V	Q						
CYP2C19	M	D	P	F	V	V	L	V	L	C	L	S	-	-	-	-	-	-	-	-	-	-	-	-	-	-	-	-	-	-	-	-	-	-	-	-	-	-	-	-	-	I	W					
CYP2C8	M	E	P	F	V	V	L	V	L	C	L	S	-	-	-	-	-	-	-	-	-	F	M	L	L	F	S	-	-	-	-	-	-	-	-	-	-	-	-	-	-	-	L	W				
CYP2C9	M	D	S	L	V	V	L	V	L	C	L	S	-	-	-	-	-	-	-	-	-	-	-	-	-	-	-	-	-	-	-	-	-	-	-	-	-	-	-	-	-	-	L	W				
CYP2D6	M	G	L	E	A	L	V	P	L	A	V	I	-	-	-	-	-	-	-	-	V	A	I	F	L	L	L	V	D	-	-	-	-	-	-	-	-	-	-	-	-	-	L	M				
CYP2E1	M	S	A	L	G	V	T	V	A	L	L	V	-	-	-	-	-	-	-	-	W	A	A	F	L	L	V	S	-	-	-	-	-	-	-	-	-	-	-	-	-	-	-	M	W			
CYP3A4	M	A	L	I	P	D	L	A	M	E	T	W	-	-	-	-	-	-	-	-	L	L	A	V	S	L	V	L	L	Y	-	-	-	-	-	-	-	-	-	-	-	-	-	-	L	Y		
CYP3A5	M	D	L	I	P	N	L	A	V	E	T	W	-	-	-	-	-	-	-	-	L	L	A	V	S	L	V	L	L	Y	-	-	-	-	-	-	-	-	-	-	-	-	-	-	-	L	Y	
CYP3A7	M	D	L	I	P	N	L	A	V	E	T	W	-	-	-	-	-	-	-	-	L	L	A	V	S	L	I	L	L	Y	-	-	-	-	-	-	-	-	-	-	-	-	-	-	-	-	L	Y

	50	60	70	80																																								
CYP1A1	P	Q	V	P	K	G	L	K	N	P	-	-	P	G	P	W	G	W	P	L	I	G	H	M	L	T	L	G	-	K	N	P	H	L	A	L	S	R	M	S	Q			
CYP1A2	P	R	V	P	K	G	L	K	S	P	-	-	P	E	P	W	G	W	P	L	L	I	G	H	V	L	T	L	G	-	K	N	P	H	L	A	L	S	R	M	S	Q		
CYP1B1	R	Q	R	R	R	Q	L	R	S	A	-	-	P	P	G	P	F	A	W	P	L	I	G	N	A	A	V	G	-	Q	A	A	H	L	S	F	A	R	L	A	R	Q		
CYP2A6	-	Q	Q	R	K	S	K	G	K	L	-	-	P	P	G	P	T	P	L	P	F	I	G	N	Y	L	Q	L	N	T	E	Q	M	Y	N	S	L	M	K	I	S	E		
CYP2B6	-	R	H	P	N	T	H	D	R	L	-	-	P	P	G	P	R	P	L	P	L	L	G	N	L	L	Q	M	D	R	R	G	L	L	K	S	F	L	R	F	R	E		
CYP2C19	-	R	Q	S	S	G	R	G	K	L	-	-	P	P	G	P	T	P	L	P	V	I	I	G	N	I	L	Q	I	D	I	D	K	D	V	S	K	S	L	T	N	L	S	K
CYP2C8	-	R	Q	S	C	R	R	R	K	L	-	-	P	P	G	P	T	P	L	P	I	I	I	G	N	M	L	Q	I	D	V	K	D	I	C	K	S	F	T	N	F	S	K	
CYP2C9	-	R	Q	S	S	G	R	G	K	L	-	-	P	P	G	P	T	P	L	P	V	I	I	G	N	I	L	Q	I	G	I	K	D	I	S	K	S	L	T	N	L	S	K	
CYP2D6	H	R	R	Q	R	W	A	A	R	Y	-	-	P	P	G	P	L	P	P	G	L	G	N	L	L	H	V	D	F	G	Q	N	T	P	Y	C	F	D	Q	L	R	R		
CYP2E1	-	R	Q	V	H	S	S	W	N	L	-	-	P	P	G	P	F	L	P	I	I	I	G	N	L	F	Q	L	E	L	K	N	I	P	K	S	F	T	R	L	A	Q		
CYP3A4	G	T	H	S	H	G	L	F	K	K	L	G	I	P	G	P	T	P	L	P	F	L	G	N	I	L	S	Y	H	-	K	G	F	C	M	F	D	M	E	C	H	K		
CYP3A5	G	T	R	T	H	G	L	F	K	R	L	G	I	P	G	P	T	P	L	P	L	L	G	N	V	L	S	Y	R	-	Q	G	L	W	K	F	D	T	E	C	Y	K		
CYP3A7	G	T	R	T	H	G	L	F	K	K	L	G	I	P	G	P	T	P	L	P	F	L	G	N	A	L	S	F	R	-	K	G	Y	W	T	F	D	M	E	C	Y	K		

	90	100	110	120																																							
CYP1A1	Q	Y	G	D	V	L	Q	I	R	I	G	S	T	P	V	V	V	L	S	G	L	D	T	I	R	Q	A	L	V	R	Q	G	D	-	D	F	K	G	R	P	D	L	
CYP1A2	R	Y	G	D	V	L	Q	I	R	I	G	S	T	P	V	V	V	L	S	R	L	D	T	I	R	Q	A	L	V	R	Q	G	D	-	D	F	K	G	R	P	D	L	
CYP1B1	R	Y	G	D	V	F	Q	I	R	L	G	S	C	P	I	V	V	L	N	G	E	R	A	I	H	Q	A	L	V	Q	Q	A	E	-	A	F	A	D	R	R	P	A	F
CYP2A6	R	Y	G	P	V	F	T	I	H	L	G	P	R	R	V	V	V	L	C	G	H	D	A	V	R	E	A	L	V	D	Q	A	E	-	E	F	S	G	R	G	E	Q	
CYP2B6	K	Y	G	D	V	F	T	V	H	L	G	P	R	P	V	V	M	L	C	G	V	E	A	I	R	E	A	L	V	D	K	A	E	-	A	F	S	G	R	G	K	I	
CYP2C19	I	Y	G	P	V	F	T	L	Y	F	G	L	E	R	M	V	L	H	G	Y	E	V	V	K	E	A	L	I	D	L	G	E	-	E	F	S	G	R	G	H	F		
CYP2C8	V	Y	G	P	V	F	T	V	Y	F	G	M	N	P	I	V	V	F	H	G	Y	E	A	V	K	E	A	L	I	D	N	G	E	-	E	F	S	G	R	G	N	S	
CYP2C9	V	Y	G	P	V	F	T	L	Y	F	G	L	K	P	I	V	V	L	H	G	Y	E	A	V	K	E	A	L	I	D	L	G	E	-	E	F	S	G	R	G	I	F	
CYP2D6	R	F	G	D	V	F	S	L	Q	L	A	W	T	P	V	V	V	L	N	G	L	A	A	V	R	E	A	L	V	T	H	G	E	-	D	T	A	D	R	P	P	V	
CYP2E1	R	F	G	P	V	F	T	L	Y	V	G	S	Q	R	M	V	V	M	H	G	Y	K	A	V	K	E	A	L	L	D	Y	K	D	-	E	F	S	G	R	G	D	L	
CYP3A4	K	Y	G	K	V	W	G	F	Y	D	G	Q	P	V	L	A	I	T	D	P	D	M	I	K	T	V	L	V	K	E	C	Y	S	V	F	T	N	R	R	P	F		
CYP3A5	K	Y	G	K	M	W	G	T	Y	E	G	Q	L	P	V	L	A	I	T	D	P	D	V	I	R	T	V	L	V	K	E	C	Y	S	V	F	T	N	R	R	S	L	
CYP3A7	K	Y	R	K	V	W	G	I	Y	D	C	Q	Q	P	M	L	A	I	T	D	P	D	M	I	K	T	V	L	V	K	E	C	Y	S	V	F	T	N	R	R	P	F	

	130	140	150	160																																							
		N107 (C219)	S122 (1A1)																																								
CYP1A1	Y	T	F	T	L	I	-	-	-	S	N	G	Q	S	M	S	F	S	P	D	S	G	P	V	W	A	A	R	R	R	L	A	Q	N	G	L	K	S	F	-	S	I	
CYP1A2	Y	T	S	T	L	I	-	-	-	T	D	G	Q	S	L	T	F	S	T	D	S	G	P	V	W	A	A	R	R	R	R	L	A	Q	N	A	L	N	T	F	-	S	I
CYP1B1	A	S	F	R	V	V	-	-	-	S	G	G	R	S	M	A	F	G	-	H	Y	S	E	H	W	K	V	Q	R	R	A	A	H	S	M	M	R	F	F	T	R	Q	
CYP2A6	A	T	F	D	W	V	-	-	-	F	K	G	Y	G	V	V	F	S	-	N	-	G	E	R	A	K	Q	L	V	R	R	F	S	I	A	T	L	R	D	F	G	V	
CYP2B6	A	M	V	D	P	F	-	-	-	F	R	G	Y	G	V	I	F	A	-	N	-	G	N	R	W	K	V	L	R	R	R	F	S	V	T	T	M	R	D	F	G	M	G
CYP2C19	P	L	A	E	R	A	-	-	-	N	R	G	F	G	I	V	F	S	-	N	-	G	K	R	W	K	E	I	R	R	F	S	L	M	T	L	R	N	F	G	M	G	
CYP2C8	P	I	S	Q	R	I	-	-	-	T	K	G	L	G	I	I	S	S	-	N	-	G	K	R	W	K	E	I	R	R	F	S	L	T	T	L	R	N	F	G	M	G	
CYP2C9	P	L	A	E	R	A	-	-	-	N	R	G	F	G	I	V	F	S	-	N	-	G	K	K	W	K	E	I	R	R	F	S	L	M	T	L	R	N	F	G	M	G	
CYP2D6	P	I	T	Q	I	L	G	F	G	P	R	S	Q	G	V	F	L	A	-	R	Y	G	P	A	W	R	E	Q	R	R	F	S	V	S	T	L	R	N	L	G	L	G	
CYP2E1	P	-	A	F	H	A	-	-	-	H	R	D	R	G	I	I	F	N	-	N	-	G	P	T	W	K	D	I	R	R	F	S	L	T	T	L	R	N	Y	G	M	G	
CYP3A4	G	P	V	G	F	M	-	-	-	K	S	A	I	S	I	A	-	-	-	E	D	E	E	W	K	R	L	R	S	L	S	P	T	F	T	S	-	G	K	L			
CYP3A5	G	P	V	G	F	M	-	-	-	K	S	A	I	S	L	A	-	-	-	E	D	E	E	W	K	R	I	R	S	L	S	P	T	F	T	S	-	G	K	L			
CYP3A7	G	P	V	G	F	M	-	-	-	K	N	A	I	S	I	A																											

	220	230	240	250
				F224 (1A1), F107 (2A6)
CYP1A1	V V V S V T N V I C A I C F G R R Y D - H N H Q - - E L L S L V N L N N N F G E V V			
CYP1A2	V V V S V A N V I G A M C F G Q H F P - E S S D - - E M L S L V K N T H E F V E T A			
CYP1B1	T V V A V A N V M S A V C F G C R Y S - H D D P - - E F R E L L S H N E E F G R T V			
CYP2A6	L S R T V S N V I S S I V F G D R F D - Y K D K - - E F L S L L R M M L G I F Q F T			
CYP2B6	F Q S I T A N I I C S I V F G K R F D - Y Q D Q - - E F L K M L N L F Y Q T F S L I			
CYP2C19	L G C A P C N V I C S I I F Q Q K R F D - Y K D Q - - Q F L N L M K R L N E N I R I V			
CYP2C8	L G C A P C N V I C S V V F Q K R F D - Y K D Q - - N F L N L M K R F N E N F R I L			
CYP2C9	L G C A P C N V I C S I I F H K R F D - Y K D Q - - Q F L N L M K R L N E N I K I L			
CYP2D6	L D K A V S N V I A S L T C G R R F E - Y D D P - - R F L R L L D L A Q E G L K E E			
CYP2E1	I G C A P C N V I A D I L F R K H F D - Y N D E - - K F L R L M Y L F N E N F H L L			
CYP3A4	F G A Y S M D V I T S T S F G V N I D S L N N P Q D P F V E N T K K L L R F - D F L			
CYP3A5	F G A Y S M D V I T G T S F G V N I D S L N N P Q D P F V E S T K K F L K F - G F L			
CYP3A7	F G A Y S M D V I T S T S F G V S I D S L N N P Q D P F V E N T K K L L R F - N P L			

	260	270	280	290
				N265 (1B1)
CYP1A1	G S G - - N P A D F I - P I L R Y L P N P S L N A F K - - - D L N E K F Y S F M Q K			
CYP1A2	S S G - - N P L D F F - P I L R Y L P N P A L Q R F K - - - A F N Q R F L W F L Q K			
CYP1B1	G A G - - S L V D V M - P W L Q Y F P N P V R T V F R E F E Q L N R N F S N F I L D K			
CYP2A6	S T S T G Q L Y E M F S S V M K H L P G P Q Q Q A F Q - - - L L Q G L E D F I A K			
CYP2B6	S S V F G Q L F E L F S G F L K Y F P G A H R Q V Y K - - - N L Q E I N A Y I G H			
CYP2C19	S T P W I Q I C N N F P T I I D Y F P G T H N K L L K - - - N L A F M E S D I L E			
CYP2C8	N S P W I Q V C N N F P L L I D C F P G T H N K V L K - - - N V A L T R S Y I R E			
CYP2C9	S S P W I Q I C N N F S P I I D Y F P G T H N K L L K - - - N V A F M K S Y I L E			
CYP2D6	S G F L R E V L N A V P V L L H - I P A L A G K V L R - - - F Q K A F L T Q L D D E			
CYP2E1	S T P W L Q L Y N N F P S F L H Y L P G S H R K V I K - - - N V A E V K E Y V S E			
CYP3A4	D P P F L S I - T V F P F L I P I L E V L N I C V F P - - - - R E V T I N F L R K			
CYP3A5	D P L F L S I - I L F P F L T P V F E A L N V S L F P - - - - K D T I N F L S K			
CYP3A7	D P F V L S I - K V F P F L T P I L E A L N I T V F P - - - - R K V I S F L T K			

	300	310	320	330
CYP1A1	M V K E H Y K T F - - E K G - - - H - I R D I T D S L I E H C Q E K Q L D E N A N V			
CYP1A2	T V Q E H Y Q D F - - D K N - - - S - V R D I T G A L F K H - S K K G P R A S G N L			
CYP1B1	K F L R H C E S L - - R P G - - - A A P R D M D A F I L S A E K K A A G D S H G G			
CYP2A6	K V E H N Q R T L - - D P N - - - S - P R D F I D S F L I R M Q E E E K N P N T E -			
CYP2B6	S V E K H R E T L - - D P S - - - A - P K D L I D T Y L L H M E K E K S N A H S E -			
CYP2C19	K V K E H Q E S M - - D I N - - - N - P R D F I D C F L I K M E K E K Q N Q S E -			
CYP2C8	K V K E H Q A S L - - D V N - - - N - P R D F I D C F L I K M E K E K D N Q K S E -			
CYP2C9	K V K E H O E S M - - D M N - - - N - P O D F I D C F L M K M E K E K H N Q P S E -			
CYP2D6	L L T E H R M T W - - D P A - - - Q P P R D L T E A F L A E M E K A K G N P E S S -			
CYP2E1	R V K E H H Q S L - - D P N - - - C - P R D L T D C L L V E M E K E K H S A E R L -			
CYP3A4	S V K R M K E S R L E D T Q - - - K H R V D F L Q L M I D S Q N S K E T E S H K A -			
CYP3A5	S V N R M K K S R L N D K Q - - - K H R L D F L Q L M I D S Q N S K E T E S H K A -			
CYP3A7	S V K Q I K E G R L K E T Q - - - K H R V D F L Q L M I D S Q N S K D S E T H K A -			

	340	350	360	370
				N297 (2A6), S304 (2D6)
CYP1A1	Q - - L S D E K I I N I V L N D L F G A G F D T V T T A I S W S L M Y L V M N P R V Q			
CYP1A2	- - - I P Q E K I V N L V N D I F G A G F D T V T T A I S W S L M Y L V T K P E I Q Q			
CYP1B1	G A R L D L E N V P A T I T D I F G A S Q D T L S T A L Q W L L L L F T R Y P D V Q			
CYP2A6	- - - F Y L K N L V M T T L N L F I G S T E T V S T T L R Y G F L L M K H P E V E			
CYP2B6	- - - F S H Q N L N L N T L S L F F A G T E T T S T T L R Y G F L L M L K Y P H V A			
CYP2C19	- - - F T I E N L V I T A A D L L G A G T E T T S T T L R Y A L L L L L K H P E V T			
CYP2C8	- - - F N I E N L V G T V A D L F V A G T E T T S T T L R Y G L L L L L K H P E V T			
CYP2C9	- - - F T I E S L E N T A V D L F G A G T E T T S T T L R Y A L L L L L K H P E V T			
CYP2D6	- - - F N D E N L R I V V A D L F S A G M V T T S T T L A W G L L L M I L H P D V Q			
CYP2E1	- - - Y T M D G I T V T V A D L F F A G T E T T S T T L R Y G L L I L M K Y P E I E			
CYP3A4	- - - L S D L E L V A Q S I I F I F A G Y E T T S S V L S F I M Y E L A T H P D V Q			
CYP3A5	- - - L S D L E L A A Q S I I F I F A G Y E T T S S V L S F T I Y E L A T H P D V Q			
CYP3A7	- - - L S D L E L M A Q S I I F I F A G Y E T T S S V L S F T I Y E L A T H P D V Q			

	380	390	400	410	420
CYP1A1	R K I Q E E L D T V I G R S R R P R L S D R S H L P Y M E A F I L E T F R H S S F V				
CYP1A2	R K I Q K E L D T V I G R E R R R P R L S D R P Q L P Y L E A F I L E T F R H S S F V				
CYP1B1	T R V Q A E L D Q V V G R D R L P C M G D Q P N L P Y V L A F L Y E A M R F S S F V				
CYP2A6	A K V H E E I D R V I G K N R Q P K F E D R A K M P Y M E A V I H E I Q R F G D V I				
CYP2B6	E R V Y R E I E Q V I G P H R P P E L H D R A K M P Y T E A V I Y E I Q R F S D L L				
CYP2C19	A K V Q E E I E R V V G R N R S P C M Q D R G H M P Y T D A V V H E V Q R Y I D L I				
CYP2C8	A K V Q E E I D H V I G R H R S P C M Q D R S H M P Y T D A V V H E I Q R Y S D L V				
CYP2C9	A K V Q E E I E R V I G R N R S P C M Q D R S H M P Y T D A V V H E I Q R Y I D L L				
CYP2D6	R R V Q Q E I D D V I G P V R R P E M G D Q A H M P Y T T A V I H E V Q R F G D I V				
CYP2E1	E K L H E E I D R V I G P S R I P A I K D R Q E M P Y M D A V V H E I Q R F I T L V				
CYP3A4	Q K L Q E E I D A V L P N K A P P T Y D T V L Q M E Y L D M V V N E T L R L F P - I				
CYP3A5	Q K L Q K E I D A V L P N K A P P T Y D A V V Q M E Y L D M V V N E T L R L F P - V				
CYP3A7	Q K V Q K E I D T V L P N K A P P T Y D T V L Q L E Y L D M V V N E T L R L F P - V				

	430	440	450	460
CYP1A1	P F T I P H S T T R D T S L K G F Y I P K K G R C V F V N Q W Q I N H D Q K L W V N P			
CYP1A2	P F T I P H S T T R D T S L K G F Y I P K K C C V F V N Q W Q V N H D P E L W E D P			
CYP1B1	P V T I P H A T T A N T S V L G Y H I P K D T V V F V N Q W S V N H D P L K W P N P			
CYP2A6	P M S L A R R V K K D T K F R D F F L P K G T E V F P M L G S V L R D P S F F S N P			
CYP2B6	P M G V P H I V T Q H T S F R G Y I I P K D T E V F L I L S T A L H D P H Y F E K P			
CYP2C19	P T S L P H A V T C D V K F R N Y L I P K G T T I L T S L T S V L H D N K E F P N P			
CYP2C8	P T G V P H A V T T D T K F R N Y L I P K G T T I M A L L T S V L H D D K E F P N P			
CYP2C9	P T S L P H A V T C D I K F R N Y L I P K G T T I L I S L T S V L H D N K E F P N P			
CYP2D6	P L G V T H M T S R D I E V Q G F R I P K G T T L I T N L S S V L K D E A V W E K P			
CYP2E1	P S N L P H E A T R D T I F R G Y L I P K G T V V V P T L D S V L Y D N Q E F P D P			
CYP3A4	A M R L E R V C K K D V E I N G M F I P K G V V V M I P S Y A L H R D P K Y W T E P			
CYP3A5	A I R L E R T C K K D V E I N G V F I P K G S M V V I P T Y A L H H D P K Y W T E P			
CYP3A7	A M R L E R V C K K D V E I N G M F I P K G V V V M I P S Y V L H H D P K Y W R E P			

	470	480	490	500
CYP1A1	S E F L P E R F L T P D G - A I D K V L S E - - K V I I F G M G K R R C I G E T I A			
CYP1A2	S E F R P E R F L T A D G T A I N K P L S E - - K M M L F G M G K R R C I G E V L A			
CYP1B1	E N F D P A R F L D K D G - L I N K D L T S - - R V M I F S V G K R R C I G E E L S			
CYP2A6	Q D F N P Q H F L N E K G - Q F K K - - S D - - A F V P F S I G K R R C F G E G L A			
CYP2B6	D A F N P D H F L D A N G - A L K K - - T E - - A F I P F S L G K R R I C L G E G I A			
CYP2C19	E M F D P R H F L D E G G - N F K K - - S N - - Y F M P F S A G K R R I C V G E G L A			
CYP2C8	N I F D P G H F L D K N G - N F K K - - S D - - Y F M P F S A G K R R I C A G E G L A			
CYP2C9	E M F D P H H F L D E G G - N F K K - - S K - - Y F M P F S A G K R R I C V G E A L A			
CYP2D6	F R F H P E H F L D A Q G - H F V K - - P E - - A F L P F S A G R R R A C L G E P L A			
CYP2E1	E K F K P E H F L N E N G - K F K Y - - S D - - Y F K P F S T G K R R V C A G E G L A			
CYP3A4	E K F L P E R F S K K N K D N I D P Y - - - - I Y T P F G S G P R R N C I G M R F A			
CYP3A5	E E F R P E R F S K K - K D S I D P Y - - - - I Y T P F G T G P R R N C I G M R F A			
CYP3A7	E K F L P E R F S K K N K D N I D P Y - - - - I Y T P F G S G P R R N C I G M R F A			

	510	520	530	540
CYP1A1	R W E V F L F L A I L L Q R V E F S V - P L G V - K V D - - - - M T P - I Y G L			
CYP1A2	K W E I F L F L A I L L Q Q L E F S V - P P G V - K V D - - - - L T P - I Y G L			
CYP1B1	K M Q L F L F I S I L A H Q C D F R A N P N E P A K M N F S Y G L T I K P K S F K V			
CYP2A6	R M E L F L F F T T V M Q N F R L K S - S Q S P K D I D - - - - V S P K H V G F			
CYP2B6	R A E L F L F F T T I L Q N F S M A S - P V A P E D I D - - - - L T P Q E C G V			
CYP2C19	R M E L F L F L T F I L Q N F N L K S - L I D P K D L D - - - - T T P V V N G F			
CYP2C8	R M E L F L F L T T I L Q N F N L K S - V D D L K N L N - - - - T T A V T K G I			
CYP2C9	G M E L F L F L T S I L Q N F N L K S - L V D P K N L D - - - - T T P V V N G F			
CYP2D6	R M E L F L F F T S L L Q H F S F - S - V P T G Q P R P - - - - S H H G V F A F			
CYP2E1	R M E L F L L L C A I L Q H F N L K P - L V D P K D I D - - - - L S P I H I G F			
CYP3A4	L M N M K L A L I R V L Q N F S F K P C K E T Q I P L K - - - - L S L G G L L Q			
CYP3A5	L M N M K L A L I R V L Q N F S F K P C K E T Q I P L K - - - - L D T Q G L L Q			
CYP3A7	L V N M K L A L V R V L Q N F S F K P C K E T Q I P L K - - - - L R F G G L L L			

	550	560	570
CYP1A1	T M K H - A C C E H F - - - - Q - M Q L R S - - -		
CYP1A2	T M K H - A R C E H V - - - - Q - A R R F S I N -		
CYP1B1	N V T L R E S M E L L D S A V Q N L Q A K E T C Q		
CYP2A6	A T I P - R N Y T M S - - - - F L P R - - - -		
CYP2B6	G K I P - P T Y Q I R - - - - F L P R - - - -		
CYP2C19	A S V P - P F Y Q L C - - - - F I P V - - - -		
CYP2C8	V S L P - P S Y Q I C - - - - F I P V - - - -		
CYP2C9	A S V P - P F Y Q L C - - - - F I P V - - - -		
CYP2D6	L V S P - S P Y E L C - - - - A V P R - - - -		
CYP2E1	G C I P - P R Y K L C - - - - V I P R S - - - -		
CYP3A4	P E K P V V L K V E S - - - - R D G T V S G A - - - -		
CYP3A5	P E K P I V L K V D S - - - - R D G T L S G E - - - -		
CYP3A7	T E K P I V L K A E S - - - - R D E T V S G A - - - -		

References

- Brändén, G. et al., (2014). Structure-based ligand design to overcome CYP inhibition in drug discovery projects. *Drug Discovery Today*, 19: 905–911.
- DeVore, N.M. et al., (2012). Structural comparison of cytochromes P450 2A6, 2A13, and 2E1 with pilocarpine. *FEBS Journal*, 279: 1621–1631.
- Hsu, M.-H., Savas, U. & Johnson, E.F., (2018). The X-Ray Crystal Structure of the Human Mono-Oxygenase Cytochrome P450 3A5-Ritonavir Complex Reveals Active Site Differences between P450s 3A4 and 3A5. *Molecular Pharmacology*, 93: 14–24. Available at: <http://molpharm.aspetjournals.org/lookup/doi/10.1124/mol.117.109744>.
- Johnson, M.S. & Overington, J.P., (1993). A structural basis for sequence comparisons: An evaluation of scoring methodologies. *Journal of Molecular Biology*, 233: 716–738.
- Reynald, R.L. et al., (2012). Structural characterization of human cytochrome P450 2C19: Active site differences between P450s 2C8, 2C9, and 2C19. *Journal of Biological Chemistry*, 287: 44581–44591.
- Sansen, S. et al., (2007). Adaptations for the oxidation of polycyclic aromatic hydrocarbons exhibited by the structure of human P450 1A2. *Journal of Biological Chemistry*, 282: 14348–14355.
- Schoch, G.A. et al., (2008). Determinants of cytochrome P450 2C8 substrate binding: Structures of complexes with montelukast, troglitazone, felodipine, and 9-cis-retinoic acid. *Journal of Biological Chemistry*, 283: 17227–17237.
- Sevrioukova, I.F. & Poulos, T.L., (2012). Structural and mechanistic insights into the interaction of cytochrome P4503A4 with bromoergocryptine, a type I ligand. *Journal of Biological Chemistry*, 287: 3510–3517.
- Sevrioukova, I.F. & Poulos, T.L., (2017). Structural basis for regiospecific midazolam oxidation by human cytochrome P450 3A4. *Proceedings of the National Academy of Sciences*, 114: 486–491. Available at: <http://www.pnas.org/lookup/doi/10.1073/pnas.1616198114>.
- Shah, M.B. et al., (2012). Conformational adaptation of human cytochrome P450 2B6 and rabbit cytochrome P450 2B4 revealed upon binding multiple amlodipine molecules. *Biochemistry*, 51: 7225–7238.

- Shah, M.B. et al., (2011). Structures of cytochrome P450 2B6 bound to 4-benzylpyridine and. *Molecular pharmacology*, 80: 1047–1055.
- Walsh, A.A., Szklarz, G.D. & Scott, E.E., (2013). Human cytochrome P450 1A1 structure and utility in understanding drug and xenobiotic metabolism. *Journal of Biological Chemistry*, 288: 12932–12943.
- Wang, A. et al., (2015). Contributions of ionic interactions and protein dynamics to cytochrome P450 2D6 (CYP2D6) substrate and inhibitor binding. *Journal of Biological Chemistry*, 290: 5092–5104.
- Wang, A. et al., (2012). Crystal Structure of Human Cytochrome P450 2D6 with Prinomastat Bound. *Journal of Biological Chemistry*, 287: 10834–10843. Available at: <http://www.jbc.org/lookup/doi/10.1074/jbc.M111.307918>.
- Wang, A. et al., (2011). Structural characterization of the complex between ??-naphthoflavone and human cytochrome P450 1B1. *Journal of Biological Chemistry*, 286: 5736–5743.
- Wester, M.R. et al., (2004). The structure of human cytochrome P450 2C9 complexed with flurbiprofen at 2.0-Å resolution. *Journal of Biological Chemistry*, 279: 35630–35637.
- Williams, P. a et al., (2003). Crystal structure of human cytochrome P450 2C9 with bound warfarin. *Nature*, 424: 464–468. Available at: <http://www.nature.com/nature/journal/v424/n6947/abs/nature01862.html>.
- Yano, J.K. et al., (2005). Structures of human microsomal cytochrome P450 2A6 complexed with coumarin and methoxsalen. *Nature Structural and Molecular Biology*, 12: 822–823.
- Yano, J.K. et al., (2006). Synthetic inhibitors of cytochrome P-450 2A6: Inhibitory activity, difference spectra, mechanism of inhibition, and protein cocrystallization. *Journal of Medicinal Chemistry*, 49: 6987–7001.



IV

SUBSTRATE SELECTIVITY OF COUMARIN DERIVATIVES BY HUMAN CYP1 ENZYMES: *IN VITRO* ENZYME KINETICS AND *IN SILICO* MODELLING

by

Juvonen R.O., Ahinko M., Huuskonen J., Raunio H. & Pentikäinen O.T., 2020

Manuscript.

Request a copy from author.



V

**A PRACTICAL PERSPECTIVE: THE EFFECT OF LIGAND
CONFORMERS ON THE NEGATIVE IMAGE-BASED
SCREENING**

Ahinko M.*, Kurkinen S.T.*, Niinivehmas S.P., Pentikäinen O.T. & Postila P.A.,
2019

* Equal contribution

International Journal of Molecular Sciences 20: 2779

DOI 10.3390/ijms20112779

Reproduced with kind permission by MDPI.



Article

A Practical Perspective: The Effect of Ligand Conformers on the Negative Image-Based Screening

Mira Ahinko ^{1,†} , Sami T. Kurkinen ^{1,2,†}, Sanna P. Niinivehmas ^{1,2}, Olli T. Pentikäinen ^{1,2,3}
and Pekka A. Postila ^{1,*}

¹ Department of Biological and Environmental Science & Nanoscience Center, University of Jyväskylä, P.O. Box 35, FI-40014 Jyväskylä, Finland; mira.m.k.ahinko@jyu.fi (M.A.); sami.t.kurkinen@utu.fi (S.T.K.); sanna.niinivehmas@utu.fi (S.P.N.); olli.pentikainen@utu.fi (O.T.P.)

² Integrative Physiology and Pharmacy, Institute of Biomedicine, University of Turku, FI-20014 Turku, Finland

³ Aurlide Ltd., FI-21420 Lieto, Finland

* Correspondence: postila@gmail.com

† These authors contributed equally to this work.

Received: 21 May 2019; Accepted: 4 June 2019; Published: 6 June 2019



Abstract: Negative image-based (NIB) screening is a rigid molecular docking methodology that can also be employed in docking rescoring. During the NIB screening, a negative image is generated based on the target protein's ligand-binding cavity by inverting its shape and electrostatics. The resulting NIB model is a drug-like entity or pseudo-ligand that is compared directly against ligand 3D conformers, as is done with a template compound in the ligand-based screening. This cavity-based rigid docking has been demonstrated to work with genuine drug targets in both benchmark testing and drug candidate/lead discovery. Firstly, the study explores in-depth the applicability of different ligand 3D conformer generation software for acquiring the best NIB screening results using cyclooxygenase-2 (COX-2) as the example system. Secondly, the entire NIB workflow from the protein structure preparation, model build-up, and ligand conformer generation to the similarity comparison is performed for COX-2. Accordingly, hands-on instructions are provided on how to employ the NIB methodology from start to finish, both with the rigid docking and docking rescoring using noncommercial software. The practical aspects of the NIB methodology, especially the effect of ligand conformers, are discussed thoroughly, thus, making the methodology accessible for new users.

Keywords: negative image-based (NIB) screening; negative image-based rescoring (R-NiB); molecular docking; rigid docking; docking rescoring; virtual screening; structure-based drug discovery; cyclooxygenase-2 (COX-2)

1. Introduction

Negative image-based (NIB) screening (Figure 1) is a rigid molecular docking methodology that combines the key strengths of both the structure- and ligand-based computer-aided drug discovery approaches [1]. The NIB relies primarily on the 3D coordinates of the target protein's structure, especially its ligand-binding cavity (Figure 1), and the geometry optimization (or rigid docking) is performed similarly to the traditional ligand-based screening.

NEGATIVE IMAGE-BASED (NIB) SCREENING / DOCKING PROTOCOL

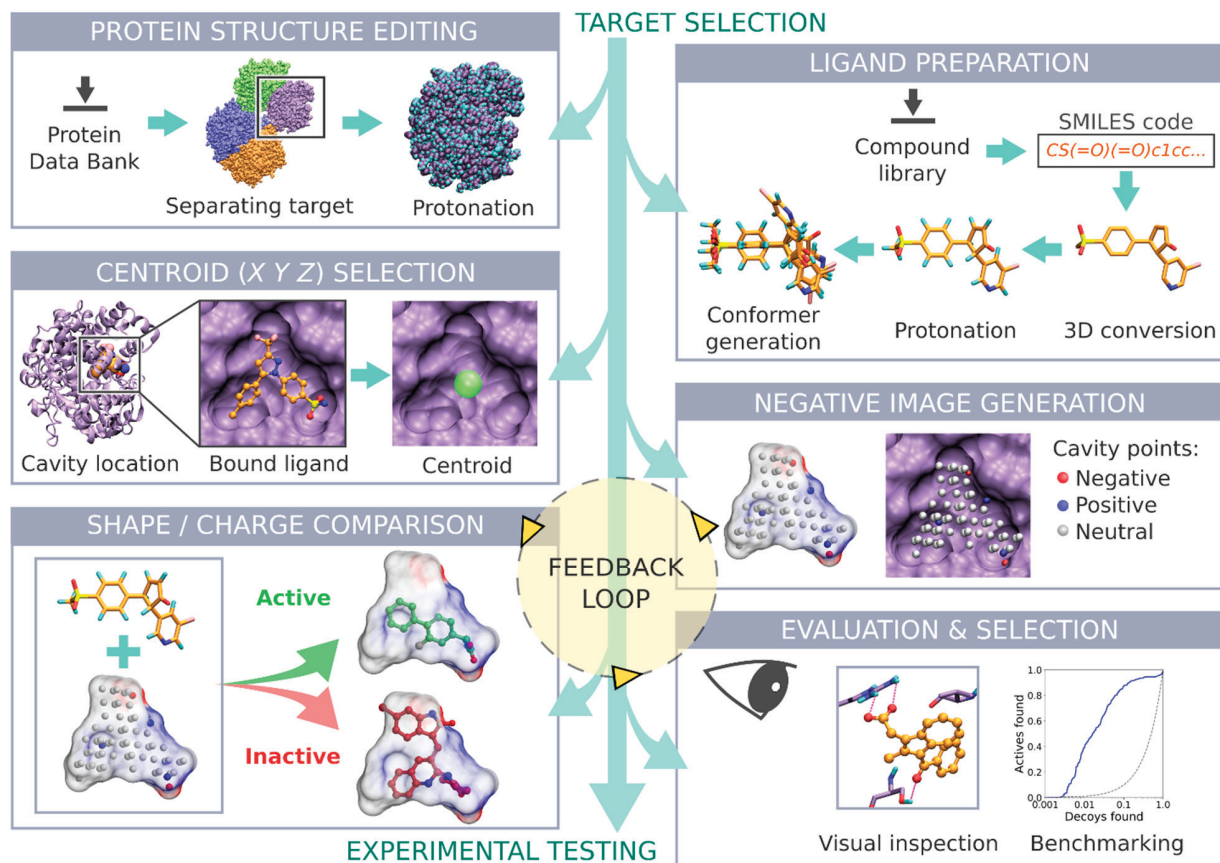


Figure 1. Negative image-based screening. The steps of a negative image-based (NIB) [1] screening or cavity-based rigid docking, which is presented using cyclooxygenase-2 (COX-2; Protein Data Bank (PDB): 3LN1 [2]; A chain) as a model system, include ligand preparation, protein 3D structure editing, cavity centroid (X Y Z) selection, negative image or NIB (negative image-based) model generation with PANTHER [3], geometry optimization or rigid docking with shape/charge comparison using ShaEP [4], visual evaluation of the highest scored ligand poses against the protein structure (e.g., BODIL [5]), and potential benchmark testing with the known ligand sets (e.g., ROCKER [6]) before the virtual screening against a commercial compound database, compound selection, and in vitro testing. In the receiver operating characteristics (ROC) plot, the blue line designates the NIB enrichment, and the dashed line outlines the random selection with the area under curve (AUC) value of 0.50.

In the NIB screening, a negative image is built based on the target protein's ligand-binding cavity shape and electrostatics (Figure 1). The NIB model ideally encompasses those key shape features of the target's cavity required for the potent ligand binding. The NIB model generation, which is done using the cavity detection software PANTHER [3], takes into account explicit water molecules, cofactors and ions, user-defined restrictions, and alternative residue protonation. A NIB model can be built based solely on protein 3D structure information (Figure 1) and, thus, without prior knowledge on target-specific active and inactive ligands. The resulting NIB model functions as a template or pseudo-ligand directly in the shape/electrostatics similarity comparison against ligand 3D conformers included in the screening compound libraries. The ligand preparation and similarity comparison against the model (Figure 1) is done using established ligand-based screening tools [4,7].

Whereas standard flexible docking relies on estimating the favorability of ligand-receptor complexes by summing up the weak interactions, such as hydrogen bonding and the hydrophobic effect, the NIB focuses squarely on the shape/electrostatics similarity of the molecular recognition process. Despite the apparent simplicity of this shape-centric approach, the benchmarking has shown that the NIB produces high enrichment as indicated by the area under curve (AUC) values and early enrichment factors with various targets [1,3,8]. The methodology is especially suitable for the targets with well-defined cavities such as nuclear receptors, but, in practice, even a sub-cavity or a shallow groove can be used to build an effective negative image. As such, the NIB has been used to assist the structure-activity relationship analysis of the 3-phenylcoumarin analog series with the 17-hydroxysteroid dehydrogenase 1 [9], monoamine oxidase B [10], and UDP-glucuronosyltransferase 1A10 [11], as well as to facilitate the discovery of novel estrogen receptor α ligands [12] and retinoic acid-related orphan receptor γ (t) inverse agonists [13].

Applying 3D similarity- or shape-based methods in the virtual screening schemes increases the diversity of the discovered compounds [14]. With the NIB, the docked ligand and protein can overlap somewhat, and, while this can weaken the compound's ranking, no ligands are skipped entirely due to the clashes as can happen with the flexible docking algorithms. The upside of tolerating the overlaps is that those novel scaffolds or functional moieties producing a good partial match with the target's cavity are readily put forward. This is advantageous because docking can put forth not only new compounds but also functional fragments to be incorporated into novel drug constructs via organic synthesis [15]. Moreover, Molecular Mechanics/Generalized Born and Surface Area (MM/GBSA) calculations, for example, can be performed to optimize the rigid docking poses inside the target protein's cavity for improving the NIB enrichment [8].

In general, flexible docking is better positioned to sample the possible ligand poses than the rigid docking approach. Therefore, the NIB methodology was recently repurposed for rescoring existing molecular docking solutions [16]. The NIB rescoring (R-NiB; Figure 2) of explicit docking poses was shown to improve the docking performance markedly, especially the very early enrichment, with several targets. This includes cyclooxygenase-2 (COX-2; enzyme commission number 1.14.99.1; Figures 1 and 2), which catalyzes the conversion of arachidonic acid to prostaglandin endoperoxide H₂ and was used as a NIB screening and docking rescoring example in this study. In short, the NIB is not only a powerful docking technique (Figure 1), but it is also a docking rescoring (Figure 2) methodology that has the potential for wide-scale application.

The study provides simple step-by-step instructions on how to perform rigid docking (Figure 1) or docking rescoring (Figure 2) using the NIB methodology with non-commercial software. The in-depth examination of the settings together with discussion on the notable exceptions is outlined using practical COX-2 screening examples (Figures 1 and 2). Furthermore, several popular ligand 3D conformer generation algorithms are tested with the COX-2 test sets and compared to outline the optimal scheme for the rigid docking with the NIB methodology.

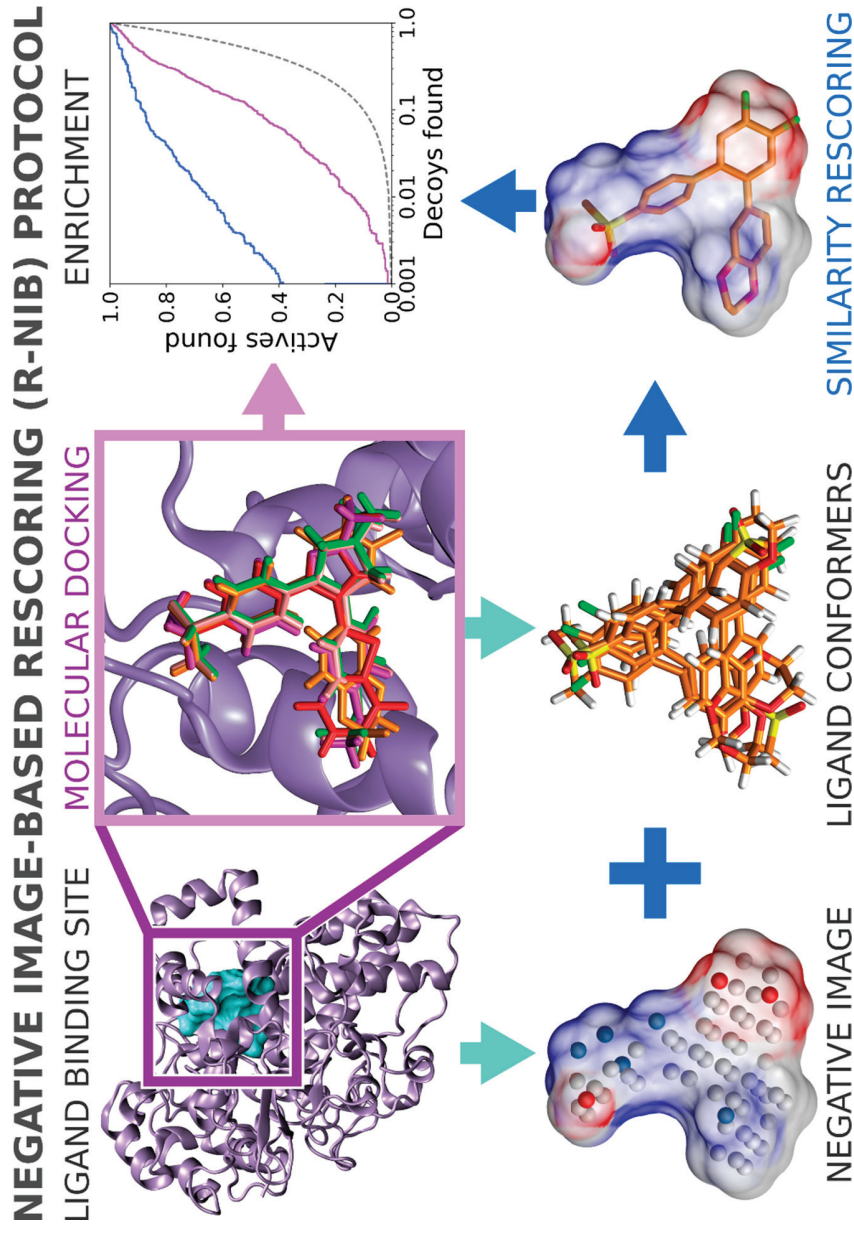


Figure 2. Negative image-based rescoring. The negative image-based rescoring (R-NiB) [16] begins with the flexible docking of ligands (green/red/magenta/orange stick models) into the binding site (magenta box) of cyclooxygenase-2 (COX-2; magenta cartoon; PDB: 3LN1 [2]; A chain) using a flexible molecular docking algorithm (e.g., PLANTS [17]). Here, the centroid coordinates of the bound inhibitor celecoxib (cyan opaque surface) are used in the docking. Several alternative flexible docking poses (e.g., $n = 10$) are output for the rescoring phase. Next, a cavity-based NiB model is generated with PANTHER [3] using the same celecoxib-based cavity centroid that was used in the original docking. The shape/electrostatics of the NiB model are directly compared against the ligand 3D conformers without geometry optimization using ShaEP [4]. With the directory of useful decoys (DUD) set [18], the initial docking enrichment (magenta line), which is already well above the random limit (dotted line), is improved by the R-NiB treatment (blue line). See Figure 1 for interpretation.

2. Results

The negative image-based (NIB; Figure 1) screening [1,3,8] and the negative image-based rescoring (R-NiB; Figure 2) [16] protocols are presented below as stepwise workflows.

The practical aspects of the NIB and R-NiB methodologies are discussed below using a virtual screening or benchmarking example, i.e., the screening is performed using the directory of useful decoys (DUD) test set [18,19] and a celecoxib-bound cyclooxygenase-2 (COX-2) protein 3D structure (Figures 1 and 2; Protein Data Bank (PDB): 3LN1 [2]). Note that the NIB protocol (commands #1–23) is executed in the BASH command line interface (or terminal) in the UNIX/LINUX environment. Furthermore, three alternative conformer generators (Table 1) were tested for the NIB in addition to OBABEL, which is used in the benchmarking example. Finally, the R-NiB is performed using the flexible docking poses generated by PLANTS to improve the enrichment. The rescoring relies either solely on the ShaEP-based complementarity or similarity scoring (commands #24–35) or the combined and re-weighted PLANTS- and ShaEP-based consensus scoring (commands #36–41).

Table 1. Ligand 3D conformers for the cyclooxygenase-2 benchmarking.

	Compounds		3D Conformer ab Initio Generation				Flexible Docking	
	Class ⁽¹⁾	SMILES ²	OBABEL ³	MARVIN ³	MAESTRO ³	RDKit ³	PLANTS ⁴	
License ⁵	-	-	OS	AF	\$\$	OS	AF	
DUD	ligs	348	3695	24,477	1650	12,850	4470	
	skipped	-	1	0	0	1	0	
	decs	12,464	620,660	695,202	89,218	329,301	118,440	
	skipped	-	201	0	3	15	1818	
DUD-E	ligs	435	9306	22,384	2322	16,069	4460	
	skipped	-	17	1	0	0	0	
	decs	23,144	1,053,413	2,405,040	212,014	807,066	247,600	
	skipped	-	1335	20	8	13	8	

¹ The ligs refer to active compounds, and decs refer to inactive decoy compounds included in the DUD/database of useful (docking) decoys -enhanced (DUD-E) databases for the COX-2. The ligs/decs skipped refer to the total amount of molecules (not conformers) that were skipped either during the ligand preparation or rigid/flexible docking. ² The original compounds were included in the DUD/DUD-E as simplified molecular-input line-entry system (SMILES) strings before the 3D conversion. ³ The ligand 3D conformer numbers used by ShaEP from the 3D conformer generation software. ⁴ The ligand 3D conformers outputted by the docking software PLANTS [17] were acquired from a prior study [16]. The conformer number was set to 10 for each compound during the flexible molecular docking. ⁵ The ligand 3D conformer generators are divided roughly into three license categories: Commercial (\$\$), academic free (AF), and open source (OS). OBABEL has GNU or general public license. RDKit is under the Berkeley Software Distribution (BSD) license. MARVIN and MAESTRO are under copyright. Not applicable sections are marked (-).

The terminal commands and further practical information are given in the Supplementary Material (README.txt, commands.txt) to assist the execution of trial runs of the protocols. The NIB protocol testing using the single low-energy conformers (Table 2) takes ~10-fold less time than with the multiple conformers (Table 3); furthermore, the R-NiB testing (Table 4) is substantially faster than the rigid docking, because the flexible docking poses are provided premade, and no geometry optimization is performed with ShaEP (Figure 3). Though the specific commands are not given to avoid repetition, the protocols were also tested using the DUD-E test set and the PDB-entry 1CX2 [20].

Table 2. Negative image-based screening using the single low-energy conformers.

PDB Code	NIB Model ¹	DUD				DUD-E			
		MAESTRO	OBABEL	MARVIN	RDKit	MAESTRO	OBABEL	MARVIN	RDKit
3LN1	Model I								
	AUC	<u>0.82 ± 0.01</u>	<u>0.79 ± 0.01</u>	<u>0.65 ± 0.02</u>	0.82 ± 0.01	<u>0.62 ± 0.01</u>	<u>0.59 ± 0.01</u>	<u>0.65 ± 0.01</u>	0.65 ± 0.01
	EFd 1%	10.1	<u>11.8</u>	5.7	12.7	0.0	<u>0.9</u>	<u>0.5</u>	<u>0.2</u>
	EFd 5%	<u>42.8</u>	<u>17.0</u>	29.9	35.7	0.7	1.4	<u>5.3</u>	3.2
	Model II								
	AUC	0.88 ± 0.01	<u>0.86 ± 0.01</u>	<u>0.73 ± 0.02</u>	0.88 ± 0.01	<u>0.72 ± 0.01</u>	0.70 ± 0.01	0.73 ± 0.01	0.73 ± 0.01
	EFd 1%	<u>23.3</u>	<u>5.8</u>	<u>9.5</u>	23.3	<u>0.5</u>	0.2	<u>0.7</u>	0.5
	EFd 5%	<u>60.1</u>	<u>18.7</u>	37.9	56.5	<u>1.6</u>	2.3	<u>26.0</u>	15.9
	Model III								
	AUC	0.88 ± 0.01	<u>0.88 ± 0.01</u>	<u>0.65 ± 0.02</u>	0.88 ± 0.01	0.73 ± 0.01	<u>0.72 ± 0.01</u>	0.73 ± 0.01	0.73 ± 0.01
	EFd 1%	31.0	<u>7.5</u>	16.4	24.8	<u>4.1</u>	0.7	12.0	7.1
	EFd 5%	58.0	<u>44.4</u>	34.5	58.8	<u>27.4</u>	<u>21.5</u>	31.6	28.5
1CX2	Model IV								
	AUC	0.83 ± 0.01	<u>0.80 ± 0.01</u>	0.78 ± 0.01	0.86 ± 0.01	<u>0.64 ± 0.01</u>	<u>0.59 ± 0.01</u>	<u>0.64 ± 0.01</u>	<u>0.68 ± 0.01</u>
	EFd 1%	15.8	<u>0.9</u>	10.6	15.3	0.0	0.2	<u>0.5</u>	0.0
	EFd 5%	41.7	<u>26.2</u>	34.5	44.1	<u>2.1</u>	2.3	<u>5.8</u>	4.1
	Model V								
	AUC	0.89 ± 0.01	<u>0.85 ± 0.01</u>	0.86 ± 0.01	0.91 ± 0.01	0.72 ± 0.01	0.68 ± 0.01	0.74 ± 0.01	0.75 ± 0.01
	EFd 1%	<u>25.3</u>	<u>6.3</u>	<u>19.8</u>	29.1	<u>0.2</u>	0.5	<u>2.5</u>	<u>0.9</u>
	EFd 5%	54.3	<u>24.2</u>	<u>54.3</u>	61.4	<u>5.7</u>	<u>4.0</u>	<u>26.3</u>	<u>19.8</u>
	Model VI								
	AUC	0.88 ± 0.01	<u>0.87 ± 0.01</u>	0.86 ± 0.01	0.90 ± 0.01	<u>0.72 ± 0.01</u>	<u>0.70 ± 0.01</u>	0.74 ± 0.01	0.74 ± 0.01
	EFd 1%	30.5	<u>13.8</u>	<u>23.0</u>	31.1	<u>0.5</u>	<u>0.5</u>	5.5	<u>3.9</u>
	EFd 5%	54.3	<u>31.7</u>	<u>51.1</u>	60.8	<u>9.2</u>	<u>7.5</u>	<u>26.7</u>	19.8

The AUC, EFd 1%, or EFd 5% values shown in bold and italics are the best scores of the DUD or DUD-E datasets within the error ranges. The scores that are higher than those produced by the multi-conformer NIB (Table 3) are underlined. ¹ The NIB Models I–III and Models IV–VI were built using PDB-entries 3LN1 [2] and 1CX2 [20], respectively. The different PANTHER [3] settings are detailed in the Results section.

Table 3. Negative image-based screening using multiple ligand conformers.

PDB Code	NIB Model ¹	DUD				DUD-E			
		MAESTRO	OBABEL	MARVIN	RDKit	MAESTRO	OBABEL	MARVIN	RDKit
3LN1	Model I								
	AUC	0.79 ± 0.01	0.73 ± 0.02	0.60 ± 0.02	<u>0.84 ± 0.01</u>	0.59 ± 0.01	0.56 ± 0.01	0.63 ± 0.01	0.64 ± 0.01
	EFd 1%	<u>12.0</u>	4.3	<u>6.3</u>	<u>15.2</u>	<u>0.2</u>	0.0	0.0	0.0
	EFd 5%	<u>36.7</u>	14.7	<u>34.1</u>	<u>50.0</u>	0.7	<u>3.1</u>	3.5	<u>3.7</u>
	Model II								
	AUC	0.87 ± 0.01	0.82 ± 0.01	0.64 ± 0.02	<i>0.90 ± 0.01</i>	0.69 ± 0.01	0.69 ± 0.01	<i>0.76 ± 0.01</i>	0.73 ± 0.01
	EFd 1%	15.5	0.0	0.6	<u>35.1</u>	0.0	<u>0.7</u>	<u>0.2</u>	0.5
	EFd 5%	53.9	3.5	<u>41.3</u>	<u>69.5</u>	0.7	<u>3.1</u>	24.7	15.9
	Model III								
	AUC	0.88 ± 0.01	0.80 ± 0.01	0.59 ± 0.02	<i>0.90 ± 0.01</i>	0.71 ± 0.01	0.69 ± 0.01	0.73 ± 0.01	0.73 ± 0.01
	EFd 1%	27.8	0.3	<u>18.6</u>	<u>43.1</u>	1.1	0.7	<i>11.8</i>	<u>8.3</u>
	EFd 5%	<u>60.7</u>	20.7	<u>42.1</u>	<u>79.9</u>	13.8	5.5	<i>39.1</i>	<u>32.9</u>
1CX2	Model IV								
	AUC	0.81 ± 0.01	0.69 ± 0.02	0.77 ± 0.01	0.85 ± 0.01	0.60 ± 0.01	0.54 ± 0.01	0.61 ± 0.01	0.64 ± 0.01
	EFd 1%	12.0	0.6	<u>11.7</u>	<u>21.8</u>	<u>0.5</u>	<u>1.0</u>	0.0	0.0
	EFd 5%	<u>38.7</u>	15.9	33.5	<u>49.1</u>	1.4	<u>3.8</u>	2.5	<u>1.6</u>
	Model V								
	AUC	0.89 ± 0.01	0.80 ± 0.01	0.88 ± 0.01	<i>0.91 ± 0.01</i>	0.71 ± 0.01	0.67 ± 0.01	<i>0.76 ± 0.01</i>	<i>0.76 ± 0.01</i>
	EFd 1%	22.1	0.0	14.9	<u>40.2</u>	0.0	0.5	<u>0.2</u>	0.0
	EFd 5%	<u>59.3</u>	11.0	49.9	<u>70.1</u>	0.5	2.4	24.7	15.4
	Model VI								
	AUC	0.88 ± 0.01	0.81 ± 0.01	0.85 ± 0.01	<i>0.91 ± 0.01</i>	0.69 ± 0.01	0.67 ± 0.01	0.74 ± 0.01	<i>0.75 ± 0.01</i>
	EFd 1%	23.5	1.7	15.5	<u>44.3</u>	0.2	0.2	1.8	0.9
	EFd 5%	<u>57.0</u>	10.4	45.6	<u>75.9</u>	2.5	2.6	24.2	<u>20.9</u>

The AUC, EFd 1%, or EFd 5% values shown in bold and italics are the best scores of the DUD or DUD-E datasets within the error ranges. The scores that are higher than those produced by the single-conformer NIB (Table 2) are underlined. ¹ The NIB Models I–III and Models IV–VI were built using PDB-entries 3LN1 [2] and 1CX2 [20], respectively. The different PANTHER [3] settings are detailed in the Results section.

Table 4. Negative image-based rescoring and consensus scoring of docking results.

Screening Method ⁽¹⁾	PDB Code	NIB Model ⁽²⁾	DUD				DUD-E			
			Weight ⁽³⁾	AUC	EFd 1%	EFd 5%	Weight ⁽³⁾	AUC	EFd 1%	EFd 5%
Docking	3LN1	-	-	0.81 ± 0.01	13.5	35.3	-	0.66 ± 0.01	5.7	21.6
R-NiB	3LN1	Model I	1.00	0.86 ± 0.01	20.1	48.3	1.00	0.63 ± 0.01	0.5	3.2
		Model II	1.00	0.94 ± 0.01	57.2	81.3	1.00	0.78 ± 0.01	11.3	30.0
		Model III	1.00	0.94 ± 0.01	54.3	79.3	1.00	0.80 ± 0.01	16.1	37.7
	1CX2	Model IV	1.00	0.86 ± 0.01	22.4	49.4	1.00	0.63 ± 0.01	0.5	3.2
		Model V	1.00	0.94 ± 0.01	64.9	83.9	1.00	0.79 ± 0.01	14.5	32.6
		Model VI	1.00	0.94 ± 0.01	58.9	77.0	1.00	0.77 ± 0.01	12.9	29.9
Consensus: Equal weight	3LN1	Model I	0.50	0.88 ± 0.01	29.0	55.5	0.50	0.66 ± 0.01	0.2	8.0
		Model II	0.50	0.92 ± 0.01	46.0	77.3	0.50	0.77 ± 0.01	13.8	32.4
		Model III	0.50	0.92 ± 0.01	48.9	75.9	0.50	0.78 ± 0.01	17.0	36.8
	1CX2	Model IV	0.50	0.87 ± 0.01	30.7	52.9	0.50	0.67 ± 0.01	0.2	10.1
		Model V	0.50	0.93 ± 0.01	56.9	77.0	0.50	0.77 ± 0.01	18.4	34.7
		Model VI	0.50	0.92 ± 0.01	51.7	74.7	0.50	0.76 ± 0.01	15.6	32.2
Consensus: Optimal weight	3LN1	Model I	0.60	0.88 ± 0.01	30.2	56.6	0.00	0.66 ± 0.01	5.7	21.6
		Model II	0.95	0.94 ± 0.01	58.3	81.6	0.55	0.77 ± 0.01	13.8	32.2
		Model III	0.75	0.93 ± 0.01	59.5	77.6	0.55	0.79 ± 0.01	17.7	36.8
	1CX2	Model IV	0.65	0.88 ± 0.01	33.0	53.7	0.05	0.67 ± 0.01	5.7	21.4
		Model V	0.85	0.94 ± 0.01	65.8	82.5	0.55	0.78 ± 0.01	18.4	35.4
		Model VI	0.85	0.94 ± 0.01	60.3	77.0	0.55	0.76 ± 0.01	16.3	32.0

The AUC, EFd 1%, or EFd 5% values shown in bold and italics are the best scores of the DUD or DUD-E datasets within the error ranges. ¹ The COX-2 DUD/DUD-E test sets were docked originally in a prior study [16] using PLANTS [17]. The 10 outputted docking poses were used in the R-NiB or consensus scoring. ² The NIB Models I–III and Models IV–VI were built using PDB-entries 3LN1 [2] and 1CX2 [20], respectively. The different PANTHER [3] settings are detailed in the Results section. ³ The R-NiB relies solely on the ShaEP scoring (weight = 1.00). The consensus scoring is done using the ShaEP scoring and the original docking scoring of PLANTS. The optimal weight between the two scoring methods was chosen based on the best EFd 1% enrichment for both the DUD and DUD-E test sets.

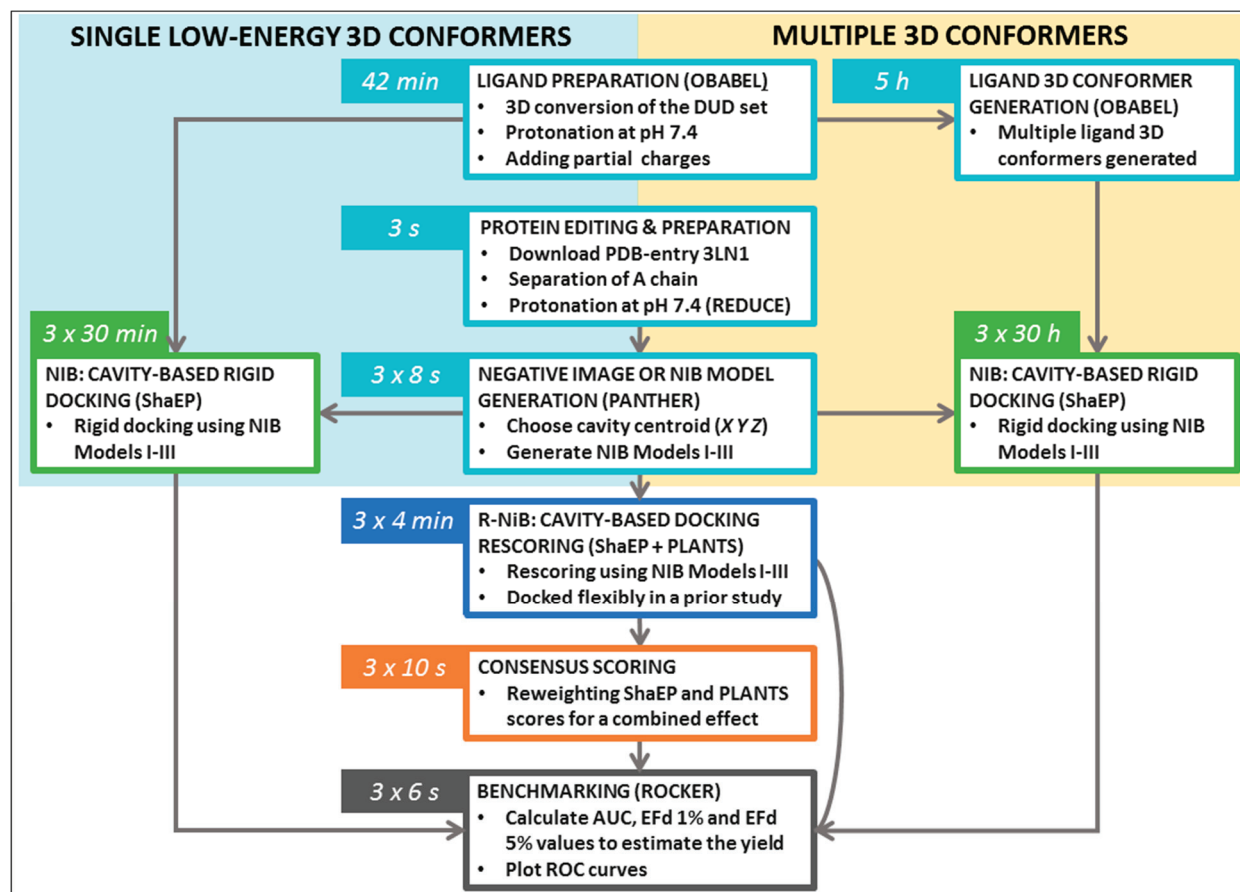


Figure 3. The duration of the protocol steps for the benchmarking example. The negative image-based (NIB; Figure 1) [1] screening or rigid docking can be done either using single low-energy conformers (Table 2) or using multiple conformers (Table 3). Going through the negative image-based rescoring (R-NiB; Figure 2) [16] protocol takes considerably less time (Table 4) because it is done using explicit PLANTS docking poses taken from a prior study [16]. Moreover, the rescoring process does not require geometry optimization in addition to the shape/charge similarity comparison. The execution of the NIB and R-NiB protocols with the cyclooxygenase-2 (COX-2) DUD test set can take less or more time depending on the used computer set-up. For simplicity, all the steps in the workflow are done using a single processor, but the process, especially the NIB screening with multiple ligand 3D conformers, can be sped up substantially by dividing the ligand sets into separate batches that are processed separately.

2.1. Ligand Preparation: 3D Conversion, Protonation, and Partial Charges

In the NIB screening (Figure 1), the rigidly docked ligand 3D conformers are generated *ab initio* with a separate software (Table 1); however, depending on the target protein and the ligand sets one can acquire high enrichment using only a few or even a single low-energy conformer. Before performing the cavity-based rigid docking with a single conformer or multiple conformers, the 3D coordinates (simplified molecular-input line-entry system (SMILES)-to-MOL2), partial charges and ionization/protonation states of the small-molecules need to be generated (Figure 1). This is achieved using, for example, LIGPREP in MAESTRO or MARVIN, but non-commercial software such as RDKit or OBABEL [21] can also be used. It is crucial that the pH is set to match the conditions of the activity assay (e.g., pH 7.4) during the protonation.

The DUD [19] ligands for COX-2 were converted from the SMILES format into the MOL2 format using OBABEL [21] (command #1). A single 3D conformer was generated for each ligand included in the set. Next, the protonation of the ligands was set to match pH 7.4 (command #2), and the partial charges were inserted using the Merck Molecular Force Field 94 (MMFF94) [22] (command #3) with OBABEL [21]. For comparison, the ligands were also prepped using LIGPREP in MAESTRO, MARVIN, and RDKit (Table 1). With COX-2, the NIB screening produces high enrichment directly using these single low-energy 3D conformers, and, for this reason, one can choose to skip the 3D conformer generation step to save time when going through the protocol (Figure 3).

2.2. Ligand Preparation: 3D Conformer Generation

Ultra-fast speed and computational efficiency are hallmarks of both the NIB screening (Figure 1) and the ligand-based screening [1,3,8]. This is largely because the different ligand 3D conformers are not sampled on the fly against the protein 3D structure during the rigid docking, as is done in the flexible molecular docking. Instead, several low-energy conformers are generated for each ligand prior to the eventual similarity screening and geometry optimization with the cavity-based NIB model (Figure 1). The ligand 3D conformer generation can be done using either non-commercial or commercial software tools with varying results (Table 1). The conformer generation, as well as the eventual cavity-based rigid docking using the multiple conformers, is a lot more time consuming than performing the NIB screening with single low-energy conformers (Figure 3). Alas, one should not expect that single conformers would work in all screening experiments, although this is the case with the COX-2 benchmarking.

The protonated ligand 3D coordinates were used as an input to generate multiple conformers using the `-confab` option in OBABEL [21] (command #4). By default, an extensive number of conformers is generated, and, to avoid this, the output was limited with two basic options: The maximum number of conformers (`-conf`; from 1,000,000 to 100,000) and the root mean square deviation cutoff (`-rcutoff`; from 0.1 to 1.0). For comparison, the ligand 3D conformer generation was also done using other conformer generators (Table 1).

2.3. Selecting the Target Protein 3D Structure

The success of the NIB screening is dependent on the input protein 3D structure, especially its ligand-binding cavity conformation, used as a template for the negative image generation (Figure 1). The input structure selection follows the basic criteria that apply to standard molecular docking as well: The resolution should be sufficiently high, and the protein conformation should be able to accommodate the binding ligand. In principle, the PDB-entry does not have to house any known active compounds prior to the model generation, but a bound ligand can affect the cavity geometry via induced-fit effects. If included, the bound ligand(s) can assist in the NIB model generation by providing centroid coordinates (Figures 1A and 4A), and they can assist in limiting the model scope to the known binding area. In some cases, using multiple protein structures in the model generation originating, for example, from molecular dynamics (MD) simulation trajectory can improve the NIB screening yield [1].

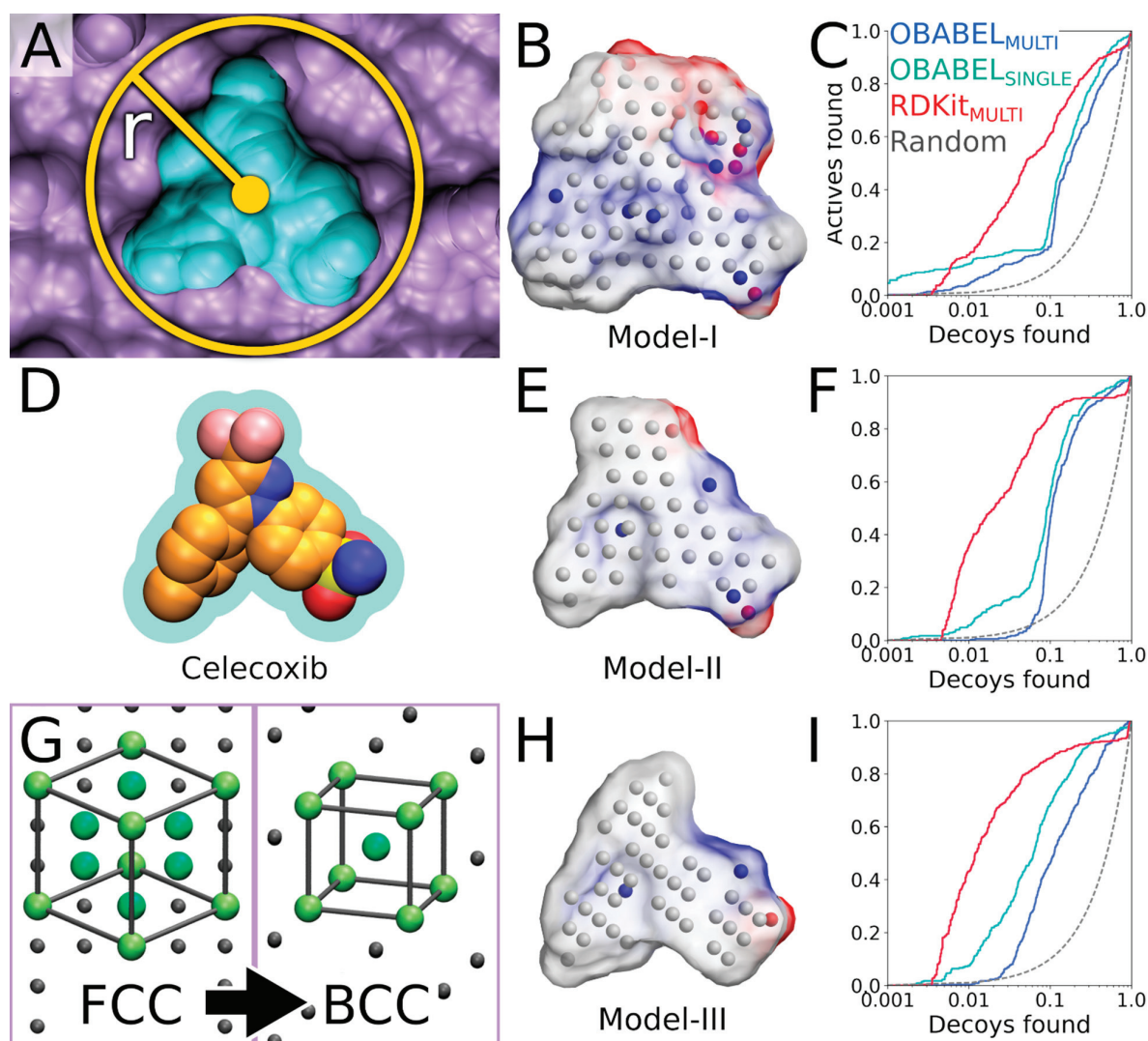


Figure 4. The negative image-based screening benchmarking evolution. (A) A cross section of the ligand-binding cavity (cyan) of the cyclooxygenase-2 (magenta; PDB: 3LN1; A chain) shown with the cavity centroid and detection radius ($r = 10 \text{ \AA}$). (B) The NIB (negative image-based) Model I, generated using the default PANTHER settings, (C) produced higher enrichment for the DUD test set using RDKit multi-conformer set (red line) than the multi-conformer OBABEL set (blue line; Table 3). The single-conformer OBABEL set (cyan line) resulted in higher early enrichment (Table 2) than its multi-conformer set. (D) The bound inhibitor (CPK model) is shown with the extra 1.5 \AA volume. (E) Model II, fashioned using the 1.5 \AA ligand distance limit, has roughly similar shape as the inhibitor (D versus E). (F) The enrichment was improved with Model II for the RDKit set over the prior model; however, the early enrichment weakened with both OBABEL sets (Tables 2 and 3). (G) Models I and II were generated using the face-centered cubic (FCC) packing. The body-centered cubic (BCC) lattice packing was used for Model III. (H) Model III has less dense packing than Model II (E versus H). (I) Model III worked best with the RDKit conformers, but the effect was lesser for the OBABEL sets (Tables 2 and 3). See Figure 1 for interpretation.

Two PDB-entries were selected for the NIB screening with COX-2. The PDB-entry 3LN1 [2] (Figures 1, 2 and 5C) is used in the practical example; meanwhile, the PDB-entry 1CX2 [20] (Figure 5C) is used as an alternative input for which the applied commands are not shown due to their redundancy. The protein X-ray crystal structure was downloaded directly from the PDB in the terminal (command #5), but it can also be downloaded manually online (e.g., <https://www.rcsb.org/>).

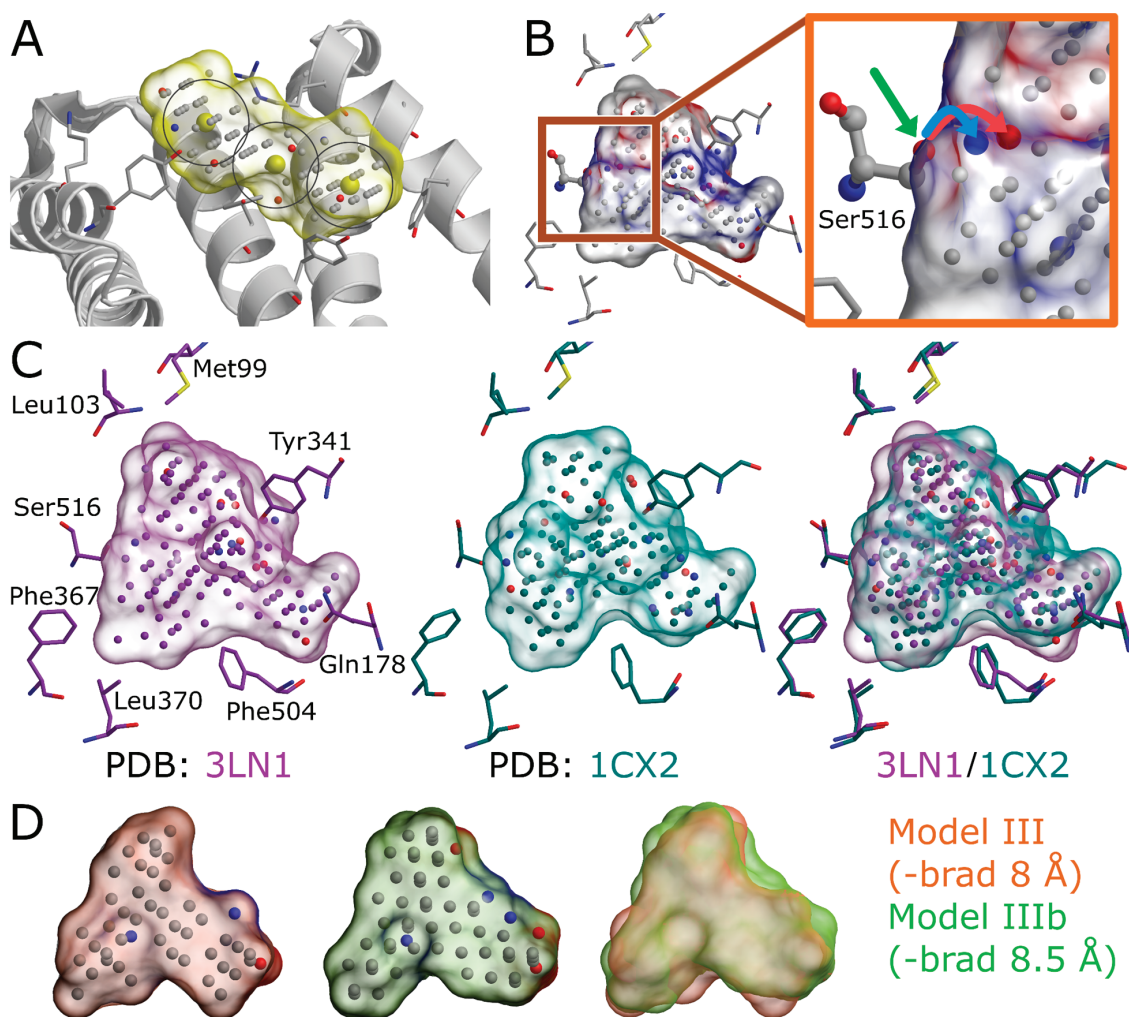


Figure 5. Valuable settings in the negative image generation. (A) A negative image or NIB (negative image-based) model (yellow surface) is built based on a shallow surface groove (white cartoon; PDB: 4BTB) [23] using three center (-center) coordinates (yellow spheres) and the multibox (-mbox) option in PANTHER [3]. (B) The effect of protonation for the model composition is shown with the hydroxyl group of Ser516 (ball-and-stick model) of cyclooxygenase-2 (PDB: 3LN1) [2]. If no specific protonation is given, two alternative angles of the hydroxyl's polar proton (polar oxygen indicated with green arrow) are considered, and, thus, two models are generated where the mirroring cavity point is either positive (H-bond acceptor; red sphere) or negative (H-bond donor; blue sphere). The opposite charge pair is highlighted by cyan and red arrows in the close-up (orange box). (C) The input coordinates affect the resulting models as demonstrated by two PDB-entries 3LN1 [2] (purple surface) and 1CX2 [20] (turquoise surface). (D) The detection radius has a substantial effect, as highlighted by the model overlay. Model III (orange surface) is generated using otherwise similarly as Model IIIb (green surface), but the box radius (-brad) of 8 Å is increased to 8.5 Å. A few residues are shown as sticks for reference. See Figure 1 for interpretation.

2.4. Protein 3D Structure Editing and Preparation

The extra chains and other non-peptidic residues do not necessarily have to be removed for building NIB models using PANTHER [3], although their removal can make the process marginally faster. Even though the NIB model generation can be performed without protons added to the protein 3D structure, this can lead to several alternative cavity-based models. This is because certain residues can have alternative protonation states or bond angles for the protons that are responsible for the H-bonding (Figure 5B) and, thus, depend on the local environment. In fact, one should be mindful on

how the added protons affect the charge distribution of the negative image and the eventual docking results. The protons can be added for the target structure and even its cofactors using external software (e.g., REDUCE [24]), in which case the alternative proton shuffling is omitted during the NIB model generation (Figure 1). The case-specific protonation of, for example, histidine and aspartic acid residues at the ligand-binding cavity, can be tricky, and, in unclear cases, one should employ protonation prediction algorithms such as PROPKA [25,26].

The A chain of the PDB-entry 3LN1 [2] was selected for the NIB model generation and, for improved computing efficiency, extracted into a separate PDB file (command #6; Figure 1) where the explicit protons were inserted using the default settings of REDUCE [24] (command #7; Figure 1). With COX-2, the outputted bond angles of the protons were visually assessed to be reasonable in BODIL [5]. Such an evaluation is necessary because, for example, the proton in the hydroxyl group of Ser516 side chain in the COX-2 active site could have an alternative angle that affects the resulting cavity point composition (Figure 5B).

2.5. Defining the Ligand-Binding Cavity Centroid

The NIB model generation using PANTHER [3] requires that the ligand-binding cavity location is designated beforehand (Figures 1A and 4A). In other words, the user needs to have a concrete idea where the ligand binding should happen to focus on a specific location inside or on the surface of the protein. For this purpose, cavity detection software such as SITEMAP [27,28] or POVME 3.0 [29] can estimate the druggability and dimensions of protein cavities. In any case, the best scenario is to begin the NIB model generation with PANTHER using the centroid coordinates of a bound ligand already included in the PDB-entry. If not applicable, the cavity detection can begin from any arbitrary coordinate point given by the user (-center(s)) or by using any residue atom coordinate present near the cavity center (-basic multipoint). Overall, the centroid selection process is highly similar to choosing the center of radius for any standard docking routine.

The COX-2 inhibitor ligand celecoxib, or CEL, (residue 682 in the A chain; Figures 1 and 4D), which is bound at the active site in the PDB-entry 3LN1 [2], was selected to define the cavity center (A-682) during the NIB model generation with PANTHER [3] (Figure 4A,D).

2.6. Generating a Negative Image of the Enzyme's Ligand-Binding Cavity

The first NIB model is typically generated using the default settings in PANTHER [3] (Figure 1), after which it is critically evaluated, and, if needed, the settings are further tweaked. For convenience, especially at the later stages of the NIB model generation, the necessary settings are inserted directly into a PANTHER [3] input file using a text editor instead of typing and executing them in the terminal, as is done in the example below.

Firstly, the default PANTHER [3] input file (default.in) is generated (command #8). Secondly, PANTHER [3] is used to generate a preliminary NIB model (command #9) in the MOL2 format (Model I in Figure 4B). If the input protein would lack protons (command #7, not executed), altogether 12 alternative NIB models would be outputted for COX-2. This is because the cavity houses several residues capable of H-bonding, and each proton of the H-bond donor groups, such as the hydroxyl group, is given an alternative position that affects the charge distribution of the model (Figure 5B).

2.7. Estimating the Negative Image Viability and Tweaking the Settings

There are at least three major concerns regarding the model viability in the NIB screening:

- (1) The NIB model must be restricted to the area of the cavity that facilitates the ligand binding.
- (2) The NIB model shape should resemble, however loosely, an envisioned or actual ligand molecule occupying the cavity.
- (3) The NIB model cavity points must contain crucial charge/electrostatics information required for mimicking the ligand-receptor H-bonding, as the shape similarity alone might not be enough for ensuring rigid docking success (Figure 5B).

The preliminary model or Model I (command #9) outputted by PANTHER [3] matches the cavity shape (Figure 4A versus 4B). It is composed of neutral filler atoms (grey dots in Figure 4B) and negatively or positively charged cavity points (red or blue dots, respectively, in Figure 4B) that have the opposite charges in comparison to the protein residues lining the cavity. The partial charges of protein (and possible cofactor) atoms must be pre-defined in a separate file, which contain by default AMBER (Assisted Model Building with Energy Refinement) force field-based charges (a PANTHER library charge.lib). In other words, the charge points face directly those residues capable of either accepting or donating protons in the H-bonds (Figure 5B). Before performing the similarity comparison with Model I (Figure 4B), a second model or Model II (Figure 4E) is generated using a 1.5 Å ligand distance limit (-ldlim) in PANTHER [3] (command #10). Though the two outputted models are roughly similar, Model II does not expand far away from the space taken by the inhibitor bound at the ligand-binding site in the input PDB-entry (Figure 4D versus 4E). In comparison, Model I, which was generated without the ligand distance limit but only relies on the 8 Å cavity detection radius, is visibly bulkier than Model II (Figure 4B versus 4E). This demonstrates that the ligand is loosely bound to the protein, the ligand does not fill the entire space available for binding, or the PANTHER parameterization for the NIB model generation is not optimal.

2.8. Rigid Docking by Aligning Ligands Against the Negative Image

The NIB screening is performed using the similarity comparison algorithm ShaEP [4] (Figure 1), which was originally developed for the ligand-based screening. The ligand 3D conformers are geometry optimized or rigidly docked based on the shape/electrostatics against the cavity-based NIB model (Figure 1). ShaEP [4] provides a similarity score from 1 to 0 for ranking the compounds from the best to the worst matches against the cavity-based model. Those ligand conformers matching the NIB model best are given the highest score, indicating the highest degree of similarity with the cavity space available for the ligand binding. If the model encompasses the key shape and charge features needed for the ligand binding, in theory, the NIB screening should put forward the best-matching molecules. While the charge can be an important factor for assuring correct H-bonding interactions in the rigid docking (Figure 4B), the shape is frequently the defining factor in the ligand-receptor complex formation.

The rigid docking is performed using the default settings of ShaEP [4] (commands #11 and 12). While this basic arrangement works well for COX-2, the yield can be improved with certain targets by either lowering or increasing the charge effect. The NIB screening success for Models I and II (Figure 4B,E) is estimated using the early enrichment and area under curve (AUC) values (Tables 2 and 3) and the receiver operating characteristics (ROC) curves (Figure 4C,F) calculated with ROCKER [6] (commands #13 and 14). The compounds skipped during the ligand preparation or the NIB screening (Table 1), if any, are not considered in the AUC calculation. The Model II screening produced a higher AUC value than the flexible docking with the DUD set; however, the very early enrichment, or EF_d 1%, was not better with either of the models using the OBABEL-generated conformers than what PLANTS produced (Table 3 versus Table 4). Notably, the enrichment was higher for both NIB models, surpassing the flexible docking yield, when the rigidly docked single/multiple conformers were generated using, for example, RDKit instead of OBABEL (Table 3; Figure 4C,F).

2.9. Feedback Loop—Fine-Tuning the Cavity Detection Settings

Following the rigid docking, one should inspect best-ranked docking poses and fine-tune the NIB models with the benefit of hindsight (Figure 1). For example, one can extract the 50 best-ranked docking poses (molpicking.bash; commands #15–20) and visualize the predicted binding modes using the preferred 3D viewer (e.g., BODIL) [5]. With the benchmark test sets, one can apply the trial-and-error approach, where the usefulness of each PANTHER setting generating the model (Figure 4B,E,H) can be assessed. This sort of training is not possible without verified active and inactive compounds or expert intuition to assess the effect of the applied changes. For COX-2, the DUD/DUD-E test sets [18,19] include both active ligands and inactive decoy molecules (Table 1) for assessing the fitness of the NIB

models. The first-tried default settings frequently work well in the NIB screening [3] (e.g., Model I in Figure 4B,C); nevertheless, visualization of the models and docking poses and fine-tuning of the cavity detection settings is recommended ($-ldlim$ 1.5 Å was used for Model II in Figure 4E,F). Better models might be acquired, for example, by varying the centroid position (Figure 4A), the cavity detection radius (Figure 4B), and the atomic radii of the protein residues (a PANTHER library *rad.lib*), the ligand distance limit (Figure 4E,F) or the filler atom packing method (Figure 4G).

The third NIB model, or Model III (Figure 4H), was generated using the otherwise same settings as Model II (Figure 4E), but the default face-centered cubic (FCC) packing was changed to the less dense body-centered cubic (BCC) method (command #21; Figure 4G). Model III can also be generated using an input file (*final_panther.in* in the Supplementary Material) instead of the elaborate terminal command. Though only the packing method was altered during the cavity-detection phase, the composition and shape of these two negative images differ markedly (Figure 4E versus 4H). The NIB screening/docking (command #22) and the enrichment analysis (command #23) indicate that Model III does not produce higher EFd 1% than the prior models when the single/multiple ligand 3D conformers were prepared using OBABEL (Tables 2 and 3; Figure 4B,E). Yet again, the NIB screening results are considerably better for the third model, far surpassing the yield of PLANTS docking, especially, if the conformer generator RDKit was employed (Figure 4C,F versus 4I; Table 3 versus Table 4).

These enrichment metrics (Tables 2 and 3; Figure 4) indirectly suggest that the rigid docking with the ab initio generated ligand conformers is able to predict the binding poses of the COX-2 active ligands reasonably well. More to the point, the NIB, that ranks the ligands based on the cavity-based similarity, fare better than the ChemPLP scoring in PLANTS (Tables 2 and 3). As with any docking methodology, it is prudent to compare the predicted poses to experimentally verified binding modes. Here, a close inspection is done for the best-ranked docking pose of an established COX-2 inhibitor included in the DUD set (Figure 6A,B). The overall alignment of the compound in question is roughly similar between the top-ranked NIB screening and the flexible docking poses (Figure 6B versus 6C,D), but, more importantly, the NIB proposes a binding pose resembling that of structurally related inhibitor celecoxib (Figure 6B versus 6E). As a result, the NIB screening provides a lot higher ranking for the inhibitor than the regular flexible docking (NIB rank #315 versus PLANTS rank #8585). The same ranking order, but to a lesser effect, is acquired for the celecoxib (NIB rank #125; PLANTS rank #295).

2.10. Negative Image-Based Rescoring of Flexible Docking Solutions

In addition to the cavity-based rigid docking (Figures 1 and 4), the NIB methodology can be used to rescore existing docking solutions for improving the flexible molecular docking performance (Figure 2) [16]. The preliminary docking with the target protein can be performed using any flexible docking algorithm such as PLANTS [17] or AUTODOCK [30]. Multiple docking poses are outputted and, if need be, converted into the MOL2 format for the rescoring with the R-NiB. Next, the same cavity space used in the flexible docking is again used to generate a NIB model, which encompasses the key shape/charge features needed for the ligand binding, using PANTHER [3]. Finally, the flexible docking poses are compared against the cavity-based NIB model using ShaEP [4] without the time-consuming geometry optimization ($-noOptimization$) that is done during the rigid docking (Figure 3).

The COX-2 ligands [18,19] were docked flexibly using the default settings of PLANTS [17] after the ligand preparation with LIGPREP in MAESTRO in our previous study [16]. The used PLANTS input file and the explicit docking poses are included in the Supplementary Material. Models I–III (and alternative PDB-entry 1CX2-based Models IV–VI) generated for the NIB screening (commands #9, #10, and #21) were directly used with the R-NiB. Altogether, 10 alternative flexible docking poses for each ligand (Table 1) were rescored using ShaEP [4] without the geometry optimization (commands #24–26) using the $-noopt$ option. The ShaEP result files containing multiple alternative poses for each rescored compound were trimmed to include only the best-ranked poses for the enrichment calculation (*trim_shaep.bash*; commands #27–29). The EFd 1%, EFd 5% and even the AUC values (commands #30–32) indicate that the R-NiB improved docking performance for the DUD set (Table 4). With the

more demanding DUD-E set, the first model did not improve the enrichment, but the R-NiB was consistently able to improve the yield with the latter two models (Table 4).

In theory, the R-NiB or any other rescoring methodology can improve the docking yield (Table 4), because, while the original docking algorithm samples the “correct” ligand binding poses, its default scoring does not rate these specific poses high enough. Again, this effect is demonstrated by inspecting the predicted binding poses of an established COX-2 inhibitor included in the DUD set (Figure 6A). The R-NiB selects an alternative docking pose for the inhibitor (Figure 6D), which remains the best-ranked NIB screening pose (Figure 6B) regarding the sulfonamide group placement than the one ranked best by PLANTS (Figure 6C). Notably, the R-NiB ranking of the example compound is substantially higher than what PLANTS or the NIB suggested (R-NiB rank #3 versus NIB/PLANTS rank #315/#8585). By comparing this best-ranked inhibitor pose to structurally similar celecoxib bound at the COX-2 active site (Figure 6E; PDB: 3LN1 [2]), it is evident that it is spot on for the sulfonamide (magenta box in Figure 6F). Again, the R-NiB also provides a far better ranking for the inhibitor celecoxib than the flexible docking or NIB screening (R-NiB rank #42 versus NIB/PLANTS rank #125#295).

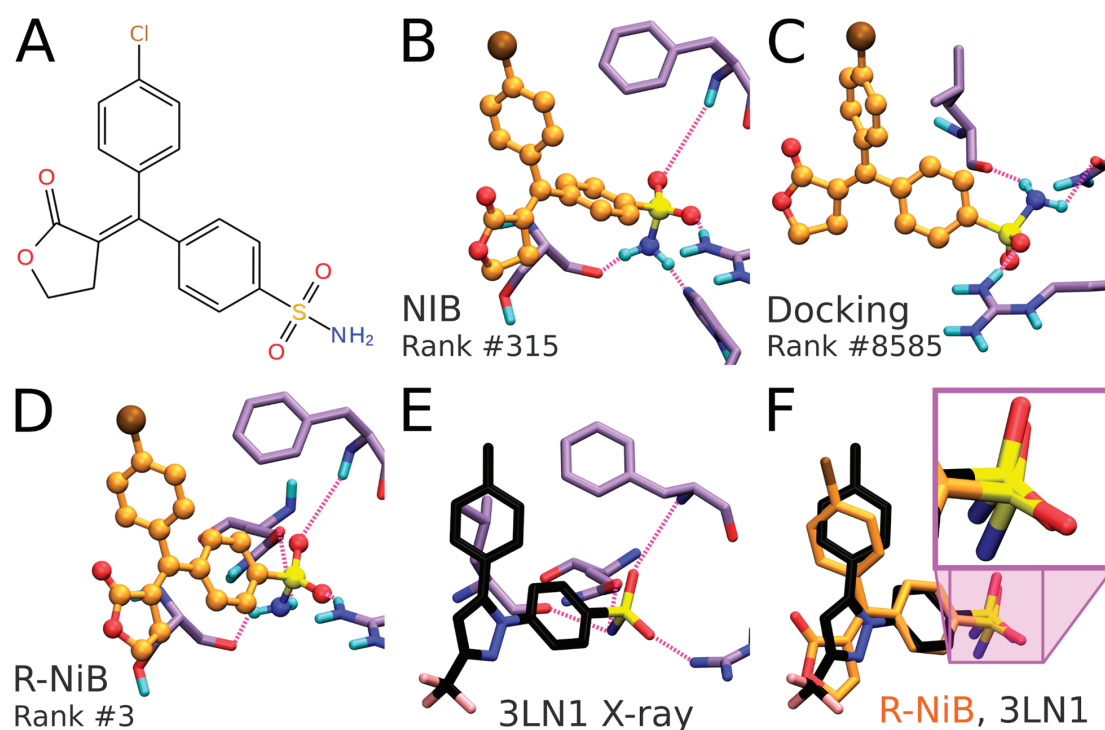


Figure 6. The predicted binding poses and ranking of a known inhibitor for comparison. (A) The 2D structure of an established cyclooxygenase-2 (COX-2) inhibitor ZINC03959950 included as an active ligand in the DUD test set [18]. (B) The negative image-based (NIB; Figure 1) [1] screening puts forth roughly similar pose for the inhibitor (yellow ball-and-stick model) as (C) the flexible docking with PLANTS [17] and (D) the negative image-based rescoring (R-NiB; Figure 2) [16]. However, the ranking of the inhibitor differs a lot between these approaches. In the top-ranked poses (B–D), the inhibitor’s sulfonamide group H-bonds (pink dotted lines) with the corresponding protein residues (purple stick models; protonated A chain of PDB-entry 1CX2 [20]) differently. (E) Notably, the verified binding mode of the inhibitor celecoxib (black stick model; PDB: 3LN1 [2]) indicates how the sulfonamide should be placed inside the cavity. (F) In fact, the comparison of celecoxib and the docked inhibitor (yellow stick model) binding modes shows that the sulfonamide placement (zoomed into in the magenta box) by the R-NiB is a match. The NIB selects highly similar alignment for the group as the R-NiB (B versus C) and the poorest choice is made by the default docking scoring of PLANTS (E versus C). The top-ranked inhibitor binding modes for both the NIB screening (conformers from the RDKit routine; Table 1) and rescoring were acquired using Model III (Figure 4H; PDB: 3LN1; Table 3).

Despite this specific example (Figure 6), the ability of the R-NiB to improve docking performance could also be explained by the low scoring for the inactive decoys that align poorly with or further away from the designated cavity area. In any case, it is always recommended to extract a few of best-ranked docking poses (e.g., ~50–100) to see if the docking or rescoring results make sense at the atomistic level (molpicking.bash; commands #33–35).

2.11. Consensus Scoring: Balancing the Scoring Functions

The ShaEP scoring can be combined with the original PLANTS scoring in the consensus scoring [16] (Figure 7A). The R-NiB scoring relies solely on the shape/electrostatics similarity calculated with ShaEP (weight of 1.00 in Table 4) and, accordingly, PLANTS is only responsible for sampling the ligand poses. Though the PLANTS docking enrichment is not as high as that of the best NIB or R-NiB results (Tables 3 and 4), the flexible docking poses contain better matching geometries with the target's cavity than what the ab initio conformer generators produce (Figure 6B versus 6D). However, the R-NiB performance can be improved in some cases by incorporating the original docking scoring to the ShaEP-based compound ranking. This requires the normalization of the scores outputted by both ShaEP and PLANTS, after which the weight of the two functions is balanced for the optimal effect (Figure 7A). In general (but not always), applying an equal weight (a weight of 0.50 in Table 4) between the scoring functions produces better enrichment than what the PLANTS docking or R-NiB produces alone; still, the optimal weight varies for different targets [16].

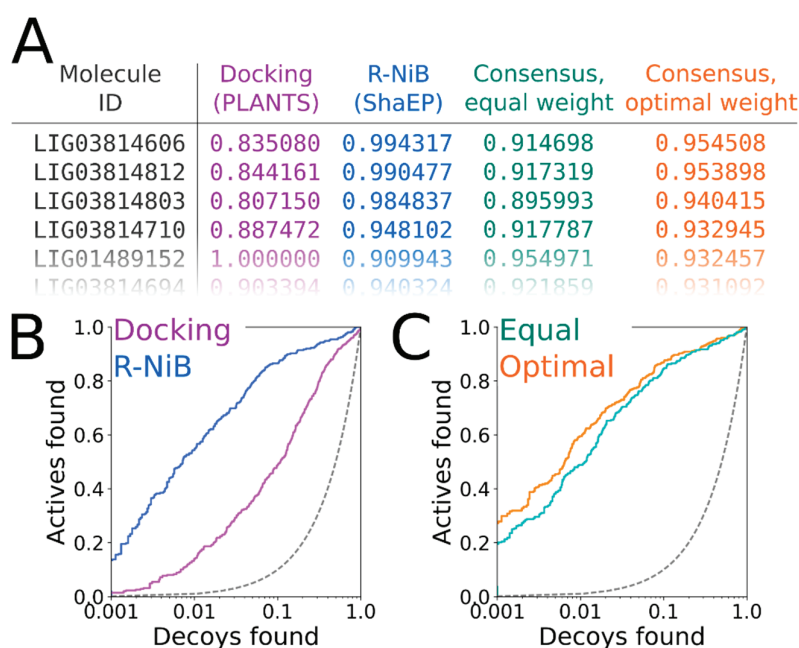


Figure 7. The consensus scoring of docking results using the negative image-based rescoring. (A) The highest PLANTS [17] scoring (magenta) and the ShaEP-based negative image-based rescoring (R-NiB) (blue) values for the docked DUD data set (both normalized from 0 to 1) are combined for the re-ranking of the compounds (green and orange). The aim was to improve the docking performance regarding the EFd 1% (Table 4) by applying either equal (weight = 0.50, green) or optimal weight (weight = 0.75, orange) on the scoring functions. The values are shown for the top-ranked molecules that were rescored using Model III (Figure 4H; Table 4). (B) Based on the semi-log₁₀ scale (only x-axis logarithmic) receiver operating characteristics (ROC) curves, the straight-up R-NiB (weight = 1.00; Table 4; blue line) clearly outperforms the original docking scoring (magenta line; Table 4). (C) When a higher enrichment is sought via systematic re-weighting, the result is a consensus score with the optimal weight (orange line; Table 4) that produces higher early enrichment than the equal weight (green line; Table 4). Accordingly, relying more on the cavity-based ShaEP scoring than the original PLANTS docking or ChemPLP scoring produces a better yield. See Figure 1 for interpretation.

The normalization and re-weighting of the PLANTS and ShaEP scoring (Figure 7A) are performed using a BASH script (consensus.bash; commands #36–38), which is specific for the combined PLANTS and ShaEP usage. The consensus scoring for the DUD docking poses produced better EF_d 1% values consistently if the optimal weight was systematically tested, whereas the equal weight scoring (commands #39–41) improved on the R-NiB yield only with Model I (Table 4). With the DUD-E set, improvements over the R-NiB were consistent but also moderate with Models I and II (Table 4), but even a minor up-tick in the early enrichment could have substantial effects for real-life screening experiments. The early enrichment improvements over straight-up R-NiB and PLANTS docking (Figure 7B) through the consensus scoring are visible in the semi-logarithmic ROC curves of the DUD set with Model II (Figure 7C) when the optimal weight was applied (Table 4).

3. Discussion

The cyclooxygenase 2 (COX-2) benchmarking example shows that the negative image-based (NIB; Figure 1) [1] screening or rigid docking is consistently producing higher enrichment than the regular flexible docking (Table 3 versus Table 4). The area under curve (AUC) values demonstrate the dominance of NIB over PLANTS [17] docking with both the DUD [19] and DUD-E [18] sets (Table 3). The NIB has been shown to outperform standard docking regarding the AUC values with a multitude of targets in prior studies [1,3,8]. On a practical level, the early enrichment values (calculated as true positive rates when 1 or 5 % of the decoys have been found) are a better measure of virtual screening success than the AUC values. Hence, it is noteworthy that the highest EF_d 1% and EF_d 5% values produced by the NIB screening with the COX-2 sets are also higher than those given by the PLANTS docking (Table 3 versus Table 4).

The better performance of the cavity-based rigid docking routine over the flexible docking suggests that the shape complementarity is a crucial factor for the COX-2 inhibitor binding, at least with the benchmark test sets. That is not to say that other docking algorithms or PLANTS cannot outperform the NIB methodology in virtual screening experiments on a case-by-case basis [3]. Both the composition of the test sets and the target's cavity geometry are bound to lower the effectiveness of the cavity-based rigid docking in comparison to the flexible docking in some cases. Moreover, the COX-2 benchmarking (Tables 2 and 3) indicate that the NIB model composition (Figure 4B,E,H), the input 3D protein structure conformation (Figure 4C), and the ligand conformer generation method (Table 1; Figure 4C,F,I) profoundly affect the rigid docking success (Table 3).

The NIB model generation is a straightforward process when the target protein's ligand-binding site is a well-defined cavity (Figures 1 and 4). The charge distribution and dimensions of the model can be improved using different PANTHER [3] options such as the cavity centroid (center(s), -cent; Figures 1 and 4A), cavity detection radius (box radius, -brad; Figures 1, 4A and 5D), and filler atom packing (packing method, -pack; Figure 4G), as well as via alternative residue protonation (Figure 4B) or input structure conformation (PDB: 3LN1 versus 1CX2; Figure 4C; Table 3). A less direct approach might be needed when dealing with shallow surface pockets, as well as large or even open cavities without clear geometrical limits. To prevent the model protruding too far from the intended cavity area, one can limit the NIB model expansion using an already bound ligand (ligand distance limit, -ldlim; Figure 4D,E) or other selected residues (basic multipoint, -bmp) inside the cavity or even lining a groove on the protein surface. In addition, the NIB model can be forced to a certain subsection of the cavity by applying the multibox option (-mbox; Figure 5A), which allows the use of several coordinate points to describe a cavity of irregular or arbitrary shape.

Importantly, the COX-2 example shows that the rigid docking (Figure 1) is not only dependent on the NIB model shape/electrostatics but that the ligand 3D conformers have a substantial effect (Table 3). In the case of COX-2, the NIB screening works remarkably well when only a single low-energy 3D conformer is used in the rigid docking for each compound (Figure 4; Table 2). In fact, the results suggest that the costly use of multiple conformers (Figure 3; Table 3) could improve the NIB screening performance consistently with the DUD set only when the conformers were outputted by the RDKit

(Table 3; Figure 4). With the more demanding DUD-E set, only the AUC values were improved consistently using the multiple conformers outputted by MARVIN or RDKit in the rigid docking (Table 3; Figure 4H,I).

Prior to this study, the ligand 3D conformer generation had been tested thoroughly for the purpose of assessing its effects on the ligand-based screening [31,32]; however, the benchmarking (Table 3) shows that the conformer composition is equally important for the NIB screening (Figure 1). OBABEL was used in the ligand preparation in the benchmarking example due to its ease of use and open source status (Table 1). The cavity-based rigid docking, especially using the single low-energy 3D conformers, produced consistently higher AUC values than the PLANTS flexible docking, regardless of the employed ligand preparation method (Table 3 versus Table 4). Nevertheless, the NIB screening done using the multiple ligand conformers outputted by OBABEL (Table 1) produced weaker enrichment than the other software such as RDKit (Figure 4C,E,I; Table 3). Though RDKit produced reasonable ligand conformations and excellent NIB screening results with the COX-2 test sets (Table 3), in practice, its successful usage requires basic knowledge of PYTHON programming and, generally, more effort than the other software (Table 1).

The effectiveness of the outputted 3D conformers differed between the software in the NIB screening. Their rigid docking performance is undoubtedly case-specific, and one should not draw too far-reaching conclusions based on the COX-2 benchmarking only. For example, the single low-energy conformers worked well with COX-2 (Figure 4; Table 2) likely due to the specific composition of the test sets and the flat or unfussy dimensions of the target cavity. The biologically relevant binding poses of the ligands, which are fundamentally sought after in the molecular docking are not necessarily close to the *ab initio* calculated energetic minima. Thus, the utilization of multiple alternative ligand 3D conformers in the cavity-based rigid docking should also improve the screening yield. The docking results vary significantly depending on the rotatable bond number of the molecules, the target protein's ligand-binding cavity properties, and, above all, the selected non-default settings. Not all permutations could be tested for the ligand preparation, and it is fully possible that there exist better settings for the tested conformer generators (Table 1). Nonetheless, the results show that the composition or "quality" of the conformers (Tables 2 and 3) is more important than their sheer quantity (Table 1) in the NIB screening.

The negative image-based rescoring (R-NiB; Figure 2) produces better enrichment than the original PLANTS docking (Table 4; Figure 7B) [16] or the standard NIB screening (Figure 1; Table 3) with the COX-2 test sets. The improvement is consistent with the DUD set, although the crudest or bulkiest NIB models did not improve the performance with the DUD-E set (Models I and IV in Table 4 and Figure 4). Accordingly, the R-NiB produced higher AUC values than the PLANTS docking with both the DUD and DUD-E sets using the alternative models (Table 4). In addition, the early enrichment improved over the docking with both test sets. The EFd 1% could be improved even further in comparison to the original docking if the scoring from both ShaEP and PLANTS was re-weighted (Figure 7A) for optimal performance in the consensus scoring (Table 4; Figure 7C).

The fact that R-NiB worked better than the NIB screening (Table 3 versus Table 4) is not surprising, because, during regular docking, the ligand conformers are sampled and optimized flexibly against the protein cavity. This structure-based sampling intrinsically affects the conformer composition and their placement against the protein's cavity for the better (Figure 6). Paradoxically, a clear downside of the R-NiB (Figure 2) in comparison to the NIB screening (Figure 1) is the inflated computational cost of the flexible docking sampling prior to the cavity-based rescoring. The rescoring itself is ultrafast (Figure 3), as no geometry optimization between the template model or the ligand conformers is needed [16]. The user simply outputs several poses for each docked ligand (e.g., $n = 10$) to have enough explicit solutions to re-rank and improve the docking performance utilizing the cavity's shape/charge information. The NIB screening (Figure 1) is faster than the regular docking precisely because the ligand conformers used in the rigid docking have been prepared in advance (Table 1), and these same

ligand sets can be used without bias for all targets [1,3,8]. In contrast, molecular docking, which treats the ligands or even the protein itself flexibly, produces more tailored and target-specific binding modes.

Flexible docking algorithms have been shown to reproduce experimentally-derived ligand binding poses (see, e.g., [33]), although they might not recognize them in all cases (Figure 6). Despite the relatively high expense of these computations, one can realistically expect that even the most costly docking simulations and post-processing schemes will become plausible if computing performance continues to improve in the post-silicon era [34]. Thus, the biggest hurdle of structure-based drug discovery (besides acquiring the relevant protein 3D structures) is not necessarily the ligand pose sampling or the computational efficiency, but the inability of the default docking scoring functions to recognize the high-affinity binding poses and the potent compounds from the vast screening databases [16,33]. Consequently, the development of reliable scoring functions and easy-to-use rescoring methodologies such as the R-NiB (Figure 2) [16] is needed to supplement the existing docking software.

4. Methods

4.1. Ligand Preparation

The test sets, containing both active ligands (ligs in Table 1) and decoy molecules that are assumed inactive (decs in Table 1) for cyclooxygenase-2 (COX-2) were acquired from the DUD (a Directory of Useful Decoys) [19] and DUD-E (a database of useful (docking) decoys -enhanced) [18] databases. The compounds were acquired in the SMILES (simplified molecular-input line-entry system) format for the 3D conversion, adding of partial charges, protonation/tautomerization, and generation of multiple low-energy 3D conformers. To avoid bias [35], the DUD set was downloaded originally in the MOL2 format and translated to the SMILES format using either OBABEL [21] or STRUCTCONVERT in MAESTRO 2017-1 (Schrödinger, LLC, New York, NY, USA, 2017).

The ligand preparation was performed using five 3D conformer generation routines (Table 1) to study the effect of the conformer composition to the efficiency of the NIB methodology. Either a single low-energy conformer or a set of multiple conformers was generated for each compound.

1. OBABEL. Open Babel Package or OBABEL 2.4.0 [21] was used to convert ligands from the SMILES format into the SYBYL MOL2 format. The protonation was set to match pH 7.4, and partial charges from the Merck Molecular Force Field 94 (MMFF94) [22] were incorporated. The 3D ligand conformers were generated using CONFAB in OBABEL [21].
2. MAESTRO. The 3D conversion of the ligands (SMILES-to-MOL2) was performed using LIGPREP in MAESTRO. The protonation was set to match pH 7.4, and potential tautomers were created. The ligand 3D conformer generation was performed with CONFGEN in MAESTRO using an OPLS3 (Optimized Potential for Liquid Simulations) force field [36].
3. MARVIN. MOLCONVERT 17.6.0 in MARVIN (ChemAxon) was used for the ligand 3D conversion (SMILES-to-MOL2). CXCALC 17.6.0 in INSTANT JCHEM (ChemAxon) was used to protonate and create the potential tautomers at pH 7.4 and generate 3D conformers for the ligands. The number of conformers was scaled from 1 to 64 according to the rotatable bond number calculated with MayaChemTools [37]. The partial charges for the ligands were set using the MMFF94 in OBABEL.
4. RDKit. RDKit open-sourced cheminformatics was used in the ligand 3D conversion (SMILES-to-MOL2) and conformer generation. The protonation at pH 7.4 was prepared using MARVIN, and partial charges were added using OBABEL with the MMFF94 force field [22].
5. PLANTS. The flexible docking poses (Table 1), which were outputted by the molecular docking software PLANTS 1.2 [17], were taken from a prior study [16] for the R-NiB testing (Figure 2). The initial ligand preparation, including the protonation and tautomerization at pH 7.4, the incorporation of OPLS3 [36] partial charges, and the 3D conversion (SMILES-to-MOL2) was done using LIGPREP in MAESTRO. The outputted docking pose number was set to 10 for each compound (Table 1). Notably, the flexible docking skipped more decoys than the ab initio generators, which biases the screening results to some extent (Table 1).

4.2. Protein 3D Structure Editing

The X-ray crystal structure of COX-2 with the bound inhibitor celecoxib (PDB: 3LN1) [2] was acquired from the Protein Data Bank (PDB) [38,39]. This PDB-entry is given as the model structure for COX-2 in the DUD-E, and, thus, it is used here to make the comparison easy against prior benchmarking studies. The BODIL Molecular Modelling Environment [5] is recommended for the examination of the screening protocols due to tested compatibility with the input/output files (Figures 1 and 2); however, other 3D viewer software should work as well. In the benchmarking example, the PDB-entry's A chain was extracted, and its amino acid residues and ligands were protonated using REDUCE 3.13 [24]. The protocol was also tested using an alternative COX-2 structure with the bound inhibitor SC-558 (PDB: 1CX2 [20]; A chain).

4.3. Negative Image Generation

The negative image, or NIB model generation, was performed using the default settings of PANTHER 0.18.21 [3], if not otherwise specified. The freely downloadable version of PANTHER [3] is available at the website (www.medchem.fi/panther). A few of the previous default settings were amended for this study (example file also available online). The fundamental input options and updates to the packing method selection in the model generation with PANTHER (Figures 4 and 5) are shortly explained below.

Center(s) (-cent) option designates the user-defined (X Y Z) center coordinate(s) for generating the NIB model. The centroid should be within a protein cavity that can accommodate the envisioned ligand binding (Figure 4A). If this centroid is defined at an unfavorable location or even outside the cavity of interest, the subsequent similarity screening with ShaEP [4] is likely to result in poor enrichment and/or wrong docking poses. In addition, the given centroid, together with the box radius (-brad) option (Figure 4A), defines where the packing of the filler atoms, constituting the negative image, begins.

Box radius (-brad) option is a key determinant of how the pocket is filled, together with the selected centroid (Figure 4A versus 4B). The packing of the filler atoms starts at the corner of the initial detection box, which is centered on the given centroid and has a vertex length of $2 \times$ box radius. Accordingly, an alternative box radius value can alter the lattice position used by the packing method and, ultimately, the reach of the resulting NIB model inside the cavity. The initial box is reduced into a sphere that, in turn, is defined by the box radius. In practice, the value for the box radius option should be set in a way that the model produces enrichment in the benchmarking (Figure 4C).

Keep (-keep)/Do not fill (-nofill) option is used to define a list of ligand residues with which the NIB model should not overlap. The area taken by these user-defined residues is excluded from the resulting NIB model. By default, some commonplace cofactors (FAD, NAP, NDP, NAI, NAD, and FDA) and water molecules (HOH and WAT) are listed for this option, but the list can be edited to include or exclude any residues of the input PDB file.

Multibox (-mbox) option makes it possible to generate a custom NIB model utilizing multiple close-by centroids. This option is especially useful when a single centroid is not enough to build a model that mimics the irregular shape of the target protein's cavity. For example, the negative image of a peptide-binding site or groove at the protein surface can be built by picking several neighboring centroids and utilizing them together with the multibox option (Figure 5A).

Basic multipoint (-bmp) option can be used to generate the pocket center based on any kind of residue included in the input PDB file (e.g., Ser516 in Figure 5B). The basic multipoint overrides the center option. This option is useful especially when there is a ligand bound at the cavity of interest to provide the centroid coordinate.

Ligand distance limit (-ldlim) option can be used to restrict the volume that the NIB model occupies based on a bound ligand residue in the cavity of the input PDB file (Figure 4D,E). When this option is used, only those filler atoms within the given distance of the ligand atoms are preserved in the resulting NIB model. While this option is generally very useful, the peril of applying too short

ligand distance is that the eventual model could mimic the existing bound ligand too closely (Figure 4D versus 4E), causing the early enrichment to fall (Figure 4C versus 4F).

Packing method (-pack) option, which is by default face-centered cubic (FCC), adds the filler atoms of the NIB model. The FCC has been altered to correspond the correct lattice in the updated version of PANTHER [3]. In addition, a body-centered cubic lattice (BCC) has now been implemented, and the cubic packing (CUBE) remains as the third option (Figure 4G). The FCC (0.74) has a higher packing fraction than the BCC (0.68; Figure 4B–E versus 4H) or the CUBE (0.52). While the FCC typically produces reasonable results, the BCC, for example, can produce better results depending on the cavity (Figure 4F versus 4I).

The input files and NIB models used in the benchmarking example (Figures 1 and 2) are given in the Supplementary Material.

4.4. Cavity-Based Rigid Docking and Similarity Comparison

The NIB screening (Figure 1) and the docking rescoring (Figure 2) are done using a similarity comparison algorithm ShaEP 1.1.2.1036 [16]. Both the shape and electrostatics of the ligand conformers are compared against the template NIB model with an equal amount of weight (electrostatics = 0.5 versus shape = 0.5) to produce the best match. It should be noted that the early enrichment values and molecule rankings can vary ~1–2% between otherwise identical NIB screening runs. These minor discrepancies likely result from arbitrary features of the geometry optimization algorithm, and the results may vary more if different versions of ShaEP algorithm are used. In the R-NiB, several ligand poses ($n = 10$) outputted by the molecular docking software PLANTS [17] are not geometry optimized, i.e., docked rigidly (-noopt) in respect to the cavity-based template model, but they are only rescored using ShaEP [4].

4.5. Consensus Scoring

By combining the ShaEP-based R-NiB scoring with the PLANTS-based molecular docking scoring, it is possible to improve the flexible docking yield further (Figure 7). This involves the normalization of both the ChemPLP scoring of PLANTS and the ShaEP scoring into a matching range from 1 to 0 and the combining of the two sets of values to acquire a consensus score. The approach used here does not focus on the same ligand poses in the scoring process; instead, the best values produced by PLANTS and ShaEP for each screened compound (not necessarily the same conformer) are used. The weighting between the two scoring functions is done using a BASH script (consensus.bash) given in the Supplementary Material.

4.6. Figure and Table Preparation

Figures 1–6 were prepared using BODIL [5], MOLSCRIPT 2.1.2 [40], RASTER3D 3.0.2 [41], and VMD 1.9.2 [42]. ROCKER 0.1.4 [6] was used to plot the receiver operating characteristics (ROC) curves with the semi-log₁₀ scale (only x -axis logarithmic) and to calculate the early enrichment and area under curve (AUC) values in Tables 2–4. The enrichment factors were calculated as true positive rates when 1 or 5% of the decoys have been found (EF_d 1% or EF_d 5%), and the standard deviation of the AUC was acquired using the Wilcoxon statistic [6,43].

5. Conclusions

This study described the practical steps and software settings to be used during the negative image-based (NIB; Figure 1) screening or the negative image-based rescoring (R-NiB; Figure 2). Cyclooxygenase-2 (COX-2; Figure 1) was used as a benchmarking example for the NIB protocol from the ligand 3D conformer generation, the protein 3D structure preparation, and the NIB model generation to the similarity comparison or rigid docking (Figure 3). The input files, specific software settings, easy-to-use scripts, and terminal commands themselves were provided with thorough user guidance. The issues that arise from this practical screening example were detailed; moreover, other

software settings relevant for the NiB implementation with different targets were discussed. A special focus was put on testing the applicability of different ligand conformer generation software for the NiB screening usage (Tables 1–3). Moreover, practical instructions were provided for the rescoring of flexible docking solutions output by the docking algorithm PLANTS using the R-NiB protocol (Figure 2). The R-NiB produces better enrichment than either the NiB screening or the flexible docking with the COX-2 example—a further boost is provided by the consensus scoring that combines the original docking scoring and the R-NiB scoring for optimal enrichment (Table 4; Figure 7). In summary, the study provides clear-cut instructions on how to perform rigid docking or docking rescoring with the NiB methodology using non-commercial software and a practical benchmarking example.

Supplementary Materials: Supplementary materials can be found at <http://www.mdpi.com/1422-0067/20/11/2779/s1>.

Author Contributions: Conceptualization, O.T.P. and P.A.P.; methodology, M.A.; investigation, M.A. and S.T.K.; validation, M.A. and S.T.K.; formal analysis, M.A. and S.T.K.; software, M.A.; data curation, M.A., S.T.K., and O.T.P.; visualization, M.A., S.T.K., P.A.P., and S.P.N.; writing—original draft preparation, M.A., S.T.K., and P.A.P.; writing—review and editing, S.P.N., O.T.P., and P.A.P.; project administration, P.A.P.; resources, O.T.P.; funding acquisition, O.T.P. and P.A.P.; supervision, P.A.P.

Funding: This research was funded by the Academy of Finland (315492 to S.P.N.), Jenny and Antti Wihuri Foundation, and Emil Aaltonen Foundation (M.A.). The Turku University Foundation is acknowledged for personal grant to S.T.K. The Finnish IT Center for Science (CSC) is acknowledged for generous computational resources (O.T.P.; Project Nos. jyy2516 and jyy2585).

Acknowledgments: Jason Ahokas is thanked for reviewing the protocol steps.

Conflicts of Interest: The authors declare no conflict of interest.

References

1. Virtanen, S.I.; Pentikäinen, O.T. Efficient virtual screening using multiple protein conformations described as negative images of the ligand-binding site. *J. Chem. Inf. Model.* **2010**, *50*, 1005–1011. [[CrossRef](#)] [[PubMed](#)]
2. Wang, J.L.; Limburg, D.; Graneto, M.J.; Springer, J.; Hamper, J.R.B.; Liao, S.; Pawlitz, J.L.; Kurumbail, R.G.; Maziasz, T.; Talley, J.J.; et al. The novel benzopyran class of selective cyclooxygenase-2 inhibitors. Part 2: The second clinical candidate having a shorter and favorable human half-life. *Bioorganic Med. Chem. Lett.* **2010**, *20*, 7159–7163. [[CrossRef](#)] [[PubMed](#)]
3. Niinivehmas, S.P.; Salokas, K.; Lätti, S.; Raunio, H.; Pentikäinen, O.T. Ultrafast protein structure-based virtual screening with Panther. *J. Comput. Aided. Mol. Des.* **2015**, *29*, 989–1006. [[CrossRef](#)] [[PubMed](#)]
4. Vainio, M.J.; Puranen, J.S.; Johnson, M.S. ShaEP: Molecular overlay based on shape and electrostatic potential. *J. Chem. Inf. Model.* **2009**, *49*, 492–502. [[CrossRef](#)] [[PubMed](#)]
5. Lehtonen, J.V.; Still, D.-J.; Rantanen, V.-V.; Ekholm, J.; Björklund, D.; Iftikhar, Z.; Huhtala, M.; Repo, S.; Jussila, A.; Jaakkola, J.; et al. BODIL: A molecular modeling environment for structure-function analysis and drug design. *J. Comput. Aided. Mol. Des.* **2004**, *18*, 401–419. [[CrossRef](#)] [[PubMed](#)]
6. Lätti, S.; Niinivehmas, S.; Pentikäinen, O.T. Rocker: Open source, easy-to-use tool for AUC and enrichment calculations and ROC visualization. *J. Cheminform.* **2016**, *8*, 1–5. [[CrossRef](#)] [[PubMed](#)]
7. Vainio, M.J.; Johnson, M.S. Generating conformer ensembles using a multiobjective genetic algorithm. *J. Chem. Inf. Model.* **2007**, *47*, 2462–2474. [[CrossRef](#)]
8. Niinivehmas, S.P.; Virtanen, S.I.; Lehtonen, J.V.; Postila, P.A.; Pentikäinen, O.T. Comparison of virtual high-throughput screening methods for the identification of phosphodiesterase-5 inhibitors. *J. Chem. Inf. Model.* **2011**, *51*, 1353–1363. [[CrossRef](#)]
9. Niinivehmas, S.; Postila, P.A.; Rauhamäki, S.; Manivannan, E.; Kortet, S.; Ahinko, M.; Huuskonen, P.; Nyberg, N.; Koskimies, P.; Lätti, S.; et al. Blocking oestradiol synthesis pathways with potent and selective coumarin derivatives. *J. Enzyme Inhib. Med. Chem.* **2018**, *33*, 743–754. [[CrossRef](#)]
10. Rauhamäki, S.; Postila, P.A.; Niinivehmas, S.; Kortet, S.; Schildt, E.; Pasanen, M.; Manivannan, E.; Ahinko, M.; Koskimies, P.; Nyberg, N.; et al. Structure-Activity Relationship Analysis of 3-Phenylcoumarin-Based Monoamine Oxidase B Inhibitors. *Front. Chem.* **2018**, *6*, 1–18. [[CrossRef](#)]

11. Juvonen, R.O.; Rauhamäki, S.; Kortet, S.; Niinivehmas, S.; Troberg, J.; Petsalo, A.; Huuskonen, J.; Raunio, H.; Finel, M.; Pentikäinen, O.T. Molecular Docking-Based Design and Development of a Highly Selective Probe Substrate for UDP-glucuronosyltransferase 1A10. *Mol. Pharm.* **2018**, *15*, 923–933. [[CrossRef](#)] [[PubMed](#)]
12. Niinivehmas, S.P.; Manivannan, E.; Rauhamäki, S.; Huuskonen, J.; Pentikäinen, O.T. Identification of estrogen receptor a ligands with virtual screening techniques. *J. Mol. Graph. Model.* **2016**, *64*, 30–39. [[CrossRef](#)] [[PubMed](#)]
13. Rauhamäki, S.; Postila, P.A.; Lätti, S.; Niinivehmas, S.; Multamäki, E.; Liedl, K.R.; Pentikäinen, O.T. Discovery of Retinoic Acid-Related Orphan Receptor γ t Inverse Agonists via Docking and Negative Image-Based Screening. *ACS Omega* **2018**, *3*, 6259–6266. [[CrossRef](#)] [[PubMed](#)]
14. Nicholls, A.; McGaughey, G.B.; Sheridan, R.P.; Good, A.C.; Warren, G.; Mathieu, M.; Muchmore, S.W.; Brown, S.P.; Grant, J.A.; Haigh, J.A.; et al. Molecular Shape and Medicinal Chemistry: A Perspective. *J. Med. Chem.* **2010**, *53*, 3862–3886. [[CrossRef](#)] [[PubMed](#)]
15. Wang, T.; Wu, M.; Chen, Z.; Chen, H.; Lin, J.; Yang, L. Fragment-Based Drug Discovery and Molecular Docking in Drug Design. *Curr. Pharm. Biotechnol.* **2015**, *16*, 11–25. [[CrossRef](#)] [[PubMed](#)]
16. Kurkinen, S.T.; Niinivehmas, S.; Ahinko, M.; Lätti, S.; Pentikäinen, O.T.; Postila, P.A. Improving Docking Performance Using Negative Image-Based Rescoring. *Front. Pharmacol.* **2018**, *9*, 1–15. [[CrossRef](#)]
17. Korb, O.; Stützel, T.; Exner, T.E. Empirical scoring functions for advanced Protein-Ligand docking with PLANTS. *J. Chem. Inf. Model.* **2009**, *49*, 84–96. [[CrossRef](#)]
18. Mysinger, M.M.; Carchia, M.; Irwin, J.J.; Shoichet, B.K. Directory of useful decoys, enhanced (DUD-E): Better ligands and decoys for better benchmarking. *J. Med. Chem.* **2012**, *55*, 6582–6594. [[CrossRef](#)]
19. Huang, N.; Shoichet, B.K.; Irwin, J.J. Benchmarking sets for molecular docking. *J. Med. Chem.* **2006**, *49*, 6789–6801. [[CrossRef](#)]
20. Kurumbail, R.G.; Stevens, A.M.; Gierse, J.K.; McDonald, J.J.; Stegeman, R.A.; Pak, J.Y.; Gildehaus, D.; Miyashiro, J.M.; Penning, T.D.; Seibert, K.; et al. Structural basis for selective inhibition of cyclooxygenase-2 by anti-inflammatory agents. *Nature* **1996**, *384*, 644–648. [[CrossRef](#)]
21. O’Boyle, N.M.; Banck, M.; James, C.A.; Morley, C.; Vandermeersch, T.; Hutchison, G.R. Open Babel: An Open chemical toolbox. *J. Cheminform.* **2011**, *3*, 1–14. [[CrossRef](#)] [[PubMed](#)]
22. Halgren, T.A. Potential energy functions. *Curr. Opin. Struct. Biol.* **1995**, *5*, 205–210. [[CrossRef](#)]
23. Anantharajan, J.; Koski, M.K.; Kursula, P.; Hieta, R.; Bergmann, U.; Myllyharju, J.; Wierenga, R.K. The structural motifs for substrate binding and dimerization of the α subunit of collagen prolyl 4-hydroxylase. *Structure* **2013**, *21*, 2107–2118. [[CrossRef](#)] [[PubMed](#)]
24. Word, J.M.; Lovell, S.C.; Richardson, J.S.; Richardson, D.C. Asparagine and Glutamine: Using Hydrogen Atom Contacts in the Choice of Side-chain Amide Orientation. *J. Mol. Biol.* **1999**, *285*, 1735–1747. [[CrossRef](#)] [[PubMed](#)]
25. Olsson, M.H.M.; Søndergaard, C.R.; Rostkowski, M.; Jensen, J.H. PROPKA3: Consistent Treatment of Internal and Surface Residues in Empirical p K a Predictions. *J. Chem. Theory Comput.* **2011**, *7*, 525–537. [[CrossRef](#)] [[PubMed](#)]
26. Søndergaard, C.R.; Olsson, M.H.M.; Rostkowski, M.; Jensen, J.H. Improved Treatment of Ligands and Coupling Effects in Empirical Calculation and Rationalization of p K a Values. *J. Chem. Theory Comput.* **2011**, *7*, 2284–2295. [[CrossRef](#)] [[PubMed](#)]
27. Halgren, T. New Method for Fast and Accurate Binding-site Identification and Analysis. *Chem. Biol. Drug Des.* **2007**, *69*, 146–148. [[CrossRef](#)]
28. Halgren, T.A. Identifying and Characterizing Binding Sites and Assessing Druggability. *J. Chem. Inf. Model.* **2009**, *49*, 377–389. [[CrossRef](#)]
29. Wagner, J.R.; Sørensen, J.; Hensley, N.; Wong, C.; Zhu, C.; Perison, T.; Amaro, R.E. POVME 3.0: Software for Mapping Binding Pocket Flexibility. *J. Chem. Theory Comput.* **2017**, *13*, 4584–4592. [[CrossRef](#)]
30. Morris, G.; Huey, R. AutoDock4 and AutoDockTools4: Automated docking with selective receptor flexibility. *J. Comput. Chem.* **2009**, *30*, 2785–2791. [[CrossRef](#)]
31. Ebejer, J.P.; Morris, G.M.; Deane, C.M. Freely available conformer generation methods: How good are they? *J. Chem. Inf. Model.* **2012**, *52*, 1146–1158. [[CrossRef](#)] [[PubMed](#)]
32. Friedrich, N.O.; De Bruyn Kops, C.; Flachsenberg, F.; Sommer, K.; Rarey, M.; Kirchmair, J. Benchmarking Commercial Conformer Ensemble Generators. *J. Chem. Inf. Model.* **2017**, *57*, 2719–2728. [[CrossRef](#)] [[PubMed](#)]
33. Chaput, L.; Mouawad, L. Efficient conformational sampling and weak scoring in docking programs? Strategy of the wisdom of crowds. *J. Cheminform.* **2017**, 1–18. [[CrossRef](#)] [[PubMed](#)]

34. Service, R.F. Chipmakers look past Moore's law, and silicon. *Science* **2018**, *361*, 321. [[CrossRef](#)] [[PubMed](#)]
35. Zoete, V.; Schuepbach, T.; Bovigny, C.; Chaskar, P.; Daina, A.; Röhrig, U.F.; Michielin, O. Attracting cavities for docking. Replacing the rough energy landscape of the protein by a smooth attracting landscape. *J. Comput. Chem.* **2016**, *37*, 437–447. [[CrossRef](#)] [[PubMed](#)]
36. Harder, E.; Damm, W.; Maple, J.; Wu, C.; Reboul, M.; Xiang, J.Y.; Wang, L.; Lupyán, D.; Dahlgren, M.K.; Knight, J.L.; et al. OPLS3: A Force Field Providing Broad Coverage of Drug-like Small Molecules and Proteins. *J. Chem. Theory Comput.* **2016**, *12*, 281–296. [[CrossRef](#)] [[PubMed](#)]
37. Sud, M. MayaChemTools: An Open Source Package for Computational Drug Discovery. *J. Chem. Inf. Model.* **2016**, *56*, 2292–2297. [[CrossRef](#)]
38. Berman, H.M.; Westbrook, J.; Feng, Z.; Gilliland, G.; Bhat, T.N.; Weissig, H.; Shindyalov, I.N.; Bourne, P.E. The protein data bank. *Nucleic Acids Res.* **2000**, *28*, 235–242. [[CrossRef](#)]
39. Burley, S.K.; Berman, H.M.; Kleywegt, G.J.; Markley, J.L.; Nakamura, H.; Velankar, S. Protein Data Bank (PDB): The Single Global Macromolecular Structure Archive. *Methods Mol. Biol.* **2017**, *1607*, 627–641.
40. Kraulis, P.J. MOLSCRIPT: A program to produce both detailed and schematic plots of protein structures. *J. Appl. Crystallogr.* **1991**, *24*, 946–950. [[CrossRef](#)]
41. Merritt, E.A.; Murphy, M.E.P. Raster3D Version 2.0. A program for photorealistic molecular graphics. *Acta Crystallogr. Sect. D Biol. Crystallogr.* **1994**, *50*, 869–873. [[CrossRef](#)] [[PubMed](#)]
42. Humphrey, W.; Dalke, A.; Schulten, K. VMD: Visual molecular dynamics. *J. Mol. Graph.* **1996**, *14*, 33–38. [[CrossRef](#)]
43. Hanley, A.J.; McNeil, J.B. The Meaning and Use of the Area under a Receiver Operating Characteristic (ROC) Curve. *Radiology* **1982**, *143*, 29–36. [[CrossRef](#)] [[PubMed](#)]



© 2019 by the authors. Licensee MDPI, Basel, Switzerland. This article is an open access article distributed under the terms and conditions of the Creative Commons Attribution (CC BY) license (<http://creativecommons.org/licenses/by/4.0/>).